# Photons and Subatomic Particles. What can these tell us about Cements, Moisture, and Nuclear Waste?

PhD Thesis

James E Vigor
The Department of Materials Science and Engineering
The University of Sheffield

May 2019

# Abstract

This thesis shows the use of advanced characterisation instrumentation to provide novel and detailed insights about the structural features of hydrated Portland cements and other cementitious systems where Portland cement has been partially substituted for an alternative, in this case blast furnace slag. Three methods were applied in this thesis to characterise the formation and chemistry of hydrates across the first hours and days after the reaction has been triggered, the properties of the pore volume, and the uptake of water into the specimen.

The thesis begins with the identification of a number of gaps in the literature and areas in to which research might extend, in Chapter 2. For example, it was apparent in the literature that very few data are available regarding the morphology and distribution of hydrates within the material across the first hours of the hydration reaction, and that the uptake of moisture in similar materials has only been observed a single time in a semi in-situ manner.

In Chapter 3, the blast furnace slag and Portland cement materials used were chemically and physically characterised. This involves qualitative X-ray diffraction, thermogravimetry, and particle size and shape analysis. In hydrated pastes based on blended cements, chemical analysis was conducted and the consumption of clinker phases and the formation of hydrates across the first year of the hydration reaction shown.

In Chapter 4, in-situ X-ray diffraction was applied to the hydrating material to reveal the chemistry of the early period of the cement hydration reaction, which is very challenging to otherwise observe. The application of the partial or no known crystal structure method to observe the early age consumption of the blast furnace slag was demonstrated, which in combination with the Rietveld method provides the phase assemblage across the first days of the reaction. The consumption of anhydrous materials and the formation of hydrates was correlated to the thermal output and the formation of hydrates showed good agreement with the observed heat flow.

In Chapter 5, computed microtomography was applied in-situ to temporally changing samples of both pure Portland cement and blended cementitious systems. This was carried out to directly observe the morphology of the hydration reaction, and how the hydration re-

action forms and defines the pore volume within the material. The formation of precipitates and deposition of hydrates was shown across the first 12 hours of the reaction. Similarly to the results presented in Chapter 4, the data produced were correlated with the thermal output, revealing the morphological processes occurring within the microstructure and the times at which these are triggered within the reaction. In completing this, automated methods of reconstruction, segmentation, and data rendering were applied, which are shown in the supplementary information. This removes the human from the process beyond the application of original parameters, which subsequently remain constant throughout. This appears to be the first application of true in-situ microtomography to the field of cement hydration.

Microtomography was then applied for a second time in Chapter 6 to study the pore volume in closer detail, characterising a distribution of pore sizes by direct imaging and avoiding the assumptions made by the Washburn equation. Mercury porosimetry requires assumptions to be made regarding the pore geometry which while perhaps correct for some materials are incorrect for cements. This invalidates the pore size distribution. Again the entire process was automated, and is shown in supplementary information.

In the final chapter moisture uptake was directly observed and quantified in the specimen by neutron radiography, which reveals the accessible pore volume and some of the potential flaws in the capillary suction test. This links the formation of hydrates to the geometric properties of the pore structure, and finally to the dynamic uptake process which occurs within the structure itself. Data were captured in-situ across 24 hours by neutron imaging, which provides good greyscale contrast between permeating moisture and the specimen and allows for a straightforward segmentation. Data were calibrated to a known moisture content, which allows for the production of spatially resolved profile within a specimen, and the extraction of the total porosity assuming full saturation in non-zero array elements. It was also possible to generate a semi-quantitative distribution of moisture contents within the specimen and observe how this changes as the degree of hydration within the specimen increases.

# Acknowledgements

There are countless people who deserve thanks for their input and help with this thesis and realistically this bit could probably go on for quite a few pages. Firstly I wish to thank my academic supervisors John Provis and Susan Bernal and my industrial supervisor Hugh Godfrey. I must also thank those who have contributed from a wider perspective to my supervision, Neil Hyatt, Claire Corkhill, Nick Collier, Oday Hussein, and Ben Palmer.

I would like at this point to thank my parents Margaret and Andrew, and my brother William, who have provided me with support throughout also require acknowledgement for their help and support with this thesis.

It would be dismissive not to also thank the other students of PGR3 and K02 who have provided me with countless hours of support and opportunities to discuss work and to throw ideas around. By no means is this list is exhaustive. I would like to thank by name (and in no particular order) Rupert, Mehul, Hilmi, Silvia, Shishir, Andy, Dilly, Joe, Sam, Laura, Steph, Luke, Andy, Colleen, Sean, Dale, Robert, Rita, Toni, Sarah, Lewis, Joe, Adam, Jack, the many Dans, and the other James. The following friends have also pushed me along and (mostly) given me encouragement: George, Rob, Ashley, Mark, Stefan, Jade, and Sarah.

The following people have provided support, advice, and opportunities to work at the facilities used in this thesis (and plenty of advice on data processing). Here I would like to thank by name Xianghui Xiao, Chiu Tang, Claire Murray, Pavel Trtik, and Jan Hovind.

The following people are owed special place here. These are the ones from the bits I can actually remember... Emily, Becky, Matt, Adrian, Connor, David, Michael and Schonke, Ray, Ollie, John, Rob, Francis, Helen, Sarah, Ewa, Dr. Watve, the guy who played the guitar, and the guy and his wife who sometimes brought the therapy dogs around. Thanks, all of you.

Velvet. Face. Church. Daisy. Red.

# Contributors

In this thesis, these contributors provided the following input to each chapter.

### Chapter 4

C. C. Tang was the principal beamline scientist for this experiment, and had overarching responsibility for operation of the instrument, and maintenance of the beamline. C. Murray was the beamline support scientist. C. L. Corkhill designed the experiment, submitted the experimental proposal and carried out sample preparation. N. C. Hyatt provided input on the experimental design and submission of the proposal, and assisted with sample preparation. S. A. Bernal provided supervisory input. J. L. Provis provided supervisory input and advice on data analysis.

### Chapters 5 and 6

X. Xaio was the principal investigator at the 2-BM beamline, and provided input on experiment execution, design, and data processing / reconstruction. S. A. Bernal provided supervisory input. J. L. Provis provided supervisory input, advice on data processing, and advice on material thermodynamics.

### Chapter 7

D. Prentice took a supporting role at the beamline and assisted with sample preparation, experiment design, and execution of the experiment. P. Trtik was the principal beamline scientist for this experiment and took a role training on beamline use, experimental configuration, execution of the experiment, and data analysis and post-processing. S. A. Bernal provided supervisory input. J. L. Provis provided supervisory input and advice on data processing and visualisation.

# Contents

# List of Figures

# List of Tables

# Abbreviations, Symbols, and Cement Chemistry Notation

The following abbreviations and symbols are used throughout this thesis.

| Symbol | Definition |
|---|---|
| $C_3S$ | Tricalcium silicate compound, $3\,CaO{\cdot}SiO_2$ |
| $C_2S$ | Dicalcium silicate compound, $2\,CaO{\cdot}SiO_2$ |
| $C_3A$ | Tricalcium aluminate compound, $3\,CaO{\cdot}Al_2O_3$ |
| $C_4AF$ | Tetracalcium aluminoferrite compound, $4\,CaO{\cdot}Al_2O_3{\cdot}Fe_2O_3$ |
| PC | Portland Cement |
| CEM-I | Portland Cement with up to 5% of additional constituents. |
| BFS | Blast furnace slag |
| XRD / XRPD | X-ray (Powder) Diffraction |
| TG | Thermogravimetry (thermal analysis) |
| MIP | Mercury Intrusion Porosimetry |
| CT / CAT / $\mu$CT | Computed (Axial / Micro-) Tomography |
| NEUTRA | Neutronenradiographie (German) |
| DLS | Diamond Light Source |
| APS | Advanced Photon Source |
| PSI | Paul Scherrer Institute |
| SINQ | Swiss Spallation Neutron Source |

# Chapter 1

# Introduction

Portland cement is the most widely used industrial material on Earth, produced in quantities of around 4 Gt p.a., and ubiquitous in application in modern society. Cements are used in almost every structure built in the modern age. From roads, to homes, to bridges, to airports, to skyscrapers, and for the encapsulation of nuclear waste [1]; you are guaranteed to find this material somewhere. However, in spite of the use of these materials to support just about everything society does, there remain some unanswered questions regarding the chemistry and how this affects the performance of these materials.

The strength and durability of cements and concretes, and thus also their sustainability credentials, are controlled by the microstructure of the hardened cement paste, and particularly by the nanometre- to micron-scale porosity inherent within the hardened cementitious matrix. This porosity results from the inability of hydrate phases to entirely fill the space within the hardened material, which is governed by the mechanism by which they form and grow to fill the initially fluid-filled spaces as cement paste hydrates. The development of a fuller understanding of the early-age development of these characteristics is therefore critical in producing materials which are durable, sustainable, and offer excellent mechanical properties at both early age and for years into the future.

## 1.1 The Fundamental Aim

The first thing to try to understand is the chemistry of the material. For example, an incorrect cement composition may result in a wholly inappropriate setting behaviour. If certain phases remain present within the material and some kind of groundwater interaction occurs some degradation process will almost certainly result. Of course for this to happen the sample itself must allow for the ingress of water, so it is important to try to form an uncerstanding of this, and the methods which might be used to quantify movement of moisture into a concrete.

Intruded water may, for example, freeze and expand, resulting in fracture of the matrix, which is another degradation process by which these materials might eventually fail.

## 1.2 What Could Possibly Go Wrong?

As well as being used by the construction industry, blended cements, in this case with a very high percentage of substitution, are used widely for the encapsulation of intermediate level radioactive wastes [1]. The cement provides both a barrier to radioactivity and a solid monolithic body in which the waste material might be contained. However, the safety of these wastes is wholly dependent on the ability of the structure to retain the encapsulated material and prevent this from entering the biosphere. Degradation processes in Portland cement based binders will have a strong and almost complete influence on this, and so it is important to form a thorough understanding of both how these react and how these might fail.

The cost of repairing damaged and degraded structures globally runs into billions of pounds per year. The likely outcome if society fails to do this properly, is that this figure of billions could end up a lot higher. Moreover, these materials are used for the encapsulation of intermediate level radioactive wastes, which places further importance on the understanding of these cements.

Taking a closer look at the statistics, it may be seen that in April 2016 [2] the projected volume of intermediate level waste by the year 2125 was 449,000 $m^3$. In the United Kingdom, intermediate level wastes are defined as wastes which exceed the upper boundaries for low level wastes (4 GBq $t^{-1}$ $\alpha$ and 12 GBq $t^{-1}$ $\beta$ & $\gamma$ in the UK)[1] but are not significantly heat generating and are therefore suitable candidates for encapsulation in a material such as a cement.

In the nuclear industry, cements do not find their only applications in the encapsulation of wastes. These materials are also used for the production and backfilling of storage vaults such as those found in the planned deep geological disposal facility [3], which remains in the pre-planning stage, and silos and ponds found on the Sellafield site. This extends the importance of having a fuller understanding of these materials. Cements are not only direcly used for waste encapsulation; there are additional barriers which surround the product. The materials which perform this task products must also show sufficient durability for this purpose.

[1] Nucleus decay reactions per second.

## 1.3 Why Do We Need High Resolution?

The solidification process of cement involves a complex sequence of chemical reactions, involving and mediated by water, as the initially-present anhydrous cement minerals are converted to an assemblage of strength-giving hydrates. However, due to the challenges associated with conducting in situ analysis of solid-fluid reactions involving up to 10 different mineral phases, taking place at a pH of up to 13.5, it has not yet been possible to fully characterise the first minutes to hours of this process, which determine the setting and hardening of the cement. It is similarly challenging to observe the pore structure, and the processes occurring therein during uptake of water into the material, which also occurs rapidly.

During the first minutes, crystalline calcium silicate, sulphate, and aluminate minerals present in the cement dissolve, and hydrate products then precipitate on and around residual unreacted particles [4, 5]. This reaction is, at least initially, strongly exothermic. As hydrate phases grow they begin to interlock, increasing the strength of the material [6]. However, key questions regarding the nature, morphology, structure, and distribution of hydration products during this early reaction remain, as yet, unanswered [4].

This gives us several challenges. Firstly it is most certainly possible to arrest the hydration reaction, as many do. However, this causes damage to the microstructure [7] and to a certain extent invalidates the result (see Chapter 2). If the reaction cannot be restarted, stopping hydration in this way will inevitably yield natural sample variation; many samples are needed to form a full picture of the reaction and each must be tested at precisely the correct time. While it is possible to observe the reaction, and this has previously been done well as shown in Chapter 2, this results in it being impossible to track a contiguous particle, region of interest, or specimen as a whole across the duration of the reaction. Using a high resolution and high flux detector it is possible to effectively freeze a snapshot of the reaction and overcome limitations in both spatial and temporal resolution which might be present on both laboratory X-ray tomographic and diffraction instrumentation.

Dynamic processes occuring within the structure over a longer period are also difficult to accurately characterise. The commonly used testing methods for observing moisture uptake, which governs the durability of the material, make numerous assumptions. For example, properties as simple as the apparent depth of the wetting front into the material are simply assumed to be represented by a method which at best provides a qualitative approximation of the true nature of this process (see Chapters 2 and 7). While these test methods might be acceptable for use on, for example, a building site or as a comparison between identically prepared samples, they are simply inadequate in both temporal or spatial resolution where processes occur over a short time period and fully quantitative data are required. Tests such

as the ASTM C1585 capillary suction test [8] also yield no information about either the distribution of moisture within the specimen, or direct quantification of the pore volume into which the moisture is intruding, which are of interest and importance.

## 1.4 This Thesis

In this thesis, several techniques were applied and exploited with the aim of expanding both the methods available to characterise cements and the knowledge base surrounding highly substituted cement-based materials. The thesis begins with a review of the literature in Chapter 2. The review starts with hydration chemistry followed by a look at the pore structure, how it forms, and how this has typically been evaluated. The shortcomings with these techniques are also discussed. Finally the review looks at how the moisture uptake in specimens is observed, again by laboratory techniques and more advanced methods, and how these tests may provide an invalid quantification.

The chemistry of the hydration reaction was then studied in Chapter 4, both of Portland cement and of substituted materials. This formed the application of a technique to a beamline experiment for the first time, with the aim of observing hydration using a quantitative method. This process formed the the basis of our understanding; how does our material begin to react?

Chapter 5 delves into the morphology of hydrate formation in three-dimensions in real time, which appears to be the first application of this technique to a full-phase representative cement material. This also revealed processes in the pore volume, such as the formation of precipitates, where these formed within the volume, and where agglomeration eventually occured. Following this, Chapter 6 looks more closely at how the pore volume formed over a longer duration; the pore volume was observed within samples up to 25 years of age. These data were analysed through the implementation of a computational method which mitigates the assumptions made by the Washburn equation [9, 10] on wider diameter pores.

Chapter 7 looks directly at the uptake of moisture into the cement by quantitative neutron imaging. The volume into which intrusion is occurring was revealed which yielded the *true* location of the front and the spatial distribution of moisture within the sample. While this was not the first application of this technique to a highly substituted cement, this does present an enormous expansion of the knowledge base surrounding the water uptake mechanism in these slag-blended materials: the materials used for radioactive waste cementation.

# Chapter 2

# The Challenge of Understanding Cement

Portland cement is the most widely used material on Earth other than water (which in itself is required to form a concrete in any case), but a full understanding as to precisely how this material reacts does not yet exist. During the hydration reaction of cement, a fluid suspension of particles reacts to form a solid monolithic binder. The correct characterisation of cements is complex. Cement consists of numerous crystalline precursor compounds, and both crystalline and disordered hydration products. These are summarised here in Table 2.1, and were identified in detail during the initial characterisation of materials used in this thesis in Chapter 3.

## 2.1 Introducing the Portland Cement Compounds

The most abundant compound found within Portland cement is tricalcium silicate, which makes up in excess of 60% of the anhydrous material by the BS EN 197-1 standard [11]. This is commonly denoted as $C_3S$ in cement chemist notation[1], which is used in order to provide some simplification to descriptions of the reactions occurring during hydration of the material. Clinker phases may also contain minor impurities, for example alumina or magnesia. In addition to this, cement contains a dicalcium silicate phase, written as $C_2S$. This phase reacts far more gradually and contributes to the strength development of the material across a longer duration. The tricalcium aluminate clinker phase, denoted as $C_3A$, is also found, which assists with early set of the material. If the reaction of this phase is not properly controlled the material flash sets which is, of course, completely unacceptable. A further clinker phase, tetracalcium aluminoferrite denoted as $C_4AF$, is found within the material. Similarly to the $C_2S$ this phase reacts slowly and contributes to the later age strength gain.

[1] C - CaO, S - $SiO_2$, A - $Al_2O_3$, H - $H_2O$, $\bar{C}$ - $CO_2$, $\bar{S}$ - $SO_3$

A number of other compounds are often found. In order to moderate the hydration of $C_3A$ and prevent flash set, some kind of calcium sulphate ($CaSO_4 \cdot nH_2O$) is added to the clinker. Typically, this is found in the form of gypsum, where $n = 2$, though calcium sulphate may actually be found as several crystalline structures which are either intentionally added to the material, or found as a result of decomposition of gypsum in the cement kiln. Anhydrite, where $n = 0$, or hemihydrate, where $n = 0.5$, are other examples of compounds which may be present. During hydration these cause the formation of ettringite within the microstructure, which is referred to as AFt. Once sulphates are consumed the and there is still surplus aluminate present, ettringite becomes unstable and forms an AFm, or an alumina ferric oxide monosulphate, phase.

In addition to some kind of sulphate bearing phase, limestone, or calcite, is also added to the cement to act as a grinding aid and prevent agglomeration of the material.

Table 2.1: The four cement clinker phases.

| Name | CCN | Formula | Common Name |
|---|---|---|---|
| Tricalcium silicate | $C_3S$ | $Ca_3SiO_5$ | Alite |
| Dicalcium silicate | $C_2S$ | $Ca_2SiO_4$ | Belite |
| Tricalcium aluminate | $C_3A$ | $Ca_2Al_2O_6$ | Aluminate |
| Tetracalcium aluminoferrite | $C_4AF$ | $Ca_2(Al, Fe)_2O_5$ | Ferrite |

Tricalcium and dicalcium silicates hydrate to form a calcium silicate hydrate type gel, which is denoted as C-S-H in cement chemist notation.

### 2.1.1 This Review

This review is a summary of the research into cement hydration in the context of this thesis. The methods applied here are discussed alongside a critique of the laboratory and testing methods for durability and the function of the pore structure. These make up a part of the difficulty in correctly carrying out a full characterisation of these materials.

To provide some context to these tests, the chemical formation of the material must first be understood. The tests discussed are very widely used in the civil engineering industry, and attempt to provide us with a simple unified method by which samples may be analysed. These are important when considering the longer term durability of these materials, as they provide the fundamental information required to come to some conclusion as to the suitability of the product.

This review is presented in three parts, beginning with a quick overview of hydration chemistry. This leads into a discussion about how the pore structure forms. Finally, the tests used to characterise the pore volume are examined, including the introduction of more advanced characterisation techniques using high-end laboratory equipment and radiographic sources.

It would be neglectful to limit this review solely to cements; some techniques have simply not found an application in this field in spite of having significant potential. For some techniques, data are either lacking or simply non-existent. Test methods for which this might be the case are also identified here, and the development of these also discussed.

## 2.2 Hydration

The hydration of Portland cement is a complex interdependent process, which occurs within the solid and liquid phases of the reacting material at a length scale of nanometres. Clearly, such processes are invisible to the human eye, and are similarly difficult to capture by laboratory-based techniques. These experimental challenges and the complexity of overlapping processes leaves discussion running to this day as to the true underlying nature of this reaction.

Many differing theories appear in the literature as to what occurs during each of the several stages, for most notably the induction period, and the precise causes of the transitions between these during hydration. No single technique is yet capable of providing all answers in such a complex system. In spite of the difficulty in characterising this reaction in full, a good deal of research has contributed to our understanding of these processes over the recent past. A number of notable reviews have been written [4, 6, 12]. Additionally the reaction of alite, the principal clinker phase, has been well reviewed by Nicoleau and Nonat [13].

### 2.2.1 Breaking Up the Reaction

Due to the complexity of the cement hydration reaction, researchers have typically broken the problem up into four or five (perhaps arbitrarily defined) stages based upon the thermal output of the reaction process. The stages are observed to occur similarly in all typical Portland cements [4]. Reactions begin the moment cement comes into contact with water, are exothermic, and are typically characterised by a number of techniques [14]. Splitting the reaction into these stages may result in problems where processes occur at a similar or poorly defined rate and these stages become difficult to isolate from one another for further investigation.

Many authors use some kind of calorimetric method to characterise or assist in characterisation of the reaction. Isothermal conduction calorimetry is discussed at some length in Chapter 3 and is the monitoring method typically applied to the early hydration reaction. This has been used to observe how variations in the particle size distribution influences the reaction of slag blended systems [15], how variations in the water-solids ratio and the addition of supplementary materials influence the reaction [16], and how the use of chemical admixtures effects the hydration process [17]. The commonly identified stages in the reaction are shown in Figure 2.1.

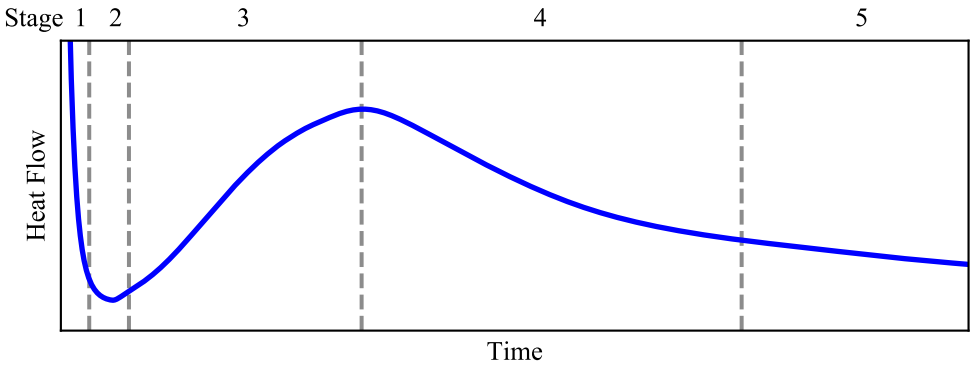


Figure 2.1: Schematic isothermal calorimetry output of a plain Portland cement.

The following stages are typically identified within the thermal output:

1. The initial reaction.
2. A period of slow reaction: the induction or dormant period.
3. The acceleration of the reaction.
4. A period of deceleration.
5. A sustained reaction at a reduced thermal output.

### 2.2.2 The Five Stages of Cement Hydration: A Brief Overview

The first step in the reaction relates to the early stage dissolution of clinker compounds and the reaction of $C_3A$ in the presence of sulphate bearing phases, to form ettringite. Ettringite has a well described needle-like hexagonal crystal structure [18, 19]. As ettringite is expansive [20], should this phase forms once the cement has hardened, the material may swell and crack [21, 22]. This occurs where excessive heat of hydration and sulphates are present. Ettringite forms on contact with water within the first minutes [23], which is also shown by the results in Chapter 4. There is also some contribution here from the heat of wetting of

the material which occurs from adsorption of water to the material surface. This is an effect observed on the surface where atoms or ions adhere.

Following this stage is a period of inactivity marked as stage two. Several differing theories exist as to the process that results in this. Stein and Stevels [24], for example, suggest a narrow band of metastable hydrate forms on the surface of anhydrous grains and passivates the surface. At the end of this stage acceleration of the reaction begins and the growth of hydrates begins, which is marked by a rise in thermal output over a number of hours.

The transition between the dormant and acceleration period is somewhat unclear. Nicoleau et al. [25] suggested that the formation of etch pits on clinker surfaces increases the available area of the clinker and therefore increases the rate of dissolution, eventually triggering hydrate growth. Jennings and Pratt [26] suggest that a semipermeable membrane is formed, and that calcium may pass through. According to this theory, the concentration of silicon on one side of the membrane increases, which forces the membrane to act as an osmotic pump. This forces water through and increases the pressure within. The membrane then ruptures in weak locations. The silicon rich and calcium rich environments then mix and react with one another, resulting in a fibrous growth as material precipitates out of solution.

Jennings and Pratt [26] took a sample grid from a transmission electron microscope and placed it in a specimen of hydrating cement for a pre-defined period of time. Grids were removed from the sample and placed in distilled water for a further 18 hours or simply dried at this point. When hydrated and placed in distilled water a significant growth of fibrous material was observed, though this was also the case for dried samples. They came to the conclusion that a membrane is formed on the cement material and that this membrane must allow ionic transport. This sort of phenomenon is difficult to observe at the length scale required to see the process occurring here. Typically a vacuum must be applied to the specimen if using a scanning electron microscope, which invariably results in drying of the sample and will result in damage of any surface hydrate which may have formed [27].

More recently, the geochemical theory of dissolution [12, 28] has been proposed as a more acceptable way to bring the theory of hydration into line with laboratory observations. This suggested the dissolution rate is controlled by undersaturation of the pore solution. Should the solution be undersaturated with respect to silicon and calcium, dissolution of alite is rapid, etch-pits form, and hydrate growth begins.

Hypotheses have generally come in and out of fashion over the years as knowledge and the availability of techniques has changed. The kinetics of the reaction are not yet fully known and while it may be possible for us to present further evidence for some kind of

mechanism, it is not possible to solve this conundrum using the data presented in this thesis. The primary focus of this review will therefore remain on the morphology of hydrate formation, and not the mechanism.

During the acceleration period a calcium silicate hydrate (C-S-H) begins to deposit on the surfaces of $C_3S$ at the solid-solution interface and the rate of hydration with respect to time increases [29]. Nucleation begins to occur in non-uniform small regions several nanometres in size, which are orientated parallel to the surface and mediated by the concentration of Ca in the solution: where the concentration decreases, the degree of hydration at the start of deceleration also decreases [30].

Logically, deceleration may result from one of three processes. Perhaps all small particles have reacted to form C-S-H and only large particles with a low specific surface area remain and react at a slower rate, or it may be that the growth of hydrate product may have reduced the space into which hydrates may grow. Alternatively, free water may have simply been consumed in the reaction sufficiently to become inaccessible to the surface of unreacted particles. Joseph et al. [31] demonstrated that the rate of reaction at this point appears to be dependent on densification of the C-S-H phase and that the decrease in reaction rate therefore results from an increasing restriction to access of mix water to the clinker-solution interface.

### 2.2.3 Simplifying the Material Chemistry

In order to simplify the system, the cement may be divided into individual mineral compounds. The literature will quite often focus on the hydration of, say, tricalcium silicate ($C_3S$) [32, 33] in isolation and effectively discard other phases to simplify the material.

For example Bergold et al. [33] synthesised monoclinic tricalcium silicate using laboratory-grade precursors and monitored the reaction in-situ by the partial or no known crystal structures (PONKCS) approach (see also Chapter 4). A heat flow was calculated from the quantified result and compared to output from an isothermal calorimeter, and showed good agreement between the two methods.

Juilland et al. [34] compared the effect of mixing methods on Portland cements and synthesised alite suspensions. The alite was ground to a similar particle size distribution to the Portland cement before mixing the materials at different rates and analysing these by isothermal conduction calorimetry.

### 2.2.4 Incorporating Slag into the Mix

Blast furnace slag is a latent hydraulic material which is commonly incorporated into the mix as a cementitious material [35], and is the supplementary material used in this thesis. Sometimes mistaken for a waste product, slag is a by-product of iron production where metal oxide impurities are removed and form as a layer on top of the iron collecting at the bottom of the furnace. The slag is tapped, and cold water jets used to rapidly cool the material. The rapid cooling prevents the formation of a crystal structure, resulting in a disordered glassy amorphous product. The material is then ground to a fine particle size for use as a cementitious product. Slag which is allowed to cool in air forms a crystal structure, is unreactive, and is commonly used as a man-made aggregate product in concretes. This is a process known as granulation.

The incorporation of slag results in a number of differences in the chemistry of the system, which further complexify the hydration reaction. The thermal output significantly decreases upon incorporation of slag, as shown in Chapter 3 and by Gruyaert et al. [36]. A third peak in the thermal output also occurs which relates to the consumption of calcium sulphate and the destabilisation of ettringite to form some sort of monosulphate-like phase [37].

#### The Activation of Slag and the Resulting Hydrates

The reaction of the anhydrous slag material is triggered by hydroxyl ions in the solution, with this reaction maintained by the presence of solid CH in the form of $Ca(OH)_2$. In substituted materials where the dissolution of aluminium into the pore solution results in high Al concentration, an uptake of this into the C-S-H product is observed [38, 39] which forms a substituted phase denoted as C-(A)-S-H. This remains the main binding product of the material.

In materials containing slag, which is high in MgO content, activated by sodium hydroxide solutions hydrotalcite, which is a crystalline compound with the formula $Mg_6Al_2CO_3(OH)_{16}{\cdot}4H_2O$ forms [40]. This is identified in Chapter 3 by thermal methods. Wang and Scrivener [40] also suggests that an AFm phase has formed, though this is challenging to observe due to the complexity of the observed diffraction pattern.

## 2.3 Building a Pore Structure

The formation of the pore structure, and hence the durability and resistance properties of the cementitious binder, are highly dependent on the hydrationreaction previously described. Due to the irregular geometry of particles and poor tessellation thereof, the reaction results in a matrix with inherent porosity within the bulk volume. An approximation of the morphological evolution of capillary porosity is shown in Figure 2.2. Porosity is also present within the C-S-H gel forming on the unreacted particle surface.

As the reaction continues, the forming products expand outward, eventually interlocking with one another as shown. This causes rigidity in the structure. Hydration continues until the point at which all cement grains are fully hydrated (which is unlikely), all free water has become chemically bound, or all free water has left the microstructure through some other alternative process. This may take an extremely long time.

The next step is to form an understanding of the basic factors that affect the pore structure, followed by a discussion of the techniques by which these might be studied. Both characterisations of the geometry of the pore structure and processes occurring within the pore structure are covered, for each property, beginning with the simplified standardised tests which may be carried out at a low cost. This is followed by the discussion of more advanced and detailed characterisation methods.

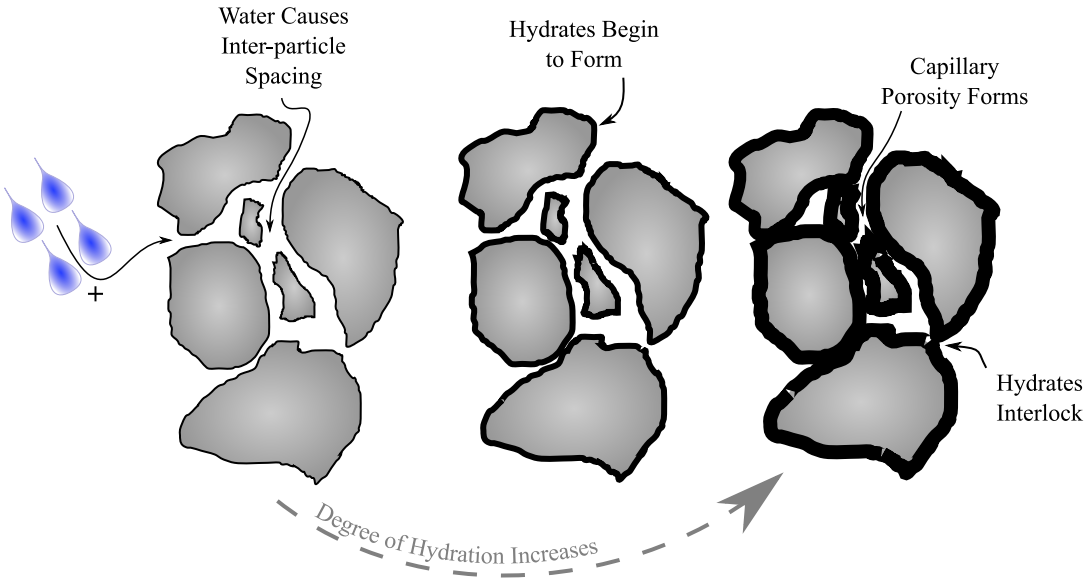


Figure 2.2: The formation of the capillary pore volume by hydrate growth.

### 2.3.1 The Water-Binder Ratio

The porosity is determined primarily by the water-binder ratio. It is fairly simple to understand how this might affect the porosity of the material. A higher water-cement ratio results in a higher porosity due to the spacing of particles within the suspension. Powers [41] measured the permeability of specimens by applying a hydrostatic head of mercury to a sample. Powers adjusted the degree of hydration, cementing content, chemical composition, fineness, drying method, and alkali content. An increase in water-cement ratio from 0.5 to 0.7 clearly resulted in an increase in the calculated permeability, in this case by a factor of $26\times$.

The work of Powers has been extensively corroborated [42–45]. These authors, and others, have all studied various parameters related to the porosity of the sample based on variations in the water-cement ratio, and have shown a very similar result; the porosity and permeability both increase with this parameter.

The final deciding factor when selecting an appropriate water-cement ratio is the workability of the concrete. Selecting a value which is too low will result in a material which is too poorly flowable to be placed on site.

BS 8500 [46] provides common exposure classes for typical concrete structures; either reinforced or mass bodies of the material. This standard sets limits to the water-cement ratio which is specified and based on the durability class applied to the given environment[2]. BS 8500 strictly limits the water-cement ratio to 0.70 (in reality 0.68 as per the margin of safety applied to the standard) where a concrete is exposed to environments where carbonation is a degenerative process. This appears to be the most aggressively applied limitation here, though in reality this is unlikely to ever be reached; the majority of exposure classes are limited to 0.55.

When discussing the water-cement ratio the minimum ratio which reasonably allows full hydration of the cement must also be considered. Jensen [47] reports a value of 0.42 for full hydration where 1 g of cement binds with 0.23 g of water and contains 0.19 g of water in the gel space. One must remember that the required water content of the mix depends on a number of conditions such as the method of curing the material (enviromentally sealed, open to the atmosphere, or fully saturated with water or lime). Should free water leave or be added to the mix, the reaction of material will undoubtedly be affected. In addition to increasing the porosity (and therefore reducing the durability) of the material, the water-cement ratio is inversely proportional to the strength; the selection of this parameter is effectively a trade-off between strength, workability, and durability.

[2]The BS8500 standard additionally sets requirements for the minimum depth of cover concrete required for the given class.

### 2.3.2 Curing Time and Condition

Curing is the term used to describe the maturing process of the cement or concrete. In this time, the cement develops its strength and properties as a solid material. Various controllable factors determine change in the degree of hydration, which in turn affects the pore structure as previously described.

The effect of curing conditions on concrete has been well reviewed by Kosmatka and Panarese [48] and is well understood to be an important factor determining the durability of cement-based materials. In 1929 McMillan varied the duration of curing and compared this to the resulting permeability of the specimen [49]. With all water-cement ratios a trend was oberved; the permeability decreases with an increasing duration of curing. Along the same lines Whiting [50] measured the permeability of concrete samples to both water and air, varying the water-cement ratio and the duration for which samples were left to cure. Whiting cured the samples for 90 days, with an initial curing period of either five or seven days in a moist environment before being left open to the atmosphere. Again, it was shown that a longer curing time results in a concrete with a lower permeability.

### 2.3.3 Supplementing the Material

The addition of supplementary cementitious materials (SCMs) may be carried out either to modify the properties of the material, reduce the cost of the material (where suitable materials are readily available) or to reduce the enviromental impact. Replacement materials may be either added to or replace cementing material within the batch. Two methods are typically used to determine a batch proportion for a supplementary constituent. By direct replacement an equal mass of cement is replaced with the supplementary material. This provides a slightly reduced cost amd reduces the environmental impact of the material which might be desirable for the client. Another method is equal strength replacement where the cementing materials replace one another based upon an equal strength product at 28 days. A number of examples of this are provided by Claisse [51].

Bijen [52] demonstrated the result of incorporating slag or fly ash. This results in a decrease in porosity from a young age, which is added to by the skewing of the pore size distribution to a finer porosity, or refinement of the pore structure. Brodersen [53] (translated by Bijen [52]) showed a reduction in the coefficient of diffusion of chloride and sodium with an increased volume of slag in the precursor material. Supplementary materials provide more desirable durability properties. Bijen [52] also demonstrates how the addition of pulverised

fuel ash (PFA) results in a higher porosity at a lower degree of hydration which then decreases as the sample ages, though fly ash is not used as a supplementary material in this thesis.

More specific studies have looked in greater detail at materials supplemented with high volumes of slag and differing curing conditions. Bouikni et al. [54] replaced a large volume of the cementing material (50% and 65%) with slag, producing a material which more closely matches those used in this thesis. Bouikni et al. [54] exposed these blends to differing curing conditions during hydration. When slag is added the pore volume increases. This is exaggerated where adequate curing conditions are not supplied to the material. With continuous water curing, where the sample remains fully saturated throughout, a far finer pore size distribution is observed. The pore sizes measured in the material ranged from 30 Å through to 1000 Å. In comparison to a Portland cement the addition of slag results in both a finer (additionally shown in [52]) and more uniform pore size distribution.

In the nuclear industry, highly substituted cements are used for encapsulation for a number of reasons [1]. A combination of the low release of heat, a significantly reduced permeability, and the generation of a reducing environment to prevent the movement of radionuclides all assist in making this a good candidate for a material to bind radioactive wastes which are not significantly heat generating.

## 2.4 Evaluating the Pore Structure

It is not possible to fully discuss all the techniques which could possibly be applied to the evaluation of the pore structure in a concise review. For example, fluoroscopy is commonly used in medical imaging to observe processes in-vivo such as the human swallow reflex or beat of the heart. The patient is marked with a contrast agent and imaged in-situ producing a time resolved dataset. It may be possible to observe mechanisms in the pore volume in this way. Some methods are outside of the scope of this thesis in spite of the fact that they may in some manner have potential. Some techniques are considerably more complicated and require access to specialist equipment such as X-ray radiation or a neutron source. These often provide a far higher accuracy at the expense of time and financial outlay. Examples of these are X-ray computed microtomography, neutron radiography, and, perhaps even mercury intrusion porosimetry. Microtomography is covered in Section 2.4.2 while neutron radiography is discussed in Section 2.4.5.

### 2.4.1 The Body of the Porous Volume

Having established how the pore structure is formed, the next logical step is to discuss how it might be geometrically characterised. The porous volume as an entity is perhaps both one of the simplest and yet most difficult of features to determine the properties of in a cement. The most straightforward test is simple to understand and does not require a significant amount of explanation. Knowing the mass of water absorbed by a dry sample and the bulk volume of the sample, the porosity may be quite readily determined. Indeed, this is precisely what the ASTM C642 [55] standard "boil test", which is targeted directly at cements and concretes does. The specimen is dried, weighed, saturated, and once again weighed. The test is carried out in either that or a similar order. This is also the case for the BS 1881-122 test method [56].

These tests however by no means yield a complete picture. What is present in cement is a complex interconnected network of non-uniform pores and some hydrate products which are damaged by drying at 105°C (Section 2.4.6). These vary in diameter (from mm to nm) Mays [57], tortuosity, and length. These properties yield a number of other characteristics such as sorptivity which cannot be characterised by such a method alone; the permeability of a specimen is not simply a function of the pore volume of the sample. The characterisation of these further properties is discussed further on in Section 2.4.3.

Having established a metric of the pore volume, interest might extend to the properties of the volume, perhaps a distribution of the pore sizes within. This is far more challenging, and is typically fraught with assumptions when carried out in a laboratory. Mercury intrusion porosimetry is a commonly used method and appears to be standardised in a number of cases: ISO 15901 [58], ASTM D4284-12 [59] (catalysts and catalyst carriers), and ASTM D4404-18 [60] (soils and rocks). The technique first appears in 1945 with details published by Ritter and Drake [61]. Brakel et al. [62] returned to the technique, with a review of the method in 1981. Mercury porosimetry may be used to resolve details of pores between 3.5 $\mu$m and 500 nm and can characterise a specimen in as little as 30 minutes [63]. The limiting minimum pore size observable is simply a restriction in the mechanics of the instrumentation which must be able to withstand an extreme pressure.

Non-wetting liquids have a contact angle greater than 90° and will sit as a droplet on the surface of the material (Figure 2.3) and not enter the capillary porosity unless a pressure is applied. As such mercury is selected as the intrusion liquid, as it is both non-wetting and has little, if any, chemical interaction with the sample.

A device known as a porosimeter applies pressure to and forces the intrusion of mercury into the sample. Pressure is applied between atmospheric and as high as 400 or perhaps even

500 MPa. The specimen is placed in a glass penetrometer, a bulb attached to a capillary, which is filled with mercury. The sample is evacuated, removing air and contaminants within the pore structure. Mercury is forced into the sample and fills the largest pores first (Figure 2.4). The pore diameter intruded is inversely proportional to the applied pressure; a low pressure resolves only high-diameter pores. At each step the pressure and volume intruded is recorded. The diameter of pores intruded is described by the Washburn equation [9]. This is provided in Equation 2.1.

$$P = \frac{4\sigma \cos\theta}{D_P} \tag{2.1}$$

Here, $P$ is the applied pressure, $\sigma$ is the surface tension of mercury in the pore, and $\theta$ is the contact angle of mercury with the material. A value is commonly assumed for the surface tension of mercury in cements at 25°C, as demonstrated by Gorce and Milestone [64] and Cook and Hover [65]. The selection of contact angle is somewhat more variable, with typical values falling between 130° and 140° [49] (see also Table 2.2). The surface tension of mercury is taken as 4.2 $\mathrm{Nm}^{-1}$.

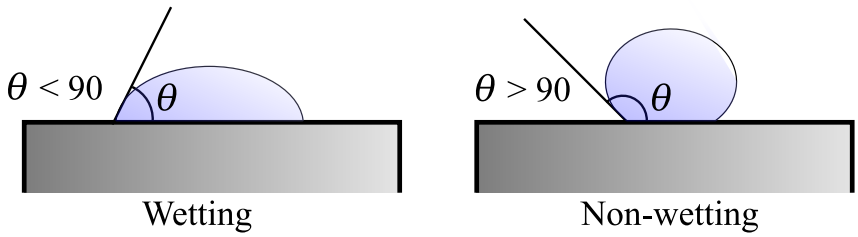


Figure 2.3: Wetting (left) and non-wetting (right) liquids.

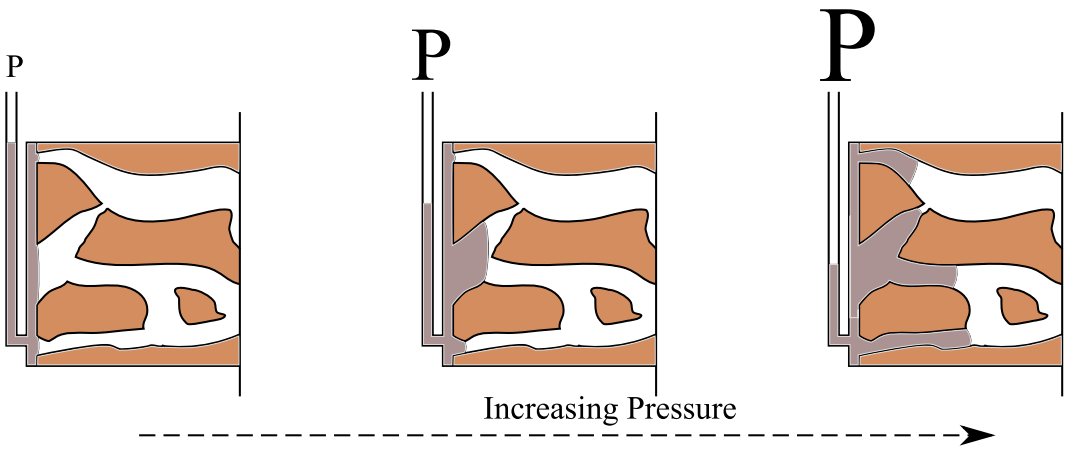


Figure 2.4: Pressure increases and mercury is intruded into progressively smaller pores.

Mercury intrusion porosimetry has been widely applied to cements [64–68]. Mercury porosimetry has also been fairly widely criticised, most notably by Diamond [10]. This is a characterisation technique which may potentially be flawed in the analysis of cementitious materials.

It is easy to imagine how pressurising a sample so significantly might damage the sample beyond recognition. Shi and Winslow [69] and Olson et al. [70] show how damage to the internal structure is caused by the pressure of the intruding mercury. Olson et al. [70] finds damage occurs from even a fairly low intrusion pressure of 10 MPa to 20 MPa, which is a fraction of that reached at the final steps in acquisition.

Assumptions about the accessibility of pores is another flaw in this technique. For a given pore to be accessible by the mercury, it must be connected to the surface of the material by a continuous uninterrupted path. Diamond [10] claimed that this is only the case for a small number of pores and that the method provides incomplete characterisation.

### The Ink-bottle Effect

The ink-bottle effect [71] is another methodological flaw which is potentially severe. If a wider pore is masked by a narrower entry pore the volume of the wide pore is registered as belonging to the diameter of the smaller (see Figure 2.5). This skews the pore size distribution significantly to a narrow diameter; results are incorrectly reported by this technique where large volumes are found connected to a smaller intrusion diameter.

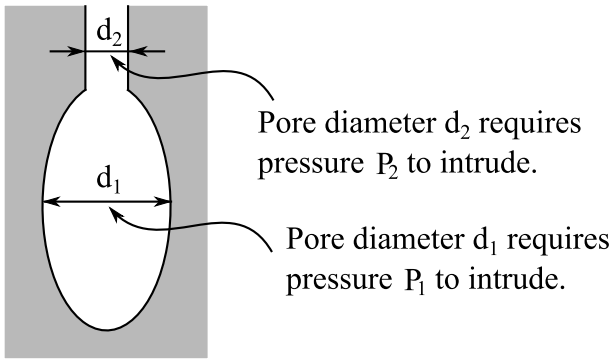


Figure 2.5: The ink-bottle effect. Intruding mercury into the specimen requires a pressure which is inversely proportional to the diameter of the intruded pore. Therefore the pressure required to intrude the pore at $d_2$ is higher than the pressure required to intrude at $d_1$. However to retain mercury in $d_1$, it is necessary to pressurise to $P_2$. Therefore the volume at $d_1$ is incorrectly assigned to the diameter of $d_2$.

There should also be a discrepancy formed here due to the ability of this method to detect only pores with connectivity to the surface and techniques which are sensitive to porosity with no accessibility such as X-ray computed microtomography, and serial sectioning, and electron microscopy which will not account for the discontinuity of pores and void spaces.

#### Assumptions in the Calculation

Finally, as previously mentioned, many assumptions are made in the calculation of the results of this test. For example, the contact angle of mercury is likely to have been assumed. This is a key value in the calculation of the intruded pore diameter and has an effect on the reported diameter for a given force. While the surface tension is generally accepted, the value adopted for contact angle shows a huge variation between studies and is wholly inconsistent throughout the literature, without even so much as showing a trend with time. Extreme values lying between 117° and 140° have been used seemingly with little consideration. Values which have been assumed in the literature are provided in Table 2.2, with a single measured value shown.

Table 2.2: Assumed and calculated values for the mercury contact angle.

| Publication | Method | Year | Value |
|---|---|---|---|
| Windslow and Diamond [72] | Measured | 1969 | 117° |
| Day and Marsh [66] | Assumed | 1988 | 140° |
| Cook and Hover [65] | Assumed | 1999 | 130° |
| Tanaka and Kurumisawa [73] | Assumed | 2002 | 140° |
| Kumar and Bhattacharjee [68] from [72] | Assumed | 2003 | 117° |
| Gorce and Milestone [64] | Assumed | 2007 | 131° |

### 2.4.2 Imaging the Three-dimensional Microstructure

X-ray computed tomography[3] (CT) is extensively used in the medical field and also has potential to characterise cements and the processes which occur in the pore structure during hydration. While it may seem of little relevance at first, the medical field is a good place from which an understanding of the development of this technique may be formed.

[3]This may also be referred to as Computerised Axial Tomography (CAT) in the literature, though this term has generally fallen from use in favour of simply CT.

### The Basis of the Technique

Tomography produces a three dimensional image stack by mathematically reconstructing a slice-series from a set of two dimensional projections. The sample is exposed to X-ray radiation which is attenuated depending primarily on the density of material encountered by incident photons[4]. Either a narrow focus, high flux, collimated beam or a divergent beam is typically used. During exposure the sample is rotated[5] through 180° ($\pi$ radians) and radiographs are acquired at discrete angles through the range. Hydrates and precipitating materials are of a lower density than clinker phases, but more dense than the water-filled pore space. As water and hydrates become bound to one another the difference in densities provides a suitable contrast for segmentation.

A good grayscale contrast is resolved between the various morphological phases in the reconstructed volume. This allows for a reasonably straightforward segmentation of features in the resulting stack. Hydrates are easily segmented from other features, though the direct observation of these materials remains challenging [74].

Reconstruction of the radiographic series to a three dimensional stack may be carried out by several techniques. Typically a filtered back projection algorithm is used. This method uses the inverse Radon transform, which is shown diagrammatically in Figure 2.6, to back project (or smear) a one dimensional slice across two dimensions at varying angles of detection. This is possibly the most basic of reconstructions and while computationally inexpensive, this results in a blurred image. To reduce this effect, a sharpening filter must be applied to the slice data. However this results in noise artefacts. Such noise may be acceptable where the aim is to observe a large feature such as a liver lesion, brain haemorrhage, or the result of a surgical feature (Figure 2.7). On smaller length scales this is not.

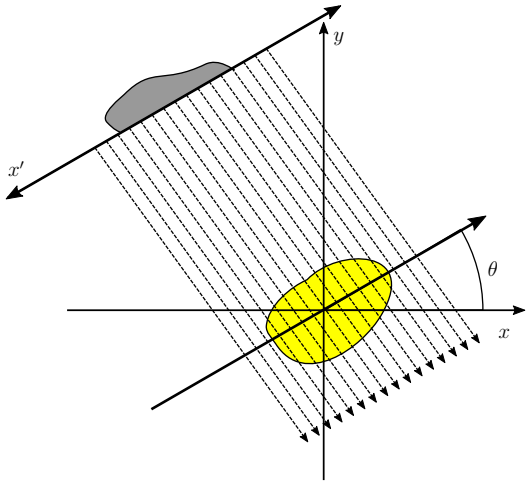

Figure 2.6: The inverse Radon transform.

As a solution several other algorithms are available [75]. Iterative reconstruction is often used. As a starting point, data are reconstructed with a filtered back projection algorithm. Assumptions are made regarding the instrument geometry, signal noise, and optics. These

[4] Also beam energy and atomic number of encountered nuclei.

[5] As opposed to the axial rotation of detector and source, the method used on a medical device.

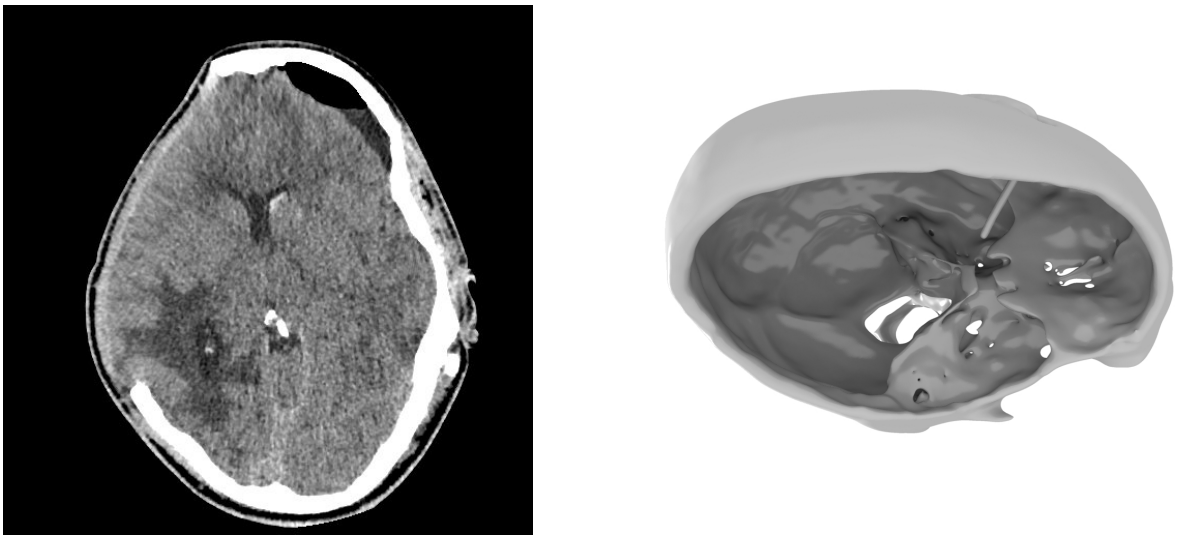

(a) CT Slice radiograph

(b) Post-surgical skull, segmented.

Figure 2.7: A human skull and brain after a subdural haemorrhage and subsequent decompressive craniotomy. Isolated slice data (a), remaining skull segmented and rendered (b). Reproduced with permission.

are iteratively adjusted on each cycle to minimise statistical noise metrics. This is *very* computationally expensive; the reconstruction must be completed cyclically many times. Where large datasets are produced this is simply inadequate. In addition to this should features be falsely identified as noise, which may occur when the aim is to observe very small objects, this will result in a poor reconstruction.

The Fourier grid reconstruction algorithm [76] makes tomography far more accessible as a technique. This method of reconstruction reconstructs points in 3D space back to an object. Using this algorithm operations that once would have taken days may be carried out in minutes even on a desktop workstation. Using a cluster it is possible to reconstruct fast tomography in almost real-time as data are captured [77]. From an experimental perspective this algorithm allows more instrument time to be devoted to data acquisition. Erroneous code in batch executions may be identified without the necessity of re-executing potentially days of data reconstruction.

### The Origins and Development of Computerised Tomography

For diagnosis and the observation of the human body tomography has provided cross sectional imaging since the early 1970s [78]. Early devices such as the EMI Brain Scanner (1971 - 1974) shown in Figure 2.8 allowed for the resolution of sequential three- or single

two-dimensional slices through the brain by repeatedly rotating an X-ray source and one dimensional detector around the head of the patient. This is known as fan beam tomography.

This instrument soon developed to a device which used a cone beam source configuration and two dimensional detector. A beam that is divergent in two dimensions allows for anatomical structures to be identified over a larger area in a single scan [79]. This "one shot" technique significantly lowers the radiation dose delivered to a sample or patient and is commonly used in dental or orthodontic treatment.

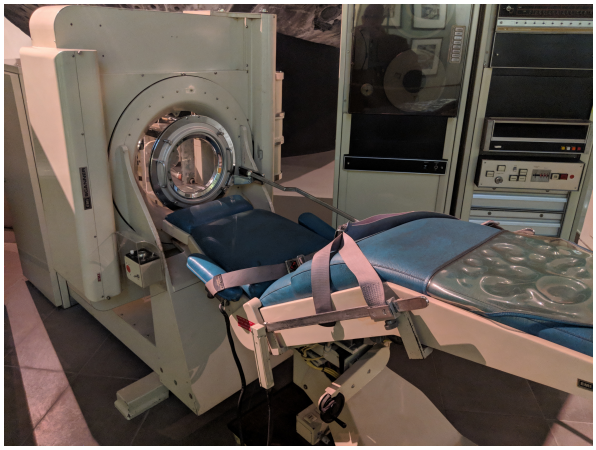

Figure 2.8: An EMI Brain Scanner on display at the Science Museum, London, UK.

Lower resolution tomographic imaging of cementitious materials first appears in the literature in the late 1970s, though this was by no means microtomography as it is known today. In 1979 the details of an instrument designed specifically for the characterisation of cements and concretes were published by Morgan et al. [80]. The instrument successfully resolved pores of approximately 1 mm in diameter, alongside cracks, and details of aggregates and reinforcement. The instrument allowed for the observation of a fairly large sample meaning the volumes segmented are more likely to be representative of the material as a whole. However the spatial resolution of this is not sufficient to directly observe volumes of hydrates and the temporal resolution appears to remain rather low.

Microtomography ($\mu$CT) is tomographic imaging on a length scale in the micrometre range. This sort of instrumentation is reported in the literature as early as 1982. The instrument resolved cross sectional features in a shell of 0.5 mm diameter at a spatial resolution of 15 $\mu$m [81]. Titled simply "X-ray Microtomography" this appears to be the first use of such a device in the sciences.

It took over a decade for the technique to be first applied to cements. In [82] microtomography was used to resolve microstructural features and the geometry of phase formation resulting from sulphate attack as early as 1994. This was carried out ex-situ and the process was not resolved continuously. In 1999 this form of imaging was used to observe the deformation of concretes in tension and compression and the resulting formation of microstructural cracks [83] which directly affect the durability of the material.

The new millennium saw quite a few studies appear in the literature as the potential of this technique began to be realised. A good proportion of this research focusses on medical cements for osteology and restorative dental purposes as opposed to cements used as construction materials.

The visible cement dataset [84], published March 2002, is an open access dataset collected at the European Synchrotron Radiation Facility (ESRF) in France. This possibly represents one of the most important advances in tomographic imaging in the cements field. The data are divided into raw files, text based descriptions, and two and three dimensional images of reference materials. The studied cements were also characterised by secondary techniques. Source code to various relevant data processing packages was also provided. As intended, the set has been used for multiple applications. A number of studies have used the data to "bootstrap" further research. Examples of use include shape analysis by spherical harmonics [85], study of how the particle shape result influences hydration [86], and quite importantly for the context of this project, the simulation of specimen permeability [87].

In 2003 Chotard et al. [88] applied microtomography to characterise the early reaction of calcium aluminate cements, and followed the reaction from post-mix to a number of hours post set. A large sample was used and the configuration yielded a voxel size in this case of 300 $\mu$m. From interpretation, this appears to be a fan beam geometry instrument with repeat isolated slices being captured, though this is not explicitly stated in the literature.

Synchrotron microtomography has been applied to observe increases in material porosity as a result of accelerated leaching [89], tortuosity in the pore structure of these materials [90, 91], and hydrate and morphological formation ex-situ [92]. Perhaps the potential of this technique for the study of cements has not yet been fully realised; the literature regarding cements, until fairly recently, has been rather sparse. Similarly to the purchase of a scanning electron microscope, the cost of instrumentation poses a significant drawback for some institutions. Since the start of the 21$^{st}$ century a good deal of literature has, however, been published. Much of the more recent literature is reviewed in [93]. In this thesis synchrotron microtomography is applied in order to characterise the pore volume of cement materials supplemented with high volumes of blast furnace slag (BFS), which are challenging to observe otherwise.

Both laboratory and medical instruments have developed to the point where it is possible to acquire tomographic datasets in a fairly short time; tens to hundreds of minutes for a laboratory based device, seconds for a clinical CT scanner, and faster still at a very high spatial resolution from a synchrotron source. It is now possible to perform fast microtomography

on a micron length scale [94] which has been fairly widely applied in geosciences. In this thesis, such an instrument is used to observe the hydration reaction from the first seconds.

### Dynamic Tomography

In recent years microtomography has evolved hugely from what was originally a fairly primitive technique [81] to a powerful imaging technique used in many fields. Methods such as pre- and post-mortem tomography, which are binary in nature, do not allow for the mid-points in a dynamic system be completely observed. Thanks to high flux and high brilliance sources, tomography may be applied to dynamically observe materials and systems on a micron or even sub-micron length scale, which is an available technique at a number of synchrotron facilities which offer the instrument characteristics required [94–96]. This presents us with an unparalleled technique by which mophological changes as a result of chemical reactions may be characterised on a very high temporal and spatial resolution, as shown in this thesis.

In-situ tomography on this length scale has been applied to the viewing of phenomena in earth sciences, reviewed by Bultreys et al. [97], and multiple degradation and failure processes in materials science and chemistry. The cracking behaviour of metals and alloys has been well studied. Singh, for example, in [98] used fast microtomography to study stress and fatigue cracking in aluminium alloys. These show considerable variation from the surface through the depth of the material when characterised in three dimensions. In this example samples were pre-cracked to induce a failure point on the specimen and then further loaded in-situ and analysed. Su [99] observed the growth of voids within aluminium alloys in samples undergoing deformation and fracture. Fast tomography at a resolution of approximately 11 $\mu$m per voxel was used by Finegan [100] to observe the failure mechanisms in lithium batteries above a critical temperature. Batteries were placed within a sample holder on a rotating stage and imaged at a rate of 1250 kHz during aggressive heating to cause failure.

Fast microtomography is by no means limited to the fields of chemistry and materials science. In other areas, in-situ microtomography has provided fascinating detail of multiple biological mechanisms [101]. Walker et al. [102] observed the mechanics of insect flight using this technique in-vivo on a living blowfly in real time. In this case the beat of the wing occurs at 145 kHz. The isolation of steering muscles of the fly which are near the diameter of a human hair would otherwise be impossible. The technique has also been applied by Lowe et al. [103] to observe the metamorphosis of an in-vivo Painted Lady butterfly. This method prevents having to mark the butterfly with a contrasting agent. This kills the butterfly.

It was possible in this case to study a single specimen throughout the time frame of the metamorphosis process.

The potential applications of this technique are vast. However its use to observe the cement hydration reaction seems to be simply non-existent at present in the literature. This is somewhat surprising due to the abundant use of cement. Here this technique is applied for what appears to be the first time in order to answer questions about the very earliest hours of hydration. This time-frame fundamentally influences the later-age durability and suitability of these materials; a poor initial reaction results in a material which has a questionable durability and may be simply dangerous for use in certain fields. The full understanding of these early hours may also prove useful for the production of novel admixtures and the use of these chemicals in materials where supplementary cementitious materials have been blended.

#### Focussed Ion Beam Tomography

Focussed ion beam tomography (FIBT) uses liquid metal ion sources, typically gallium, to image the specimen in a similar manner to a scanning electron microscope. Ions strike the surface and sputter small amounts of the material which leave the surface as secondary ions. By this process, secondary electrons are also produced. The beam covers the sample surface in a raster scan, and the signal resulting from the sputtered ions and electrons is collected and produces an image. This comes with the disadvantage that image acquisition is a destructive process, which results in the inability to observe processes in-situ within the specimen. Imaging also requires the application of a vacuum which removes water from the pore volume.

FIBT has been applied to multiple geological samples [104], to observe crack propagation [105], and to study the morphology of graphite [106]. In cement science, this has, perhaps, been less widely used for three-dimensional imaging than traditional microtomographic techniques, though a number of studies do appear in the literature. Trtik et al. [107] analysed a CEM-I 42.5N Portland cement sample blended with a water-solids ratio of 0.3 which demonstrated the potential use of the method in the study of cements, Holzer et al. [108] used the method on a nanoscale to characterise the topology of particle interfaces, and the surface roughness of hardened pastes by Trtik et al. [109].

### 2.4.3 Observing Water Uptake

Now that the volumetric properties of the pore structure have been established, it might be desirable to attribute this and the hydration of a specimen to some kind of water absorption mechanism. This is both well reviewed and explained by Hall [111] who describes the origins

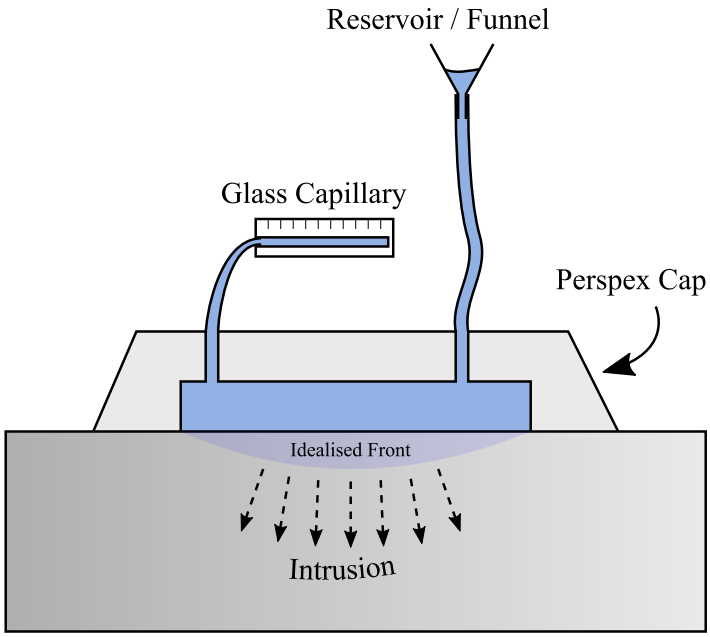


Figure 2.9: The initial surface absorption test (ISAT). The funnel will typically be additionally connected to a valve which is not shown here. Figure after and front idealised from Claisse [110].

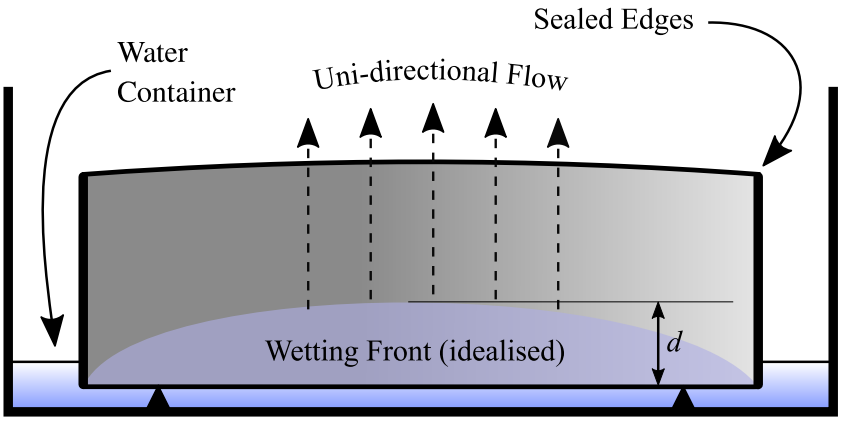


Figure 2.10: The ASTM C1585 test. The front depth is denoted as $d$, the curve is idealised after figures provided from Claisse [110].

of the test and the calculations surrounding the determination of the sorptivity metric. A number of techniques may be used to characterise the uptake of water in a cement or concrete sample. These are typically standardised, the examples covered here being the BS 1881-208 [112] initial surface absorption (ISAT) and the ASTM C1585 [8] capillary suction tests. The primary focus here will be on the ASTM standard, the test method used in this thesis.

### The ISAT

The ISAT first appears in the literature in the early 1970s being reported by Levitt [113]. The apparatus required by BS EN 1881-208 [112] are shown in Figure 2.9. There appears to be no specific geometric limit on the sample; this is defined simply as a result of the geometry of the testing apparatus. A cap is placed upon the surface of the material. The cap has an inlet and measurement scale attached to an outlet. Water is poured through the inlet and fills the cap device and appears on the scale. As water is absorbed by the sample, liquid moves along the capillary tube. Knowing the diameter of the capillary and the length of water movement along it, the uptake of water by the specimen may be determined.

### The Capillary Suction Test

The ASTM C1585 test [8] is somewhat more straightforward. Cement cylinders of 100 mm in diameter and 50 mm in depth, with a small allowance made for error, are used. This test is shown in Figure 2.10. Here the sides of the specimen are sealed to the environment which ensures unidirectional flow through the sample. The sample is supported by a pair of narrow supports which may be prismatic or cylindrical in cross section to ensure the area in contact with the sample is as small as possible, and the movement of moisture upward remains unrestricted. The mass of the sample is periodically measured on a mass balance. Equation 2.2 provides the apparent relationship between mass and front depth, where $I$ is the intrusion in mm, $a$ is the cross sectional area of the specimen in mm$^2$, $m_t$ is the mass change of the specimen in g, and $\rho$ is the density of water in g mm$^{-3}$.

$$I = \frac{m_t}{a \times \rho} \tag{2.2}$$

This approximation assumes a flat front. This is not the case (the idealised front is shown in Figure 2.10 and directly observed in Chapter 7), though may very well be the best approximation of the front moving unidirectionally through the sample.

Critically, the depth of water penetration appears to assume the volume of water which is taken up by the sample is equal to an *entire* cylindrical block of the same mass the water

absorbed. This will most certainly yield a large discrepancy between the water absorbed and the actual uptake of the specimen, which is *precisely* what is observed in Chapter 7. To attempt to describe the volume as a solid cylinder of the same diameter as the specimen is simply an incredibly poor representation of what is the actual case. Indeed, McGlinn et al. [114] observed this sort of a discrepancy between data captured from a neutron source (Section 2.4.5) and data captured by the ASTM test [8], though do not appear to have given a detailed description of why this might occur. A similar discrepancy is observed and analysed in Chapter 7.

### 2.4.4 Proton ($^1$H) Nuclear Magnetic Resonance Relaxometry

Hydrogen nuclear magnetic resonance ($^1$H NMR) relaxometry has been fairly widely applied to characterise porous media [115], and has subsequently seen common use in the study of cementitious materials [116, 117]. This provides the user with the benefit that drying of the specimen is not necessary prior to testing in this manner. The spin-lattice, and spin-spin relaxation times are measured, where the relaxation time is the time taken for the orientation of the excited atom to return to its original state after the application of an oscillating magnetic field, and provide details about the state of hydrogen contained within the bulk volume of the material.

In $^1$H NMR experiments two relaxation times, $T_1$ and $T_2$, are typically measured. $T_1$ emanates from the spin-lattice relaxation time and $T_2$ the spin-spin relaxation time. These differ significantly for chemically bound hydrogen, surface-adsorbed hydrogen, and hydrogen in water-filled narrow-diameter pores. Water which has become chemically bound during the hydration reaction generally shows both a very long $T_1$ relaxation time greater than 100 ms [118] coupled with a very short $T_2$ relaxation time, which lies in the order of 10 $\mu$s [119]. Hydrogen in gel-pores shows a short relaxation time between 0.5 and 1 ms as these are dominated by interactions at the surface. In large capillary pores, relaxation occurs between approximately 5 and 10 ms. As the relaxation times are controlled by the surface interactions occurring within the material, these may be used to provide a surface area to volume ratio and subsequently the pore size in which the interaction is occurring.

NMR relaxometry has been used to study how the addition of water saturated lightweight aggregates affects curing of cement materials [120], how fine fraction oxidic additive materials influences the hydration reaction [121], to observe the densification of C-S-H during hydration [122], to probe the water present in different states in cement pastes [123], to provide validation for pore size quantification by other techniques [124], and to spatially resolve the ingress of water into dried cement samples [125].

### 2.4.5 Firing Neutrons at a Sample

Imaging with neutrons is based on the neutron scattering properties of the material being observed, which are expressed as the cross section, the barn (b). The unit is perhaps best thought of as the probability of an interaction involving a nucleus and an incident neutron occurring. Radiography with neutrons obtains these particles almost exclusively from high-flux sources such as a spallation source [126] or fission reactor [127], though smaller sources have been used with the limitations of these requiring a longer exposure time and providing a lower spatial resolution[6].

#### The Origins and Development of Neutron Radiography

Neutron radiography appears to date back to the late 1940s and early 1950s. In a review and overview paper published in 1956, Thewlis [128] described the earliest details of the technique. The provided descriptions included detectors, typical experimental criteria, and some examples of work carried out on the BEPO nuclear reactor at Harwell (Oxfordshire, UK, decommissioned in 1968). To provide some context and understanding of how far the technique has advanced, Kallmann [128, 129] reported an acquisition time of approximately four hours compared to a matter of seconds at a modern facility (Chapter 7). In 1969 Hawkesworth [130] provided a review of the technique in the context of nondestructive testing including detail of a number of sources available at the time and images for direct comparison with X-ray radiography. The values reported in the literature appear to indicate a flux in the range of $10^6$ n $cm^{-2}s^{-1}$ was possible from both common small-scale sources and reactors, which was an order of magnitude lower than the reported flux recorded at modern facilities. For example, the SINQ based NEUTRA instrument [131] yields a flux of between $10^6$ and $10^7$ n $cm^{-2}s^{-1}$ depending on the sample position adopted, and the ISIS based IMAT [132, 133] beamline provides flux in excess of $10^7$ n $cm^{-2}s^{-1}$ at the radiography endstation.

Neutron imaging of cements has been used fairly extensively in the literature [134, 135]. However, beyond an isolated study of a system at a 90% slag substitution by McGlinn et al. [114] research appears to have neither significantly nor specifically extended to either blast furnace slag cements or cement materials substituted beyond the 65% limitation of the CEM III/A class.

McGlinn et al. [114] obtained data in a semi in-situ manner by removing the sample from the container from which water permeates at specified time intervals before exposure. This is similar to the method outlined in the ASTM standard [8]. The adopted method of

[6]This is also likely to be a result of advancement in detector technology.

acquisition relies upon beam time allocation, which may be challenging, and the availability of equipment at the facility. Studying the uptake fully in-situ increases the quantity of results available, and allows for better prediction of the sorptivity characteristics of these materials over an extended testing time without sample disturbance.

The results allow for comparison to data acquired by the ASTM sorptivity method [8], which is reported by McGlinn et al. [114] to provide a reduced rate of absorption. Additionally, the technique has been applied to self-healing [136, 137], and cracked [138] and cracked steel reinforced concretes [139]. The release of curing water from aggregate materials has also been studied by Trtik [140].

Being used for the encapsulation of wastes makes these types of materials significant. Degradation processes are widely accepted to be significantly related to the ability of these matrices to remain undamaged by permeating water [141]. McGlinn et al. [114] showed that samples which had undergone leaching showed a higher sorptivity, using a configuration similar to that used in this thesis. Moreover, an understanding of the performance of these materials will become more important as more sustainable cements inevitably become sought after in industry.

Taking a look into wider scientific fields yields some other interesting results which are discussed briefly here. Zhao [142] used the technique to observe the permeation of water and change of water distribution in dry sandstones in-situ with an experimental configuration appearing similar to that used in this thesis (Chapter 7). Quantification is in this case carried out by the Avizo-Vemira (FEI Visualization Sciences Group) package using separately acquired tomographic data; no direct quantification from neutron data appears to have been attempted.

Outside of geology, neutron imaging has been used to observe the water uptake in and root growth of a germinated Lupin seed [143] and the effect of root type on moisture uptake in the corn (maize) plant [144]. In 2011 Smith et al. [145] used neutron radiography to image the interior of a bronze Egyptian Horus the Child statuette estimated to originate from approximately 1802 BC. The artefact was damaged in 2007 when excessive pressure was applied to the fragile object during mounting for an exhibition. This was carried out on the SANRAD beamline at the SAFARI-1 source in South Africa, and showed previously restored areas and corrosion layers within the artefact.

In addition to the previously described work, neutron tomography has been applied to observe the flow of coolant in a modelled boiling water reactor by Kickhofel [146], and by Takenaka to monitor the behaviour of water in electrolyte fuel cells [147].

### 2.4.6 Preconditioning: Dehydration and Re-saturation

Excluding for a moment the assumptions made by the calculations performed in the processing of capillary suction test data for cements, the tests described in Section 2.4.3 are all based on fairly sound scientific theory. However, before to the initiation of testing, the sample must be subjected to some kind of drying process; no water will be absorbed into a specimen which is already saturated.

All of these tests have a drying process. Most of these differ from one another in some way and most have changed over time. Of course, such a drying process is entirely necessary. To naturally dry the specimen will require a *very* long time. During the preconditioning process, samples may be exposed to temperatures of up to 115°C to aggressively remove free water from the structure. A summary of thermal treatment parameters is provided in Table 2.3.

Aggressive drying damages the specimen. Galle [148] found that treatment such as oven drying has a noticeable impact on the recorded porosity of the specimen, and recommended the use of significantly lower temperatures than those specified by the standard test procedures.

Table 2.3: Thermal treatment specification for commonly used tests.

| Test | Year | Temperature | Duration |
|---|---|---|---|
| ASTM C642 [149] | 1997 | 100°C to 110°C | > 24 hrs. |
| ASTM C642 [150] | 2006 | 105°C ± 5°C | > 24 hrs. |
| ASTM C642 [151] | 2011 | 110°C ± 5°C | > 24 hrs. |
| ASTM C642 [55] | 2013 | 110°C ± 5°C | > 24 hrs. |
| ASTM C1585 [152] | 2004 | 50°C ± 2°C | 3 days |
| ASTM C1585 [153] | 2011 | 50°C ± 2°C | 3 days |
| ASTM C1585 [8] | 2013 | 50°C ± 2°C | 3 days |
| BS 1881-122 [56] | 1996 | 105°C ± 5°C | Const. Mass |
| BS 1881-208 [112] | 2011 | 105°C ± 5°C | Const. Mass |
| Sabir et al. [154] | 2008 | 40°C | 22 to 26 days |

There are two mechanisms which may result in degradation. Firstly the formation of pressure within the specimen may cause fracture and splitting of the concrete which is commonly associated with spallation of cover concrete in a fire. Fire is a reasonably good place

to start, as the research into the response of structural elements to significantly elevated temperature is reasonably extensive. However these do not really show conditions which might be expected in the case of boiling off water in an oven. In research looking at fire conditions higher temperatures are often tested at post flashover in the fire scenario, when the temperature reaches a sufficient value to cause instantaneous combustion of materials within the vicinity.

Spalling occurs in various samples loaded in different manners at a range of temperatures and is observed by Zheng et al. [155] who studied the spalling observed in pre-stressed structural elements at raised temperature. This occurs as a result of an increase in pore-pressure. The pressure builds in the pore volume and cannot escape due to either the tortuous or disconnected nature of the pore volume. This was tested by Kalifa et al. [156] who measured the pressure and temperature at a series of depths within a concrete specimen between 10 mm and 50 mm from the surface. Piasta et al. [157] characterised samples heated between 20°C and 800°C. The pore pressure rises within the specimen when the sample reaches 100°C. However the increase observed here is rather low and so the pore pressure is likely not to be a significant problem. This type of failure of the material is a very significant and hazardous problem in pre-stressed elements though is not likely to be a significant concern in the drying ovens used in a laboratory, which are of a lower temperature.

In the drying process the sample will remain in the drying oven until the point at which a constant mass is achieved. This results in cracking of the specimen and decomposition of hydrates which is shown by Wong et al. [158] and Piasta et al. [157]. The result of this is an overestimation in the pore volume and permeability of the specimen. Micro-cracks may resolve themselves into the pore volume, modify the tortuosity, or introduce a path to a previously inaccessible void through which moisture may penetrate. This preconditioning step renders the sample useless for further testing. The pore volume also coarsens at a low temperature which was shown by Rostasy et al. [159] with the pore distribution not necessarily increasing but shifting toward a higher diameter. As established, this clearly is not a particularly good way of preconditioning a sample. However, it must be concluded that in spite of this, there is simply no other viable way to remove free water and that such preconditioning remains entirely unavoidable for the time being.

The sample is by definition first dehydrated and re-saturated by these tests. Saeidpour and Wadsö [160] tested cements subsituted with high volumes of silica fume, fly ash, and slag (the slag substituted to 50% and 85%, matching fairly well the degrees of substitution used in this thesis). These were analysed in a dynamic water-vapour sorption instrument which continuously records the mass of the sample while exposed to a varying relative humidity

(RH). Samples were cyclicly exposed to decreasing and then increasing relative humidities between 0% RH and 95% RH, and a hysteresis loop with the absorbed mass of upon each cycle observed. However, the tests performed by Saeidpour and Wadsö [160] appear to have been carried out at room temperature and do not make any reference to raised temperatures such as those used in the drying oven. Rehydration of the sample will clearly cause further modification of the specimen as the permeating fluid interacts with the dehydrated material. Farage et al. [161] tested cement pastes hydrated and sealed for seven years at ambient temperature and heated these to a maximum temperature of 300°C before re-saturating them. Here an increase in the injected mercury volume in the low pore diameter range after heating was attributed to the collapse of C-S-H gel. However, Wu et al. [162] found that the rehydration of C-S-H in the specimen is not necessarily problematic. The water vapour sorption isotherms show little difference before and after saturation of the sample, and so this remains somewhat unclear due to these slightly differing results.

The standardised tests make no account for any microstructural change which might be taking place during the test period. This is especially problematic for young materials such as those tested at 28 days. The initial surface absorption test specified in ASTM C1585 [8] is carried out over 8 days, which in a 28 day old sample is approximately 30% of the life of the material before testing. On a fundamental level, the sample with which the test began is quite possibly dissimilar to the sample on which the test is carried out. This is also the case for the sample recovered at the end. Quite simply, a systematic fault in the test procedure may be responsible for the occurrence of micro-structural changes in the cement, which are significant enough to cast doubt into the validity of any experimental results. This does not mean that the test has no merit. For applications where a quick and simple measure of permeability or porosity are required, such tests may very well be sufficient. This is also the case for comparative tests on samples treated in the same manner. However for applications where clear-cut, precise results are needed, this technique may not be sufficient.

## 2.5 Questions That Need to Be Answered

In this thesis a number of gaps identified in the literature are filled.

**1. Diffraction**

Using in-situ X-ray diffraction, the chemistry of very early hydration by crystal structure refinement and amorphous content quantification by PONKCS in a complex system is shown. This is the first time use of this technique for cement hydration reaction from synchrotron data.

**2. In-situ Tomography**

The hydration reaction is observed in-situ using X-ray synchrotron microtomography, which appears to be the first use of this technique for the observation of cement hydration in the literature. Using this it is possible to demonstrate the morphology and distribution of hydrates within the material, and observe processes occurring within the pore volume across the first hours of the life of the material.

**3. Analysis of the Pore Volume**

A technique is developed to quantify the pore volume in three-dimensions using tomographic data, which eliminates the ink-bottle effect shown by mercury intrusion porosimetry, albeit with the caveat that a longer length scale is being quantified. This correctly captures larger pore volumes and provides a result with a total pore volume similar to that given by porosimetry and neutron imaging.

**4. Moisture Uptake and the ASTM C1585 Test**

Finally, the water uptake into highly substituted specimens of the cement compositions that are used for the encapsulation of intermediate level radioactive wastes by neutron radiography is observed. The data are quantified and compared with alternative techniques. By this, the knowledge base surrounding cementitious systems of high slag substitution is extended. The actual difference between the uptake observed by neutron imaging and the ASTM C1585 test is observed, and a discussion of how significant these differences might be is also provided.

# Chapter 3

# Fundamentals: Materials and Methods

To come to any kind of conclusion as to the suitability of a material for a given purpose it is important to have an understanding of the fundamental baseline properties such as the chemical
composition and physical characteristics. In this chapter several techniques were introduced and applied to the materials, with the aim of performing an initial characterisation of the materials used. This chapter begins with the physical properties of the material: the density, fineness, and particle size distribution of the powder. Following this a number of both qualitative and quantitative assessments of the materials were performed, such as the chemical composition by X-ray fluorescence, isothermal conduction calorimetry, thermogravimetry, and X-ray diffraction. Cements of a variety of ages were studied to observe how the characteristics of the material developed with time and varied with composition. Some of the advanced characterisation equipment used in this thesis is discussed in Appendix A.

## 3.1 The Materials

The materials used in this thesis were a Hanson Ribblesdale works CEM-I 52.5N Portland cement (PC) meeting the EN 197 standard [11] and a Hanson REGEN Blast Furnace Slag, which did not appear to have been provided to a publicly available standard. These materials were provided by Hanson Cements and the National Nuclear Laboratory (UK) for use in this thesis. The materials were also chemically and physically identical to the materials used for the encapsulation of intermediate level radiological wastes in the United Kingdom. The selected blend proportions matched closely those used for this purpose.

### 3.1.1 Producing a Sample

Upon consultation with the National Nuclear Laboratory the following mix proportions were selected for study: 75% BFS by mass (3:1 BFS to PC), 78% BFS by mass (3.44:1 BFS to PC), 82% BFS by mass (5.67:1 BFS to PC), and 90% BFS by mass (9:1 BFS to PC). While these may seem less relevant to the construction industry as a whole, high supplementary-fraction blended cements may very well become more widely used as the construction industry seeks to lower its carbon footprint.

Due to the closeness in proportion, the 78% BFS material was studied selectively, and the same was applied to the 82% BFS material where a mid-point between the three compositions may be desired. All samples used in this thesis had a water-cement ratio of 0.35 unless otherwise stated. This ratio was selected in order to maintain relevance to the nuclear industry. The low w/c did not result in poor compaction except in cases where a very fine capillary or Kapton tube was used.

The correct mass of powder was batched on a 2-dp balance and homogenised in a figure-eight mixer. The correct mass of water, sourced from the mains supply, was then measured and placed into a second mixer. The homogenised powder was added to this on a slow speed setting for five minutes followed by more vigorous mixing for a further five.

Moulds for samples selected for larger scale testing[1] were sprayed with silicone free release agent. Each sample was tamped 100 times to remove entrapped air. For chemical and smaller scale tests samples were cast into 15 mL or 50 mL centrifuge tubes and compacted using a vortex mixer. No release agent was used. Tube samples were sectioned using a Buehler Isomet low speed saw.

### 3.1.2 Arresting Hydration

For some tests it was unfortunately necessary to arrest the hydration reaction. For ex-situ chemical testing this was carried out on all samples regardless of the specimen age to prevent methodological variations affecting the result. To prevent further hydration, sectioned samples were repeatedly quenched in isopropyl alcohol, removed, and weighed until a constant mass was reached. Samples were then transferred to a vacuum desiccator. Powdered samples were pulverised using a percussion mortar and were ground in isopropyl alcohol, before being passed through a 63 $\mu$m sieve to produce a finely ground powder.

[1] 50 mm cubes are used for the Capillary Suction test and 40 mm $\times$ 100 mm prismatic samples for neutron imaging.

### 3.1.3 Sourcing a 25 Year Old Specimen

As a part of this thesis, a 25 year old specimen was provided by the National Nuclear Laboratory (UK) for characterisation [163]. The sample was prepared in approximately 1990, and tested during characterisation for this project in the middle of 2015. The sample consisted of a historic Magnox encapsulation plant (MEP) wasteform containing corroded simulant Magnox swarf. These were prepared in a reusable mould and as such the wasteform did not have protection from the stainless steel container in which wastes are typically encapsultated. A full characterisation of the specimen appears to have been carried out in approximately 2003 or 2004. For context, this characterisation provided a porosity value of 9% after 12 years of hydration performed by gas expansion pycnometry (Section 3.2.1). The remainder of those results are not reported in this thesis.

## 3.2 Physical Properties

A number of techniques are available with the aim of characterising the physical properties of cement materials. To begin with, the density of the material was characterised and the results used in determination of the fineness. Finally, laser diffractometry was carried out on these samples to determine a particle size distribution and observe regions in particulates which may prove problematic for other characterisation methods used here.

### 3.2.1 Density by Gas Expansion Pycnometry

Before calculating the fineness of the material by the Blaine fineness method, the density of the material must first be known. A Eureka Can is commonly used for this, though in this case the cement will react with the displacing water and the technique is ineffective. In order to determine this accurately a gas expansion pycnometer was used, which provides a result to a higher precision. Chambers, which are connected to pressure transducers, are sequentially filled and vented to determine the sample volume. The calculation is provided by [164].

#### Method: Determining the Density

In this thesis densities were determined using a Micromeritics AccuPyc 1340 with a helium gas feed with three repeats for each material. A sample of each powder was weighed to 4-dp and placed into the 1 mL sample holder. 20 purge cycles were applied to the instrument, followed by 30 measurements, repeated twice for each powder. A fill and purge pressure of 0.045 MPa was used to prevent sample disturbance.

**Density of Cementing Materials**

The determined densities are provided in Table 3.1. The calculated densities lie close to the values quoted in [165]. As a standalone property, the density is not thought of to be of any particular concern; a density requirement is not stipulated in either BS EN 197 [11] or ASTM C150 [166]. However, the density was required to determine the material fineness and was also useful for calculating accurate masses for batch proportions. Typical values of density of Portland cement are also quoted by Lamond [167] as lying between 3.05 and 3.25 $gcm^{-3}$ The tested sample lies in the center of this range.

Table 3.1: Powder densities as determined by gas expansion pycnometry (helium).

| | | | | Densities / $gcm^{-3}$ | | |
|---|---|---|---|---|---|---|
| | | Mass / g | Vol / $cm^3$ | Typical [165] | Result | Mean |
| PC | 1 | 0.6630 | 0.2112 | 3.15 | 3.139 | 3.139 |
| | 2 | 0.6537 | 0.2082 | | 3.139 | |
| BFS | 1 | 0.6855 | 0.2400 | 2.90 | 2.857 | 2.855 |
| | 2 | 0.6544 | 0.2293 | | 2.854 | |

### 3.2.2 Fineness by Air Permeability

The fineness of Portland cement is usually determined by the Blaine fineness (air permeability) method and is commonly used to measure the consistency of grinding between batches during manufacturing. The fineness is inferred knowing the time taken for a given volume of air to pass through a bed of assumed porosity. The configuration of the apparatus is shown in Figure 3.1.

A mass of cement is placed into a calibrated chamber of known volume. The material is compacted to form a bed of assumed porosity. A partial vacuum is formed on the right hand side of the instrument and the system sealed. Air is allowed to pass through the bed by removing the cap. The time for a specific known volume to pass through the bed is measured. The fineness is determined by comparing the time for the volume to that determined for a reference material. The specific surface area is calculated by Equation 3.1, given in BS EN 196-6 [168]. $e$ is the porosity of the bed, which is taken as 0.5. $K$ is the instrument constant determined during calibration (interested readers are referred back to the BS EN 196-6 standard in which the procedure is provided). $\eta$ is the viscosity of air which is

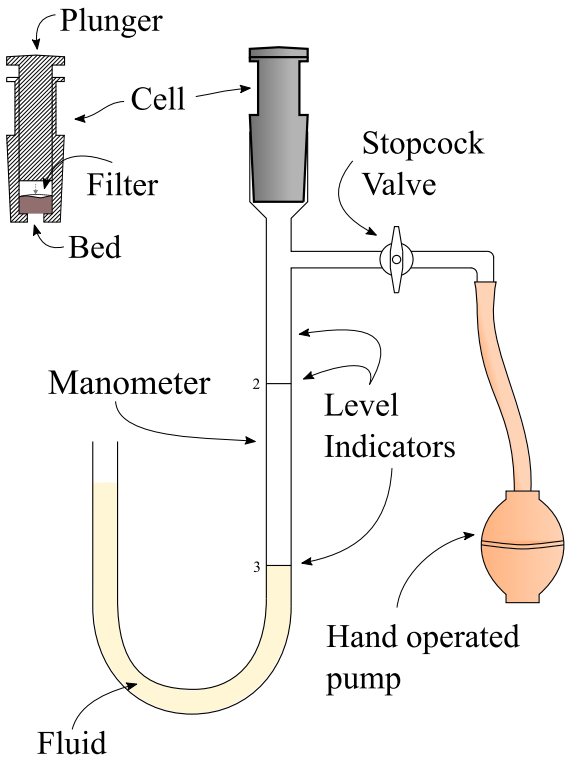


Figure 3.1: A typical Blaine fineness air permeability apparatus.

determined by linear interpolation of table 1 of EN 196-6 [168]. $t$ is the time taken for the air volume to pass through the bed.

$$S = \frac{K}{\rho} \times \frac{\sqrt{e^3}}{1-e} \times \frac{\sqrt{t}}{\sqrt{10\eta}} \tag{3.1}$$

**Method: Determining Fineness**

Here, the fineness of the cement was calculated to the BS EN 196-6 standard [168] using a Controls Group 62-L0041 Blaine air permeability apparatus. The density was determined as per Section 3.2.1. A bed of powder of each material was weighed, which resulted in a mass requirement of 2.25 g of PC and 2.05 g of BFS. The sample was batched twice, and each bed was compacted as per the requirement stipulated in the standard method [168].

**Fineness of Cement Materials**

The material fineness calculated by the air permeability method is provided in Table 3.2. ASTM C150-12 places limits of 2600 $cm^2$ $g^{-1}$ (260 $m^2$ $kg^{-1}$) as a minimum and 4600 $cm^2$ $g^{-1}$ (460 $m^2$ $kg^{-1}$) as a maximum on the fineness of cement classes. All British Standards place

Table 3.2: Blaine fineness results calculated in accordance with BS EN 196-6 [168]. Quoted values are mean values of 3 repeats.

| | Time | | Specific Surface Area / $m^2$ $kg^{-1}$ | |
|---|---|---|---|---|
| Test | PC | BFS | PC | BFS |
| 1 | 27.6 | 20.7 | | |
| 2 | 29.0 | 20.6 | 388 | 494 |
| 3 | 29.8 | 21.7 | | |
| 4 | 23.6 | 20.9 | | |
| 5 | 25.8 | 21.5 | 364 | 493 |
| 6 | 26.3 | 20.5 | | |
| | | Mean: | 376 | 493 |

no requirement on the cement fineness, from BS EN 197 [11] all the way back to the BS 12 standard of 1910 [169]. British Standards appear to leave the value for the manufacturer to judge based on the observed strength development of the resulting powder. However, it is mandatory for cement manufacturers to report the fineness value for conformity to BS EN 197.

Many of the mechanistic effects observed during hydration of cement, for example the rate of hydration, are determined by the fineness of the material [167], which was studied by Bentz in 1999 [170]. Where a higher surface area is in contact with the mix water the rate of hydration increases. This value allows for a differentiation between, for example, a CEM-I 42.5R and CEM-1 52.5N PC which reach their respective ultimate compressive strengths at a different rate. A rapid hardening cement such as the 42.5R will have a finer grading which will increase the rate of reaction of the material. The fineness will also modify the workability of the paste.

### 3.2.3 Particle Size Distribution

Here, the distribution of particles in each material was determined. This was reasonably straightforward for the PC, though required some modification of the BFS powder to provide a valid result. The particle size distribution may be determined by a number of techniques such as a sieve analysis where material is passed through progressively finer sieves and the residual mass on each sieve is weighed. Here, a slightly more advanced technique was used. Laser diffraction infers a particle size distribution by the Mie solution to Maxwell's equations

Table 3.3: Parameters for Laser PSD

| Parameter | | Value |
|---|---|---|
| Fine | Feed Pressure | 0.4 MPa |
| | Feed Rate | 50% |
| | Aperture | 1.0 mm |
| Coarse | Feed Pressure | 0.4 MPa |
| | Feed Rate | 50% |
| | Aperture | 2.0 mm |
| | Obscuration | 0.5% to 6.0% |
| | Acquisition | 10 Seconds |

[171]. Upon contact with a spherical particle, coherent electromagnetic radiation scatters predictably. An incident beam striking a particle of a given diameter results in a given degree of scattering, which is inversely proportional to the particle size.

The powder stored in a hopper is fed into the path of the laser at a controlled rate by a vibrating plate and compressed air. By scanning the laser at a sufficiently high speed across a sufficient volume of the powder, a statistically significant number of measurements may be taken. As the laser scans, a bank of detectors at varying angles records incidences of radiation at given angles.

**Scanning the Particulate**

Here a Malvern Instruments Mastersizer 3000 PSA was used, equipped with an Aero S dry dispersion unit. This was connected to a compressed air feed regulated at 0.6 MPa. The BFS powder has a bi-modal particle size distribution, and, therefore, exhibited a *very* wide range of particle sizes. The dynamic range (the ratio of largest to smallest value which can be measured) of the instrument was insufficient to completely observe this material should the fractions have remained combined with one another. The BFS was passed through a 150 $\mu$m sieve prior to analysis. The fractions were added back together by scaling each fraction relative to the mass retained on the sieve . Instrument parameters are provided in Table 3.3.

### The Particle Size Distribution

The particle size distribution is shown in Figure 3.2. The midpoint and ranges of particle sizes are quoted using $D_{x(10)}$, $D_{x(50)}$, and $D_{x(90)}$ values which are provided in Table 3.4. $D_{x(10)}$, $D_{x(50)}$, and $D_{x(90)}$ values describe the diameter which 10%, 50%, and 90% of the material is lower than respectively. The PC gives a well-graded uniform distribution throughout the range with particles ranging from $10^{-1}$ $\mu$m through to $10^{2}$ $\mu$m.

Table 3.4: $D_{x(10)}$, $D_{x(50)}$, and $D_{x(90)}$ values for BFS and PC powders.

| | Fraction | $D_{x(10)}$ / $\mu$m | $D_{x(50)}$ / $\mu$m | $D_{x(90)}$ / $\mu$m |
|---|---|---|---|---|
| PC | All | 2 | 14 | 42 |
| BFS | All | 3 | 26 | 594 |
| | Coarse | 158 | 496 | 920 |
| | Fine | 2 | 14 | 46 |

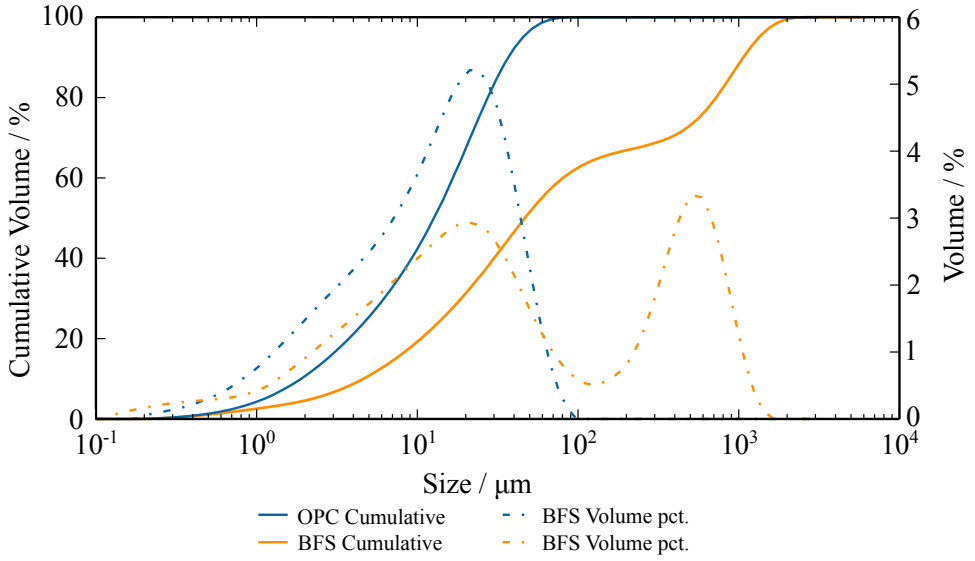


Figure 3.2: The particle size distribution of BFS (orange) and PC (blue) materials as determined by laser diffraction.

The distinct fractions found in the BFS powder were a result of the manufacturing and blending process. During production Hanson Scunthorpe ground granulated blast furnace slag (GGBS) is blended with coarse ground Calumite which is sourced from chemically identical materials ground to a higher particle size. The use of these blends provide workability for waste encapsulation without the use of chemical admixtures [1, 15].

The effect of particle size distribution on reaction kinetics has been well studied. Both real world [172, 173] cement systems have been characterised and simulated materials [170] analysed. Bentz [170] showed how a coarser cement resulted in a longer setting time, lower heat of hydration, higher diffusion coefficient at an equal degree of hydration, and a higher volume of capillary porosity. Celik [172] and Zhang [173] found that the fine fraction of particulate had a larger impact on the early strength while later strengths were more related to the reaction of coarser volumes.

## 3.3 Chemical Properties

In a cement the chemical properties of the precursor material are of a similar fundamental importance to the geometric proeprties previously analysed, and so must also be considered. These properties have a strong bearing on the chemistry of the forming hydrate phases, and so it is important to correctly characterise these to form a baseline for any research concerned with the hydration reaction. Several techniques were applied to do thus, with the aim of understanding these materials. The chemical characterisation begins with an analysis of the precursor materials by X-ray fluorescence spectroscopy. The data from this technique were used throughout this thesis. X-ray florescence provided the oxide composition of the powder, which was then used to determine a composition of clinker minerals by the Bogue calculation [174]. The techniques of X-ray diffraction and thermogravimetry are complementary to one another, and were also applied to observe phases present within the material across a longer length of time.

### 3.3.1 X-ray Fluorescence

X-ray fluorescence was carried out externally by London & Scandinavian Metallurgical Co. Ltd on the BFS and by Sheffield Hallam University Materials and Engineering Research Institute for the analysis of the PC. Data expressed as oxide fractions are provided in Table 3.5. Typical data for cements and supplementary cementitious materials are also published by Claisse [51] and may be used for comparison. In the PC CaO was found to make up a large portion of the weight fraction of the material. There were also fairly significant fractions of $SiO_2$ and $Al_2O_3$ which are also abundant in clinker compounds. $SO_3$ was found, and will be present in any sulphate phase in the clinker. This phase prevents flash set. It was not apparent from these data which crystalline or compositional form this was present in (see Section 3.3.2 and Chapter 4). The $Fe_2O_3$ content is related to the iron content of the calcium aluminoferrite $C_4AF$ phase.

Table 3.5: X-ray Fluorescence Results. The minor mass fraction provided was calculated as the total mass of compounds above 2% subtracted from 100%. Though slightly unusual, conversion to wt% was applied to match common practice in the cement industry.

| Oxide | wt.% | |
|---|---|---|
| | PC | BFS |
| CaO | 65.37 | 39.68 |
| $SiO_2$ | 19.99 | 36.6 |
| $Al_2O_3$ | 4.55 | 12.15 |
| $SO_3$ | 3.23 | * |
| $Fe_2O_3$ | 3.12 | 0.43 |
| MgO | 2.09 | 8.35 |
| Minor | 1.65 | 2.79 |

* Not analysed.

The slag used was found to contain large volumes of CaO and $SiO_2$ which are impurities extracted during the process of iron manufacturing, alongside added limestone. Note the *very* low volume of $Fe_2O_3$ that has been found in the slag. This is an intentional result of the process, where very little raw ferrite has been removed from the iron material.

The composition of clinker compounds is not particularly well described by the oxide composition and was determined by the Bogue calculation [174] in the initial part of this thesis (Equations 3.2 through 3.5). Results are given in Table 3.6.

$$\%C_3S = 4.071(CaO) - 7.60(SiO_2) - 6.72(Al_2O_3) - 1.43(Fe_2O_3) - 2.85(SO_3) \quad (3.2)$$

$$\%C_2S = 2.867(SiO_2) - 0.7544(CaO) \quad (3.3)$$

$$\%C_3A = 2.650(Al_2O_3) - 1.6920(Fe_2O_3) \quad (3.4)$$

$$\%C_4AF = 3.043(Fe_2O_3) \quad (3.5)$$

This calculation was additionally performed by crystal structure refinement in Chapter 4, and by Prentice et al. [175] using the modified Taylor-Bogue method [176] and $^{29}Si$ magic angle spinning (MAS) nuclear magnetic resonance spectroscopy (NMR). These methods showed sufficiently reasonable agreement with the results presented here bearing in mind the changes in chemical composition which have occurred in cements since the method was published.

Table 3.6: Mass fractions by Bogue Calculation [174].

| Compound | Weight Fraction / % |
|---|---|
| $C_3S$ | 70.0 |
| $C_2S$ | 4.5 |
| $C_3A$ | 6.8 |
| $C_4AF$ | 9.5 |
| Total | 90.8 |

By this calculation is has been confirmed that the cement conforms to the EN 197-1 [11] standard. In order to conform the material must be made up of in excess of 66% calcium silicates ($C_3S$ and $C_2S$) and the fraction of magnesium oxide must not exceed 5%.

### 3.3.2 X-ray Diffraction

X-ray diffraction is a characterisation technique which works on the principle of Bragg diffraction, and was extensively used in this thesis (Chapter 4). When encountering an incident ray, a crystal structure will cause scattering of the ray based on the properties of the crystal lattice and the wavelength of the incident radiation. Diffraction occurs only when the wavelength of radiation is in close proximity to the dimension of the lattice spacing.

#### Method

Laboratory diffraction profiles were acquired using a Siemens D5000 diffractometer with a copper X-ray source producing radiation with a characteristic wavelength of 1.5419 Å. The instrument was run at an operating voltage of 40 kV and current of 40 mA.

In order to prevent preferred orientation effects, the sample was smoothed with a 1.0 mm glass slide and rotated through 360° during analysis. However, it was not always possible to mitigate preferred orientation. In certain scans the reflections from hydrate phases such as Portlandite may arbitrarily increase or decrease without reason. This is preferred orientation.

#### Precursor Phases

Figure 3.3 shows the diffractograms acquired of the precursor materials. The PC is shown at the top of the figure with the slag toward the bottom.

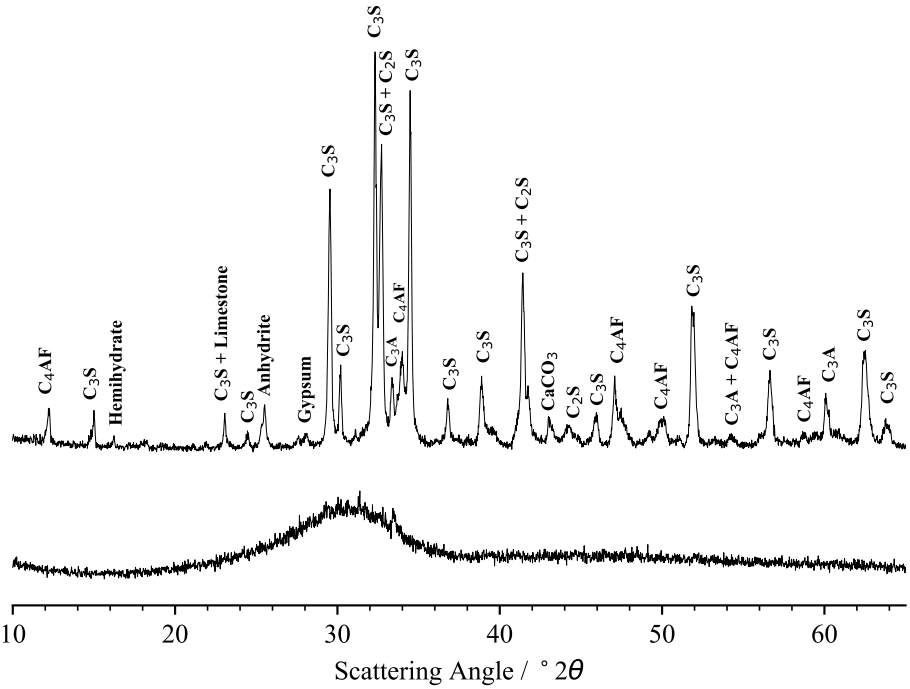


Figure 3.3: Diffraction of the precursor PC and BFS materials, with key phases identified.

Here the four principal clinker compounds were found, and are identified in the profile provided. Gypsum and anhydrite have been added to the material as discussed in Chapter 2 during manufacture. A *very* small reflection from hemihydrate was also found. These phases result from the addition of calcium sulphate to the cement; anhydrite and hemihydrate have either been directly added or have resulted from decomposition of gypsum in the cement kiln.

The BFS showed extensive, almost complete, diffuse scattering in the range 15°2$\theta$ to 38°2$\theta$. Reflections of the sorosilicates gehlenite and akermanite were also found, though these were insignificant to the extent that they did not appear in scans of the blended powder and were neglected for further analysis. Calcium carbonate was present, but was shown only by thermogravimetry as this compound may be either amorphous in nature, or found in trace amounts which are not visible above the background noise of the instrument.

### Hydrate Phases

Hydrated phases are identified in Figures 3.4, 3.5 and 3.6 for the 75%, 78%, and 90% BFS materials respectively. The hydration of all specimens prepared for analysis by X-ray diffraction was arrested as per Section 3.1.2 before materials were ground in an agate pestle and mortar and passed through a 63 $\mu$m sieve.

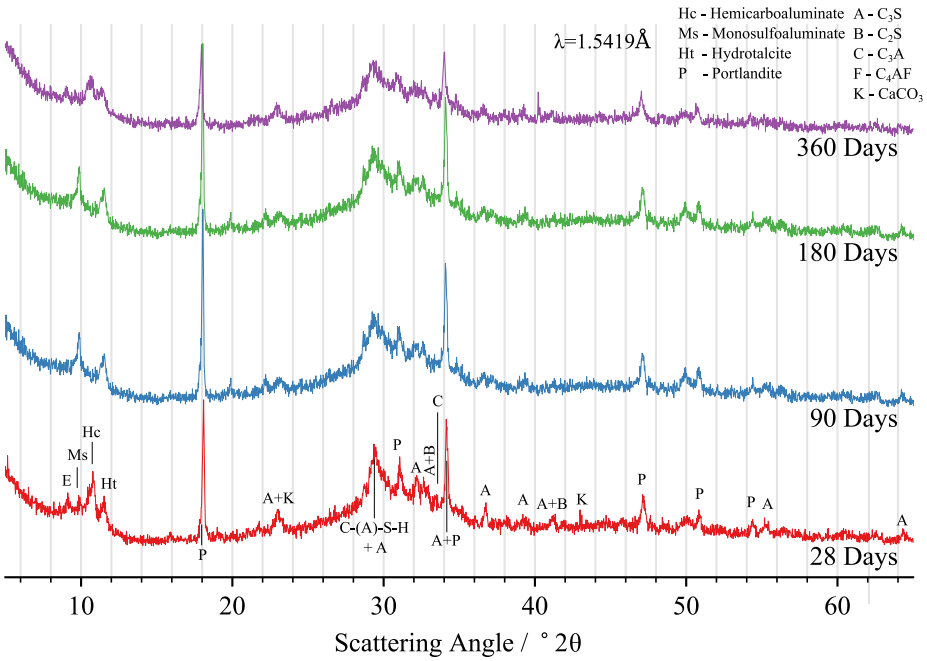


Figure 3.4: Hydration of the 75% BFS material up to 360 days observed by XRD.

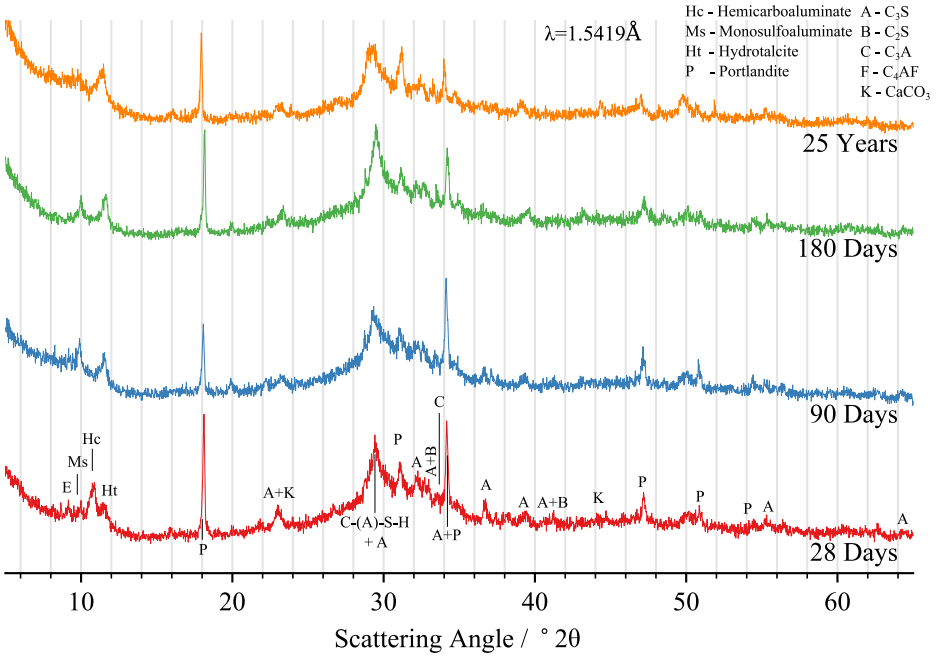


Figure 3.5: Hydration of the 78% BFS material up to 25 years observed by XRD.

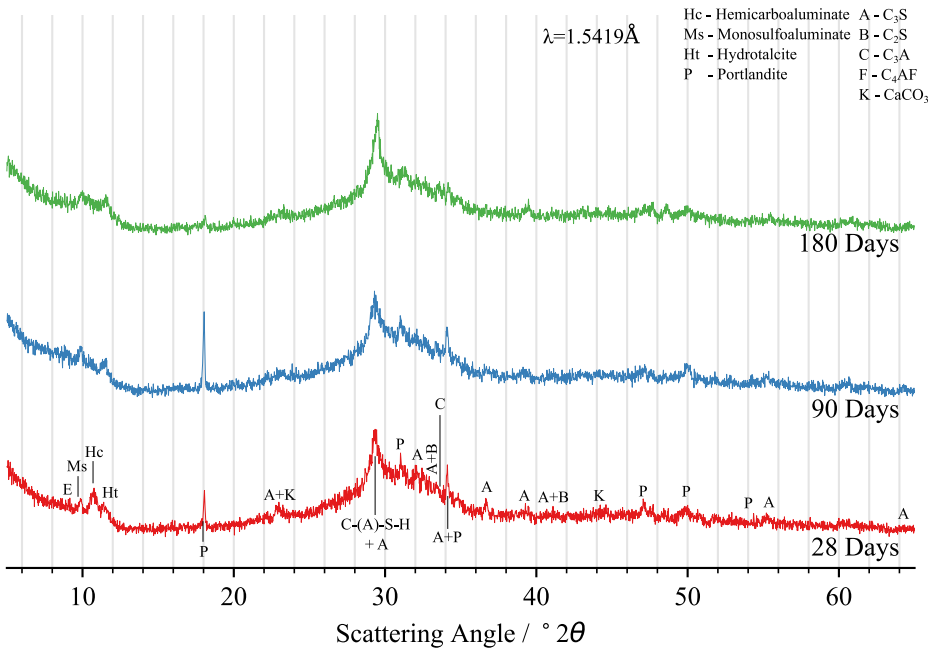


Figure 3.6: Hydration of the 90% BFS material up to 180 days observed by XRD.

The formation of multiple phases within the matrix was shown across this period from compounds both crystalline and amorphous in structure. Ettringite forms early in the reaction, being present from the first datum. Monosulphate has also formed here which is a result of the conversion of ettringite once calcium sulphate in the material is consumed. Either the two peaks appeared to merge together, or the ettringite has become depleted to the extent that it was no longer possible to resolve this phase within the material. Portlandite was formed in abundance with a major reflection around 8.7 Å $d$-spacing. A reflection was found at 5.2 Å, though this was masked by the lower resolution of the laboratory instrument and merged with the $C_3S$ reflection lying in close proximity. $CaCO_3$ identified at 4.1 Å. The data presented in Figure 3.5 showed hydrates all the way from 28 days to 25 years. Calcium silicates have not reacted entirely by 25 years; there is still some potential for hydration to continue should water become accessible to the clinker-product interface on the surface of these phases.

### 3.3.3 Thermogravimetry: Breaking Hydrates Down

Thermogravimetry allows for the phases present in a material to be characterised by studying the mass loss of the material as it is heated through a set profile. In a typical instrument, a sample is placed on a constant read-out high-precision mass balance within a temperature controlled furnace. The furnace is heated at a specific fixed rate and the mass recorded. This

takes place in an inert environment to prevent reaction of the sample. Nitrogen or argon which are inert are used.

### Method of Thermal Analysis

In this thesis, analysis was carried out using a Perkin Elmer TGA 4000 instrument. The hydration of all specimens prepared for analysis by thermogravimetry was first arrested as per Section 3.1.2 before materials were ground in an agate pestle and mortar. A mass of 35 mg was batched on a 3-dp laboratory mass balance at ambient temperature, and placed into the instrument. The mass was first allowed to equilibrate in the instrument for 30 minutes. The sample was sealed within with a 19.8 $cm^3$ $min^{-1}$ flow of nitrogen gas, and was heated from 30°C to 995°C at a rate of 10°C $min^{-1}$ after the equilibration time.

### Cementing Precursors

The results of thermogravimetry of the anhydrous PC and BFS precursor materials are provided in Figures 3.7a and 3.7b respectively. A decomposition temperature range for each phase is provided in Table 3.7 from the data provided by Ramachandran et al. [177].

A number of decomposition reactions were observed in the PC, and some to a lesser degree in the BFS. Some free water appears to have at least entered the materials during storage. This has resulted in some pre-hydration, which was only minor in the case of the samples analysed here, and this was deemed insignificant. Some portlandite was observed, which presented a mass loss of approximately 0.5%. This minute mass loss indicated the insignificance of any partial hydration.

The PC also was found to contain calcium carbonate, which was either Limestone added during the manufacture of the material or alternatively the reaction of any $Ca(OH)_2$ with

Table 3.7: Decompositions of PC (1, 2, and 3) and BFS (4, 5, and 6) materials, after [177].

| | Temperature / °C | Decomposition / Reaction |
|---|---|---|
| 1 | 30 to 150 | Loss of free water, C-S-H decomposition |
| 2 | 350 to 450 | Portlandite, $Ca(OH)_2 \longrightarrow CaO + H_2O$ |
| 3 | 550 to 875 | Carbonate / limestone $CaCO_3 \longrightarrow CaO + CO_2$ |
| 4 | 30 to 150 | Loss of free water |
| 5 | 550 to 600 | $CaCO_3$ by $CaCO_3 \longrightarrow CaO + CO_2$ |
| 6 | 850 to 950 | Change of oxidation state |

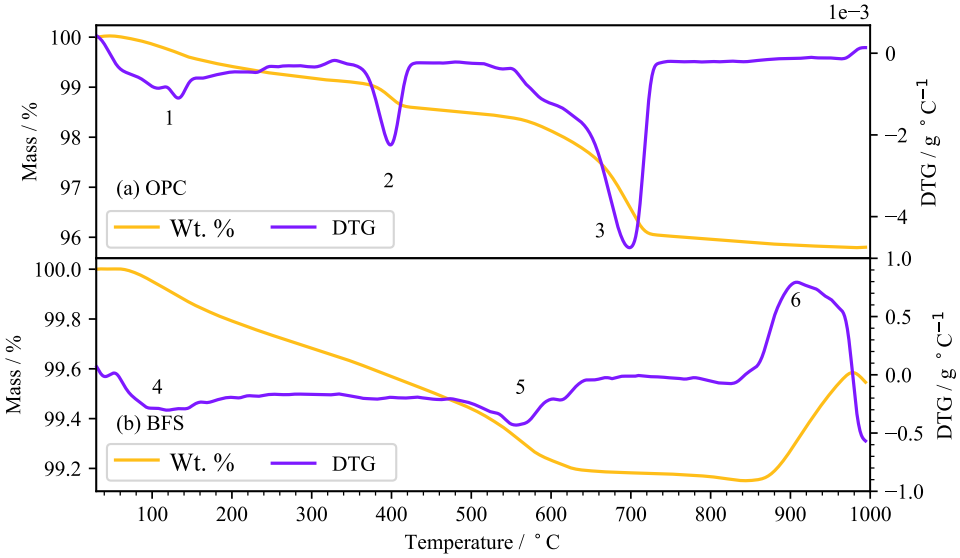


Figure 3.7: Thermal analysis of PC (a) and BFS (b) materials.

$CO_2$. Given the volume observed, it was likely that former situation is more probable, and that carbonation has probably not occurred significantly in products of partial hydration.

This appears to have also occurred in the BFS sample, which appears to have also had some moisture uptake. However, this has happened to a much lower extent. Though some of the slag may react with water, as a latent hydraulic material, this will occur in the slag at a *much* lower rate. Some $H_2O$ has left the material at a maximum rate of mass loss at approximately 100°C. Between 550 and 600°C, the cement appeared to reduce in mass as a result of the evolution of $CO_2$, resulting from the decomposition of $CaCO_3$. Between 850°C and 950°C a mass gain occurs. Ramachandran et al. [177] attributed this gain to the reaction of the sample with any small amounts of oxygen present, resulting in the transition from sulphide $S^{2-}$ to sulphate $S^{4+}$.

### The Forming Hydrates

Profiles of cements at 75%, 78%, and 90% BFS replacement hydrated for 28 and 90 days are shown in Figures 3.8 and 3.9. Figure 3.10 shows a sample of 78% BFS hydrated for 1 and 25 years. C-(A)-S-H is identified along with residual free water in the microstructure, which was not entirely removed by the drying process. The maximum loss rate occured at 100°C at which point free water is removed from the sample. Monosulphate has formed by 28 days; it would appear that all $CaSO_4 \cdot nH_2O$ has been consumed by this point, and ettringite has destabilised and formed some kind of AFm phase. This was also shown by qualitative

analysis of the XRD profiles in Section 3.3.2. The precise time at which this occurs was not resolvable with precision by the data shown in this chapter.

The reaction of magnesium, which is abundant in the slag, with aliminium, carbonate, and water has formed the layered double hydroxide hydrotalcite. Portlandite has formed as expected which is a common hydrate phase resulting from the hydration of $C_3S$ and $C_2S$, discussed in Chapter 2. Two regions of calcium carbonate decomposition were also observed. The calcium carbonate has not reacted with any secondary phases and has remained present in the specimen to 25 years, and will therefore possibly remain for the life of the material. In addition to being added during manufacturing the $CaCO_3$ may also form as a result of the reaction of $Ca(OH)_2$ with residual atmospheric $CO_2$.

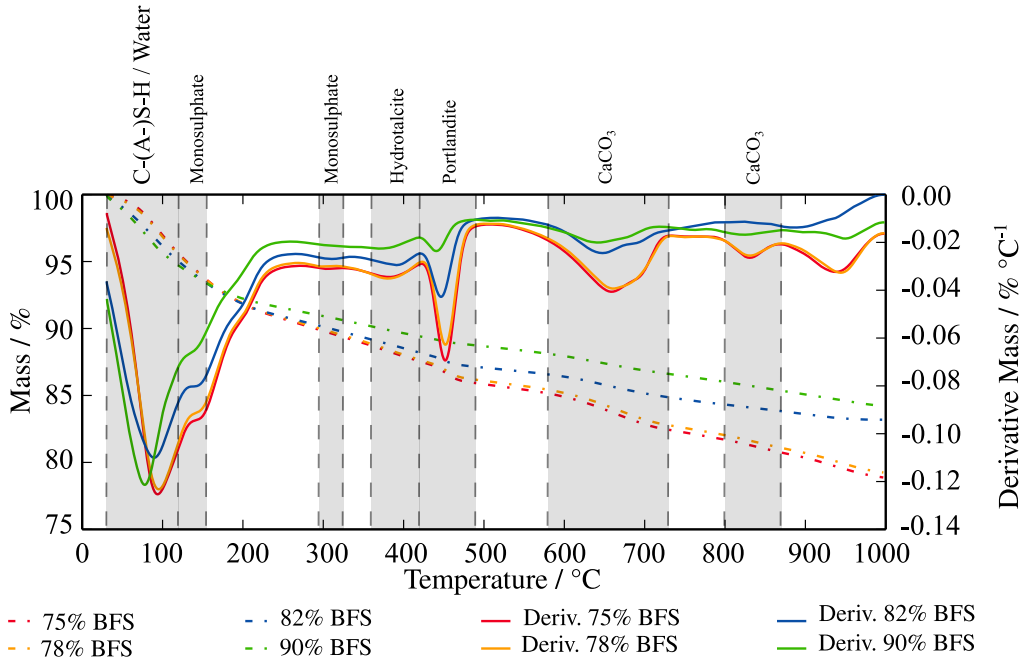


Figure 3.8: Thermogravimetry of specimens as labelled at 28 days hydration.

### 3.3.4 Isothermal Conduction Calorimetry

In this chapter the thermal output of the cement is observed using isothermal conduction calorimetry, which is briefly discussed in Chapter 2. The heat output of the specimen is measured using a thermopile heat flow sensor placed above a heat-sink. The thermopile device is comprised of multiple thermocouples connected in series. Heat emitted is drawn downward toward the heat-sink across the thermopile, which produces a signal. Before testing of a specimen, this is calibrated by placing a heater which produces a known thermal flux into the

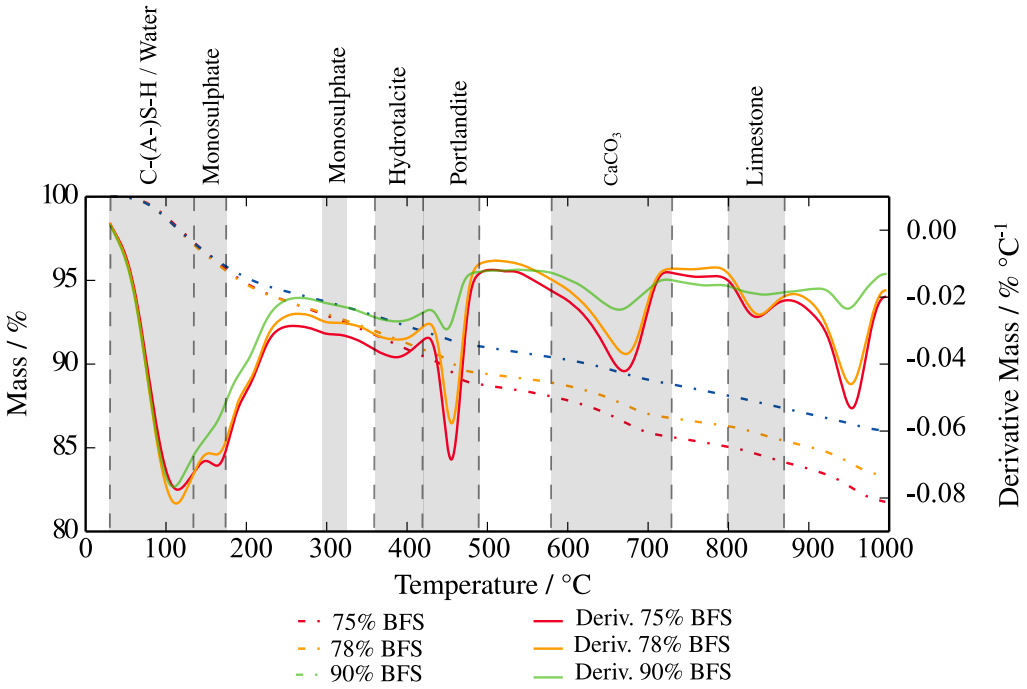


Figure 3.9: Thermogravimetry of specimens as labelled at 90 days hydration.

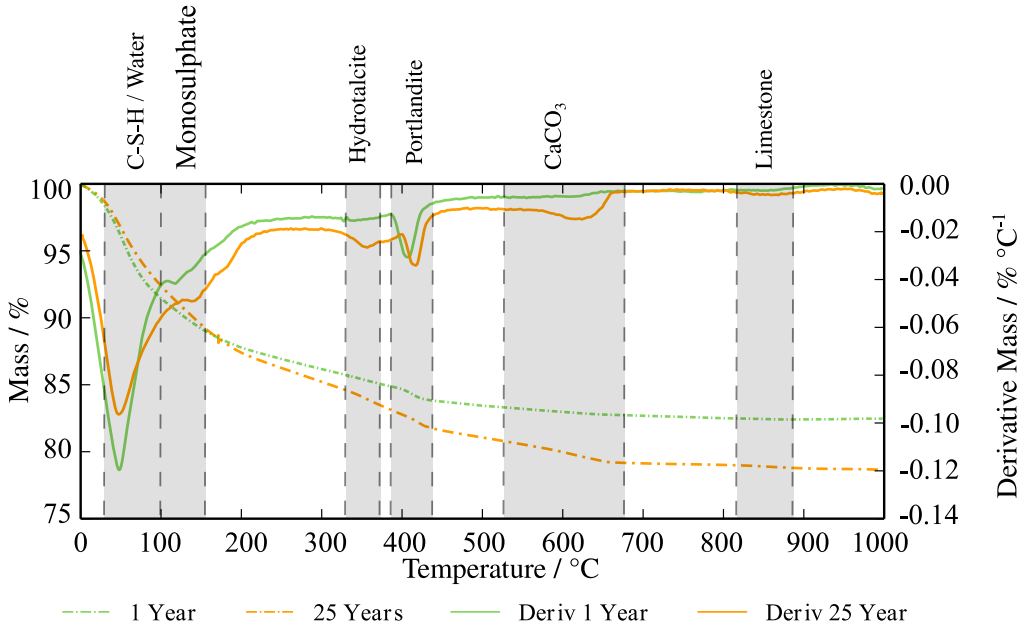


Figure 3.10: Thermogravimetry of specimens as labelled at 360 days and 25 years hydration.

calorimeter. The voltage is measured by a data logger at a very high sample rate. The sample may be left undisturbed in the calorimeter for a number of weeks to observe the reaction over an extended period of time. The unit is also thermally insulated and temperature controlled, which allows for the reaction of the sample to be observed at the varying temperatures which

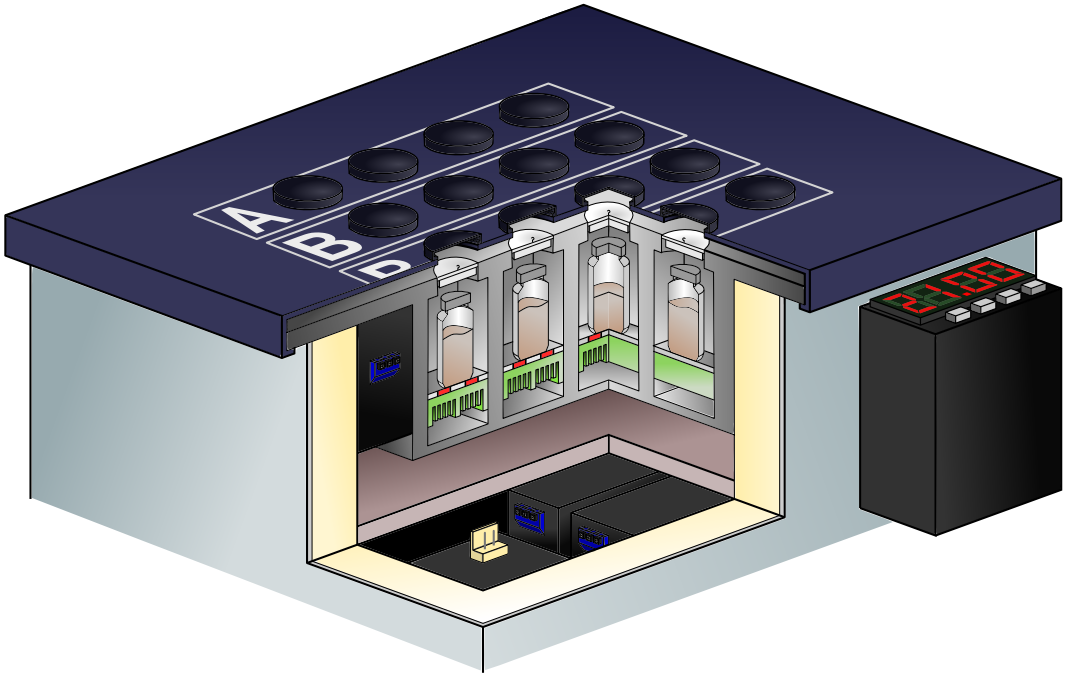


Figure 3.11: An isothermal conduction calorimeter similar to the TA Instruments TAM Air instrument.

may be found in an industrial conditions. A typical instrument is shown in Figure 3.11 (based upon the TAM Air instrument).

### Measuring the Heat Released

Isothermal calorimetry was carried out using a TA instruments TAM Air microcalorimeter in an identical manner for each degree of substitution analysed, including a sample of unblended Portland cements analysed in Chapters 4 and 5. The heat output was observed from immediately post-mixing. Samples were discarded after testing.

The cement was prepared by hand blending in a plastic beaker until well homogenised. The sample was then mixed with the correct amount of distilled water and placed into a 20 mL high density polyethylene (HDPE) ampoule alongside a reference standard. The total mass of the specimen was approximately 25 g. The sample was immediately transferred to the isothermal calorimeter unit.

### Hydration Observed by Isothermal Calorimetry

The thermal output of the system across the first 48 hours of the reaction is shown in Figure 3.12. Figure 3.13 shows the time of peak isothermal output after the first stage. This appears to be dependent on the degree of substitution of the blast furnace slag.

The design of the calorimeter necessitated the external mixing of the sample and so the first peak was partially missed. This peak was of overall insignificance due to the relative brevity of the high thermal output which occurred here. The thermal output was divided into the five stages described in Chapter 2. These are indicated in Figure 3.12.

The data showed quite clearly that the thermal output of the system was dramatically reduced upon substitution of PC. The cumulative thermal output of the 90% slag material was almost half that of the 75%. In regular applications of this material the lowered thermal output allows for the construction of large and bulk structural elements without thermal cracking.

The time at which sulphate depletion appears to occur was entirely dependent on the degree of substitution of the material, and appears to trigger earlier with a greater slag content. As the cement content reduced the sulphate content also reduced while the mass of cementing material remained the identical, shifting the peak to the left.

### Extending With Time

Hydration continues for an extended duration, and may never cease in its entirety. In the pure PC material, no sulphate depletion point was shown in the first 48 hours of the reaction. Beyond the final datum presented hydration has a *very* low thermal output. In Chapter 6 a 25 year old specimen was observed using X-ray tomography, and still showed anhydrous material in the microstructure, in spite of the age of the sample. The long term changes of this material was shown to be gradual beyond 48 hours and there was little of interest in the thermal output. Presenting these data resulted in compression in the early time range from which all stages may be easily isolated.

## 3.4 Conclusions

In this chapter the fundamental physical and chemical properties of the materials used in this thesis have been investigated. The reaction of clinker phases to form hydrates across the first year of the hydration reaction have also been shown, and several techniques applied to for this purpose. All techniques showed at least qualitative agreement with one another. The

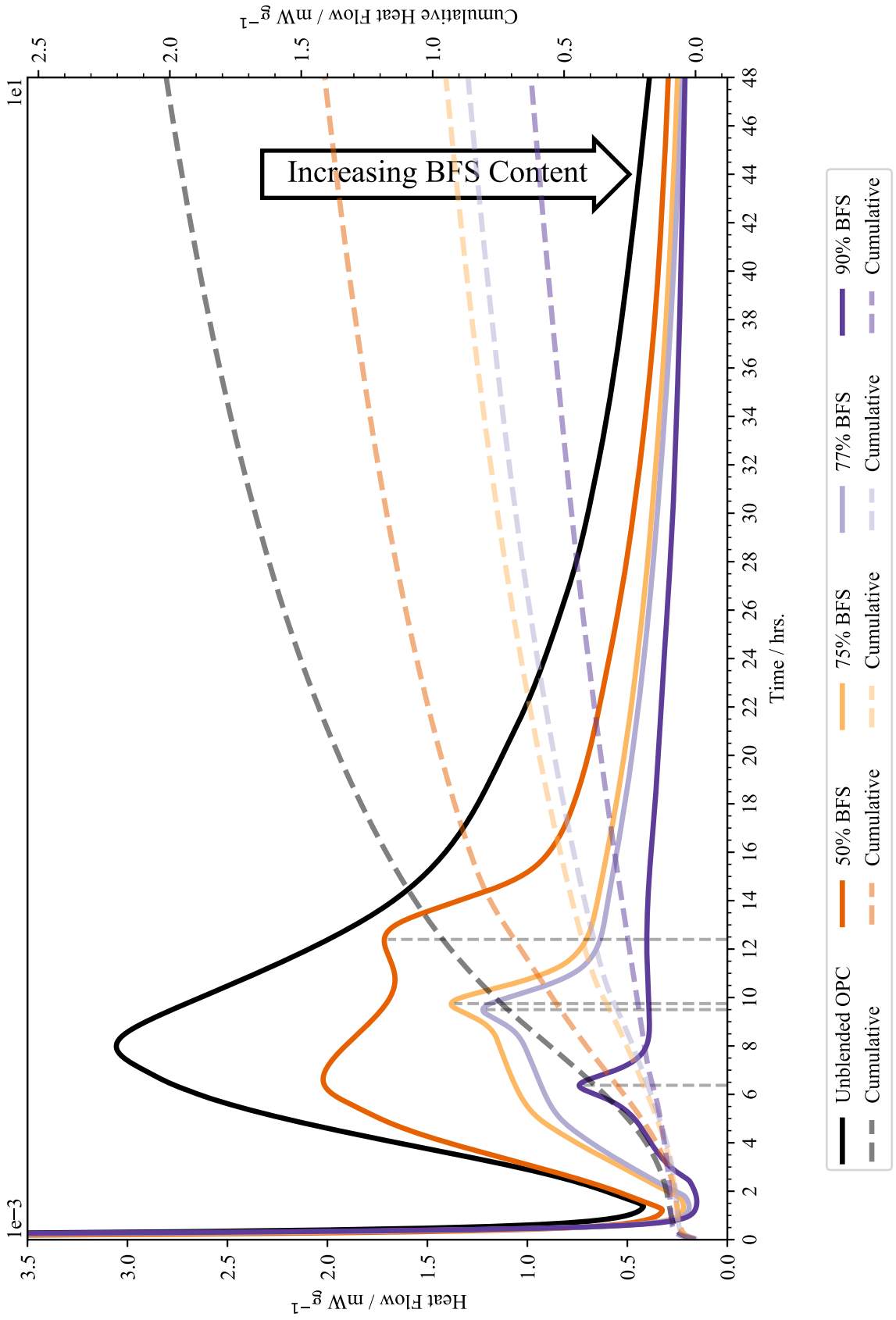


Figure 3.12: Isothermal calorimetry for hydrating materials as indicated. Time zero is recorded from the point at which water first came into contact with the sample (approximately 7 minutes 30 seconds).

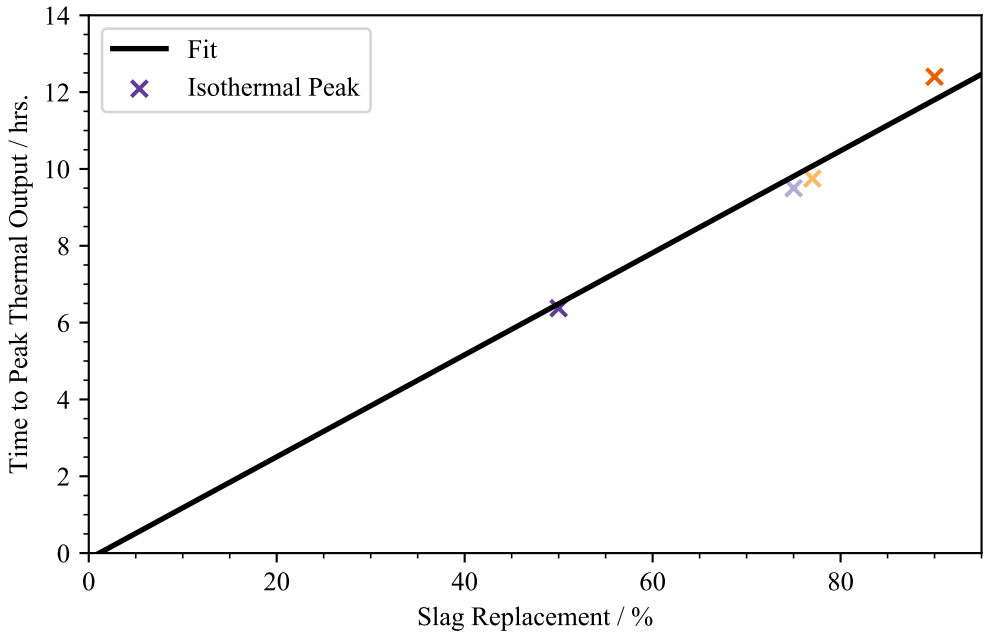


Figure 3.13: Time dependency of peak isothermal output (sulphate depletion) for slag bearing materials.

clinker contained the typical compounds as per the BS EN 197-1 specification [11] and it can be confirmed that this material was precisely what was expected by this standard.

The slag contained large fractions of silicon and calcium which were found as impurities in the iron-making process and are removed from the material during this. The slag contained a very low ferrite content; ferrite remained in the iron and is not significantly removed in the slag product. However, due to the nature of the process, the presence of at least a small amount was fully expected, which was precisely what was observed here. The sorosilicates gehlenite and akermanite were identified and were barely visible above the diffuse scattering. The diffuse scattering was broad throughout the range and of significant intensity in the profile.

During the hydration reaction, the formation of a number of individual phases were identified. Ettringite was formed as a result of the reaction of $C_3A$ and $CaSO_4{\cdot}nH_2O$ which had taken the form of gypsum, anhydrite, and hemihydrate (*very* minor) during manufacture of the precursor. Monosulphate formed as a result of the destabilisation of ettringite once full reaction of surplus $C_3A$ had happened. Thermogravimetry also showed the decomposition of this phase.

C–(A)–S–H formed in abundance in the microstructure alongside portlandite. $C_3S$ and small volumes of $C_2S$ have reacted in the presence of the Al rich slag with water, forming

these phases. C–(A)–S–H is entirely amorphous and resulted in diffuse scattering in the diffraction profiles observed throughout the time frame studied here. The portlandite, however, showed clear Bragg peaks at this point, which occurred within the first 28 days of the reaction (see also Chapter 4). Isothermal calorimetry showed all of the stages of initial hydration with the thermal output significantly reducing beyond approximately 24 hours and on a composition-by-composition basis. The addition of a higher mass of slag decreased the thermal output significantly. A distinctive isotherm was identified which directly relates to the degree of substitution of slag, which was attributed as the sulphate depletion point.

The PC showed a uniform particle size distribution with a specific surface area of 376 $cm^2g^{-1}$ (see also Table 3.2). The BFS had an angular and "jagged" geometry. A bi-modal particle size distribution was found which results from the Calumite fraction in the slag which was combined to provide a workable grout [15] during manufacture. In spite of the presence of the Calumite fraction, the slag showed a higher specific surface area than the PC. This highlighted how fine the region of low particle size is. The densities of these lay close to the values published by Claisse [51].

# Chapter 4

# A Dissection of Hydration Chemistry

*This chapter is based upon a paper in preparation for submission, authored by J.E. Vigor, C.A. Murray (beamline science) C.C. Tang (beamline science), C.L. Corkhill (experimental and supervisory, N.C. Hyatt (experimental and supervisory), S.A. Bernal (supervisory), and J.L. Provis (supervisory).* The contribution of individual authors is detailed on page iv.

As established in Chapter 2, the hydration reaction of a Portland cement system governs the chemical and structural evolution of the binder matrix. Hence, this process is responsible for the characteristics such as the pore structure, transport properties, and strength evolution of the grout. Highly substituted slag-Portland cement systems have previously been studied by a number of authors, at early age[1] by Wu et al. [178] using isothermal calorimetry, late ages[2] by Taylor et al. [179] and under various conditions of hydration[3] by Escalante-Garcia and Sharp [180]. However this has not yet been carried out in a quantitative manner with a rapid time resolution such as that shown by Schlegel et al. [5].

The rapid rates at which chemical reactions in the hydration of Portland cements and supplementary cementitious materials take place necessitate a sufficiently high capture rate to observe changes on both a micron length-scale (spatially resolved) and crystallographic (in the case of this chapter) scale. Within the first hours of the reaction, highly exothermic reactions take place as alkali-containing clinker phases dissolve into solution, described further in Chapter 2. Brown and LaCroix [23] showed by diffractometry how the first crystalline phases form almost immediately on contact of the anhydrous cement material with water in

[1] the first 24 hours with compositions of 100% PC, 60% PC and 40% BFS, 50% PC and 50% BFS, and 35% PC and 65% BFS

[2] 20 year old samples containing 0% to 100% BFS with a water-solids ratio of 0.4

[3] PC substituted with 30% pulverised fuel ash (PFA), PC substituted with 60% BFS and PC substituted with 22% volcanic ash (VA) at a water-solids ratio of 0.5.

1985, though the modern X-ray sources available today allow here for a significant expansion of this work.

A very common technique used to monitor the heat output of the hydration reaction as a function of time is isothermal conduction calorimetry, as shown by Bensted [181] and Pane and Hansen [16], and in Chapter 3. However, it is difficult to isolate contributions from individual reaction processes in these data, or to produce quantitative information regarding the mechanics of phase formation, without complementary information obtained from other time-resolved techniques that is sensitive to mineralogy.

The reaction of cementitious materials is incompletely quantified [4], and due to their abundant use in society it is of high importance to ensure that both these early reactions and reactions occurring across a longer duration are fully characterised and well understood. This assists in the production of a safety case for the understanding and pursuit of cementation as a method of encapsulating intermediate level wastes, and also for civil engineering purposes where structures might be exposed to an aggressive climate.

In this Chapter, results are presented from the analysis of hydration of three highly substituted BFS-PC materials from data captured on a synchrotron based powder diffraction instrument, in addition to a sample of pure Portland cement. The amorphous slag content is described by a Pawley $hkl$ phase [182], which is fitted to the precursor material and scaled as the slag reacts, via the partial or no known crystal structure method (PONKCS) [183]. The growth of early hydrates and loss of clinker phases is shown, as is the application of the PONKCS technique in the analysis of the slag amorphous content during this time.

## 4.1 X-ray Powder Diffraction

A key technique commonly applied for the investigation of phase formation and mineralogy in cements is X-ray powder diffraction (XRPD). Rietveld full-profile refinement analysis may be used to obtain information about phases and structures present within the material [184]; instrument and material parameters are iteratively adjusted (within reasonable limits) until the simulated profile represents a good match to that produced from the instrument. This technique can be used to determine, from initial or published values, information such as the crystalline lattice parameters, crystallite sizes, material strains, and the fraction of each phase present within a complex bulk composition.

Typical laboratory XRPD instruments are able to generate scans of sufficient quality for quantitative refinement within a matter of hours. The crystalline composition of a cement system which has reached a steady state or whose hydration has been artificially halted is

thus readily analysed in this manner. In such cases, the rate of change of composition of the material is insignificant in comparison to the acquisition time. However, during the earliest moments of hydration, it remains impossible to achieve the temporal resolution necessary to see the complex changes taking place. In order to overcome this problem, an instrument with a time-resolved high flux and high sensitivity capability must be used; this can be achieved using a high-brightness synchrotron XRPD beamline, as has been successfully used in previous studies of hydrating cementitious systems [185–187]. This study is presented in the context of the I11 instrument at the Diamond Light Source, shown in Figure A.2 in Chapter 3. This instrument allows for significant improvements in both the scan resolution and time resolution compared to a standard laboratory-based instrument. Technical descriptions of the beamline are provided by Thompson et al. [188, 189].

It, therefore, becomes highly attractive as an option to make use of an instrument which has both a high X-ray flux and a high resolution detector. This effectively allows these challenges to be resolved. An example of an instrument meeting these desired characteristics may be found on a synchrotron, a facility making use of the emission of high energy electromagnetic radiation as electrons are passed around the circumference of a near-circular accelerator facility (A.1). It becomes possible to study these chemical reactions in an entirely in-situ manner, essentially freezing a snapshot of the chemical reaction at any given time without the need to arrest hydration. Sample variation is also reduced as the same sample is repetitively analysed.

The advanced instrumentation available at the facility allows a high resolution full in-situ diffraction profile to be acquired in a matter of seconds, reducing the time required by an order of magnitude from that needed by a laboratory instrument. The data are fully analysed using the Rietveld method [184] to quantify the time resolved distribution of phases within the specimen.

### 4.1.1 Rietveld Crystal Structure Refinement

This method was first reported in the literature in 1969 by Rietveld [184]. Rietveld refinement is commonly used to resolve crystal structure properties from the profiles captured by X-ray and neutron diffraction. The technique was initially used to characterise pyrolytic graphite with a profile captured by neutron diffraction. Experimentally, a detector was scanned through the $2\theta$ range and measured the intensity of the signal in each step. The instrument background in that study was calculated by interpolation of the profile and subtracted, which is a rather rudimentary approach, and more sophisticated approaches to the treatment of the background have been demonstrated since that time.

A profile is simulated based on a number of parameters which are represented by a collection of Gaussian type peaks. The peak shape, width, and preferred orientation of crystallites within the powder may be iteratively adjusted and corrected for. For each particular peak the peak position is described by the Miller indices $hkl$ and the lattice $d$-spacing parameter.

### 4.1.2 Quantifying a Distribution of Phases

The method for computing a phase distribution using Rietveld refinement is well documented [190]. Describing each material component in this manner allows for the contribution of each phase in the structure to be determined. Each phase is assigned a scale parameter $S_p$ which is adjusted based upon the intensity of peaks describing said phase. The volume of the unit cell, say $V_p$, may be determined knowing the lattice parameters $a$, $b$, and $c$ determined previously and the unit cell geometry. Knowing the chemical composition of the phase, the relative atomic mass, $M_p$, of the unit cell for each phase is then computed.

The weight percentage of material that is present for each particular phase is calculated as per Equation 4.1, where $Q_p$ is defined by Equation 4.2 as a function of the scale factor $S_p$, the unit cell mass $M_p$, the unit cell volume $V_p$ (which was previously calculated) and the Brindley spherical correction $B_p$ which corrects for differing absorption based on the sphericity of particles in the material [191]. This provides the weight percentage of each phase within the mixture.

$$w_p = \frac{Q_p}{\sum_{p=1}^{N_p} Q_p} \tag{4.1}$$

$$Q_p = \frac{S_p M_p V_p}{B_p} \tag{4.2}$$

### 4.1.3 Analysing Cements

The highly crystalline nature of anhydrous Portland cements makes them a suitable candidate for study using this X-ray diffractometry [192]. However, matters are complicated by high volumes of glassy or amorphous components found in supplementary cementitious materials such as BFS. This results in characteristic scattering in a diffraction profile. It remains challenging (though by no means impossible) to quantify such phases. Often, an internal or external reference standard will be used [193]. This enables the volume of amorphous content to be resolved.

### 4.1.4 The Partial or No Known Crystal Structure Approach

The addition of a finely-divided powder as internal standard can either lead to chemical reaction with the hydrating Portland cement if the spike is chosen inappropriately, or seeding effects which alter the rate of reaction even if an inert additive is used [194, 195]. Another option is to adopt the "partial or no known crystal structure" (PONKCS) refinement approach [183], based on a limited number of assumptions about the rates of reaction of clinker phases which are effectively treated as internal standards. This is the methodology opted for in this chapter.

As previously discussed, in a traditional Rietveld refinement, the weight fraction of a phase may be determined as a function of its Rietveld scale factor, the $Q$ constant for the given phase, and the scale factor and $Q$ constants for all other phases [196]. As described in the preceding section the constant $Q$ is determined as a function of the formula units in a unit cell, the molecular mass of the formula unit, and the unit cell volume. The weight fraction of a phase is consequently determined from Equation 4.1. However, in materials where the structure of a given phase is unknown, by definition, $Q$ for that phase is also unknown. In these cases, it remains impossible to determine the quantitative weight fraction using conventional analysis.

Using the partial or no known crystal structure (PONKCS) approach, it becomes possible to empirically calibrate $Q$ for a given material and instrument. This is carried out through the analysis of a "pure phase" specimen to which an arbitrary profile is fitted, and a synthetic mixture in which the weight percentage of specimen material is known.

Equation 4.3, for which a detailed derivation is given in [183], is then applied in order to determine the $Q$ parameter. Here, $W_\alpha$ is the weight percent of the unknown material, $W_S$ is the weight percent of the standard material with which it is mixed, $S_S$ is the Rietveld scale factor applied to the standard material, and $S_\alpha$ is the same factor refined to the unknown material. $Q_S$ is refined from the structural parameters of the standard material.

$$Q_\alpha = \frac{W_\alpha S_S}{W_S S_\alpha} Q_S \tag{4.3}$$

### 4.1.5 Necessary Assumptions

In using this technique it is unfortunately necessary to make some further assumptions regarding some of the less reactive phases in the material. Here $\beta$-$C_2S$ is assumed to be unreactive across the first 60 hours. This phase has been shown by computational modelling to have fairly little chemical reaction across the first hours of the hydration of Portland cement

clinker [197]. The quantity of this phase is determined in the analysis of anhydrous materials. This allows the quantity of amorphous phases within the microstructure to be resolved. This study appears to be the first occasion in which such a technique has been applied to the analysis of the first hours of the reaction of cementitious materials fully in-situ.

## 4.2 Observing the Reaction

Precursor materials consisted of Hanson Ribblesdale Works CEM I 52.5N Portland cement (PC), and Hanson REGEN Ground Granulated Blast Furnace Slag (BFS). Materials were provided by Hanson Heidelberg Cement Group and the UK National Nuclear Laboratory. Oxide compositions for these materials, as determined by X-ray fluorescence spectroscopy, are given in Table 4.1 (method provided in Section 3.3.1). Anhydrous powders were placed directly into an identical 0.7 mm capillary and scanned for approximately 30 minutes using the high-resolution multi-analyser crystal (MAC) detector to acquire a high resolution baseline suitable for further analyses.

Table 4.1: Oxide compositions for the reacting CEM-1 52.5N PC and the BFS determined by X-ray Fluorescence (data reproduced from Section 3.3.1). Though slightly unusual, conversion to wt% was applied to match common practice in the cement industry.

| Oxide | wt.% | |
|---|---|---|
| | PC | BFS |
| CaO | 65.4 | 39.7 |
| $SiO_2$ | 20.0 | 36.6 |
| $Al_2O_3$ | 4.6 | 12.1 |
| $Fe_2O_3$ | 3.1 | 0.4 |
| $SO_3$ | 3.2 | - |

Materials were prepared in an on-site laboratory at the Diamond Light Source synchrotron facility before being transferred to the I11 end-station for analysis. Cement was blended with the correct mass fraction of slag before being placed into a Kapton tube. Here, samples of the same precursors were blended in ratios of 1:1 (50% BFS), 3:1 (75% BFS), and 9:1 (90% BFS) parts BFS to PC. Before loading into the Kapton, the water-cement ratio was raised slightly from 0.35 to 0.5. The Kapton tube is then placed within a 0.7 mm diameter borosilicate glass capillary to be transferred directly to the hutch and mounted within the sample

changing cassette. The time from mixing to first acquisition ranges between 15 and 20 minutes.

Steps in the reaction were captured using an array of Mythen-2 silicon micro-strip position sensitive detectors (PSD) with a 90° aperture which gives sufficient temporal resolution (subseconds / pattern) to observe the reaction unfold [189]. These were mounted on the $\delta$ circle of the I11 instrument. The output from each strip was summed during acquisition. This provided the high temporal resolution necessary to observe the reaction as it unfolds. Here, the temporal resolution was constrained only by the ability to process data.

Once mounted, samples were repeatedly scanned. Each complete scan took approximately 15 seconds for the entire operation. The PSD was positioned to cover an angular range between $2°2\theta$ and $92°$ $2\theta$, with a step size of $0.004°$ $2\theta$ at a wavelength $\lambda = 0.82570(1)$ Å. Samples remained in the experimental hutch for 60 hours, being periodically scanned in this manner for the duration of the experiment.

Between the collection of profiles, samples were retained within the cassette before being placed within the instrument. This allowed for manipulation (placement) of the sample without human access to the hutch being required. The cycle of the instrument was only broken should another sample be added to the cassette or the beam dumped. In cases where a break in the beam occurs, and to produce resolvable data back to a time of zero, data are filled by bilinear interpolation.

### 4.2.1 Isothermal Conduction Calorimetry

Isothermal conduction calorimetry was carried out as part of this thesis study using a TA Instruments TAM Air micro-calorimeter (Section 3.3.4). The instrument was held at 25°C matching closely the temperature of the hutch at the synchrotron. Samples were prepared in the same proportions detailed above, and were externally mixed then placed into HDPE ampoules before being transferred immediately into the calorimeter. Data were recorded for 60 hours, matching the time-scale used in the synchrotron experiment.

## 4.3 Putting the Parts Together

The reaction was quantified by the Rietveld method [184] using the Bruker AXS Topas package [198]. Using this method a diffraction profile is simulated and iteratively adjusted by least squares regression fitting to provide a best fit which iteratively converges on a residual value. Select refinements were verified by eye before continuing to the following scan to ensure all crystalline phases provide sharp Bragg peaks and were not accidentally fitted to the profile of diffuse scattering from the material. The weight percentage of each phase is determined as per Section 4.1.2.

Crystal structures are set initially to the published values with structures provided in Table 4.2. Lattice parameters are refined to $\pm$ 2.5% of the published value by refinement of precursor data acquired on the MAC detector and subsequently fixed in the refinement; the lattice parameters of all clinker materials must remain constant throughout. The lattice parameters for hydrate phases are refined in the final scan where these are most abundant, and are also fixed before being back-applied to improve the calculations for the reacting material.

Table 4.2: Structures for refinement of PC precursor compounds.

| Phase | ICSD Code | Compound Formula | | State |
|---|---|---|---|---|
| $C_3S$ | # 94742 | $Ca_3SiO_5$ | [199] | Crystalline |
| $\beta$-$C_2S$ | # 81096 | $Ca_2SiO_4$ | [200] | Crystalline |
| $\alpha$-$C_2S$ | # 81097 | $Ca_2SiO_4$ | [200] | Crystalline |
| $C_3A$ | # 1841 | $Ca_3Al_2O_6$ | [201] | Crystalline |
| $C_4AF$ | # 9197 | $Ca(Al, Fe)_2O_5$ | [202] | Crystalline |
| Gypsum | # 15692 | $CaSO_4\,2\,H_2O$ | [203] | Crystalline |
| Anhydrite | # 16382 | $CaSO_4$ | [204] | Crystalline |
| Calcite | # 80869 | $CaCO_3$ | [205] | Crystalline |
| Ettringite | # 155395 | $Ca_6Al_2(SO_4)_3(OH)_{12}{\cdot}26H_2O$ | [206] | Crystalline |
| Portlandite | # 15471 | $Ca(OH)_2$ | [207] | Crystalline |
| Hc-AFm * | # 263123 | $(Ca_4\,Al_2\,(OH)_{12}){\cdot}0.4OH\,0.8CO_3\,4H_2O$ | [208] | Crystalline |
| C-(A)-S-H | Standard† | $1.8\,(Ca_3SiO_5)\,(0.8\,Al_2O_3)\,SiO_2\,H_2O$ | | Amorphous |
| Slag | PONKCS | Calibrated to XRF (Table 4.1) | | Amorphous |

*Hc-AFm. - Calcium hemicarboaluminate (AFm Structure).

† Internal standard to $\beta$-$C_2S$ Content

As discussed in Section 4.1.5, the amorphous content was calculated by assuming that negligible $\beta$-$C_2S$ has reacted during the first 60 hours of hydration. The nature of these systems and the method of acquisition was such that materials did not necessarily appear to react in an entirely linear fashion; the beam flux tended to vary and so the reader must bear in mind that with any such in-situ technique the aim must be to observe a trend and not a step-wise linear reaction which perfectly fits the hypothesis. The reaction was *entirely* unrestrained in weight fraction during the refinement. In this manner $\beta$-$C_2S$ appeared to decrease in intensity in certain profiles which provided a negative amorphous content. In these instances the refinement was simply repeated, which in most cases yielded a result which obeyed the laws of thermodynamics.

Refinement control files for each cement blend were generated systematically, with the results from the previous scan determining the starting condition for the next, with the exception of the first which is set to the published values (Table 4.2). The scale factor for the monoclinic $C_3S$ phase was scaled to a randomised floating point value $K$ in the range $0.95 \leq K \leq 1.05$ in an attempt to prevent the refinement becoming stuck on a particular value. This was not always successful. After refinement of the precursor scan, the lattice parameters of all phases present in the PC were fixed, and remained so for the entire analysis. The instrument background was determined using this scan, and also remained thereafter. Lattice parameters were constrained to within 2.5% of their published value.

Where present, the non-slag amorphous component (i.e. amorphous hydrate phase content) was assumed to be zero at the first scan. Control files were verified post-refinement to ensure none of the applied limits were reached, and that all generated phase quantities were within reason.

### 4.3.1 Precursors at a High Resolution

Prior to refinement, results from the MAC detector w ere re-binned, sampled from a step size of 0.002° $2\theta$ to 0.005° $2\theta$, to improve counting statistics without compromising the angular resolution. This was carried out as per the standard method applied by the beamline scientists. The diffraction pattern resulting from the scan of the PC powder is shown in Figure 4.1, and the data showed the presence of the expected clinker phases as per those identified in Chapter 3: $C_3S$, $C_2S$, $C_3A$ and $C_4AF$, including multiple polymorphs of each of the silicates, but no evidence of any deviations from cubic structure for the $C_3A$ identified. Minor additional phases have also been observed; gypsum and anhydrite to prevent flash-set of the cement, and calcite added as a grinding aid during clinkering [165]. The calculated profile from refinement is also shown in the figure, alongside the difference profile originating

Table 4.3: Calculated phase proportions of the PC by Rietveld refinement. Also included are the calculated phase proportions by the Bogue method (see Chapter 3).

| | Weight Fraction / wt.% | |
|---|---|---|
| Phase | by Rietveld | by Bogue |
| $C_3S$ | 60.9 | 70.0 |
| $C_2S$ | 12.6 | 4.5 |
| $C_3A$ | 13.3 | 6.8 |
| $C_4AF$ | 5.0 | 9.5 |
| Gypsum | 1.4 | n/a |
| Anhydrite | 3.2 | n/a |
| Calcite | 3.7 | n/a |

All phases identified and quantified here are fully crystalline in the precursor material.

from comparison between the calculated and observed patterns. Table 4.3 gives the refined weight fractions of phases present, which were significantly dissimilar to those given by the Bogue method, which is an observed effect resulting from the inability of the Bogue calculation to remain representative of a modern cement, or stoichiometric differences in newer materials. Reflections from hydrate phases are identified in Figure 4.2.

### 4.3.2 Validating the Composition

Data acquired by X-ray fluorescence were previously provided in Table 4.1. The molar mass of calcium in the first scan was calculated from the weight fractions of calcium bearing phases in the PC, assuming a mass of unity. If it is assumed that a negligible amount of calcium has entered the solution at this point, it is possible to compare these data to the X-ray fluorescence results provided. The fraction of calcium in the system by XRF was 47.1%. Taking the relative atomic mass of all material components which are identifiable by this technique yielded an excellent agreement between these data: the calcium content by XRD of 48.5% provides a discrepancy of 1.4%, which was completely acceptable considering the strong likelihood of non-stoichiometry in the actual calcium-bearing clinker phases in a commercial cement.

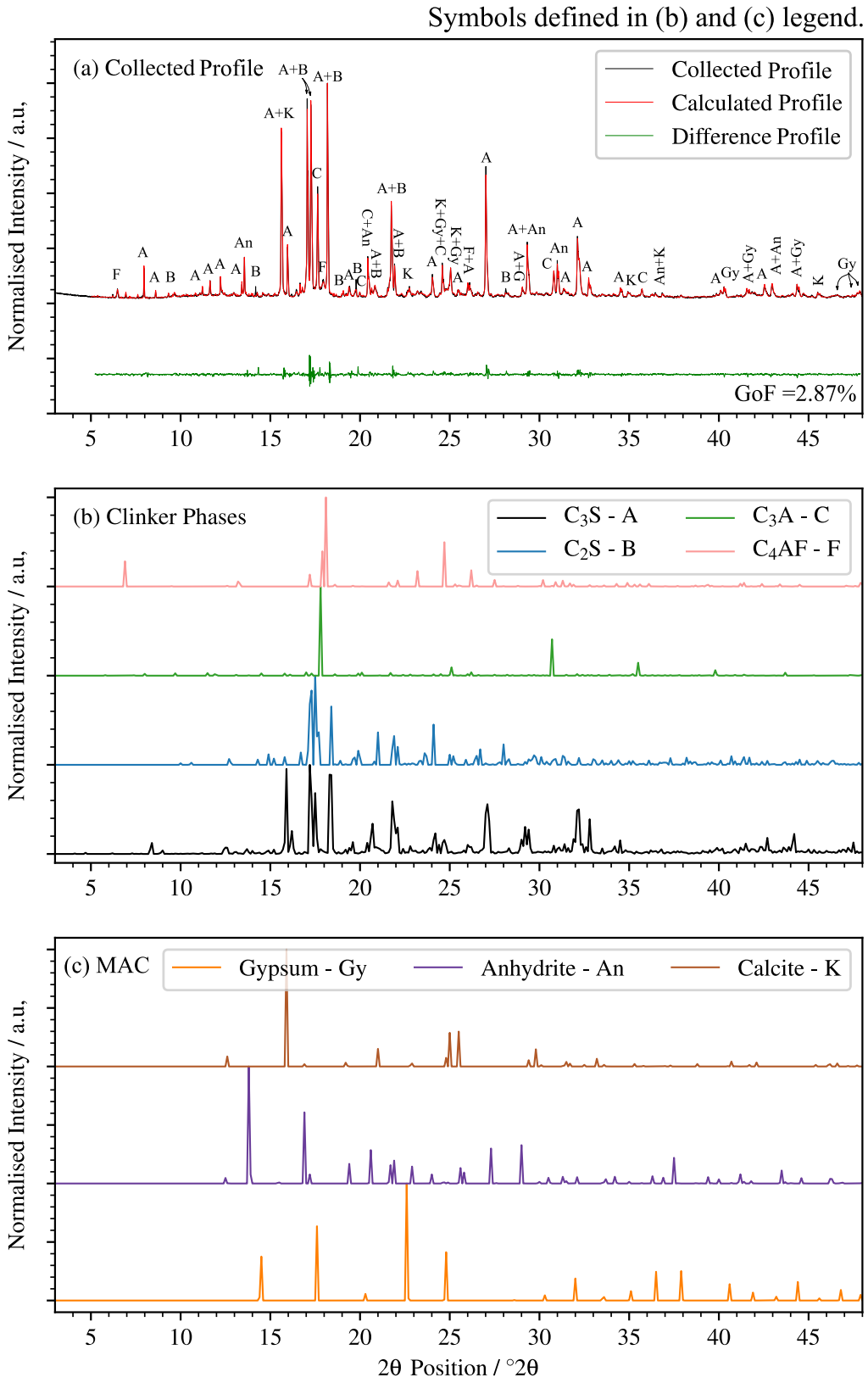


Figure 4.1: Clinker phases, as identified from commonly known phases [209] (a) with simulated phases shown (b & c). Simulated are for published structures as per Table 4.2 *with no refinement*, data generated from the Inorganic Crystal Structure Database [210].

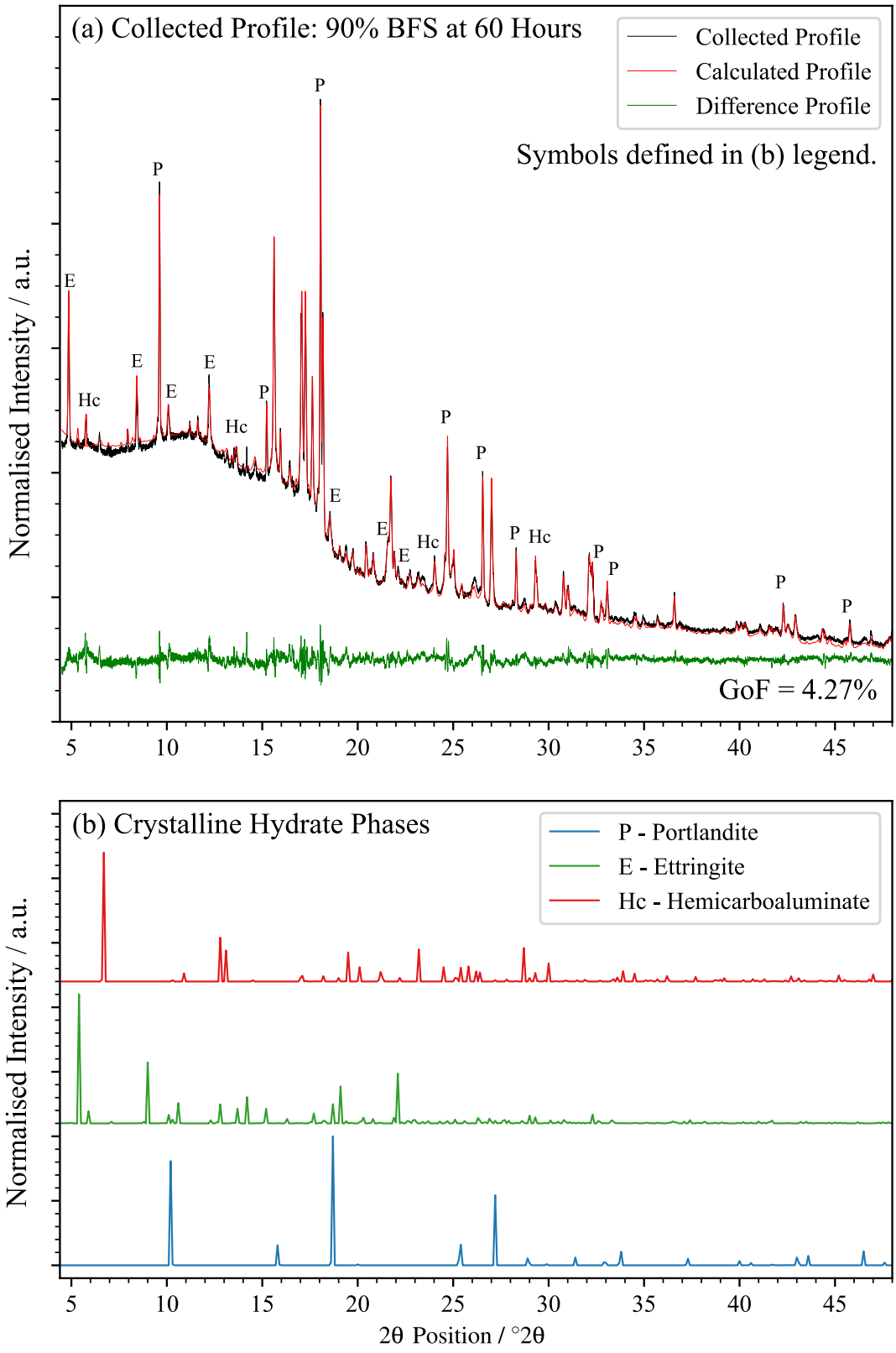


Figure 4.2: Hydrate phases, as identified from commonly known phases [209] (a), with simulated phases shown (b). Simulated data are for published structures per Table 4.2 *with no refinement*, data generated from the Inorganic Crystal Structure Database [210].

### 4.3.3 Configuring a PONKCS Model

In order to carry out a quantitative analysis of the reaction of the blast furnace slag by the PONKCS method, it is necessary to calibrate the $hkl$ phase produced from the BFS in a mixture where the weight percentages of BFS and a standard material are known (and in Equation 2, respectively). This was carried out assuming that in the first scan of the reacting material (acquired approximately 15 to 20 minutes post-mixing), all phases except the BFS remain fully crystalline.

The $Q$ constants were determined for all precursor phases by refinement. It was assumed here that the degree of reaction of the slag was zero at the first scan and as a consequence, 50% of the scanned material by weight was slag. The calculated model is shown in Figure 4.3. A high degree of diffuse scattering was observed from the glassy component in the material, with the most intense region centred at approximately 17° $2\theta$. Some minor crystalline reflections were also found by the slag. These were neglected as they were unresolvable in scans obtained once the material had been blended.

The $Q$ calibration value was set in Topas by the `MVW(0,0,0)` macro where the parameters represent the mass, volume and weight fraction of the phase. By adjustment of the first parameter the weight percentage may be set to a known value. In this case the $Q$ value was set such that the refined weight percentage of amorphous BFS in the 50% BFS material was as close to this value as was reasonably achievable by trial and error. In order to verify this calibration value, it was applied identically to the first scans of both of the other systems considered in this study. The refined weight percentages of slag in these systems are 75.40%, and 90.68% for the 3:1 (75%) and 9:1 (90%) BFS materials respectively. This is an exceptional agreement which is deemed entirely acceptable for the analysis presented here.

### 4.3.4 Correcting for Bound Water

Water was difficult to observe by the technique applied here, and for this reason the total mass of calcium in the material appeared to arbitrarily decrease as the cement hydrates, which caused the reaction to appear as though it is occurring at a slower rate.

Here, it was assumed that all calcium present in the solid phase at the first scan ought to have remained therein across the observed experiment duration. The mass of calcium present in each phase was determined knowing the relative atomic mass of all atoms within the material. The molar masses of C-S-H and C-(A)-S-H were calculated assuming a calcium / silicon ratio of 1.8 and an aluminium / silicon ratio of 0.2, lying in close agreement with Faucon et al. [211]. The value for the slag was calculated from XRF data (Table 4.1).

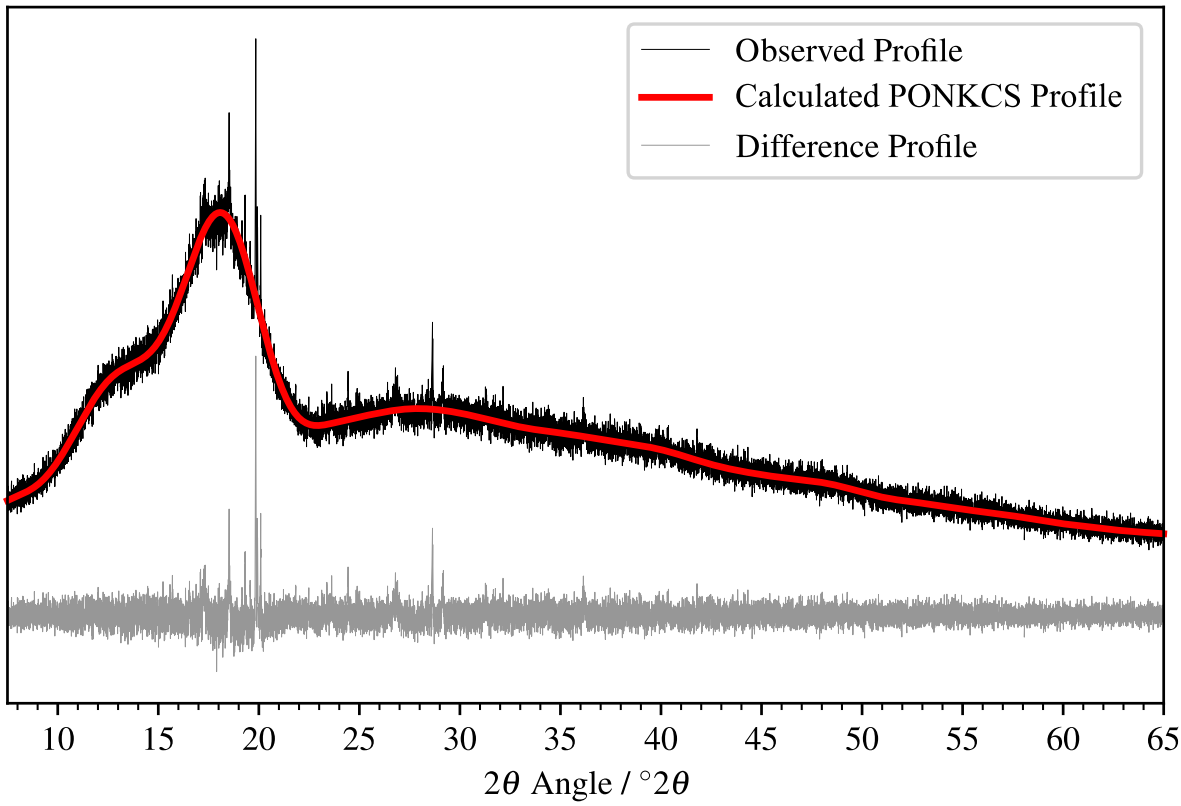


Figure 4.3: The simulated, observed, and difference profiles calculated for the PONKCS representation of the amorphous slag. Crystalline phases (akermanite and gehlenite) are neglected here.

Each scan was then iteratively scaled to the calcium content in the first, which yields a value of grams of hydrate per hundred grams of unreacted material. This showed the solid phases within the system increasing in mass correctly as water binds. The fraction of calcium was determined for each phase, each of which was scaled as per Table 4.4 to normalise to the first scan calcium content.

### 4.3.5 Plotting a Trend

Once data had been corrected for the mass of chemically combined water a trend line was fitted to the data by least squares regression fitting, with an example shown in Figure 4.4. The fitted function was selected based upon the best representation of the observed trend in the corrected result. Phases were generally fitted to a third order polynomial curve, though where no significant trend is observed or correlation is poor, a linear fit was selected.

These functions were not guaranteed to entirely represent the data in a correct fashion and so the curve, where required, is clipped to a minimum or maximum should an increase

Table 4.4: Calcium content of each phase based on component relative atomic masses.

| Phase | $C_3S$ | $C_2S$ | $C_3A$ | $C_4AF$ | Gyp. | Anh. | Ettr. | Portl. | C-S-H* | C-(A)-S-H† | BFS |
|---|---|---|---|---|---|---|---|---|---|---|---|
| Factor | 0.53 | 0.47 | 0.45 | 0.42 | 0.23 | 0.29 | 0.19 | 0.54 | 0.41 | 0.39 | 0.28 |

∗ Assumed calcium / silicon ratio 1.8

† Assumed aluminium / silicon ratio 0.8

or decrease in the phase which breaches the thermodynamics of the have been observed. For example in the plain PC material, when portlandite is formed and reaches a maximum weight, this is restricted such that the trend line may not decrease as portlandite should not be consumed. This is not the case, however, in the substituted material where the consumption of portlandite may occur during activation of the slag. This limitation is not hit.

## 4.4 Chemistry of the Hydration of Portland Cement

The diffraction profile of the plain CEM I 52.5N material is shown in Figure 4.5. Here significant variations in instrument background have occurred across the duration of the test. One might expect such a response to have been apparent due to the consumption and formation of amorphous material, though in this case the effect was somewhat cyclic. In reality this was simply variations in the beam intensity as the synchrotron ring depletes and fills.

The quantification of the hydration of the pure non-substituted Portland cement material is shown in Figure 4.6. As cement came into contact with water ettringite was immediately formed, and was observable from the first scan captured on this instrument. Small volumes of amorphous content had additionally formed at this time, and are observable with a slow growth rate at this point[4].

The reaction slowed considerably across the first half hour in-line with the calorimetric data, though the process which has resulted in this is not apparent from crystallographic data in isolation. The drastic reduction in thermal output marks the beginning of the dormant period where the material remains workable in a reduced state of activity. Toward the end of the dormant period the thermal output began to increase, though it is also unclear from this technique what triggered this point in the reaction of the material. Several hypotheses exist

[4]In Chapter 5 a very small layer was shown to grow during the initial period of vigorous thermal output, and the formation of amorphous content here was probably the formation of this or the formation of disordered calcium hydroxide across the first minutes of the reaction.

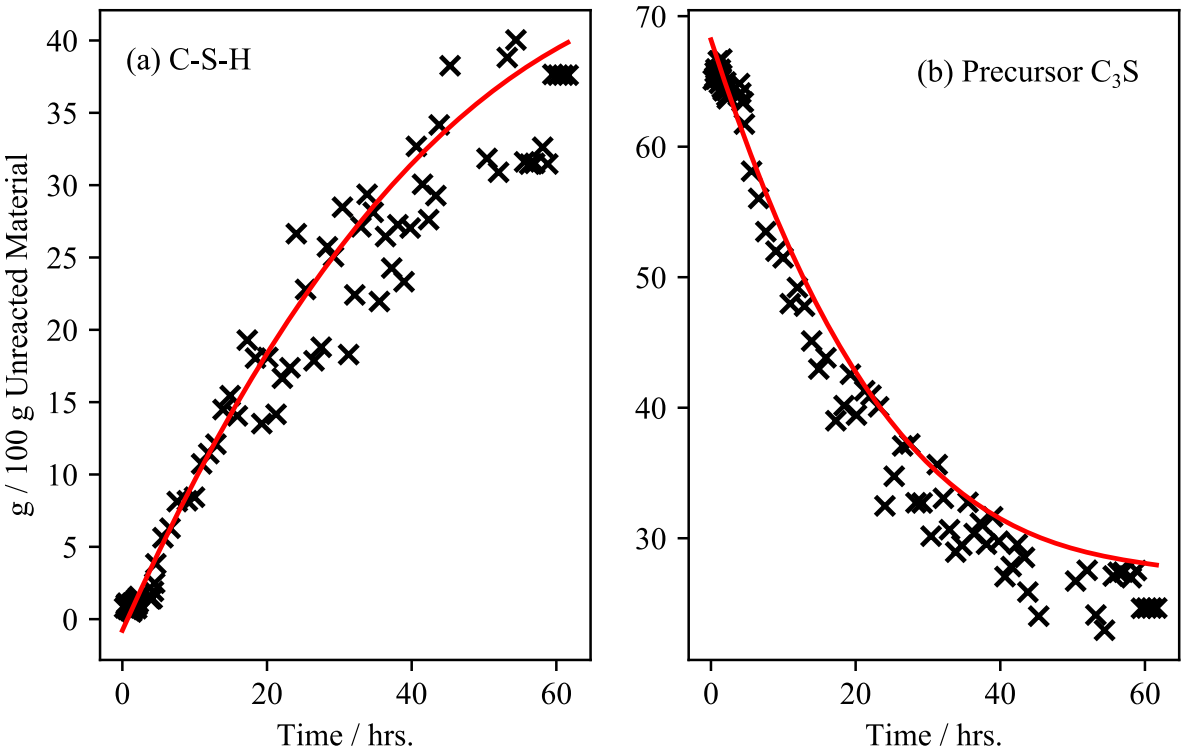


Figure 4.4: Fits to the C-S-H hydration product (a) and the reacting $C_3S$ clinker phase shown as an example of a typical fit. Data taken from the CEM I 52.5N material.

in the literature for this which are discussed in some detail by Bullard et al. [4], though it is not possible to provide an answer to this question from the results presented in this thesis at present.

$C_2S$ did not react, and was constrained by the system to remain at the same weight fraction throughout the duration of the analysis in order to resolve the C-S-H or C-(A)-S-H content. Any variation of the $C_2S$ phase resulted from variations in other phases propagating through the analysis during normalisation of the dataset to the calcium content of the material. This was, therefore, unavoidable. $C_3A$ reduced in mass fraction but did not react entirely across the first 60 hours. Ettringite remained a stable phase; the formation of monosulphate was not resolved in this material. Sulphate in the form of gypsum appeared to remain present though this may have been an artefact of the fitting of a small quantity phase by the Rietveld method where this does not quite reach zero, or an artefact caused by least squares regression fitting where the attainable curve does not precisely match the data. No sulphate depletion was observed in the isothermal calorimetry, however, which suggests either that the sulphate depletion is masked with the peak reaction of $C_3S$, or that an excessive content of sulphate has been added.

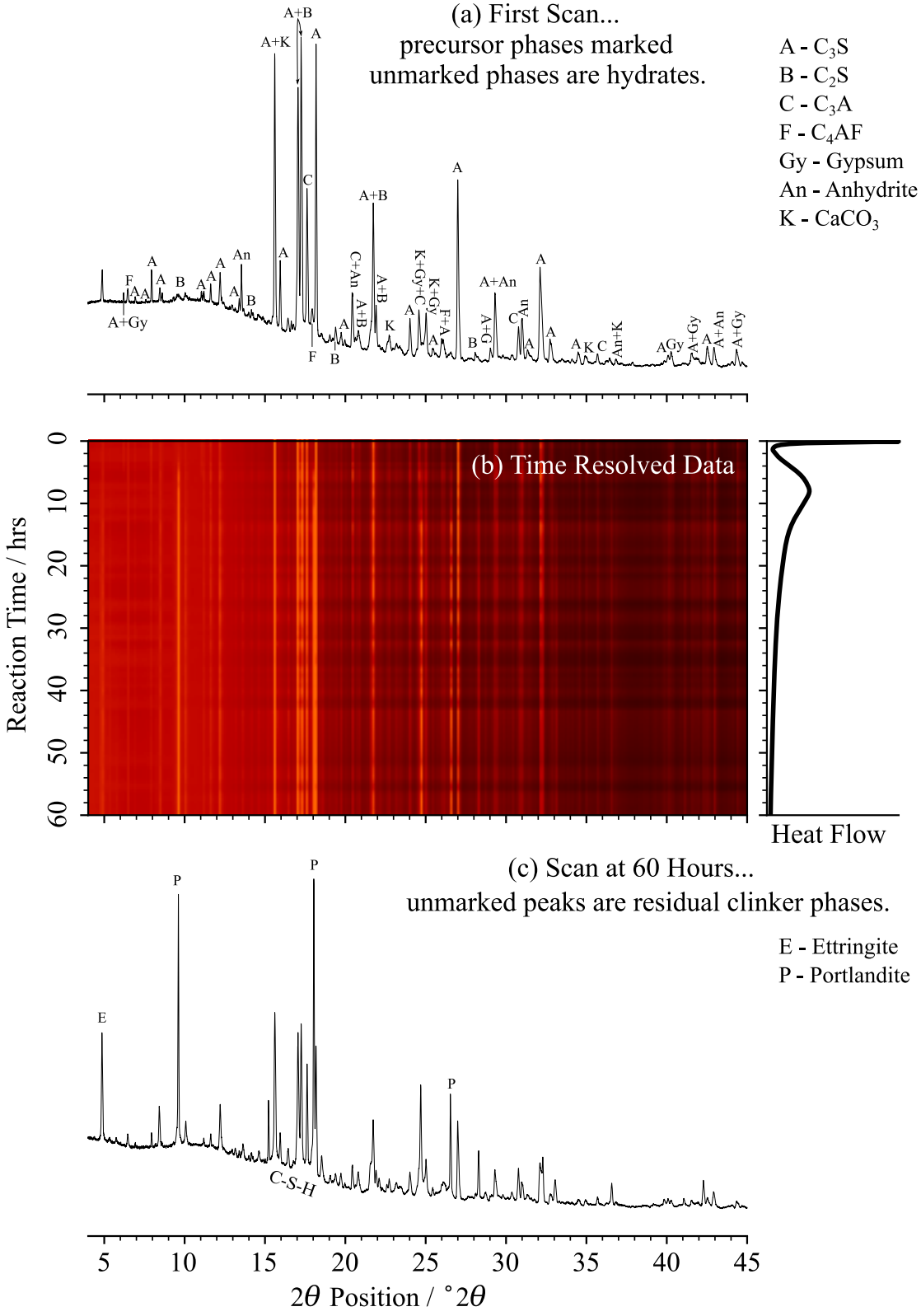


Figure 4.5: Data at first time point (a), time resolved profile of the CEM-I 52.5N PC in isolation (b) and the profile at the final time point.

The expected chemical reactions: $A + H \longrightarrow C-S-H + P$, $B + H \longrightarrow C-S-H + P$, $C + Gy + H \longrightarrow E$, $C + Gy + K \longrightarrow Hc$ occur.

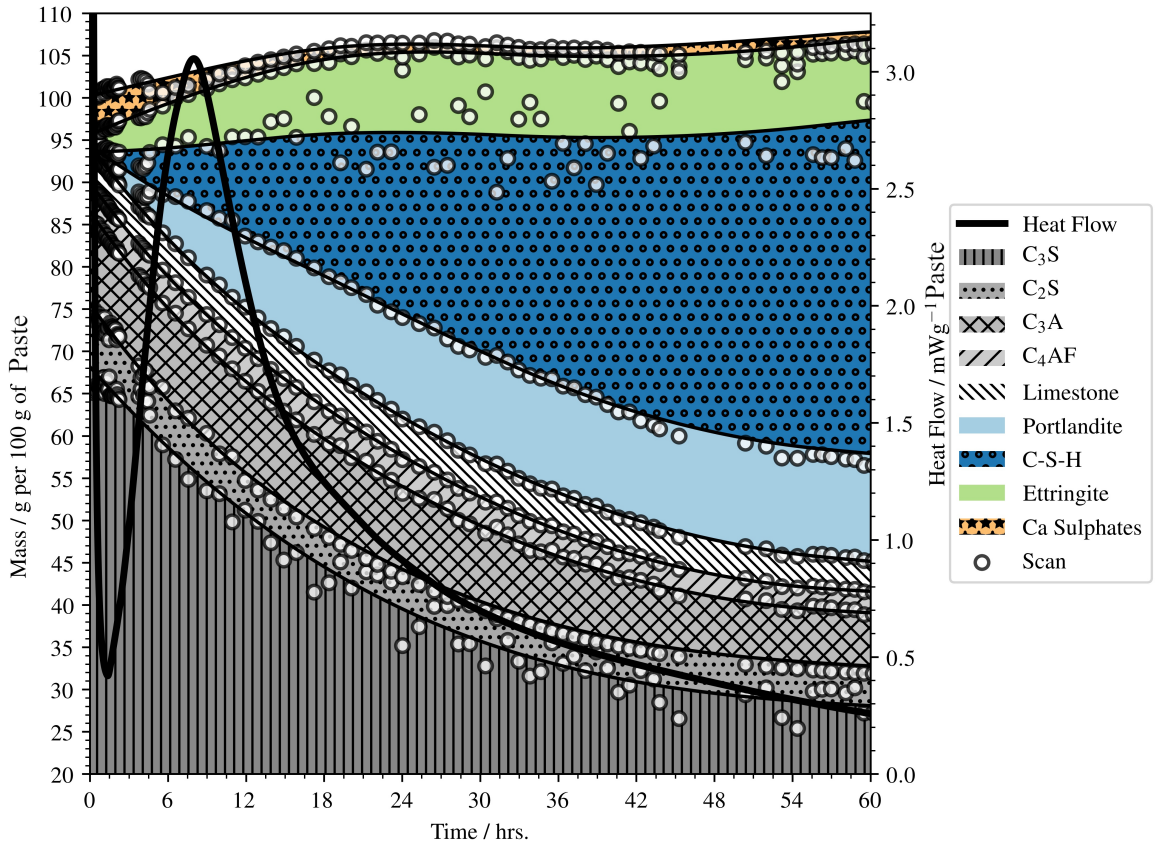


Figure 4.6: Phase proportions of the hydrating Portland cement between 0 and 60 hours, as calculated by crystal structure refinement. For clarity the $y$ axis below 20 g / 100 g is neglected as this contains only $C_3S$.

## 4.5 The PONKCS model and Hydrating Slag Cements

The slag model described in Figure 4.3 was applied in a reacting system in a manner similar to a crystalline phase. The arbitrarily defined structural parameters of the model remained fixed to ensure a constant profile fitting the diffuse scattering, while the scale factor was free to decrease as necessary. A uniform decrease in the profile was assumed to occur as the system reacts. The model was re-applied to the first scan, allowing this time for the presence of early hydrate phases such as ettringite and portlandite.

The resulting mass fraction of each component phase across the time of analysis are shown in Figures 4.7, 4.9, and 4.11 for each degree of substitution. Calorimetry data are also shown for the same duration.

Ettringite formed within the first minutes, most likely immediately on contact with mix water. This phase proceeds to grow across the first hours of hydration, and slowed by the

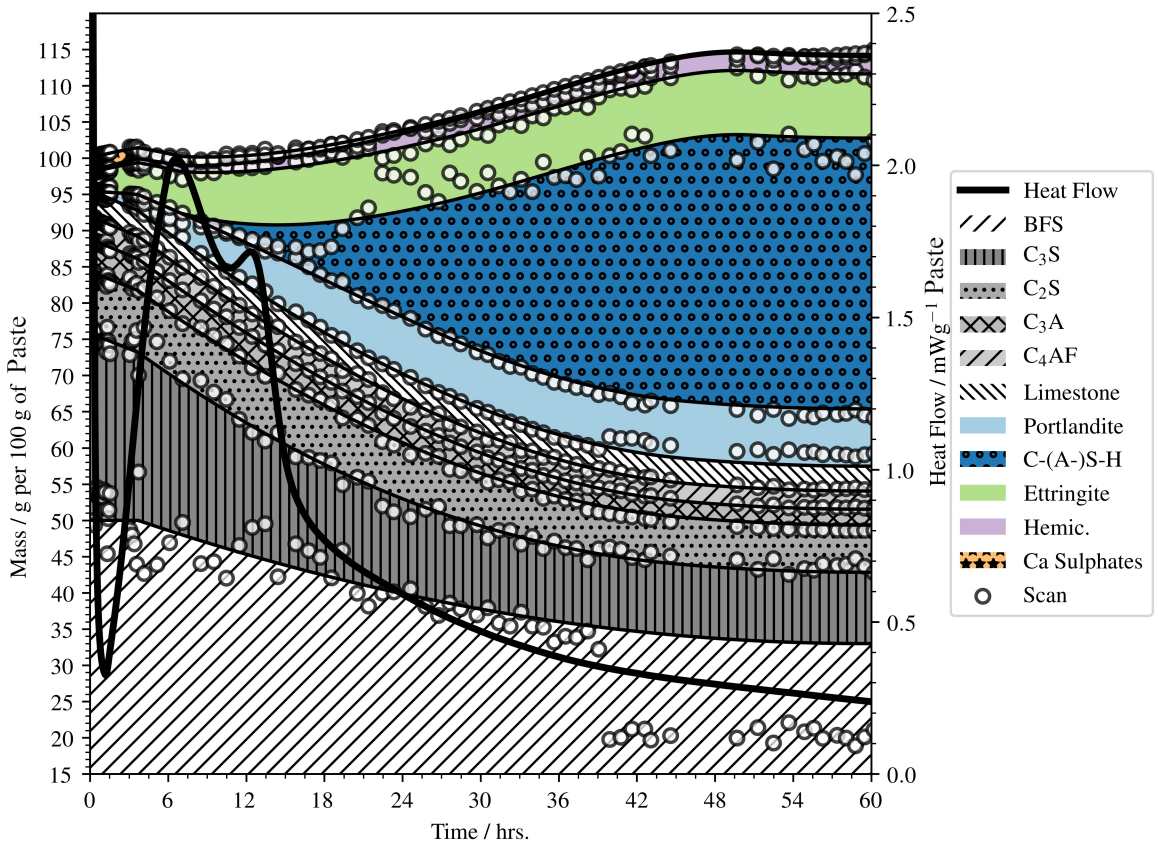


Figure 4.7: Phase proportions for the 50% BFS material across the first 60 hours of hydration. The $y$ axis below 15 g / 100 g is neglected, as this contains only BFS.

end of the acceleration phase as the initial sulphate containing phases react. The volume of portlandite formed at a very early age is *very* low, such that it could not be seen in the diffraction profile within this timeframe. Should any calcium hydroxide have formed here, it was almost certainly structurally disordered. Crystalline portlandite began to appear in the matrix during the induction stage, though only in *very* low volumes. This additionally grew during acceleration of the reaction, and coincides with the nucleation of C-(A)-S-H.

The sulphate phases from the original cement were almost certainly completely consumed across the first hours of the reaction in cases where slag has been substituted. As sulphate depletes, hemicarboaluminate began to form. In Chapter 3 this was masked by the lower resolution of the laboratory diffractometer, and the peaks merged with one another.

Amorphous content began to form abundantly at the same time as the increase in thermal output during acceleration. Here, $C_3S$ and slag reacted with mix water to form the binder product which resulted in rigidity within the microstructure. The formation of this slows, but continues at a reduced rate to the end of the observed period. The decrease in the rate

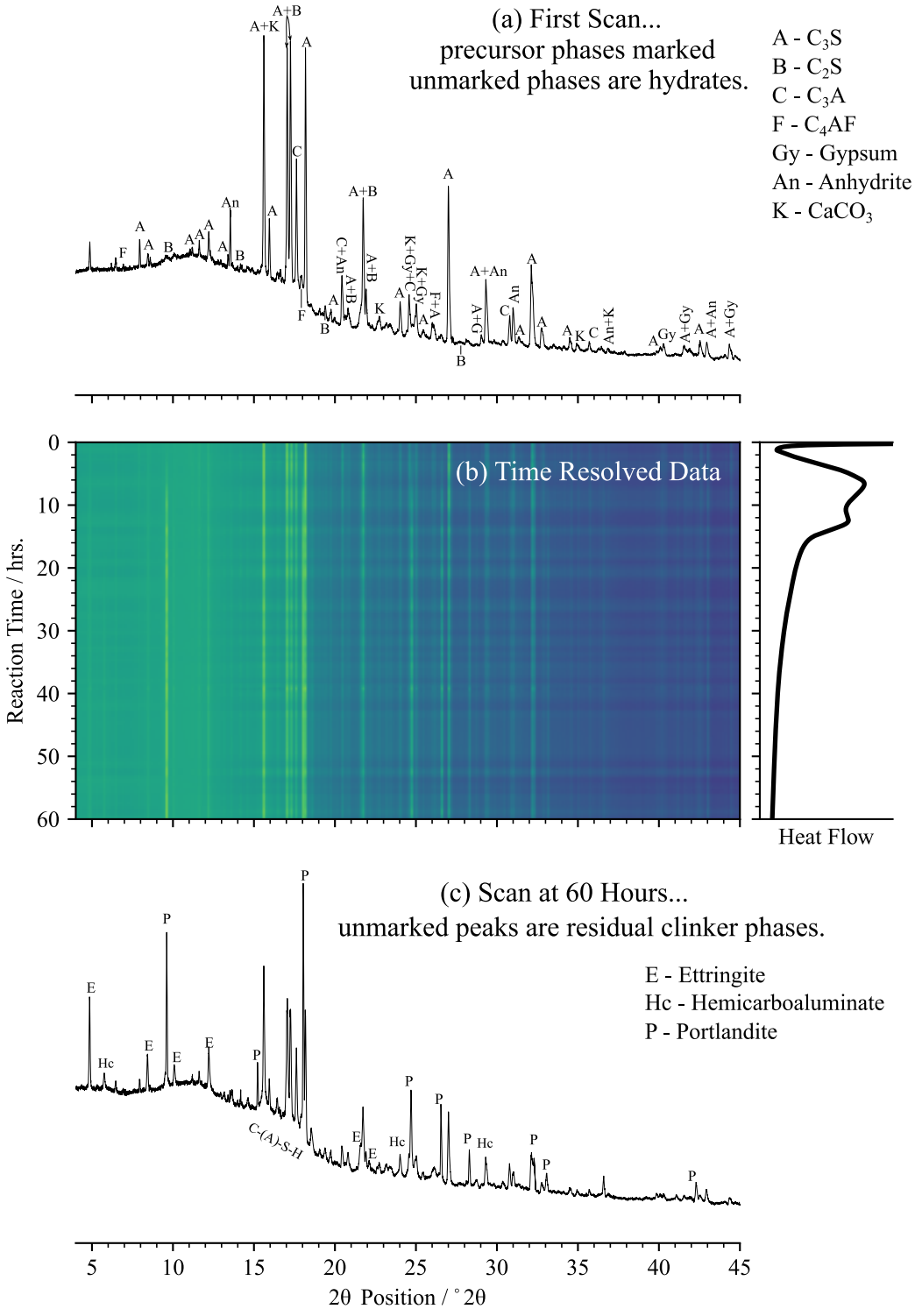


Figure 4.8: Data at first time point (a), time resolved profile of the 50% BFS material (b), and the profile at the final time point (c).

The expected chemical reactions: $A + H \longrightarrow C-S-H + P$, $B + H \longrightarrow C-S-H + P$, $A + K\,(^{+}BFS) + P + H \longrightarrow C-(A)-S-H$ (through slag activation), $C + Gy + H \longrightarrow E$, $C + Gy + K + H \longrightarrow Hc$ occur.

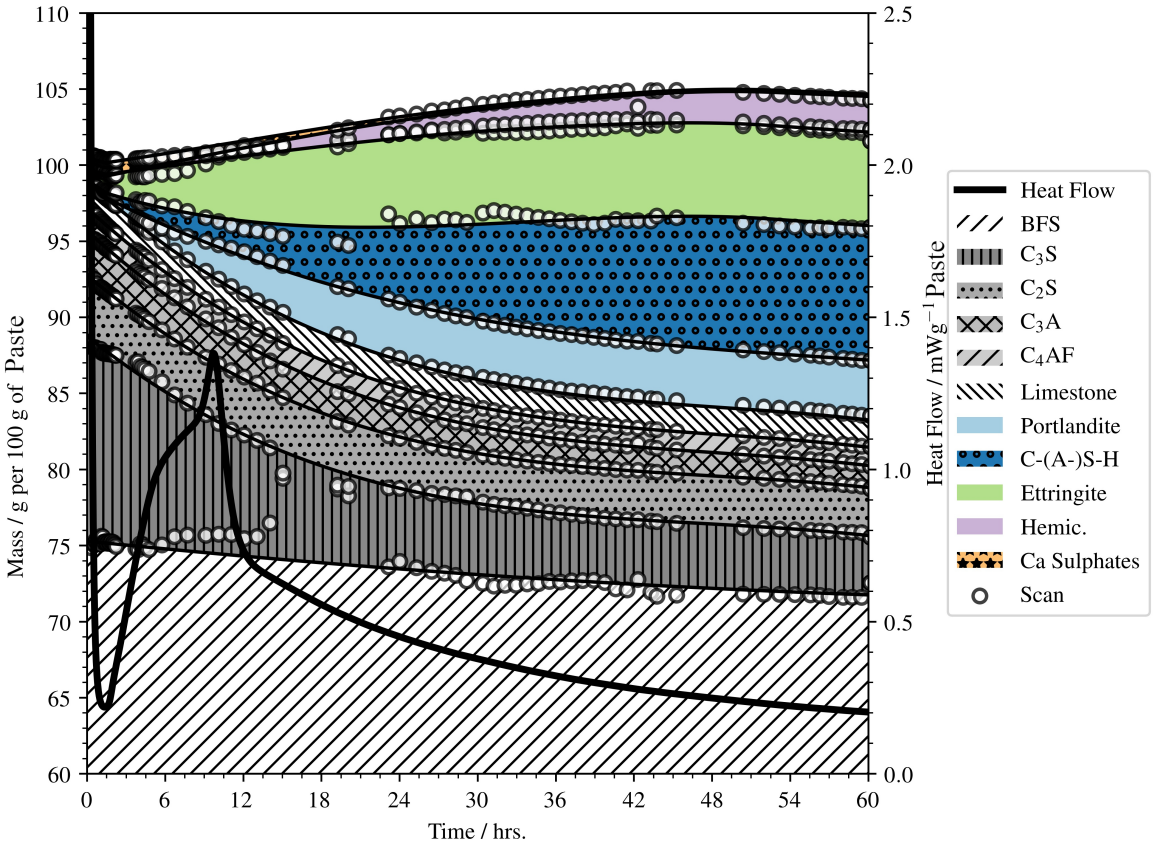


Figure 4.9: Phase proportions for the 75% BFS material across the first 60 hours of hydration. The $y$ axis below 60 g / 100 g is neglected, as this contains only BFS.

of reaction in cements may be a result in the thickening of the layer which is described in Chapter 5, which restricts mix water from coming into contact with anhydrous material. An alternative suggestion might be that all fine material has reacted, leaving only coarse particles and the specific surface area of these is low enough to reduce the rate of hydration.

### 4.5.1 Quantifying Noise?

The technique applied here generally showed a good response, though this was somewhat dependent on the degree of substitution of the cementing material and this was sensitive to any beam flux variations, as previously discussed. While the 50% and 75% slag containing blended cements refined well, this was not so much the case at 90% of slag substitution, the collected unrefined data from which are shown in Figure 4.12. The content of slag compressed the range over which each phase was identified. This effectively lowered the resolution; a phase within the clinker which may have reduced from 35% to 25% in mass relative

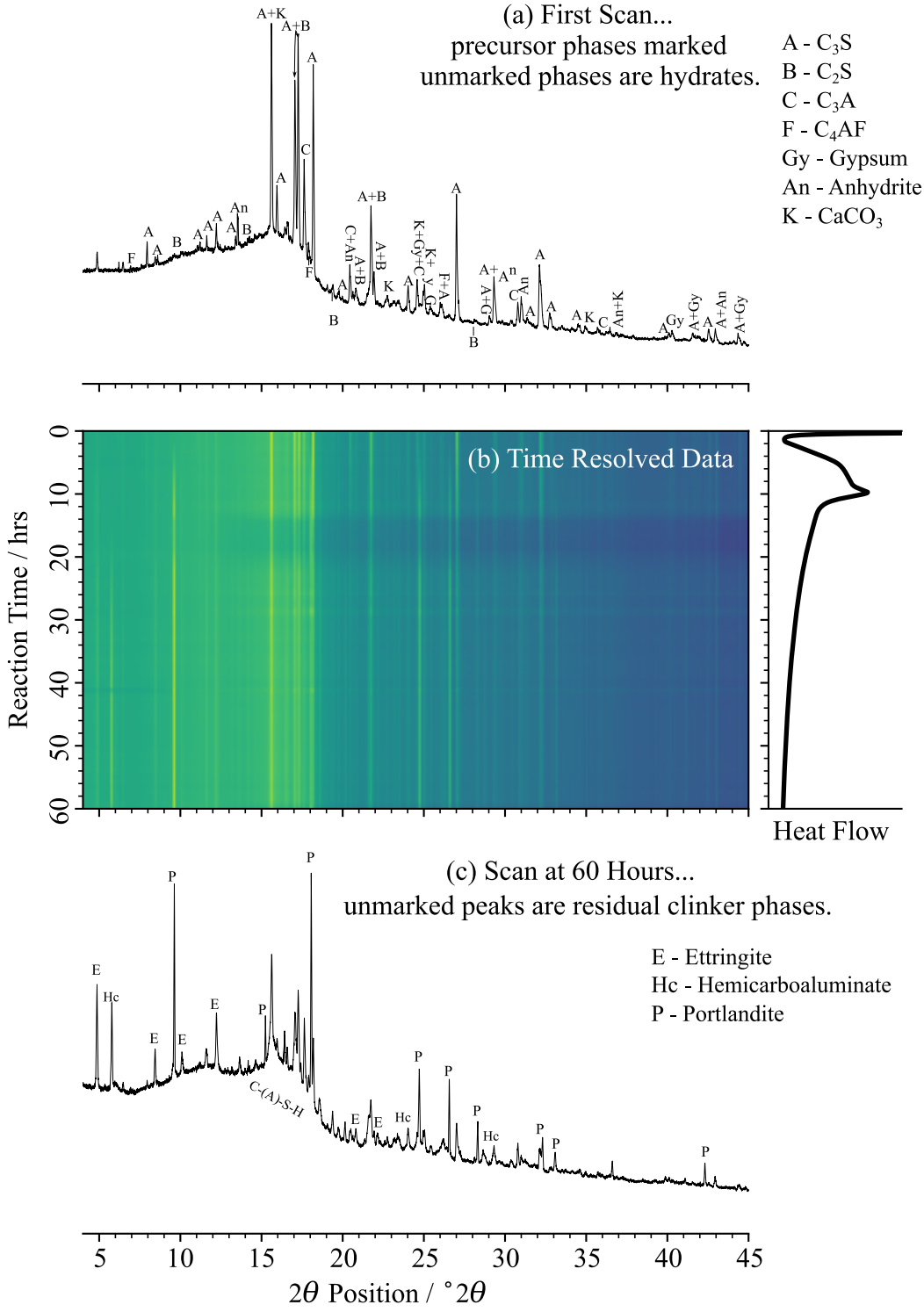


Figure 4.10: Data at first time point (a), time resolved profile of the 75% BFS material (b), Horizontal scale shown at the bottom of (c)

The expected chemical reactions: $A + H \longrightarrow C-S-H + P$, $B + H \longrightarrow C-S-H + P$, $A + K\,(^{+}BFS) + P + H \longrightarrow C-(A)-S-H$ (through slag activation), $C + Gy + H \longrightarrow E$, $C + Gy + K + H \longrightarrow Hc$ occur.

to the cement within the blend will be shown as reducing from 3.5% to 2.5% overall within the blend, and very small changes may have not been observable at all. Flux variations in the beamline instrument also affect the analysis. In the first time point on Figure 4.11, for example, the first scan was resolved to containin almost precisely 90% BFS substitution. However the flux appeared to have arbitrarily increased rapidly between the first and second scans. This caused the slag to have appeared as though it had increased in volume. The reader must remember that this analysis effectively attempts to quantify noise. Of course, this results in some unexpected outcomes, such as the trend which was observed in the BFS content in the material substituted at 90% (Figure 4.11) which has in this case been restrained thermodynamically through limiting the gradient in the fitted function to a maximum of zero a decrease must be observed. In reality this was not required.

A second instance of this occurred in the 50% BFS containing cements shown in Figure 4.7 at approximately 38 hours. Here, the beam current appears to have decreased (note additionally the banding apparent in the scan at this time, shown in Figure 4.8). This decrease in intensity then effectively propagated through the analysis as the refined "erroneous" result became the starting point for the following refinement. The background approximation filled the difference, and beyond this the refined weight percentage did not self-correct due to the large change required in the calculation to fit the profile. Thermodynamic restraint would have been of little assistance in this instance, as for the restraint to have been valid, a decrease in precursor content must have been allowed for.

### 4.5.2 Clinker, Slag, and Minor Additional Phases

For each composite cement component, the initial reaction progress measured by the synchrotron XRD analysis occurred in good agreement with the thermal output. The first peak in the calorimetry after the dormant period is associated with the initial reaction of alite to form calcium silicate hydrate, which appeared as amorphous content in the refinement, and portlandite, a crystalline phase. The portlandite content was less well defined in the 90% slag cement, where either a high level of replacement seems to have retarded this effect considerably, or due to the difficulty of fitting a small quantity phase, which was additionally shown in refinement of sulphate-baring phases in the pure PC material. The reaction of slag in here was also quite possibly retarded by the low portlandite content, and was challenging to observe in any case as a result of the background variation.

The second exotherm represents the beginning of the slag reaction. Here, sufficient amounts of $Ca(OH)_2$ have been liberated by the reaction of the PC to activate the slag [36]. Calcium aluminium silicate hydrate was formed at the same stage in the reaction. This is

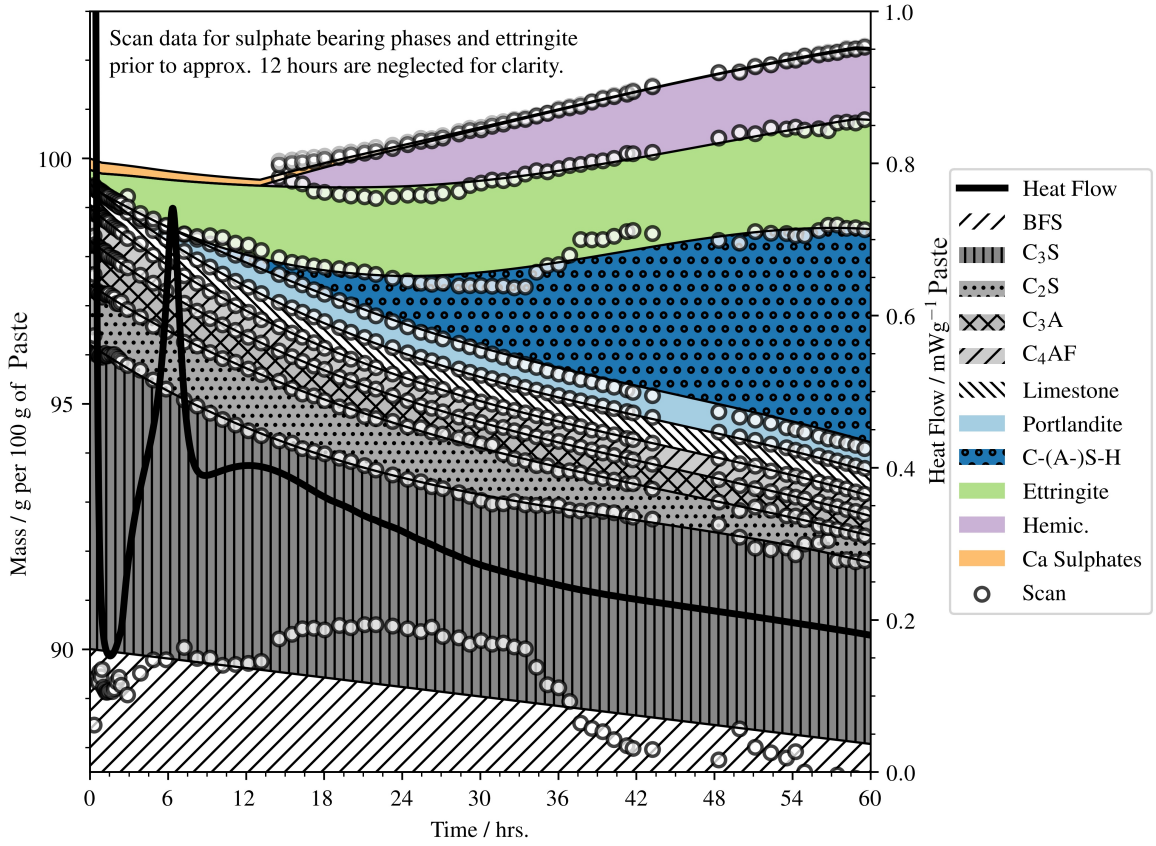


Figure 4.11: Phase proportions for the 90% BFS material across the first 60 hours of hydration. Note that first 30 data points relating to sulphate-bearing phases are not shown to retain clarity within the figure, and are provided in supplementary information (Appendix B). The $y$ axis below 87.5 g / 100 g is neglected, as this contains only BFS.

most clear in the 75% slag blend, where a notable drop in amorphous slag content occurs during this time. In the 90% slag system, the volume of replacement was sufficient to prevent the reaction of the slag remaining clear.

### 4.5.3 Additional Observations

The reaction of $\beta$-$C_2S$ was not observed, as this phase was fixed in the analysis so that the amorphous content may be resolved. The $\alpha$-$C_2S$ phase (shown combined with the $\beta$-$C_2S$ in the phase quantification plots) which was not constrained shows a negligible extent of reaction at all three degrees of substitution across the first 60 hours of hydration, which indicates that the assumption of constant $\beta$-$C_2S$ content was likely to be valid. Similarly, minimal reaction of the calcite phase was shown. The formation of ettringite was almost

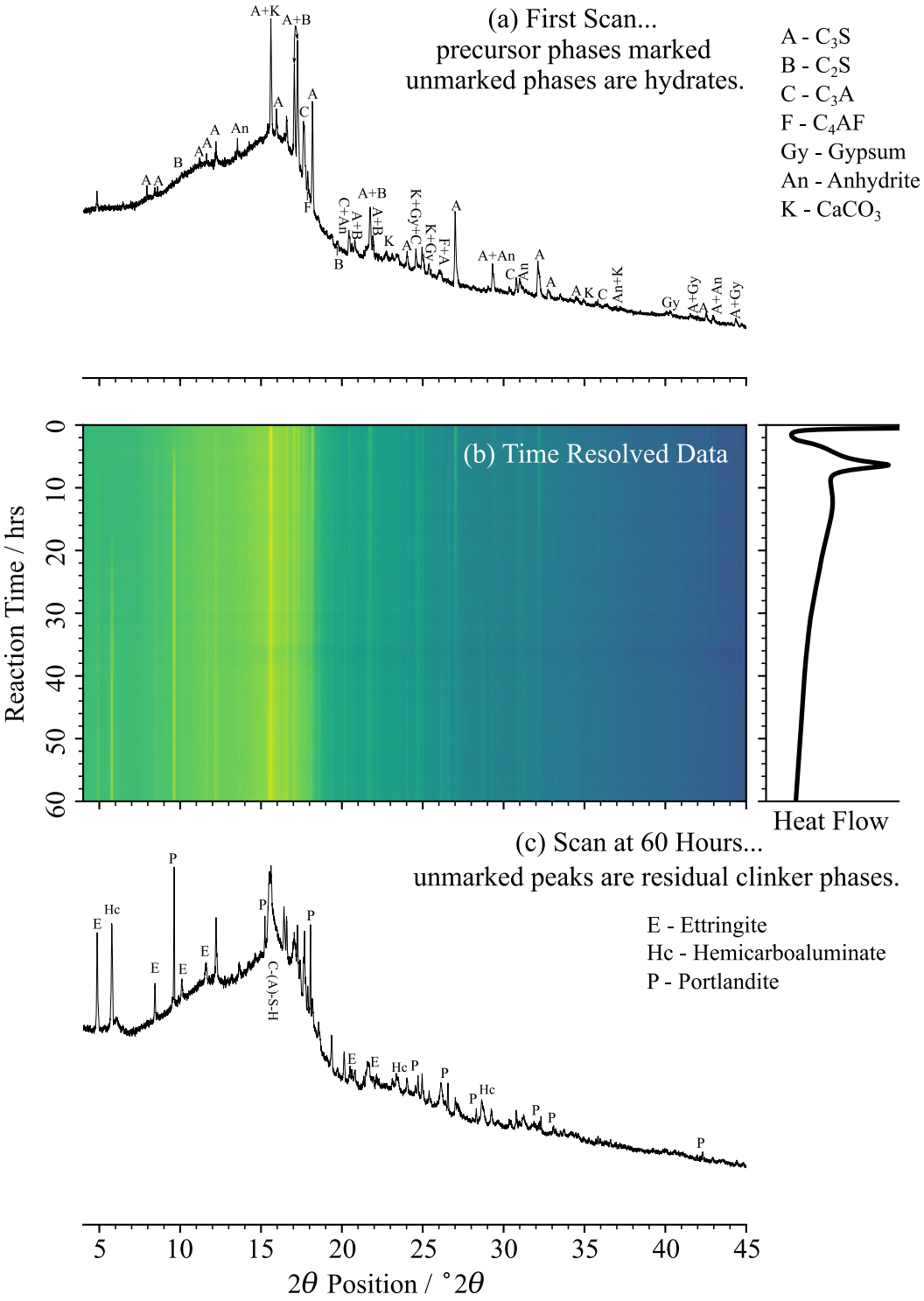


Figure 4.12: Data at first time point (a), time resolved profile of the 90% BFS material (b) and the profile at the final time point (c).

The expected chemical reactions: $A + H \longrightarrow C-S-H + P$, $B + H \longrightarrow C-S-H + P$, $A + K\,(^{+}BFS) + P + H \longrightarrow C-(A)-S-H$ (through slag activation), $C + Gy + H \longrightarrow E$, $C + Gy + K + H \longrightarrow Hc$ occur.

immediate upon contact of the cement with the water, consistent with previously published in situ synchrotron X-ray diffractometry analysis of PC hydration [5], and with laboratory characterisation [23]. The formation of ettringite occurred during the initial period in the first few minutes of the reaction before induction. This phase continued to form throughout the first hours of the reaction. The volume of ettringite formation agreed well with the reaction of other phases, particularly the consumption of the $C_3A$ from the clinker.

## 4.6 Conclusions

The successful development and application of a methodology for the in-situ analysis of reacting cementitious systems with and without substitution containing a high initial content of amorphous anhydrous precursor (blast furnace slag) using the Diamond Light Source I11 XRPD instrument has been demonstrated.

The reaction of clinker phases across the first 60 hours of the hydration reaction has been successfully shown in the analysis. $C_3S$ reacts significantly across the first hours of the reaction and forms C-(A)-S-H, in good agreement with the thermal output. The reaction of $C_3A$ does occur but is retarded by the presence of $CaSO_4{\cdot}nH_2O$ and is incomplete by 60 hours. When $CaSO_4{\cdot}nH_2O$ does deplete, crystalline hemicarboaluminate forms within the material and contributes further as a product of the reaction of $C_3A$. The crystalline $CaCO_3$ content does not decrease, however, and so the carbonate component of this phase must result from amorphous carbonates contained within the slag material. (calcium carbonate is also identified in the slag by thermal analysis in Chapter 3). The formation of hemicarboaluminate is slightly masked by the trend line fit, and it does not necessarily appear that these occur at precisely the same moment, which one might expect. Amorphous phases which are indirectly quantified show high variations across the scan times, though show a strong trend, and appears to be intrinsic to the technique.

This method has shown very good promise for use on other cementitious systems for time-resolved studies. Moreover, the PONKCS technique has been applied to quantify the reaction of the amorphous blast furnace slag phase in the material, and this may be more straightforward in materials where a lower mass fraction of amorphous material has been substituted. This technique comes with a few caveats which are especially apparent when using a variable-flux instrument such as a synchrotron beamline. With such a high amorphous precursor content the background of the instrument provides the metric of the slag content and if this should vary significantly from the first scan this may provide an unexpected result. While the entire scan ought to scale uniformly where the flux varies this is not necessarily

apparent. Regardless of this, a good result is provided showing the reaction of clinker materials and the production of crystalline hydrate phases, with amorphous content which has been quantified based on interpretation of these weight fractions.

# Chapter 5

# Imaging the First Hours of Hydration

*This chapter and parts of Chapter 1) are based upon a paper in preparation for submission, authored by J.E. Vigor, X. Xiao (beamline science), S.A. Bernal (supervisory), and J.L. Provis (supervisory).The contribution of individual authors is detailed on page iv.*

Using the high-flux X-ray sources and advanced detectors available at synchrotron facilities, it is now possible to acquire high-resolution crystallographic [188, 189] and microtomographic [77, 212] data with an unprecedented time resolution. Although synchrotron X-ray diffraction techniques (Chapter 4) have previously enabled the materials science of cements to be observed and quantified [5, 213, 214], data regarding changes in the morphology and structure of these materials on short time scales have remained elusive [4].

For many situations, microstructural imaging is carried out using an optical or high resolution scanning electron microscope (SEM) or environmental SEM (ESEM) [215, 216]. While offering a very high spatial resolution and able to yield a great deal of data, the use of an electron microscope leaves a number of difficulties.

Firstly, the preparation time for a sample to be analysed using an electron microscope does not allow for the best observation of hydrate development. The reaction must be arrested. This has been shown to cause microstructural damage to the sample by Collier et al. [7] and was touched upon in Chapter 2. Regardless of any arrest to the reaction the sample must be placed under vacuum, resulting in dessication of the specimen. Damage such as crack formation easily results in the misinterpretation of data. Resulting from this is reduction of confidence in the reliability of results. Removing water from the pore structure removes the ability to observe processes occurring within the pore structure itself. Such processes are observed in this chapter through the application of in-situ X-ray baseds characterisation methods.

The pore volume will undoubtedly increase or the tortuosity decrease should the sample fracture. Further damage may result from artefacts such as remnant precursor grain "pull-out" which leaves large holes in the structure if the sample is incorrectly prepared, increasing the apparent pore volume. This is especially the case where a coarse precursor, such as the slag used in this thesis, is used. A soft sample may deform or simply break apart when removed from a mould or sectioned, which means that characterisation at an early age is very challenging.

Finally, artefacts resulting from sample variation may be avoided should an identical sample and volume be repeatedly analysed. Even if unintentional, slight variations between samples may result in differing results. Volumes or regions would ideally be segmented from the sample in each acquisition to eliminate regional changes or variation.

A two dimensional image may quite easily reveal features in and morphology of a well hydrated cement [217] though with perhaps some of the caveats previously discussed. This is well shown in the literature. Ylmén et al. [218] periodically arrested hydration by freeze drying of specimens which easily fracture before being analysed by an electron microscope. Imaging the pore structure in this manner, however, requires assumptions to be made regarding the depth profile of the material. Of course, it is both possible and simple to avoid this assumption should the material be directly observed in three dimensions, though this also provides a number of additional challenges.

In this chapter, the cement hydration reaction was observed by synchrotron microtomographic imaging. This powerful technique allowed for the comprehensive characterisation of the hydration reaction as it unfolds. The hydration of two systems: a plain CEM I 52.5N Portland cement, and a system comprised of Portland cement blended with 75% or 90% ground granulated blast furnace slag is shown, which is a blended cement that finds important applications in construction where high durability is required (CEM III/B or CEM III/C in the standard classification of BS EN 197-1 [11]) and also as a grout for the long-term immobilisation of nuclear waste [1]. In this way, new insights into the previously unseen chemical processes occurring during the critical first few minutes to hours of the lifespan of this complex, dynamic material are provided.

## 5.1 Tomography: Challenges of its Own

In the successful application of microtomography, the spatial resolution, the resolution of the feature which may be reliably observed, is part-related inversely to the sample diameter, and this must therefore be kept to a minimum. With any technique where a sample only a few mm

in dimension is analysed there will always be some question as to whether the sample is truly representative of a system as a whole. This is an unfortunate constraint, though necessary to reach the potential of the technique. It is not yet possible to observe a large volume across multiple length scales.

In spite of the quality of results achievable through the application of modern tomographic imaging it remains difficult to quantify the phase composition of a microstructurally complex material such as hydrated cement based on these data. This is a problem due to significantly overlapping greyscale intensities in the reconstructed data [74]. Phase quantification is carried out by quantitative in-situ crystallography in Chapter 3. Combining those data with those presented in this Chapter, complete pictures of both the geometry and chemistry of the reaction may be produced, which in combination show the very early reaction in five dimensions: spatial, time domain, and phase chemistry.

Reducing bias is a challenge which must be overcome in the application of tomography to the analysis of complex materials. This is also the case with many experimental techniques. The concern here is bias where certain data might be erroneously discarded, skewing the result toward the desired hypothesis. This is clearly methodologically incorrect.

Here, even a minute variation in a segmentation may result in an *entirely* different quantification. When a hypothesis has been formed, or an existing hypothesis is present in the literature, the production of an unbiased dataset becomes more difficult still without some kind of control in place. In this research, a method is provided which attempts to overcome this. The operation is automated in its entirety, and the human is removed from the process beyond the application of an original methodology. All data were analysed in an identical manner. A secondary analysis is also applied to highlight areas of hydration from a two-dimensional region of interest (ROI) which is qualitatively analysed in isolation to reinforce confidence in the result.

Through this research all three of the typical difficulties in imaging cementitious materials across the first hours are resolved. In this Chapter the hydration reaction is observed across the first hours of thermal output; no arrest is necessary due to the *very* rapid acquisition time of the instrument. The reaction is observed entirely in-situ from the first minutes. Formation of the pore structure is also observed from the first moments of the reaction. A very high spatial resolution is achieved, revealing the morphology and distribution of hydrates across the first hours of the reaction.

A contiguous volume of particles is segmented in-situ which is assisted by digital image cross correlation. The cementitious particles suspended in the mixing water rapidly sediment during the first minutes of hydration, and this algorithm allows the same set of particles to be

located within every reconstructed stack. The same region of interest is segmented throughout the duration of the experiment which corrects for the shift of particles both laterally and vertically. The same particles may be followed from the first minutes of the reaction all the way through to the hardened state. The material is observed as geometric stability is reached, and for a number of hours after set of the material has occurred.

## 5.2 Sample Preparation

In this thesis the hydration processes of three cement systems were studied in-situ using the 2-BM instrument described in Section A.3. The endstation hutch remained approximately at ambient temperature throughout all experiments, so no further temperature control was applied. A Hanson Ribblesdale Works CEM I 52.5N Portland cement was blended with BFS at fractions of 75% and 90% and hydrated at a water-cementitious materials ratio of 0.47. A lower ratio of 0.35 was insufficient to place the cement within the 2.0 mm diameter glass capillary, and was increased to 0.47. This remained within typical limits provided by BS 8500 [46] (see also Page 13).

Due to the large particle size of the blast furnace slag currently used by the UK nuclear industry [15] the coarse fraction of the material was removed for in-situ imaging by separating the volume fractions using a 150 $\mu$m sieve. Material compacted into the capillary using an oscillating head. Due to the ease of fracture of the capillary full compaction was not possible, though many well filled regions were found. As such, the cement does not entirely fill the depth of capillary, though for this experiment this is unavoidable. The material sediments with air rising and solid grains falling toward the base, especially across the first minutes. It may have been possible to modify the workability of the paste using an additive plasticising agent, though this was not carried out to prevent the possibility of interaction with the thermodynamics of the material. Exposure to incident radiation was very brief and the sample was well ventilated, which avoids excessive heating as radiation interacts with the specimen.

## 5.3 Instrument Configuration

The configuration of the instrument is shown diagramatically in Figure A.3. Once prepared (Section 5.2), samples were transferred to the beamline and mounted on the rotating stage shown within the figure. The time to transfer the sample was variable and ranged between six and ten minutes from the moment water contacted the cement.

For dynamic imaging of the reaction a PCO.Dimax CMOS imaging device was used. A micron length-scale voxel size of typically between 1.6 and 2.0 $\mu$m per voxel was achieved by this camera, though the realistic spatial resolution lay between 3.0 and 5.0$\mu$m per voxel as a result of source and detector artefacting. The value was later verified by direct image measurement. The camera was set to a moderate voxel size (2 $\mu$m per voxel) with a higher frame rate for imaging the Portland cement in which a more rapid reaction was observed, while the BFS was captured at 1.6 $\mu$m per voxel. This produced, in both cases, total acquisition and refresh times within 10 seconds.

The temporal resolution was also somewhat limited by the read-out time of the capture device (approximately 20 minutes should the buffer be filled entirely), and so certain gaps and irregularity in capture points inevitably resulted when closely-spaced data sets were collected in the early stage of the Portland cement hydration reaction. Here, the time step of the instrument was set based on the thermal output. Data were captured for approximately 12 hours with additions toward the end should scheduling have allowed. For imaging of slag substituted material the buffer was discharged on every step and so the time resolution was unaffected. The very large data processing requirement also limited the capture rate from both a storage and data procesing perspective.

## 5.4 Data Processing

Reconstruction was carried out subsequent to data collection, rather than on-line, which allowed for scheduled time to be devoted to capture. Data were reconstructed using the Tomopy package [219] which is developed in-house at APS. Code providing an example of the reconstruction method is provided in supplementary information (Appendix C).

Initially, outliers were removed from the unreconstructed dataset and open beam acquisitions. The operation was executed on an NVIDIA Quadro K2000 GPU (graphics processing unit) using tomocuda [219], which allowed for corrections to be performed on compatible hardware. The processing time was significantly reduced (the interested reader may also find detail of GPU processing by integration of the ASTRA toolbox in [220], though this was not carried out in this thesis). Dark current and open beam artefacts were removed, and processed data written was to disk in a binary format to prevent the operation having to be repeated in its entirety should it fail. Stripe artefacts, which may be caused by defective regions on the detector or dust on the scintillator, were removed from the dataset by the Fourier wavelet method [221].

Following this, the centre of rotation must be located for each sample. A correct location is signalled by the closure of circular or ring features within a reconstructed image. An isolated slice was reconstructed in each stack with the axis of rotation set through a given range, with the centre point located by eye. An alternative automated method is provided by [222] but was found to provide an inadequate result in processing of the data collected here.

Phase contrast was extracted using the method provided in [219, 223] and was combined with the imaging contrast result to a regularisation parameter of 0.001 which was selected based upon isolated trial and error reconstructions and the standard procedure carried out on the beamline. Reconstruction was carried out using the Fourier grid reconstruction algorithm [76, 219].

## 5.5 The Same Particles Every Time?

Particles sedimented in the capillary rapidly, and to accurately and rapidly segment these correctly the ability to track them as they fall through the glass capillary was important.

Initially, reconstructed data were cropped to remove a large portion of the air region surrounding the sample reducing the storage requirement. The stack is also written to disk as a series of 8-bit integer lossy compressed images. Loss of precision by downsampling in this process is relatively, unimportant; this stack is used simply for volume tracking and not quantification. A volume of interest is chosen[1] with a constraint applied that the volume must not lie within 25 $\mu$m of any large entrapped voidage or within 10 $\mu$m of the capillary wall. This is optically verified, and re-executed should a poor match be found. A volume of $250^3$ $\mu$m is extracted which is further cropped to $100 \times 100 \times 250$ $\mu$m for visualisation. The second crop prevents large particles from significantly obscuring the view.

Pre-processing and VOI tracking was carried out using the OpenCV C++ library [224] and graphical user interface implemented with the GTK+ library [225] which is shown in Figure 5.1. In Appendix D an identical method is provided in the Python language using the Scikit-Image module [226] to provide a more semantic implementation for the interested reader. A volume of interest was located in each scan by digital image cross correlation. By this algorithm, a two dimensional template matrix is slid across each slice and a matrix correlation coefficient calculated for each $x, y$ position, in each slice by Equation 5.1 (after [227]).

[1] Numpy random module, numpy.random.randint() constrained to lie within the capillary wall.

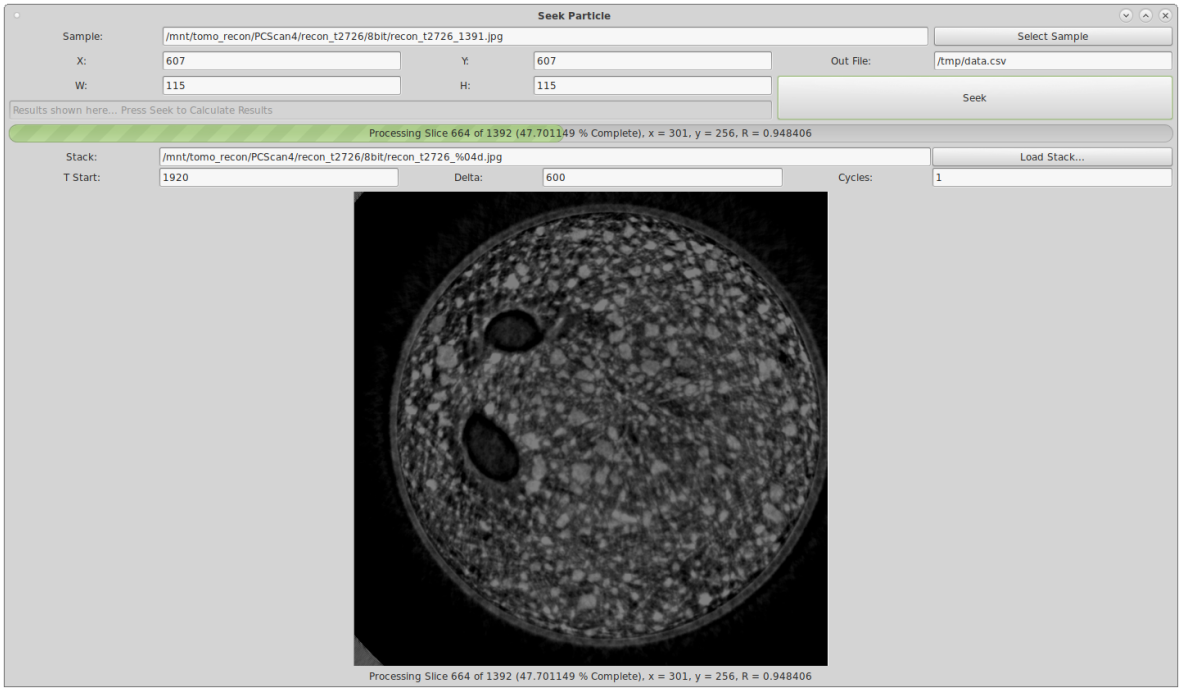


Figure 5.1: Hard coded implementation of the particle tracking algorithm in C++ / OpenCV [224]. Here, the output is written to a .csv file for secondary processing.

$$R(x,y) = \frac{\sum_{x',y'} \left(T\left(x',y'\right) \cdot I\left(x+x',y+y'\right)\right)^2}{\sqrt{\sum_{x',y'} T\left(x',y'\right)^2 \cdot \sum_{x',y'} I\left(x+x',y+y'\right)^2}} \tag{5.1}$$

Here, $T\left(x',y'\right)$ is the value of the pixel at position $x',y'$ in the template image $T$, while $I\left(x+x',y+y'\right)$ is the corresponding pixel in the target image $I$. The function yields the score $R(x,y)$ for each pixel in the coordinates $x,y$.

For each slice the location of the maximum correlation coefficient was then determined. The coefficient was written to a vector array containing the maximum of each slice in the $z$ direction (through the depth). The argument to the maximum of the $z$-depth array was then located, which yielded the position of the region of interest in the $z$ direction. The $x$ and $y$ locations were then extracted. Figure 5.2 shows the determination of the regression coefficient in the $x,y$ plane. This is carried out through the $z$ axis as shown diagramatically in Figure 5.3. Figure 5.4 demonstrates the extent to which the correction is required to produce useful data from this study.

Figure 5.2: Determination of the correlation coefficient by Equation 5.1 in the $x, y$ plane.

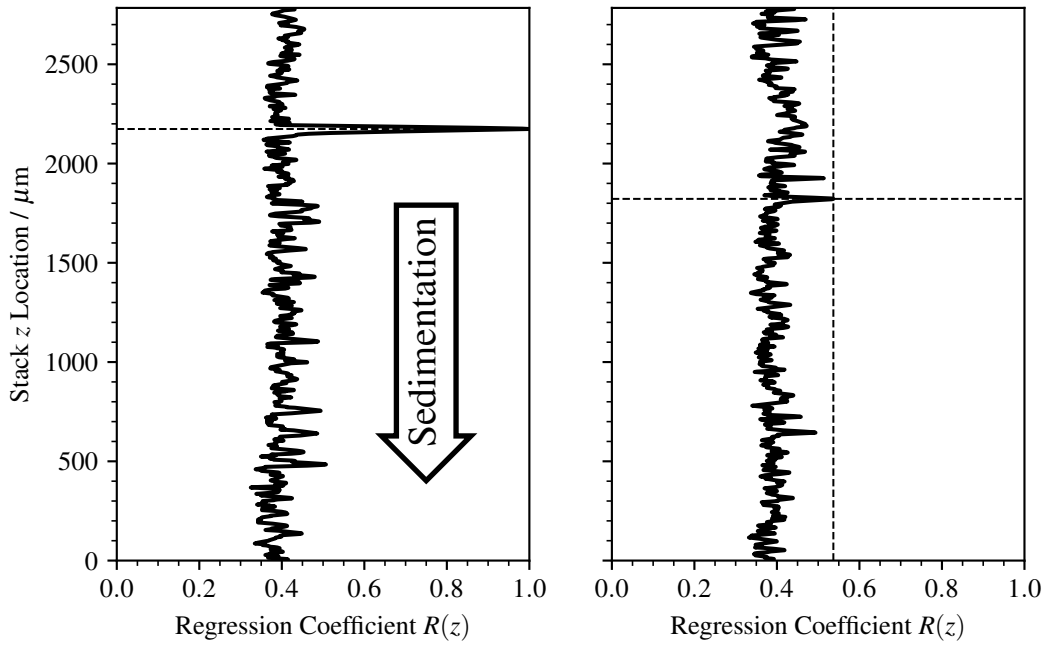


Figure 5.3: Maximum regression coefficient $R(x, y)$ (determined by Equation 5.1) in the first and last scan, of a subset extracted in the first scan. A value of 1.0 represents a perfect match.

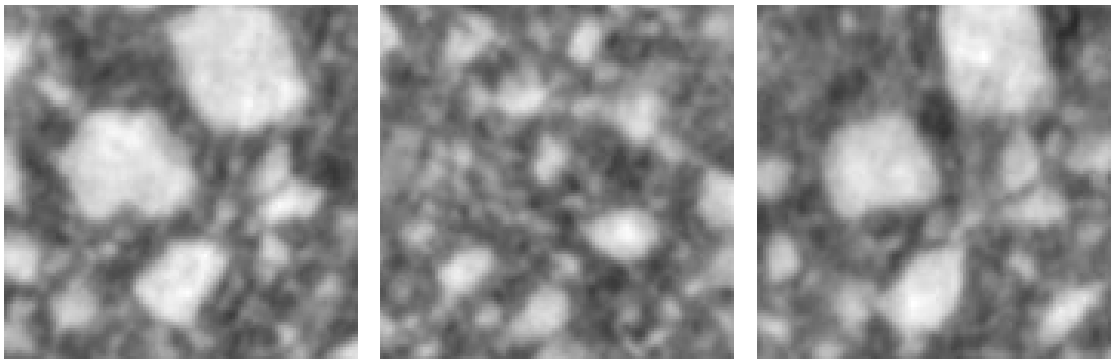

(a) (b) (c)

Figure 5.4: Corrected and uncorrected slices.

Slice acquired at 8 minutes (5.4a), the same geometric location at 13 hours and 45 minutes (5.4b), and the corrected geometric location at the same time (5.4c). Here, the particle has moved from $(538, 609, 1129)$ to $(524, 616, 999)$, which equates to a drop of 230 $\mu$m. The subset shown is 250 $\mu$m in $x$ and $y$ dimension.

### 5.5.1 Structural Similarity Index

In order to highlight regions of growing hydrates and changes in the pore structure the structural similarity index (SSIM) was computed from variations between slices taken at 30 minutes of all systems and in the final scan. The structural similarity index [228] is a development of the universal quality index [229] which produces a spatially resolved measurement of the quality of an image based on the measured difference between a reference and deformed signal. The calculation is carried out based on the mean, variance, and covariance of the reference and image in which the deformation has occurred (Equation 5.2).

$$SSM(x, y) = \frac{(2\mu_x\mu_y + c_1) \cdot (2\sigma_{x,y} + c_2)}{(\mu_x^2 + \mu_y^2 + c_1) \cdot (\sigma_x^2 + \sigma_y^2 + c_2)} \tag{5.2}$$

Here, $\mu_x$ is the average value of $X$, $\mu_y$ is the average value of $Y$, where $X$ is the test image and $Y$ the comparator. $\sigma_x^2$ is the variance of $x$ and $\sigma_y^2$ is the variance of $y$, while $\sigma_{xy}$ is the covariance of $x$ and $y$. $c_1$ is a constant calculated as $c_{1,2} = (k_{1,2}L)^2$ where $L$ is the dynamic range of the values contained within the image, in this case 255. Typically $k_1 = 0.01$ and $k_2 = 0.03$.

In this thesis the first scan at which geometric stability is apparent was taken as the reference, while the final scan was used as comparison to this. Geometric stability was defined here as having occurred where a change in the $x$ and $y$ axes of no greater than 1.75 $\mu$m (2 voxels) in the extracted volume of interest became resolvable by the cross-correlation. At

these time points, the system ceased to show any significant separation of particles in the $x, y$ plane, or rotation of particles. Data were clipped only to highlight regions displayed; no quantitative metrics were derived from this calculation.

## 5.6 The Resolved Structure

Typical examples of identified features are shown in Figure 5.5 with a typical histogram of the same time point shown in Figure 5.6. Regions are identified as segmented by thresholding of the histogram provided.

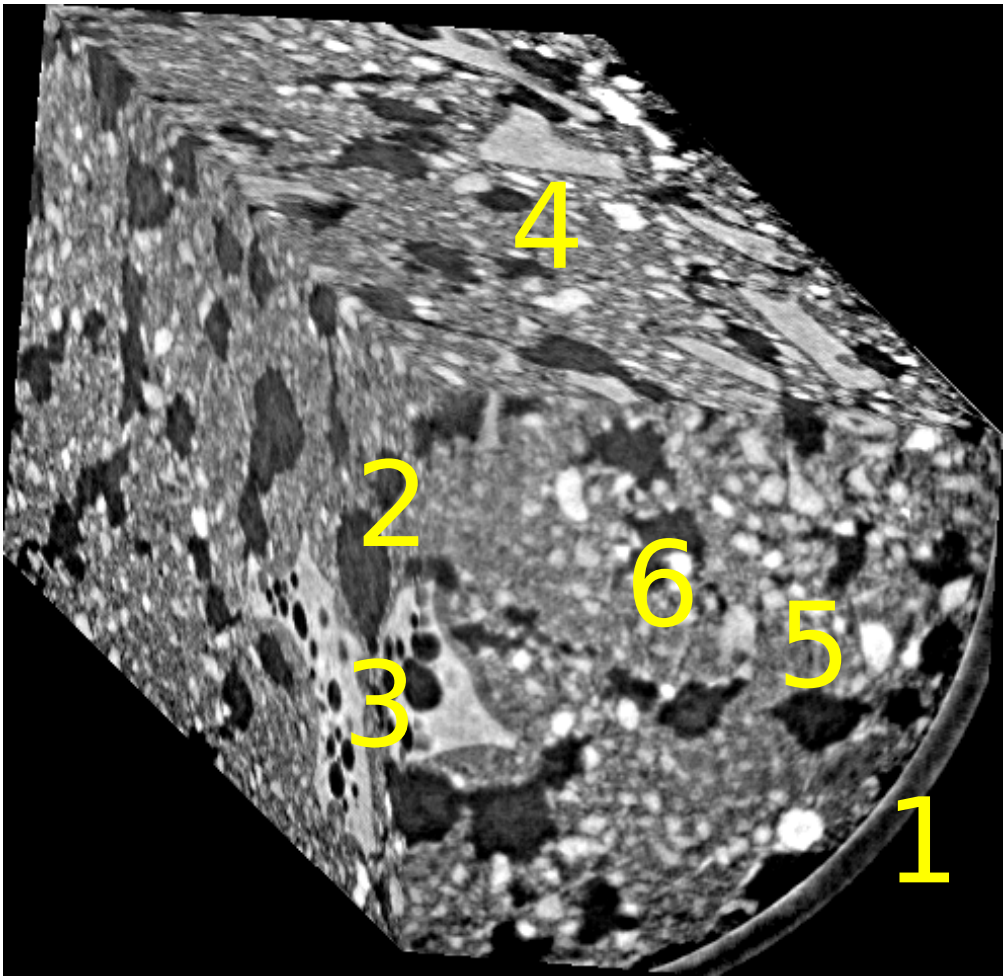


Figure 5.5: An example slice from the initial test of the 75% BFS-blended cement at 12 hours of hydration. **1** is the glass capillary, **2** is an internal trapped air void, **3** are voids enclosed within slag particles, **4** is a region of hydrate formation around residual clinkers, **5** is a high density particle observed as a bright spot, and shown to the right of **6** is a capillary pore.

### 5.6.1 Rendering & Transfer Function

Data were batch rendered using the Python interface to the ParaView package [230]. The volume is rendered in three dimensions with both an opacity and greyscale transfer function providing colourisation and the removal of extraneous features.

Defining a valid transfer function is difficult, though imperative for the production of a reliable result. A number of methods have been proposed for segmentation by image thresholding. Automated thresholding methods such as Quality Threshold Clustering (QT) (detailed in [231]) are used commonly in medical image segmentation. This may automate the process to a certain degree, assuming that data are grouped to discrete classes. However user intervention may still be required where an unoptimal result has been produced. Automating the process leaves the method somewhat out of the hands of the operator, though this may be seen as advantageous in certain test types. Other methods such as taking valleys in the greyscale histogram or peaks in the rate of change of the cumulative histogram with increasing intensity [90, 232] have also been suggested in the literature. In the case of this thesis, a method developed as an adaptation of [215] and [90] is used. The resulting threshold, which remained constant, is shown in Figure 5.6.

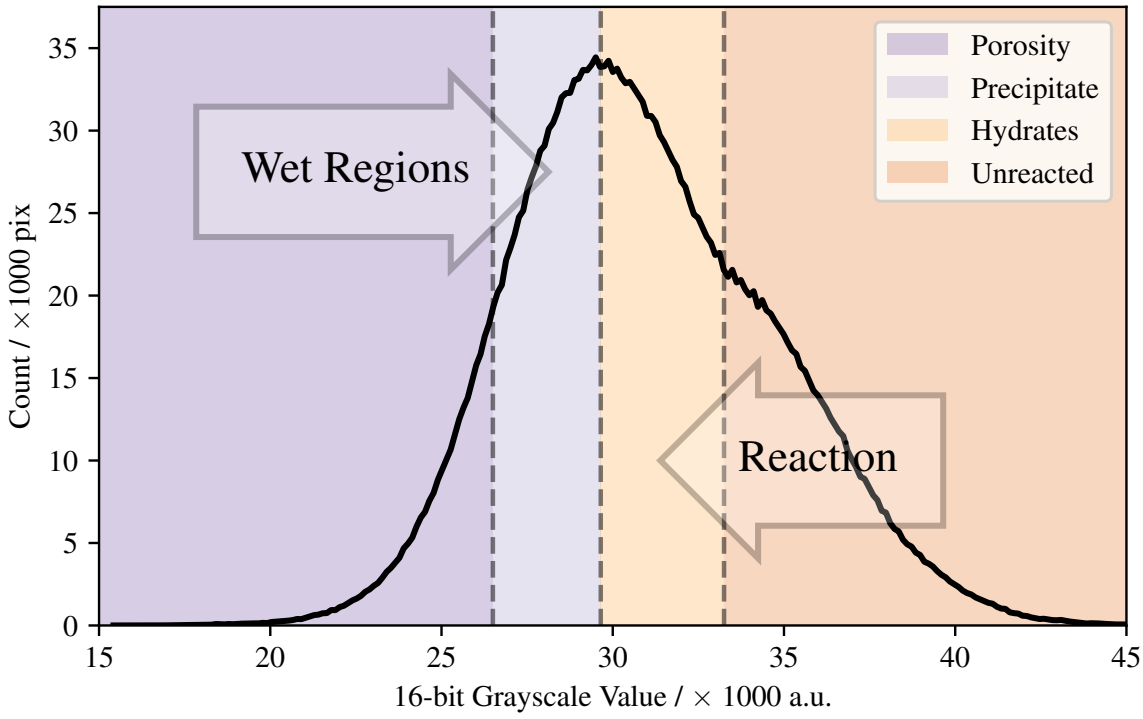


Figure 5.6: A typical 16-bit grayscale histogram. Reacting regions are shown to the right, and pore regions to the left.

In combination, the transfer function and look-up table (LUT) are similar to a binary threshold procedure with the former setting a colour mapping and the latter the threshold itself. Hydrates were rendered in transparent blue with a tail-off toward the surface of the unreacted volume, highlighting the boundary. Unreacted materials were rendered in grey with 100% opacity. In certain cases this resulted in problematic particles towards the edges of the render which obscured the view. The volume was rotated to account for this.

Once set in the final acquisition, the transfer function was fixed such that it remained constant throughout the duration; in the final analysis it was possible to observe hydrates, unreacted materials, and porosity including any phase which may have formed within the volume of the pore structure itself. Should the beam current have varied, this may have resulted in images where the threshold does not provide an entirely expected result, though data were collected in top-up mode to maintain beam current as close to constant as possible and mitigate this. Additionally, due to the closeness in densities of various hydrates it is not possible to segment individual phases in isolation as discussed previously.

## 5.7 Hydration Reaction of Portland Cement

Figure 5.7 shows the structural similarity indices of the two end slices of the region shown, captured at 30 minutes as a reference and the final scan (13 hours 45 minutes) as a comparator. The result is inverted.

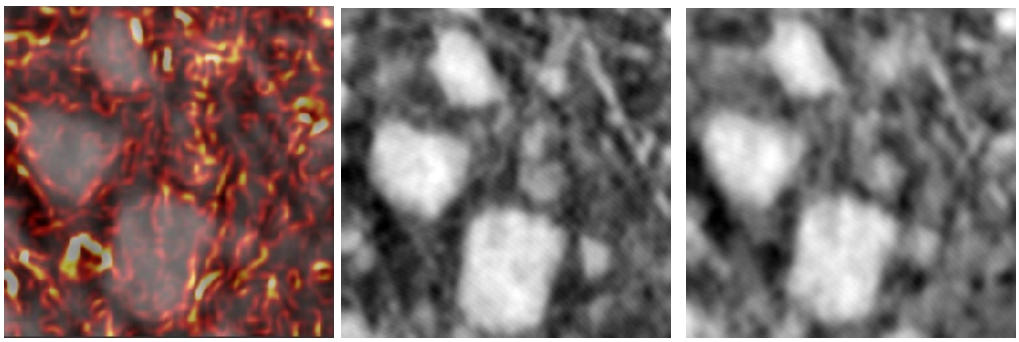

(a) SSIM (b) 30 Minutes (c) 13.5 Hours

Figure 5.7: Structural similarity index map (5.7a) between slices acquired at 30 minutes (5.7b) and final (5.7c). Image dimensions 250 $\mu$m $\times$ 250 $\mu$m.

In Figure 5.7a regions of variation are shown both within the pore volume and surrounding particle surfaces are highlighted. Clearly some hydration has occurred here. Large re-

gional changes are shown, occurring extensively within the pore structure itself and additionally in a non-uniform manner on the surface of the unreacted grains.

The development of hydrates within the material across the first minutes is shown in Figure 5.8, while the formation of the pore structure is shown in Figure 5.9.

Over the first minutes of the reaction the material sedimented rapidly with certain regions dropping up to 37.5 $\mu$m through the capillary. Additionally, a very narrow layer of hydration product appears to have deposited on the surface of the Portland cement grains. Recent studies have suggested that an altered layer forms on the surface of pre-hydration $C_3S$ even before the exposure of material to the mix water [233], though it is likely that any initial alteration layer would not be observable as it is far narrower than the spatial resolution of the instrument used here ought to allow. Ettringite [23] and very limited amounts of hydrates (Chapter 4) are also formed at this time. This suggests that this surface hydrate layer consists of disordered C-S-H which has formed a layer that partially coats the surface of the reacting $C_3S$ grains. Soft X-ray spectromicroscopy has shown the formation of a similar layer within 84 minutes of the beginning of the hydration reaction by Bae et al. [234] and it is concluded here that a layer has probably formed before the first point demonstrated by Bae et al.. The spatial resolution apparent from the results presented by Bae et al. [234] appear to lie within close proximity to the voxel size of the instrument used for observation in this thesis.

The decrease in thermal output here is a result of the fact that the initial very rapid heat release is related to particle wetting and the dissolution of highly reactive minor cement constituents, particularly alkali-containing sulphates such as syngenite $K_2Ca(SO_4)_2{\cdot}H_2O$ [235], which are then depleted.

The formation of the hydrous calcium aluminium sulphate ettringite inhibits the rapid formation of calcium aluminate hydrates within the material which would otherwise cause flash set. These form needle-like structures within the matrix [215] which are not observable here due to overlapping greyscale intensities [74] of chemical phases.

Prior to the beginning of the induction period the initially formed layer appears to have thickened slightly, and during this stage in the reaction the narrow layer remained present on the surface of the anhydrous grains. Toward the end of induction, the solid phase has become permeable to mix water which triggered further hydration of the clinker materials. Significant morphological changes appear to have occurred within the dormant period; no setting of the material has yet happened.

Two distinct volumes within the pore structure were shown. As the solution reached saturation with respect to calcium and silicate phases, flecks of hydrates precipitated from the pore volume. These propagated through the pore structure and eventually agglomerated on

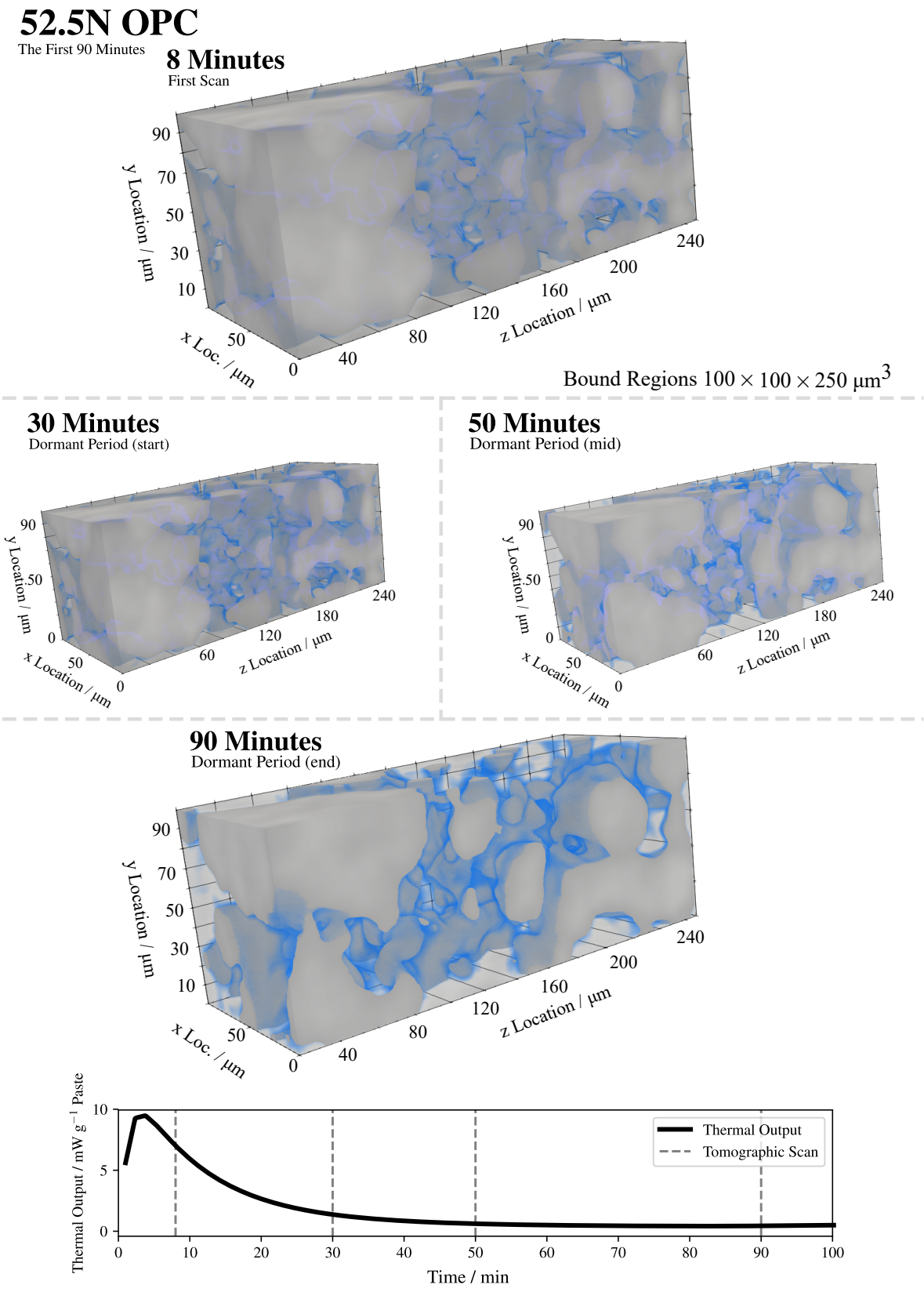


Figure 5.8: Formation of hydrates within the CEM-I 52.5N Portland cement across the first 90 minutes of the hydration reaction.

the wall or outer surface of the hydrated layer and contributed to the reduction in pore volume. This continued throughout the early stages of the reaction. These were eventually identified as surface hydrates by the segmentation though it is not possible here to differentiate between inner and outer product resulting from C-S-H densification [31] at this stage.

Precipitates remained within the pore structure throughout the dormant period though the production of these appears to have slowed as the formation of the hydrate surface has possibly inhibited the rate of dissolution into the fluid. This observation appears to agree with the theory that the controlling mechanism during the dormant period is the rate of dissolution [236]; as dissolution from the clinker interface ceases, the formation of precipitates within the pore volume also slows. These regions of precipitate must have remained present; accounting for these greyscale regions as surface deposits leads to the calculation of a very high hydrate volume which is not the case at this time shown by the results presented in Chapter 4. The pore structure showed increasing constriction, which resulted from both the nucleation of hydrates and the agglomeration of these precipitates. Hydrates formed both as a result of this and alteration of particle surfaces causing the appearance of hydrate pushing out. In addition to the unreacted material, this forms the solid phase.

The end of induction marks the beginning of the nucleation and growth period, which was shown by a rise in thermal output. Hydrate volumes acquired during this period are shown in Figure 5.10. As the thermal output increased, the hydrate layer noticeably thickened, though it is difficult to come to a conclusive answer as to what triggers this growth. It has been hypothesised in the literature that nucleation begins to occur after the formation of a metastable barrier on the $C_3S$ surface [4] though some doubt has recently been cast on this due to results suggesting that nucleation of C-S-H occurs far closer to the time at which water is first combined. Here, the observable length scale does not necessarily offer a complete answer to this and observations of dynamic processes occurring within the pore fluid below the length scale offered here are necessary, ideally by a technique which is also sensitive to the pore fluid chemistry or composition.

During the early acceleration a low-density product is formed which appears to thicken as a result of both the growth of hydrates from particle surfaces and the propagation of hydrates by precipitation through the pore volume. It was not possible to resolve this as fibrous growth due to the limitations in spatial resolution of the instrument. The agglomeration of these was not immediate. By six hours a thickening band of hydrate appears to have formed upon the surface of the cement grains, which was accounted for as hydrate shells by Gallucci et al. [237]. This caused the beginning of the interlock of the material that resulted from the formation of outer hydration products.

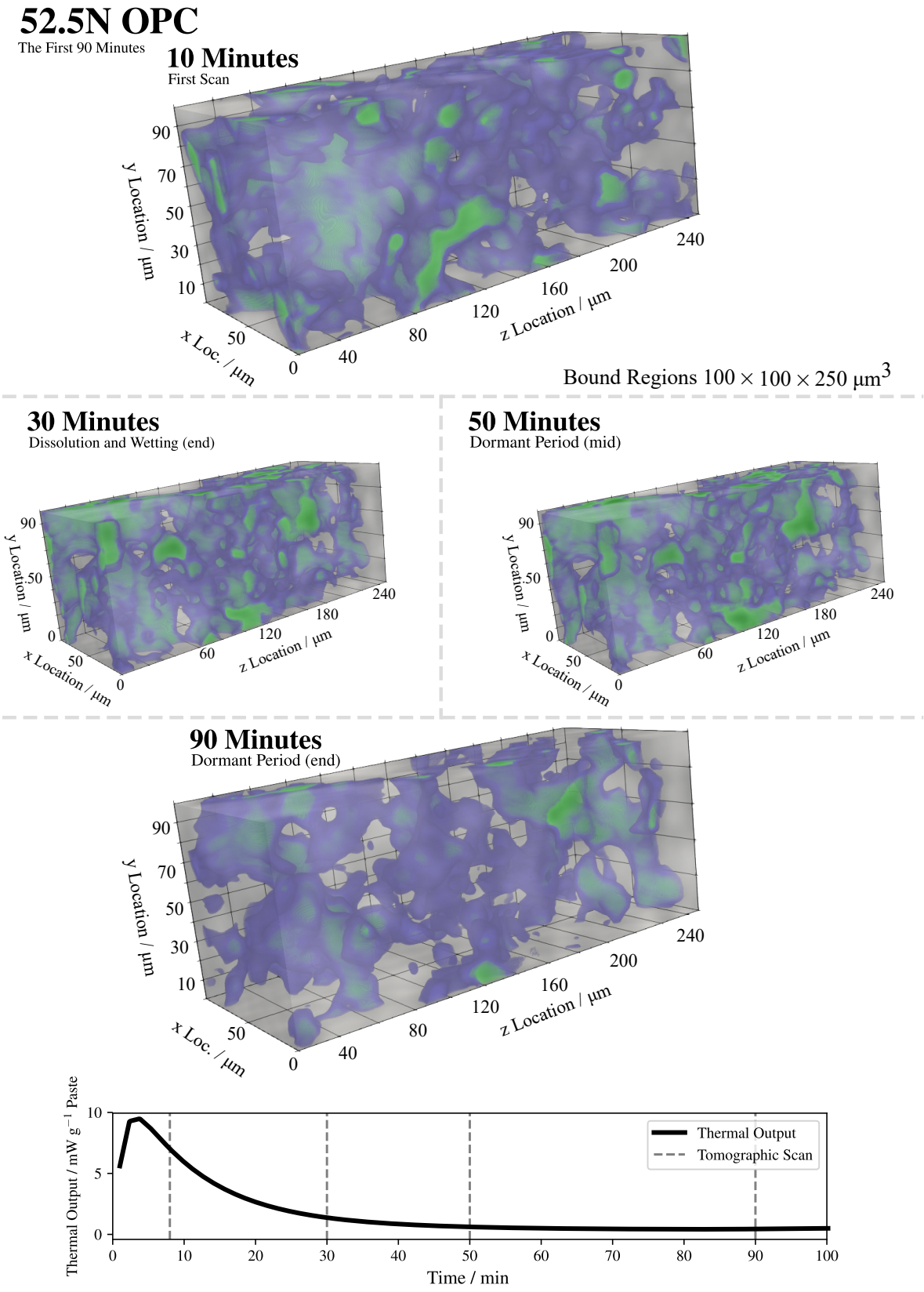


Figure 5.9: Formation of precipitates (purple) and pore volume (green) within the CEM-I 52.5N Portland cement across the first 90 minutes of the hydration reaction.

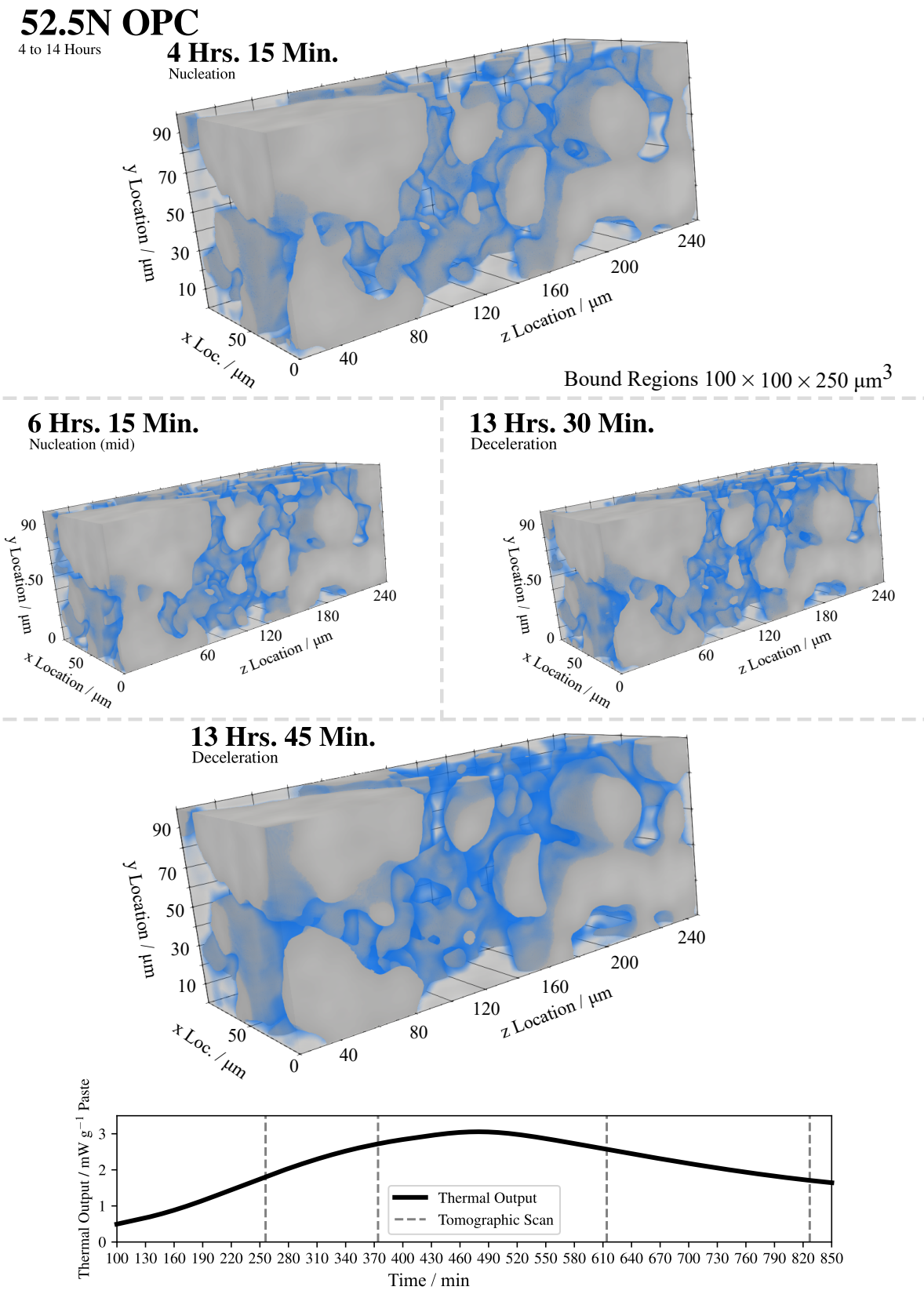


Figure 5.10: Formation of hydrates within the CEM-I 52.5N Portland cement across the nucleation and growth period.

Toward the end of the nucleation period hydrates have deposited upon the surface of unreacted materials and the access of free water to the unreacted clinker has become once again inhibited. The result was the slowing of precipitation and a gradual reduction in the thermal output as the layer thickens and the reaction slows.

Once deceleration begins these hydrates have formed significantly. Here, the surface of precursor grains becoming coated with these was observed, and precipitates remained abundant within the pore volume (Figure 5.11). By visual inspection, the total degree of hydration remained fairly low at this time. Across the first 90 minutes (Figure 5.9), these two volumes were dissimilar, though by 4 hours the material appears to have reached stability with any geometric differences being attributed here to retreat of the particle surface and pore-volume infilling.

The formation of hydrates (blue regions) at the time of capture of the final tomographic data set (13 hours and 45 minutes) is shown to the base of Figure 5.10. Hydrates have formed significantly both on the surface of materials and within the pore structure (Figure 5.11) though the total degree of hydration remains fairly low at this time, as hydrates have deposited the access of free water to the unreacted clinker has been inhibited. The result is the slowing of precipitation and a gradual reduction in the thermal output as the layer thickens. Interlocking of these hydrates in the manner shown fundamentally results in the rapid strength gain of the material across the first days of the hydration reaction.

The volume of hydrate formation appears to match well the data provided in Figure 5.7, though no quantitative comparison of this is made in this thesis as these are fundamentally different metrics taken from differing baselines and so are not directly comparable. The nucleation of hydrates on surfaces and the wall and agglomeration of precipitates has caused the pore structure to constrict, reduce in volume, and become more tortuous. Note the vertical pore observed at 6 hours 15 minutes in Figure 5.11 at the 60 $\mu$m to 100 $\mu$m $z$ location. This pore shows both constriction and disconnection from the surrounding pore structure.

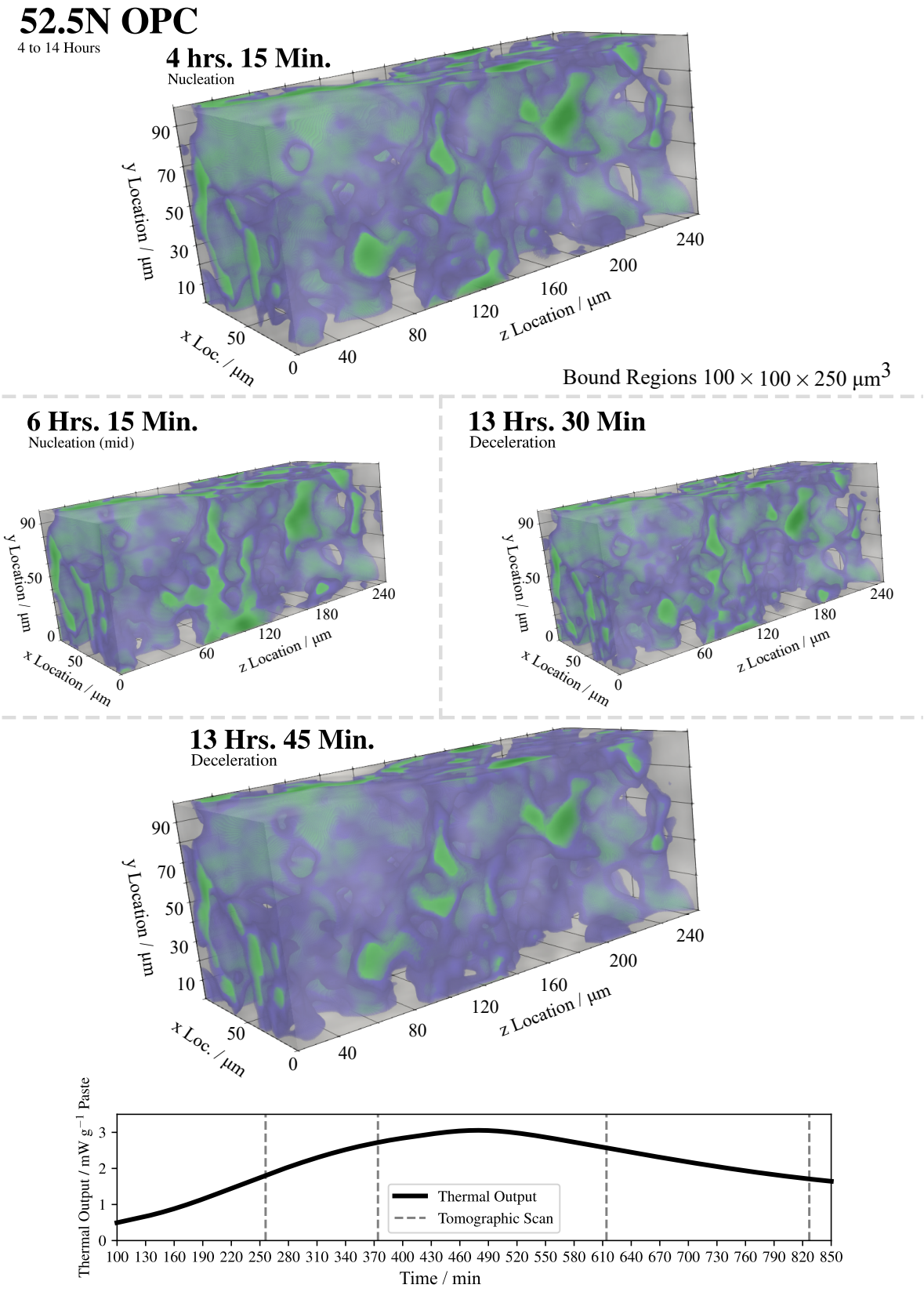


Figure 5.11: The formation of the pore volume and precipitation of hydrates within during the nucleation and growth period.

## 5.8 Hydration of Slag Cement

Having formed an understanding of the processes observed during the hydration of pure Portland cement, the natural progression is to substitute part of the Portland cement by a supplementary cementitious material. In the case of this thesis the same Portland cement is substituted to a high degree of 75% and 90% BFS, which falls close to the CEM III class designations in BS EN 197-1 [11], and cements widely used in the nuclear industry for waste encapsulation [1] as previously noted. In the case of this experiment a uniform time spacing is used which yields a render approximately every ten minutes. Selected renders across the first 90 minutes are shown in Figures 5.12 (75% substitution) and 5.13 (90% substitution) for the first 90 minutes and Figures 5.17 (75% substitution) and 5.18 (90% substitution) for the remainder of the 12 hour period.

Here, a narrow layer at the interface is once again observed at both degrees of substitution. The layer is very challenging to identify, and the presence of this is only revealed by the method of alculating the threshold values for the various morphological phases in the final scan, and subsequently applying these to all data sets acquired. This appears to grow quite extensively during the dissolution and wetting period of the reaction. This is perhaps some kind of layer which slows the hydration reaction toward the dormant period, or may be a leached layer as the material has likely not yet reached supersaturation, which would be required to yield high volumes of precipitation in the solution. The barrier appears to be non-uniform and the hydrate may deposit more extensively on the PC solid phase, while the slag remains fairly untouched. This reinforces the hypothesis that this is a leaching process. The modified layer grows across the first half hour of the reaction while dissolution of clinker materials into the pore solution slows. The result of this is the clear reduction in the rate of hydration through the dormant period; the layer does not significantly grow in thickness across this stage.

During the dormant period separation of initally agglomerated particles is observed as the material settles within the capillary. The particle identified toward the centre of Figure 5.12 is multiple particles which have agglomerated together and separated as the capillary moves slightly within the instrument. The material does show, however, a significantly higher stability than that exhibited by the PC previously studied, in this case settling in the capillary by only 2 or 3 $\mu$m across the first 30 minutes.

The appearance of a reduction in dissolution rate is further suggested when observing the formation of precipitates within the pore structure. These appear to form within the pore volume, propagate through, and become most identifiable forming on the wall of the pore volume or the surface of the hydrate material, similarly to the PC. As previously noted,

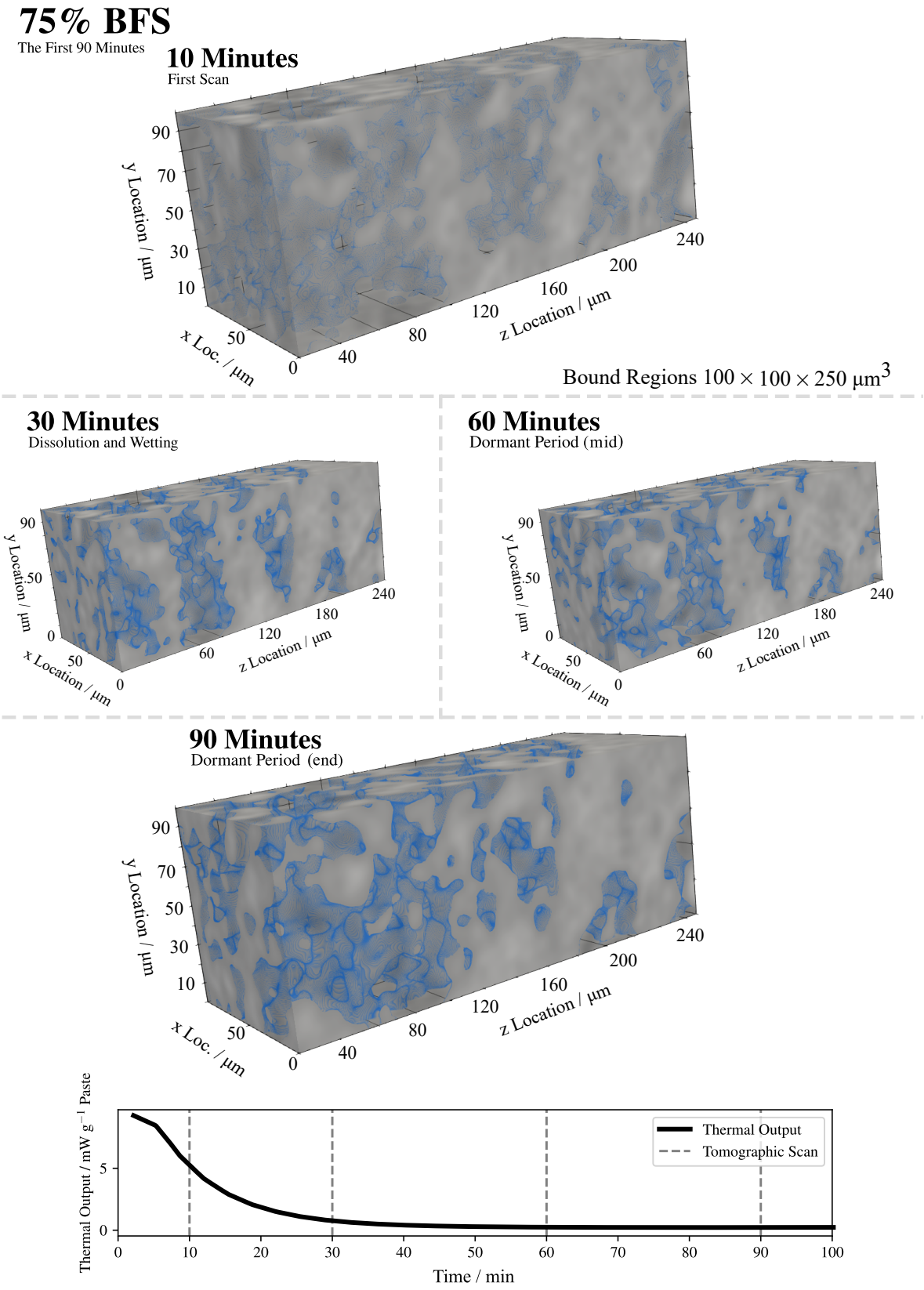


Figure 5.12: The formation of hydrates (blue regions) across the first 90 minutes of the reaction of the cementing material substituted with 75% BFS.

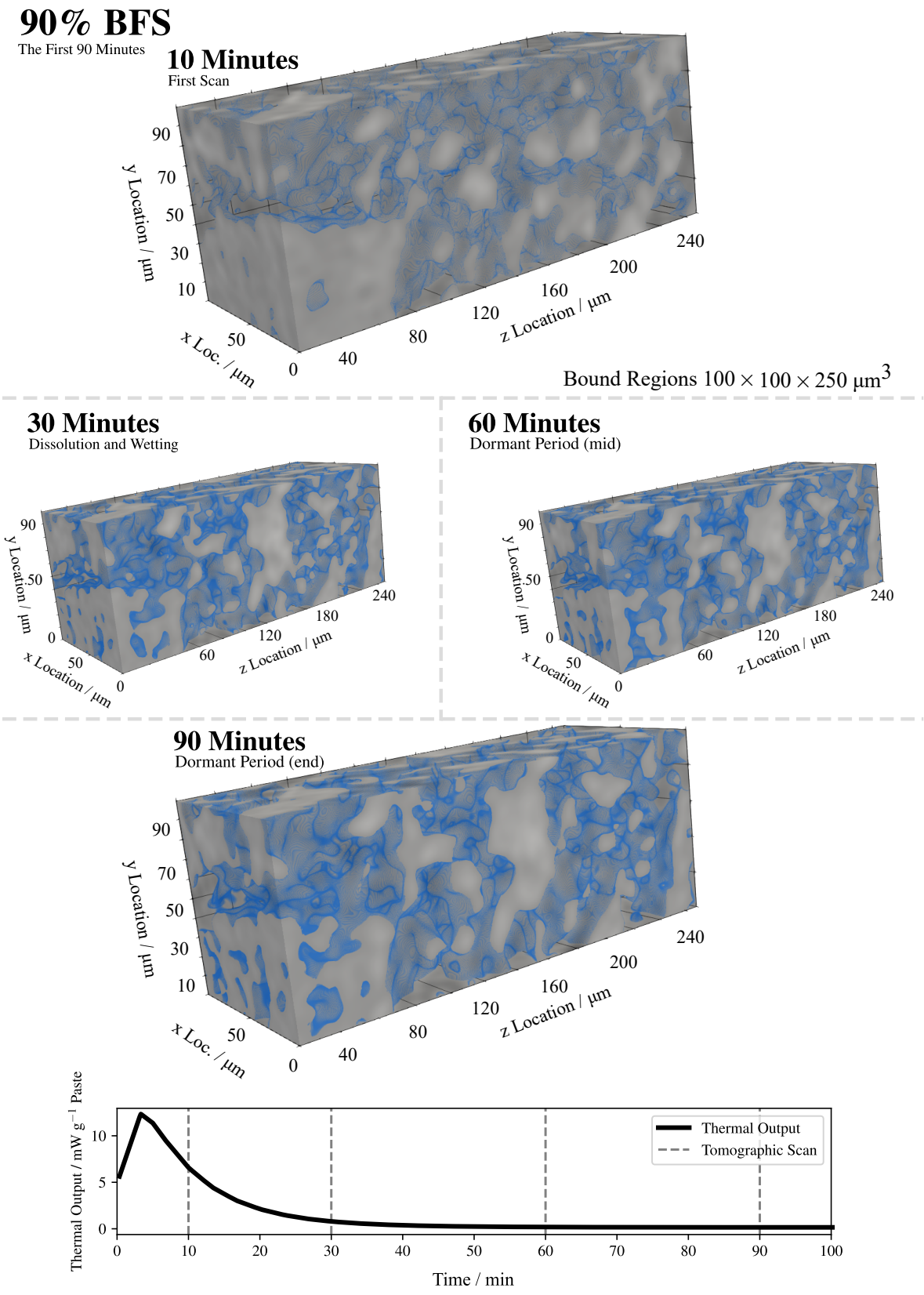


Figure 5.13: The formation of hydrates (blue regions) across the first 90 minutes of the reaction of the cementing material substituted with 90% BFS.

segmenting these as a hydrate volume produces an extremely high hydrate volume, so is deemed unrealistic.

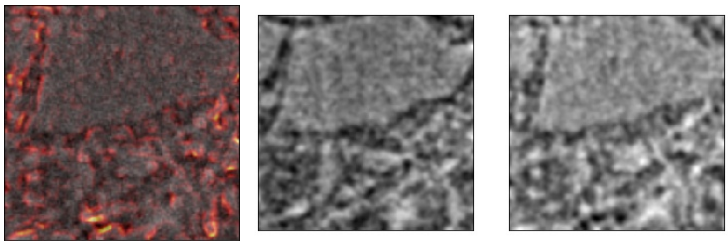

(a) SSIM (b) Slice 10 Min. (c) Slice 12 Hrs.

Figure 5.14: Mapped structural similarity index (5.14a) of the 90% substituted BFS material. Dimension shown 250 $\mu$m $\times$ 250 $\mu$m.

These regions have formed within the first ten minutes of the reaction during the dissolution and wetting period, which is marked by a significantly raised thermal output. The pore volume shows high variability at this point. Precipitates were shown to form also in the volume to the top right of the material, which confirms this as not a large particle but instead a series of small particles agglomerated together which separate within the first half hour; setting of the material is not yet observed.

During the dormant period between 60 and 90 minutes only a very minor variation in the precipitating volume is seen in both materials studied. At this point the material has become stable within the capillary and no movement is shown, though this is by no means set; the cumulative volume of hydrates in the matrix is still very low.

Accessibility of particles to the mix water is limited by the formation of the protective layer and only a limited reaction of these particles occurs. Observe for example the pore at $x, y$ location $(25, 30)$ in Figure 5.15 between 60 and 90 minutes. This pore shows variability, albeit only qualitatively low. In the system substituted with 90% BFS the material appears to contain a high volume of porosity in the first scan. Again, no setting of the material is observed across the first hours, though geometric stability in the microstructure is.

Hydration is confirmed by structural similarity index map shown in Figure 5.14 (isolated for the 90% BFS material, calculated as per Section 5.5.1).

The end of the dormant period sees acceleration begin. Data from these times are shown in Figures 5.17 and 5.18. The protective barrier appears to somehow become breached. This is similar to the reaction of the Portland cement, and the anhydrous particulate becomes accessible to the mix water once again. This occurs near to the end of the dormant period. However the spatial resolution of the instrument does not allow for close observation of the

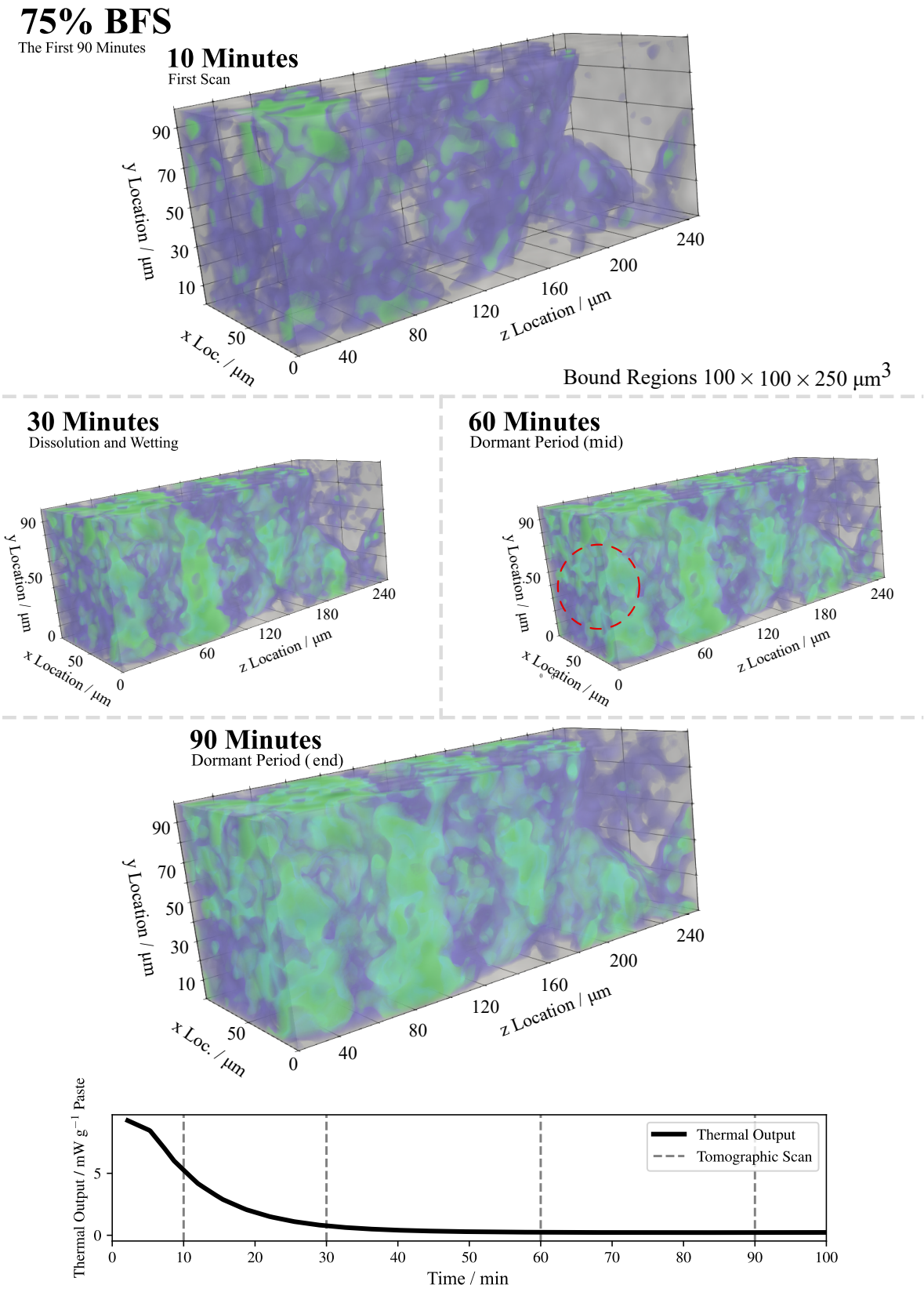


Figure 5.15: The precipitation of materials (purple) and the pore volume (green) across the first 90 minutes of the hydration reaction. The material is substituted with 75% BFS.

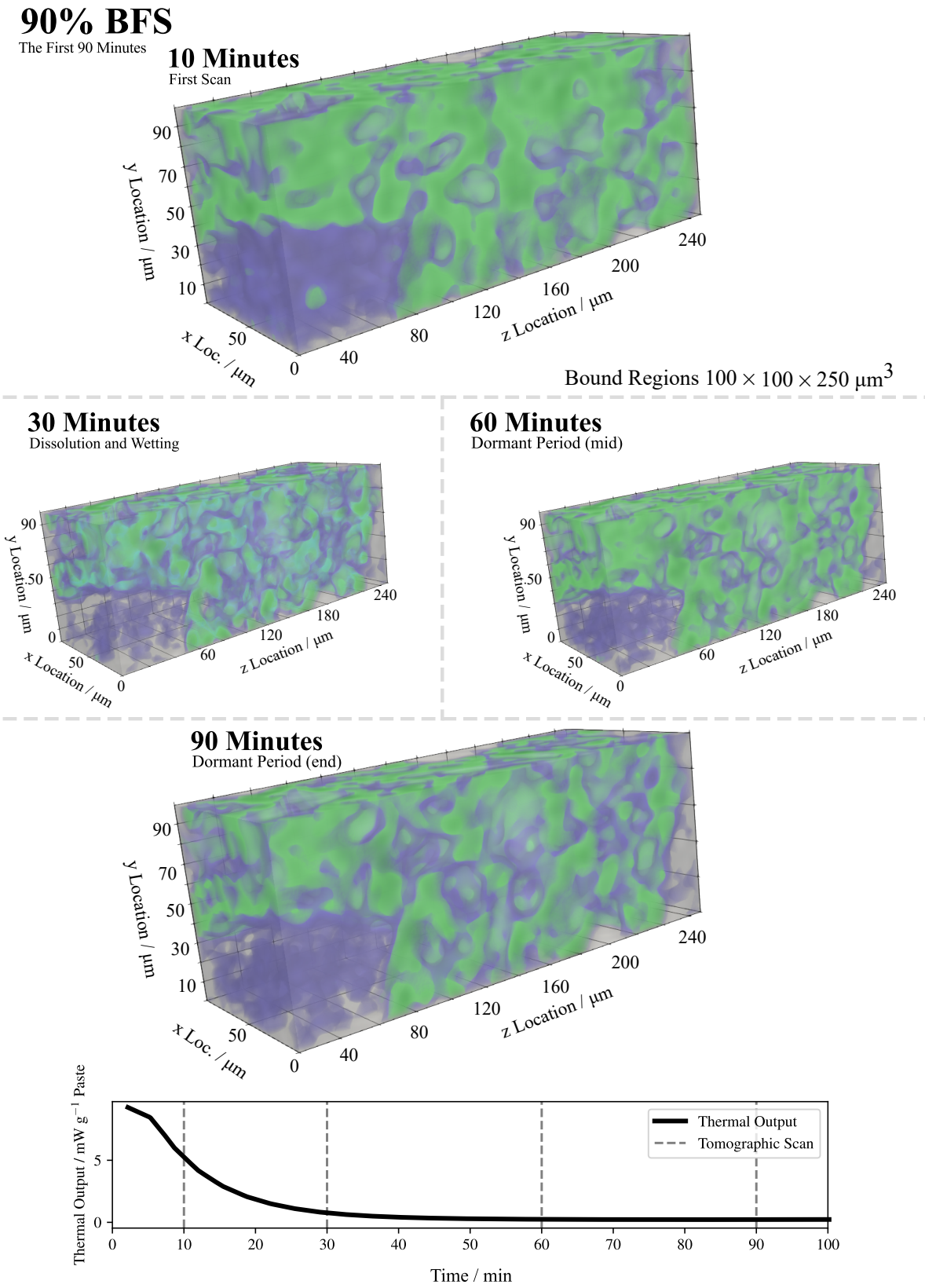


Figure 5.16: The precipitation of materials (purple) and the pore volume (green) across the first 90 minutes of the hydration reaction. The material is substituted with 90% BFS.

region between the particulate and the barrier which has formed, and it is once again difficult to know precisely why this has happened. The barrier has now become permeable and the surface of unreacted particles comes into contact with the mix water causing the formation of hydrates (blue regions) within the material.

Between four and eight hours this becomes fairly significant as hydrate formation results in interlocking of anhydrous material. It is reiterated that it is not possible to segment outer hydration product from inner using this method, but suggested that the barrier formed within the first 90 minutes of the reaction is of a low density and that the hydrates forming result in rapid increase in density of the matrix and an increase in rigidity.

Here, the pH of the system has risen as a result of the hydration of $C_3S$ and a sufficient volume of calcium hydroxide (in the crystalline form portlandite) which activates the reaction of the BFS [238] has formed. This occurs during the exotherm observed between four and eight hours in the thermal output of the system and continues across the longer duration of the reaction through to and beyond twelve hours.

Across the longer duration of the reaction precipitates have a tendency to further agglomerate, deposit on the surface of the outer layer of the surface hydrate, and reduce the volume of the pore structure. As a result of this the empty pore volume (green) decreases in size significantly though the total pore volume remains high in both systems at this time. During nucleation the rate of precipitation remains high; the surface layer of hydrates has not yet sufficiently restricted access of free water to the anhydrous material.

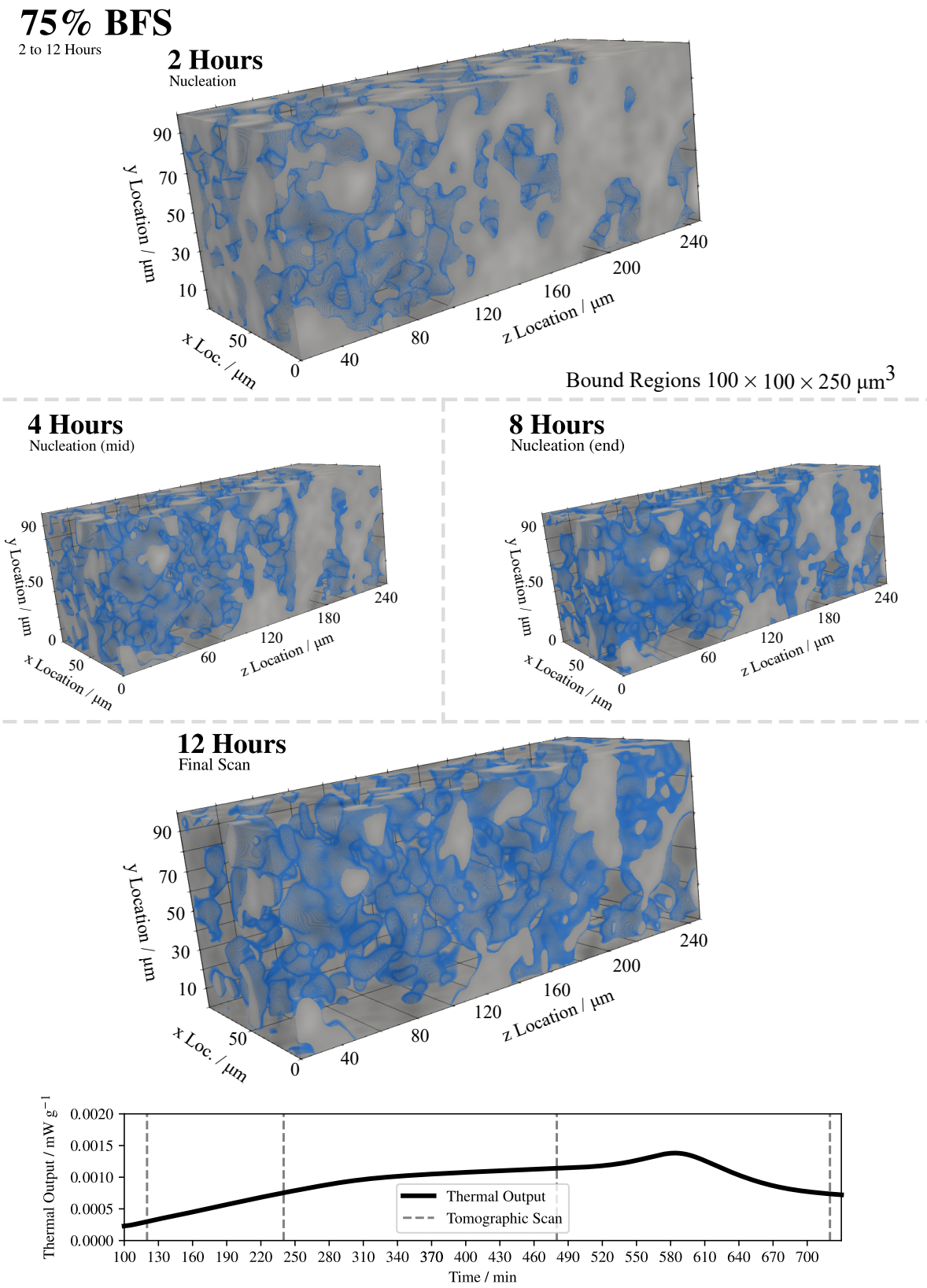


Figure 5.17: The formation of hydrates (blue regions) in the 75% BFS-substituted cement within the observed volume between 2 hours and 12 hours.

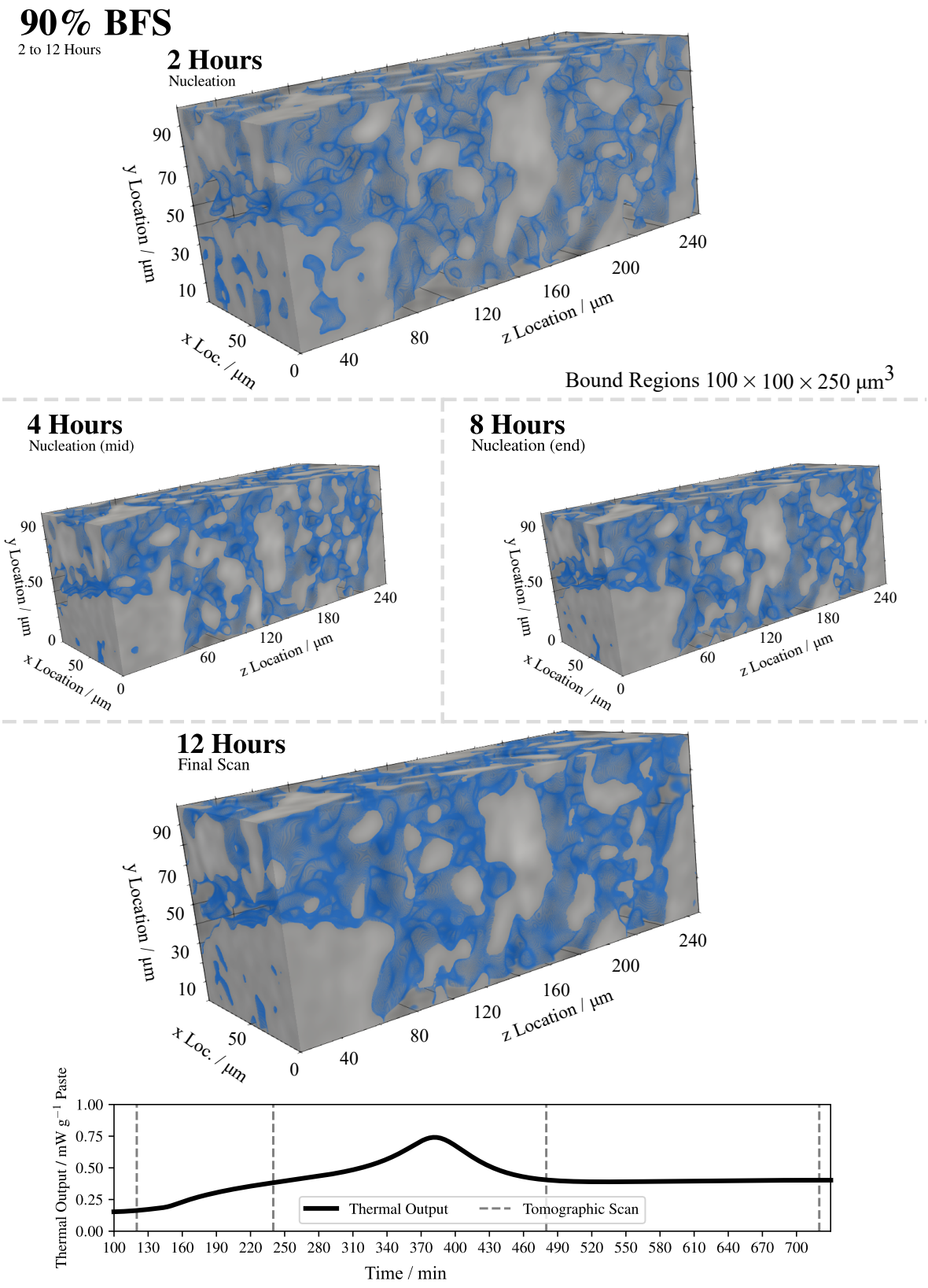


Figure 5.18: The formation of hydrates (blue regions) in the 90% BFS-substituted cement within the observed volume between 2 hours and 12 hours.

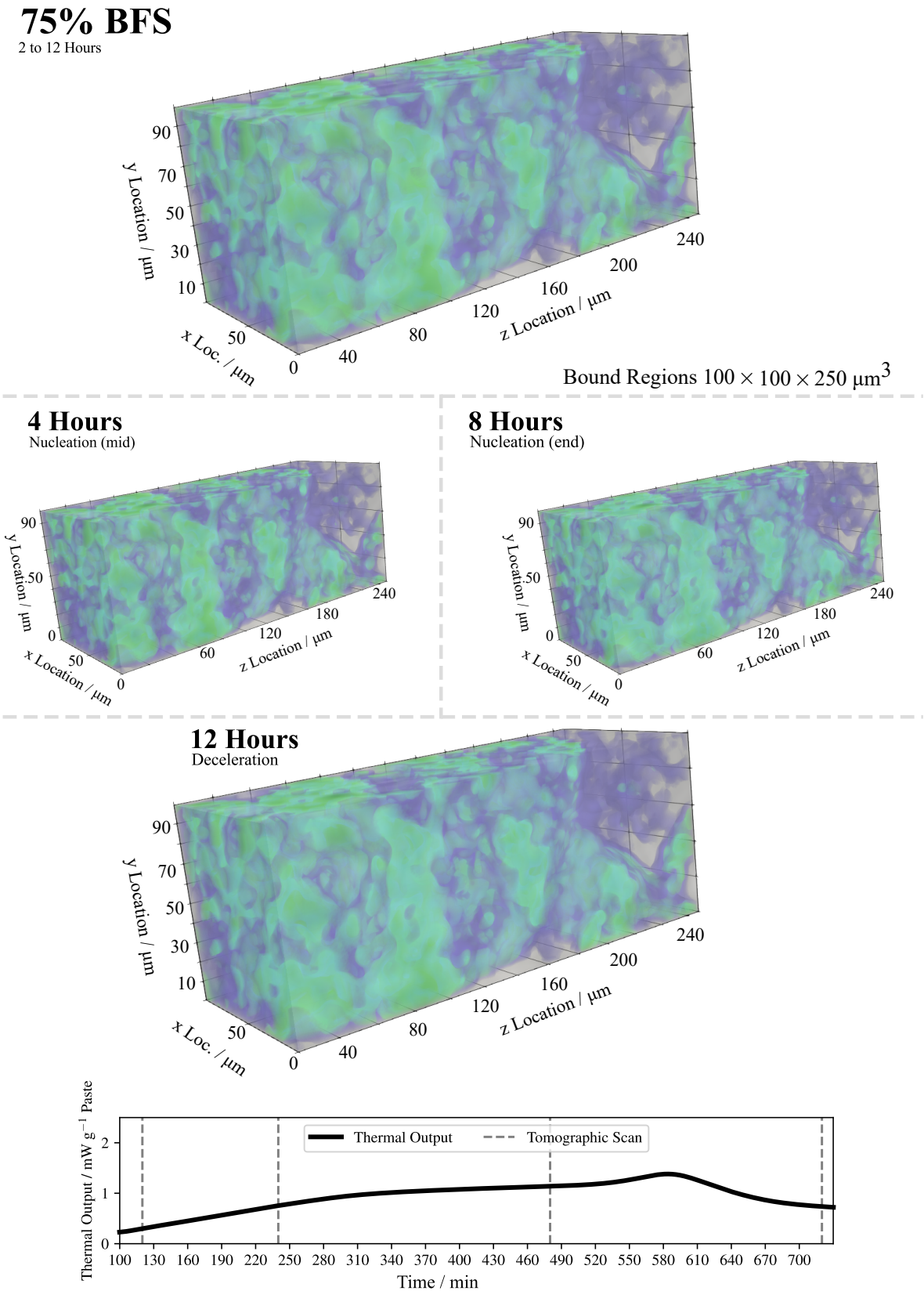


Figure 5.19: he precipitation of materials (purple) and the pore volume (green) across the remaining 12 hours of the hydration reaction. The material is substituted with 75% BFS.

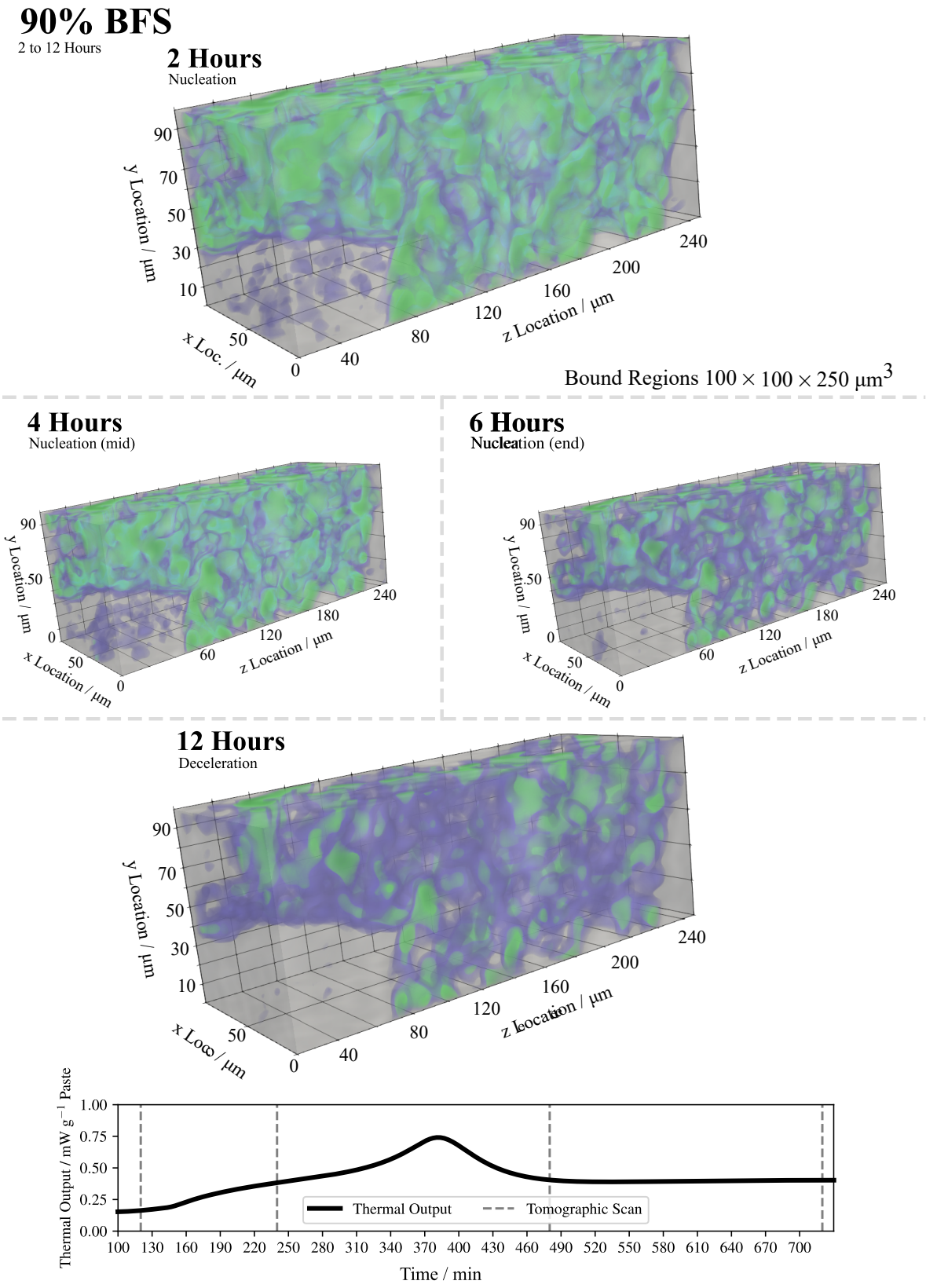


Figure 5.20: he precipitation of materials (purple) and the pore volume (green) across the remaining 12 hours of the hydration reaction. The material is substituted with 90% BFS.

## 5.9 Conclusions

In-situ microtomography has provided a new insight into the reaction of both Portland cement and blended cements highly substituted at 75% and 90% slag. The morphology and distribution of hydrates within the material across the first hours were revealed by this technique. From the earliest times in the reaction, a narrow barrier is formed upon the surface of the unreacted material. This remains the case for all systems, and most likely results from the early hydration of $C_3S$ and $C_3A$ in the cement clinker and could also be a result of dissolution from or the formation of variations in the surface during early hydration.

Precipitates ceased to form in the dormant period, which was consistent with the theory that the controlling mechanism in the dormant period is the rate of dissolution, as shown by A. Bazzoni [236]. The end of the dormant period remains somewhat unclear, and cannot be fully observed by the technique shown here due to the limitation in spatial resolution of the instrument.

Set of the material occurs as a result of interlocking of particles in the material by the expansion of hydrate products. This happens during the acceleration period between four and 12 hours, though the full potential strength of the binder is not met. The pore structure shows reduction in volume and an increase in tortuosity as hydrates fill the volume. This is a result of surface growth and the agglomeration of precipitates on the wall of the pore, and this contributes to the hydrate volume in the final acquisition.

These results show that between eight and twelve hours the BFS reacted in small amounts in the high volume blended cements studied here. Small amounts of surface retreat and the consumption of slag particulates was shown, though it was not possible to identify precisely which phase was represented by which anhydrous volume, due to the overlapping greyscale intensity of these materials which was significant, and this remains an assumption based on the statistical probability of the isolated volumes being slag or cement.

The reaction slowed alongside the thickening of hydrates upon the surface of clinker grains. The accessibility of the anhydrous material to water was reduced, which lowered the rate of hydration. Interlocking of the hydrates also occurred as a result of the outward expansion of these products. Hydrate volumes connect with one another and increased the microstructural rigidity.

In the future this research could be further extended to observe the precise nature of the surface of the material, apply the technique to other supplementary cementitious systems, or study systems where the activator of the slag is some other alkali. In the case of this

experiment, the spatial resolution of the camera for in-situ testing of the PC was lowered to increase the volume of data which could be acquired without filling the buffer. It may be a better idea to use a higher resolution and reduce the time-step to decrease the voxel size and potentially increase the spatial resolution of the acquired data.

Finally, similar materials are likely to come into further use as low impact cements become more desirable in the construction industry, and also importantly as binders for the encapsulation of more troublesome waste products [239]. The study of these will inevitably also be of interest.

# Chapter 6

# Evolution of the Porous Volume

In this thesis, microtomography has previously been used to reveal the morphology and distribution of hydrates within the material in Chapter 5. The technique has provided direct imaging of the reacting microstructure and shown the morphological formation of hydrate phases within the first hours of the reaction. The formation of minor volumes of hydrate within the first minutes, which appears as though it may be linked to the induction period, has been shown. The pore volume then continues to initially fill as a result of the transport of precipitates and the deposition of surface hydrates on the unreacted clinker materials.

Beyond the initial, rapid, thermal output, far more gradual changes to the microstructure occur across a long duration [165] which are more difficult to observe in-situ. The chemistry of the hydrate products in aged samples of systems substituted with BFS has been well characterised by alternative techniques by, for example, Richardson [240].

Using a more traditional method, typically one such as mercury intrusion porosimetry (MIP) or Brunauer–Emmett–Teller (BET) theory, to characterise the pore structure is fraught with assumptions regarding, for example, the resistance of the material to fracture due to the high intruding pressure [10]. The limitations of this and assumptions made in the processing of data from this technique are further discussed in the literature review in Chapter 2. For example, ink-bottle pores result in significant skewing of the pore-size distribution toward finer porosity in samples analysed this way [71].

Perhaps the incorrect analysis of ink-bottle pores might be avoided should sequential slices through the entire depth be considered by serial sectioning of the microstructure, though the sectioning of the sample is time consuming and alignment of the image stack also challenging [241]. Using microtomography this may be carried out on a slightly longer length-scale than achievable by an electron microscope, though it is demonstrated here that this is still sufficient to observe capillary porosity within the specimen. By sectioning the sample situations where a narrow entry is observed and a wider pore is located below be-

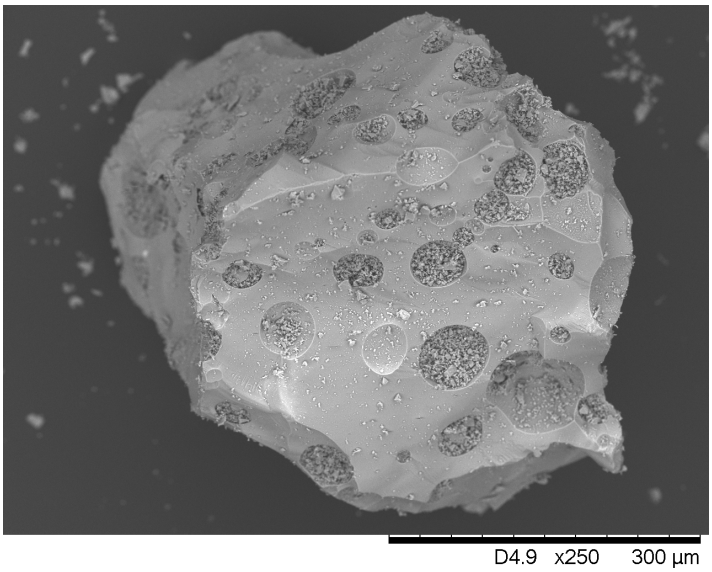


Figure 6.1: A micrograph of a large particle of blast furnace slag (BFS) contained within the Hanson REGEN BFS product, captured on a Hitachi TM3030 scanning electron microscope.

come less problematic; each diameter is assigned to the correct diameter bin as there is no assumption of pore shape or uniformity made by the Washburn equation [9].

Should the slag not fracture or the volume be otherwise inaccessible, pores held within the volume of the slag material will be invisible to mercury porosimetry. Should sufficient surface retreat occur across the life of the material, which in the context of nuclear waste is likely to be thousands of years, these may become accessible to the surrounding volume. These most certainly make up a considerable portion of the observable volume if the specimen is correctly sectioned: see, for example, the micrograph and segmented slag particles in Figures 6.1 and 6.2 respectively. A large amount of the particle surface clearly consists of a small angular pit-like geometry from the entrapment of air or steam during granulation of the slag, which are revealed to the surface by the subsequent grinding. Logically, it follows that gas is trapped within. This is indeed the case; the interior of large slag volumes is clearly porous and shown in Figure 6.3. To an extent neglecting these pores is perhaps misleading. Some of these pores partially fill and air becomes entrapped (Figure 6.3).

In this chapter, tomographic data are analysed with the aim of revealing the pore size distribution and total pore volume using automated image segmentation, and shows a good agreement with alternative techniques carried out in this thesis. This leads to a direct observation of the pore volume within the microstructure and eliminate the ink-bottle effect from larger length-scale pore volumes. The pore size distribution is calculated as the system ages,

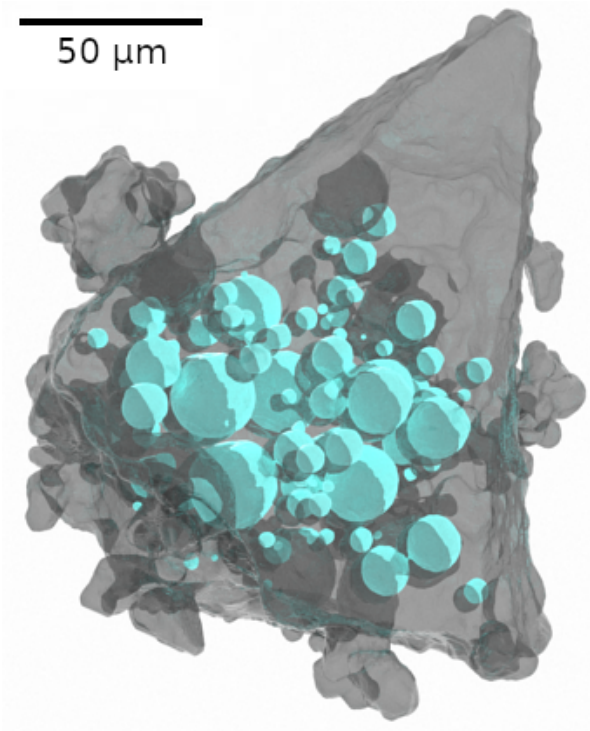


Figure 6.2: Slag voids contained within a particle of BFS. Internal voids are shown in turquoise while the particle geometry is shown in dark gray. Segmented with ITK-snap [242] and ray traced.

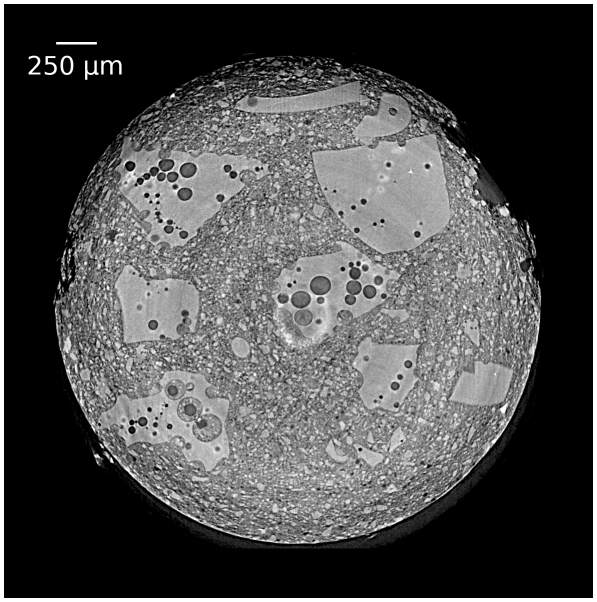


Figure 6.3: A slice in a tomographic stack showing porosity trapped within the solid slag grains that are embedded within the hardened cement.

showing the in-filling of the volume by the reaction of anhydrous materials and the reduction of porosity in the fine range as a consequence of this.

## 6.1 Imaging the Samples

Here, as in Chapter 5, imaging was carried out using the 2-BM beamline at the Advanced Photon Source which provided both a rapid capture rate and the spatial resolution required to observe porosity on the length scale desired [243].

Before arrival at the beamline samples were blended to the specified degree of substitution at a water-cement ratio of 0.35 in a rotary mixer with the exception of the PC which was neglected for this study due to data volume requirements. Details of the samples are given in Table 6.1. Samples to the age of 28 days were cast in a polytetrafluoroethylene block bored with 3.0 mm diameter hole with tape sealing the base. These were wrapped in plastic and cured sealed to the environment, but with no addition of water. Samples of an age of one year were cut from larger volumes of cement cast in 25 mL centrifuge tubes using a low speed saw, again, cured sealed. No demoulding agents were used for either sample type. Paste was compacted on a vibrating surface before the block was sealed from the environment to remove entrapped air.

Table 6.1: Paste formulations for pore structure characterisation.

| | Sample Age / day(s) | | | | | |
|---|---|---|---|---|---|---|
| Material | 1 | 3 | 5 | 7 | 28 | 25 Years |
| 75% BFS | ✓ | ✓ | ✓ | ✓ | ✓ | |
| 78% BFS | ✓ | ✓ | | ✓ | ✓ | ✓ |
| 90% BFS | ✓ | | ✓ | ✓ | ✓ | |

Samples were prepared and cured at ambient temperature for the required duration before being demoulded using a 2.5 mm blunt rod. Hydration of all specimens was arrested by quenching in isopropyl alcohol for 15 minutes, regardless of the age of the specimen to ensure consistency in the analysis. Samples were placed within a vacuum desiccator before being shipped to the instrument. Arrest of the hydration reaction here was necessary due to instrument scheduling.

### 6.1.1 The Instrument

The configuration of the instrument was very similar to that shown in Figure A.3. The top of the adjustable stack was replaced with a Kapton sample holder which restrained the specimen within the beam. A PCO.edge scientific charged metal oxide semiconductor (sCMOS) camera acquired 1500 projections as the sample is rotated through 180°. The output resolution of the camera (1950 × 2180 px.) and 7.5× magnification objective lens yields a voxel size of 0.875 $\mu$m per voxel which was easily sufficient to observe the capillary pore volume. A radiographic series was acquired in approximately two minutes which was discharged immediately to disk in the HDF5 format ready for reconstruction.

### 6.1.2 Reconstruction

Similarly to the method provided in Chapter 5, data were reconstructed by the Fourier grid reconstruction method [76] for rapid implementation and code debugging. The reconstruction was implemented in Python using the Tomopy module [219], and code describing the reconstruction is provided in Appendix C. Reconstructed images were written to storage as a 32-bit tiff stack which was left uncropped for data storage due to the lower volume than that presented in Chapter 5. Here each stack required merely 48 GiB of storage.

### 6.1.3 Segmentation and Rendering

Segmentation of data is the final step in the production of results and is possibly the most challenging. Thresholding the image is the most simple and ubiquitous of segmentations and is simply a cut-off or clip function. Its simplicity leads to some significant drawbacks. Minor adjustments in the threshold value yield a large variation in the observed result. This makes reproduction difficult. A statistically based method has been proposed [232] and used in the literature [90], and is the method used here. This allows us to segment by an identical methodology for each isolated slice in each sample analysed even in cases where a shift in beam current results in a change in the grayscale intensity of the specimen.

### 6.1.4 Extracting the Porous Volume

The segmentation of size distributions was implemented in Python by the scikit-image module [226] which is shown in Appendix E[1]. Due to a requirement for a large volume of random

[1]Porosity resulting from shrinkage cracking is not accounted for by this method.

access memory (RAM), data were processed slice-wise and memory is freed on each iteration. This also prevents regions of beam hardening influencing the threshold value for the entire sample volume if these are not correctly accounted for in reconstruction.

Each slice was first cropped to remove extraneous air surrounding the specimen. Clearly this volume would produce an entirely incorrect overestimation of the pore size. The stack was inverted to show porosity as a low grayscale intensity and particulate as high for visualisation. This yielded an image similar in appearance to those acquired on a scanning electron microscope [217]. A histogram was produced for each slice, with a typical histogram shown in Figure 6.4. The points at which data are thresholded are additionally shown on the figure. The transition point method [90, 232] was used to isolate the pore volume from the stack with additional confidence provided by segmentations of volumes of known porosity. Each 32-bit slice was binary-thresholded at the calculated cut-off, and the morphological volume appended as an 8-bit integer to a three dimensional array. The original slice was then freed from RAM.

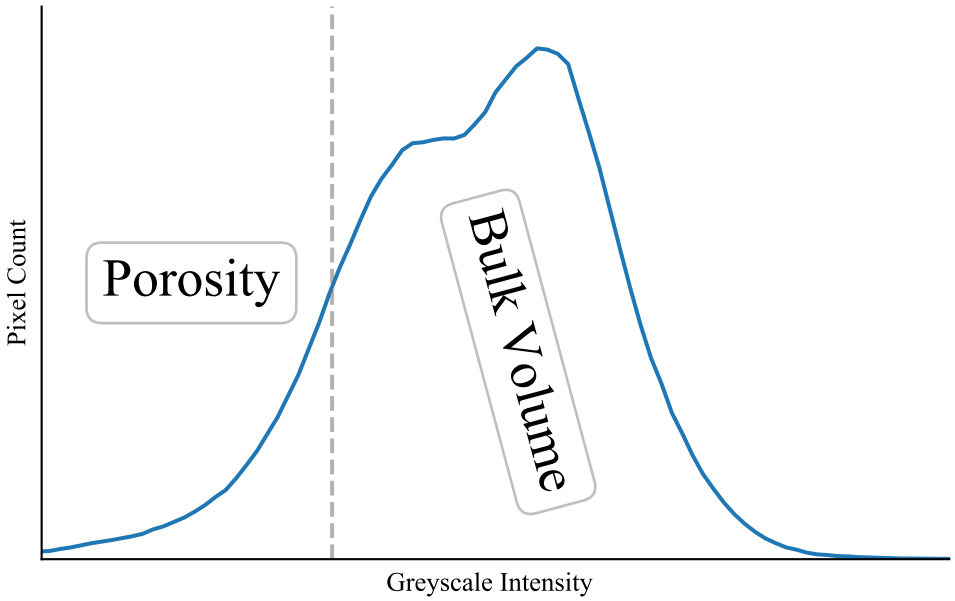


Figure 6.4: Typical histogram segmentation to observe the pore volume of the specimen.

As a first step the total volume of non-zero elements (elements which are positively identified as porosity) in the array is determined and used to calculate the volume of the morphological phase. This may also be carried out using the cumulative histogram, though this yields the same result and so is neglected here.

### 6.1.5 Generating a Size Distribution

The stack was then once again iterated through, and each pore region assigned a unique identifier within the volume in each slice. Typically in the range of $10^5$ individual regions were identified as porosity in each slice. The properties of each region was determined. The diameter was approximated by calculating the diameter of a circle of equal area; it was assumed here that pores are spherical in nature, though this was simply a best approximation and not entirely the case. This eliminated the ink-bottle effect in wider diameter pores; regions which widen below a narrow entry were binned correctly to the observed diameter.

A histogram distribution of volumes and diameters was then produced. This included the diameters of *all* regions in the isolated volume, including those which are found abundantly within the slag itself, regardless of how interconnected to the remainder of the volume these may have been.

## 6.2 Rendering and Visualisation

Rendering is carried out using the Python interface to the ParaView package. The stack was segmented by binary thresholding as per Section 6.1.4. The binary threshold was applied to directly segment these from the stack. The stack was visualised and sliced through to reveal the pore volume within in the context of the surrounding matrix and internal slag voids, where applicable. The shown volumes were segmented at random from the stack depth, which is analysed as a whole; these simply show examples of the analysed volume and not the whole.

The rendered pore volume showed a dispersed capillary structure spread fairly uniformly throughout in all samples apart from regions which are located within the slag, which are entirely spherical in nature. The volume also appeared to be fairly well interconnected. This appeared to be large, perhaps larger than that suggested by the quantified volume, due to the dispersion of the identified volume and variable spatial position which these occupy. The result was a volume which is challenging to observe unless via a direct quantification. Pore volumes within slag particles were also found in these materials and, except for a few isolated cases, these appeared to be entirely disconnected from the slag surface.

Table 6.2: Pore volume statistics. The standard deviation represents the slice-wise variability through the depth of the specimen.

| Composition | Age | Porosity / % | Standard Deviation / % | Standard Error / % |
|---|---|---|---|---|
| 3:1 (75%) BFS | 1 day | 12.7 | 13.8 | 0.32 |
| | 3 days | 9.8 | 8.6 | 0.20 |
| | 5 days | 9.4 | 6.9 | 0.16 |
| | 7 days | 8.0 | 4.9 | 0.11 |
| | 28 days | 7.3 | 4.3 | 0.11 |
| | 360 days | 7.1 | 1.6 | 0.04 |
| 3.44:1 (78%) BFS | 1 day | 14.4 | 11.6 | 0.27 |
| | 3 days | 13.7 | 12.2 | 0.28 |
| | 7 days | 11.8 | 11.1 | 0.26 |
| | 360 days | 5.9 | 2.0 | 0.05 |
| | 25 years (1) | 6.4 | 2.0 | 0.05 |
| | 25 years (2) | 7.3 | 2.1 | 0.05 |
| | 25 years (mean) | 6.9 | - | - |
| 9:1 (90%) BFS | 1 day | 18.7 | 17.3 | 0.40 |
| | 5 days | 13.8 | 9.5 | 0.20 |
| | 7 days | 10.3 | 10.8 | 0.25 |
| | 28 days | 7.8 | 5.6 | 0.13 |
| | 360 days | 5.6 | 1.2 | 0.03 |

## 6.3 Characterisation of the Pore Volume

Quite clearly, the next logical step once the volume had been rendered was to determine the total total pore volume, which is perhaps the simplest property to characterise. The pore quantified pore sizes are summarily provided in Table 6.2. The response of the pore volume to time evolution of the microstructure is shown in Figures 6.5 (render), 6.6 (quantified), 6.7 (render), 6.8 (quantified), and 6.9 (render) 6.10 (quantified) for the 75%, 78% and 90% BFS materials respectively. The standard error is also shown, though this tends to be low due to the high total count of characterised slices, and may be neglected. If the thresholding is incorrect there may be potential for a larger systematic error but this is not assessed here.

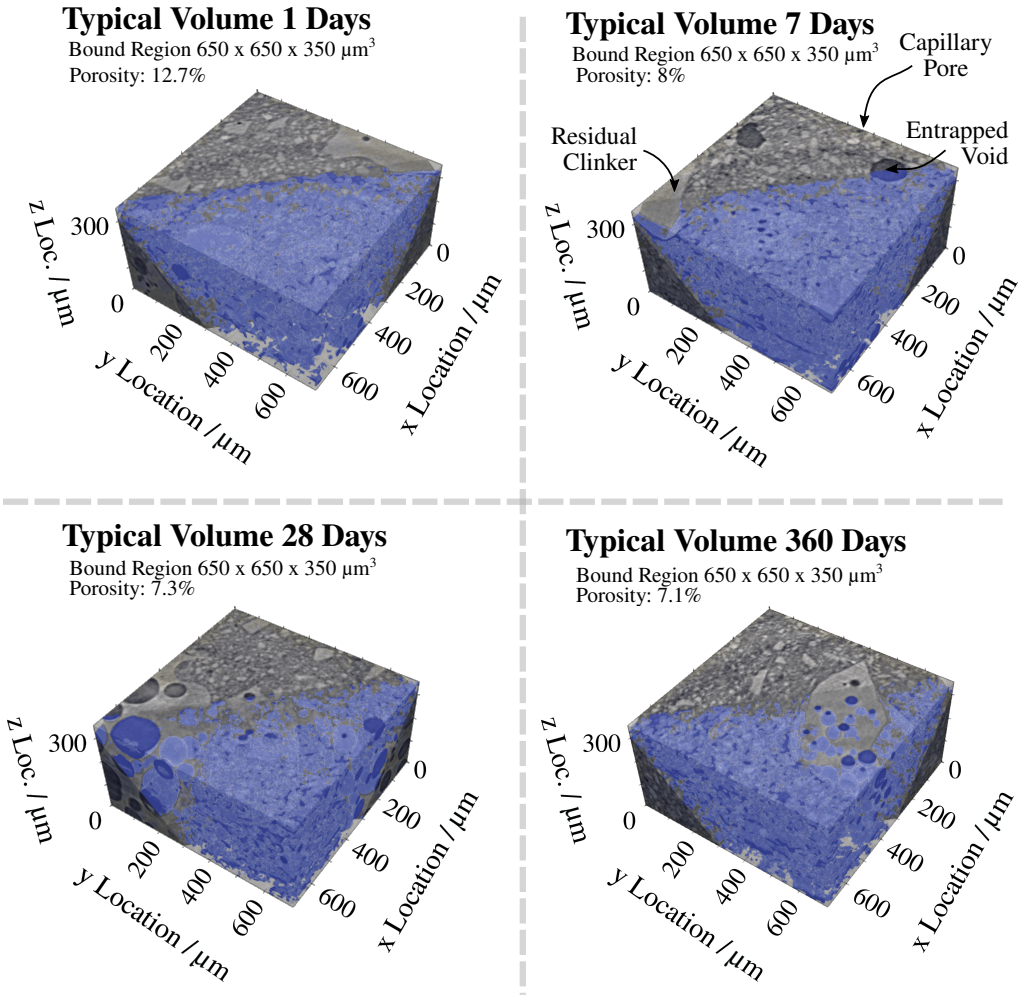


Figure 6.5: The pore volume (blue regions) of the 75% BFS material at the times identified. Air voids are generally entirely spherical, commonly found within the slag, and contain only entrapped air. Water filled voids may also exist in the specimen.

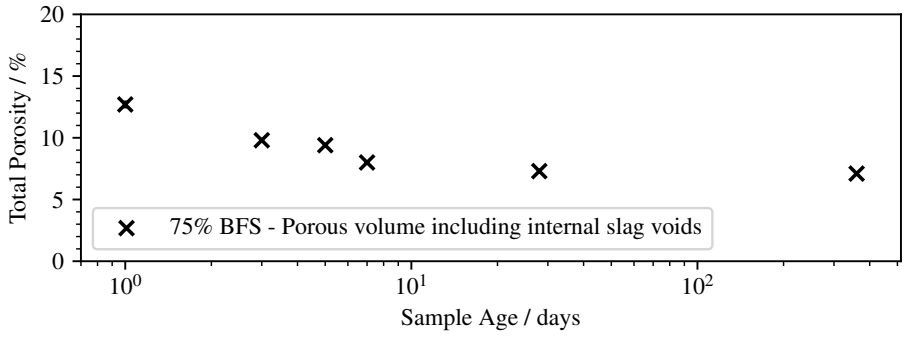


Figure 6.6: The time resolved pore volume of the 75% BFS material.

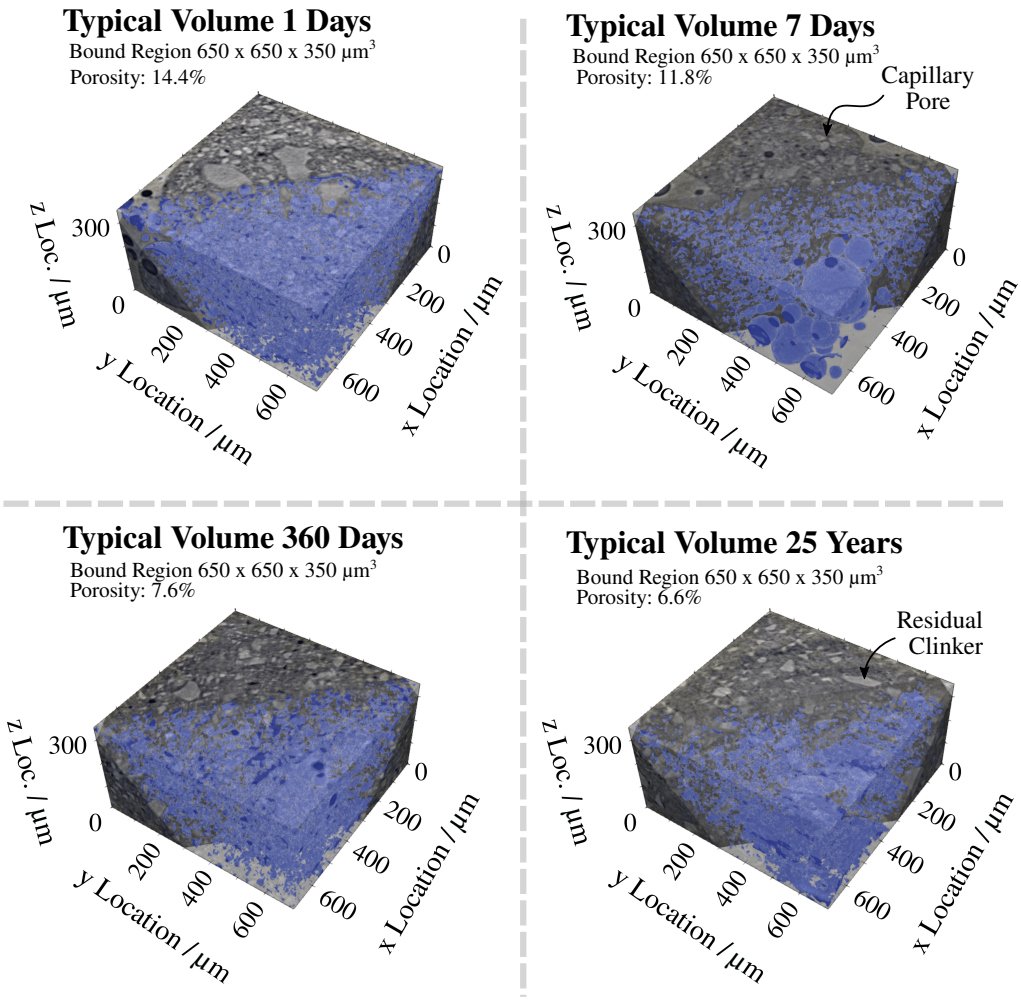


Figure 6.7: The pore volume (blue regions) of the 78% BFS material at the times identified. Air voids are generally entirely spherical, commonly found within the slag, and contain only entrapped air. Water filled voids may also exist in the specimen.

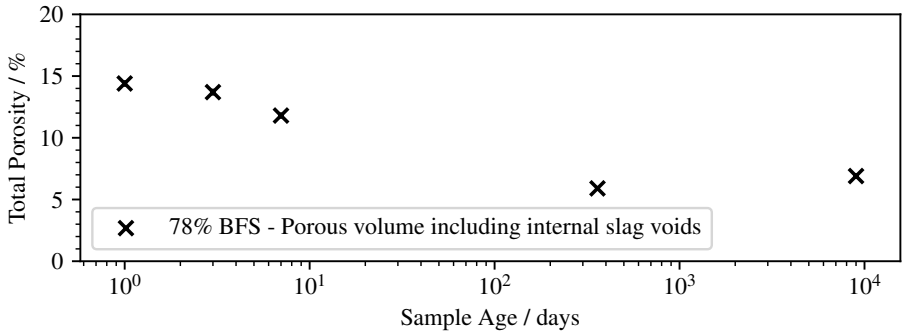


Figure 6.8: The time resolved pore volume of the 78% BFS material.

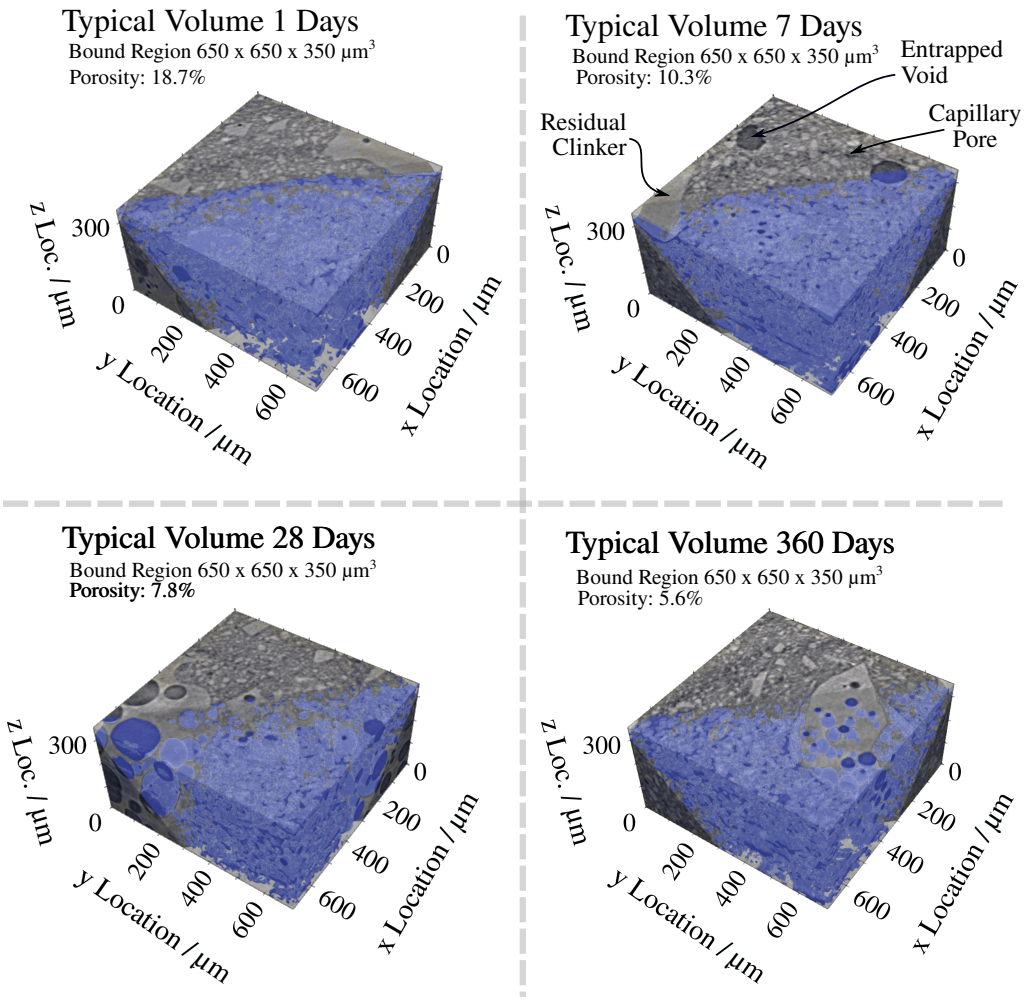


Figure 6.9: The pore volume (blue regions) of the 90% BFS material at the times identified. Air voids are generally entirely spherical, commonly found within the slag, and contain only entrapped air. Water filled voids may also exist in the specimen.

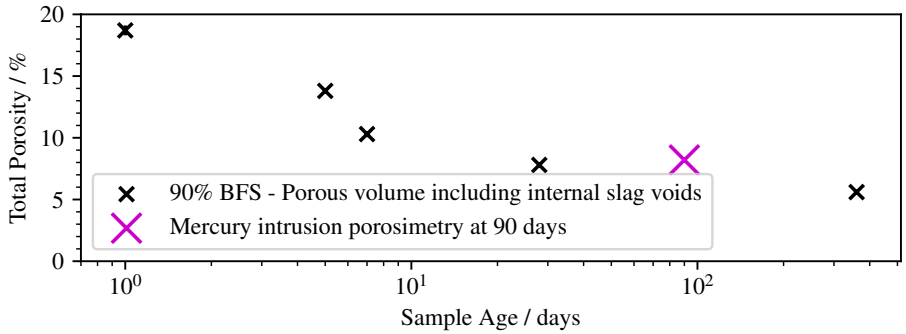


Figure 6.10: The time resolved pore volume of the 90% BFS material.

## 6.4 The Pore Size Distribution and Time

The size distributions of pore volumes calculated as per the method described in Sections 6.1.4 and 6.1.5 are shown in Figures 6.11, 6.12, and 6.13 for the 75%, 78% and 90% BFS blended cements respectively. The portion of each figure marked (a) shows the size distribution of early age specimens, while those over the full time frame are shown in the portion of the figures marked (b).

A significant decrease in pore volume was shown as the sample hydrates. The most dramatic decrease in volume occurred across the first 5 days of the hydration reaction as fine particulates react and free water becomes bound to the microstructure and progressively more inaccessible to the anhydrous material. Some samples may have lost water to the atmosphere surrounding the specimen, which is more likely to have occurred in small diameter samples cast in the PTFE block which were sealed into a plastic bag. The results here showed good agreement with the calculation of the pore volume by alternative imaging methods (Chapter 7). A summary of the pore volumes calculated by all techniques is reported in Chapter 8, which includes a brief discussion as to why slight variations are observed between these tests.

Beyond 28 days the reduction in pore volume dramatically slowed, and eventually converges on a low porosity between 5% and 7%. The porosity in the most highly substituted material, while remaining high across the initial duration of the reaction, eventually reduced to the lowest value of all three samples. This the longer duration reaction of the slag having a dramatic effect on the microstructure. The slag also contains a slightly higher volume of very fine particles which is shown in Figure 3.2 which contribute to the in-filling of the porous volume with hydration product. The reaction is evidently far slower, though in spite of this the porosity decreases extensively by 360 days, and surpasses even that of the material substituted with slag to a lower degree after 25 years. Across the long duration, the very slow reaction of the large slag mass fraction has allowed the material to exhibit a reduced pore volume, and the substitution of this material almost certainly provides a final product with a significantly improved durability, especially at higher degrees of substitution. This will be looked at in more detail in Chapter 7.

In Figure 6.10 the volume determined by mercury intrusion porosimetry matches with the trend, with only a minor variation. This was a result of the slightly different length scale on which the pore volume is observed by the technique. The space contained within the C-(A)-S-H hydration product (or any other product which might be porous) could not be identified using tomographic imaging as the spatial resolution is insufficient to resolve these volumes. This is not the case with the mercury porosimeter which uses such a high

pressure that even the pore volume down to a few nm in diameter was observed. However, as mentioned previously, this may result in destruction of the volume and so data acquired by pressurising the sample may be unreliable to begin with [10]. Moreover, these techniques used fundamentally differing methods to analyse these materials, and as such it was not necessarily possible to draw a direct comparison and conclude that one is necessarily superior to the other.

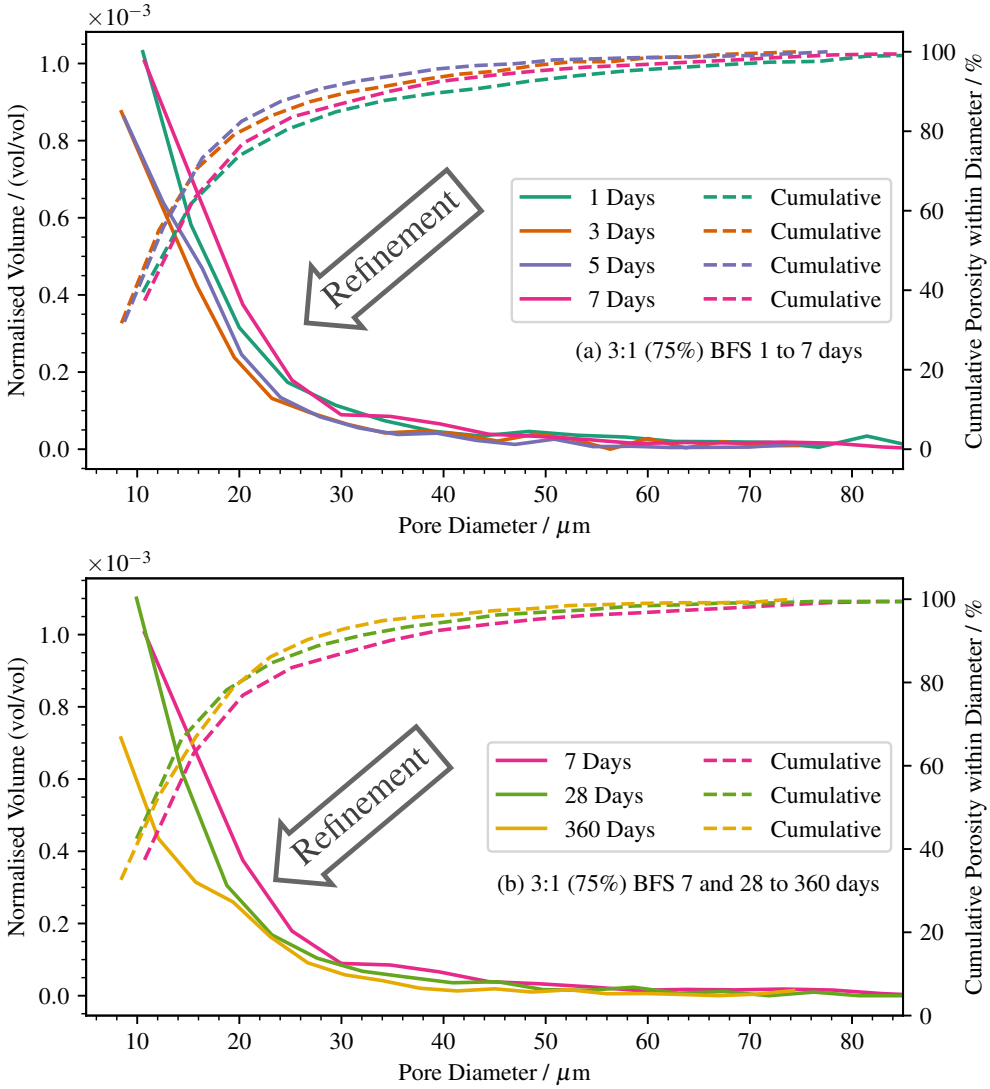


Figure 6.11: The pore size distribution in the 75% BFS material up to 7 days (a), and 7 days to 360 days (b).

While in reality the instrument is hypothetically able to observe a pore down to 0.875 $\mu$m in diameter should the spatial resolution and voxel size be equitable, the realistic cutoff for these is found between 6 and 10 $\mu$m only where voxels are grouped together in a sufficiently

high volume. Very fine capillary porosity has filled in as a result of the formation of hydrate product in the matrix which expands into the voidage resulting from the inability of particles to fully interlock. Porosity present in the C-(A)-S-H is not observable at this spatial resolution, and attempts at characterisation on the required length scale may be made by alternative techniques such as BET and MIP. Although the quoted voxel size provided by the instrument was fairly high for fast microtomography (875 nm), these regions appear to merge with hydrates and do not contribute significantly to the volume as the actual spatial resolution lies at a higher value.

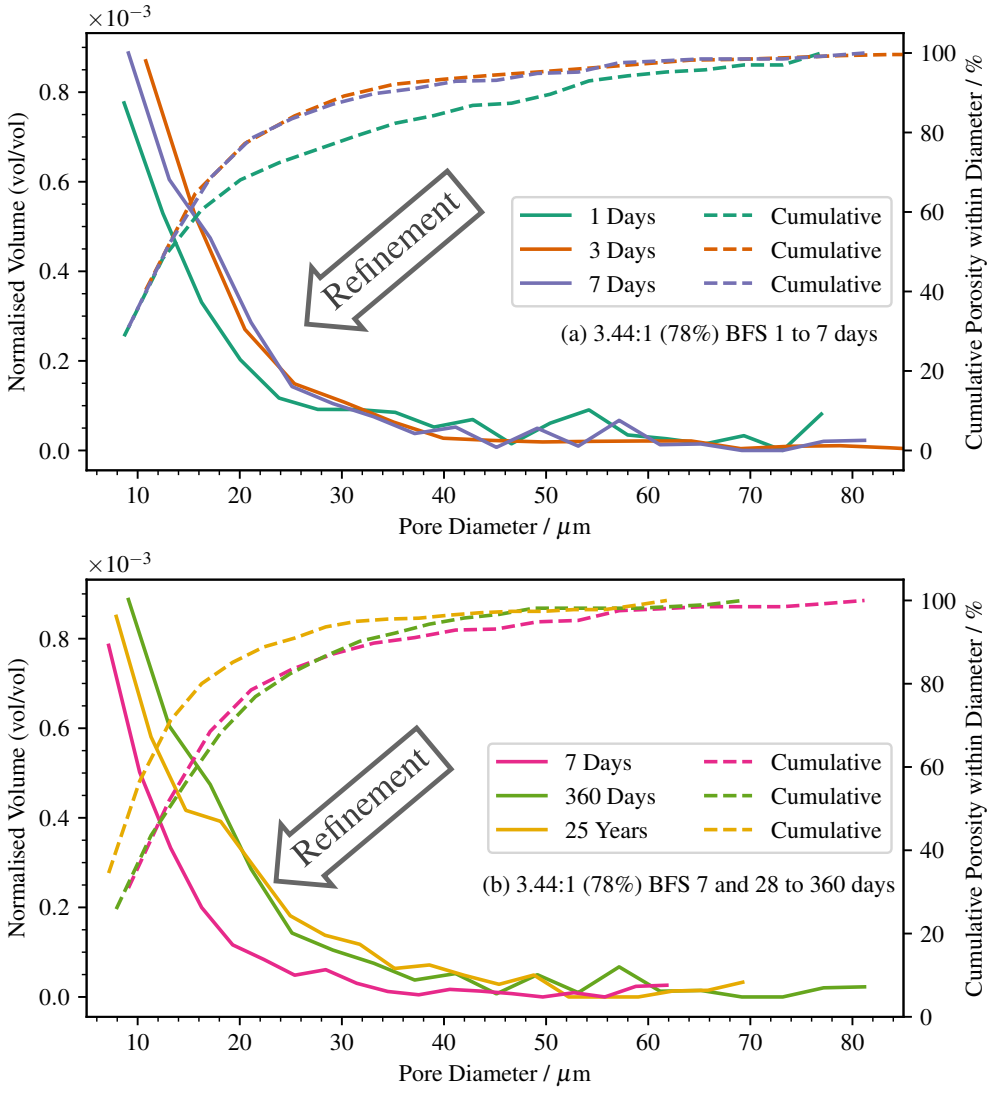


Figure 6.12: The pore size distribution in the 78% BFS material up to 7 days (a), and 7 days to 25 years (b).

It might be expected that the pore size distribution would skew toward finer porosity as the hydration reaction progresses and voids become in-filled with hydrate product. This was generally the case, with a few exceptions resulting from specimen variation. A larger sample set is required here, though a limitation in data storage and collection time results in this being challenging.

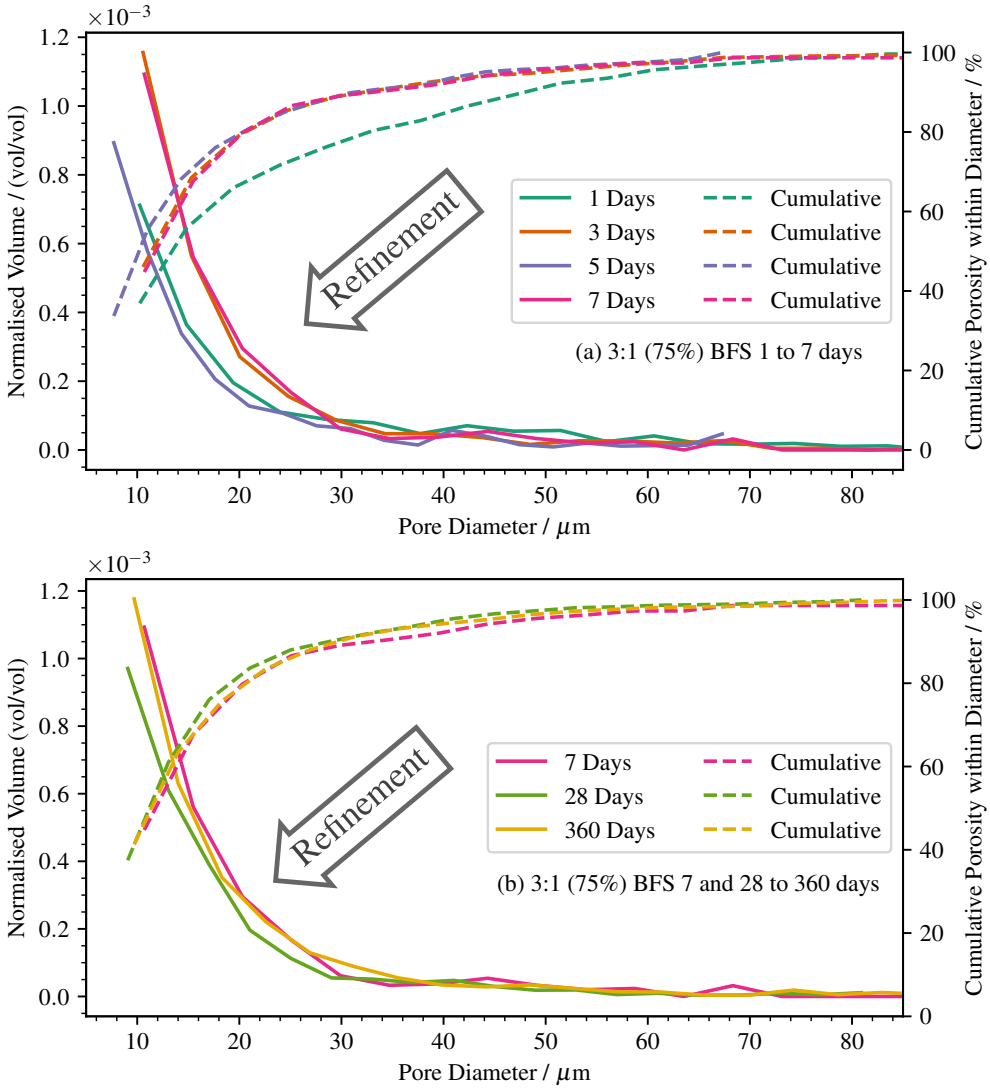


Figure 6.13: The pore size distribution in the 90% BFS material up to 7 days (a), and 7 days to 360 days (b).

Infilling occurs initially by the refinement of porosity from a coarse toward a fine structure [53] and the volume reduces [244, 245]; large pores appear to be filled initially which results in a shift at the wide diameter pore volume toward the fine. This is exhibited by two regions on the figure. The maximum pore diameter observed within older specimens reduces, and

in certain cases does so significantly. Take for example the 75% BFS material shown in Figure 6.11(b). The maximum diameter observed by the analysis has reduced from 85 $\mu$m to 72 $\mu$m by 360 days. Wide volumes are in-filled with C-S-H and portlandite during the hydration reaction. The volume of porosity within the specimen reduces, which will have been matched by an increase in tortuosity, which is observed in unblended Portland cements [90, 91]. This, however, shows a high variation which is almost certainly a result of the low number of samples.

## 6.5 Conclusions

Here the distribution of pores and the total volume of porosity contained within the matrix have been determined using a combination of X-ray microtomography and image analysis, and have shown good agreement with alternative techniques used elsewhere in this thesis (Chapter 7).

The pore volume is highly dependent on both the degree of substitution and the degree of hydration of the material, the latter of which was not explicitly characterised here. Once again the results showed the closeness in composition of the 75% and 78% BFS materials, which was also observed this in the chemical analysis performed in Chapter 3, and so is somewhat expected from these results. The inclusion of the 78% BFS material allowed for a sample to be characterised up to 25 years in age which would not otherwise be possible should this composition have been neglected.

At the beginning of the hydration reaction, samples showed a high porosity due to the lower rate of reaction of the slag, which caused rapid in-filling of the volume across the first 7 days of hydration. This was most prominent in the material comprised of 90% BFS which had a high early-age porosity which rapidly reduces, resulting in a matrix of low porosity. The variation here is attributed to natural variation between samples; a wider array of samples is ideally required for this sort of an analysis, though the data processing requirement and time-limitation for acquisition makes this challenging.

In reality the porous volume in the slag did not account for an enormous amount of the total porosity, and does not significantly appear in the pore size distributions shown in Figures 6.11, 6.12, and 6.13.

The pore volume reduces rapidly across the first days of the reaction and a significant decrease in volume is observed all the way through across the first 360 days. The reduction in volume then slows. Free water has been either consumed in the reaction or has left the matrix by another process. Water has likely been removed from the matrix as a result of the

reaction in all cases aside from the 25 year old sample of 3.44:1 BFS cement; the condition under which the sample was stored was not entirely apparent from historical records. The analysis of this sample ideally requires the analysis of more specimens. This water removal results in a slowing or simply a cease in the reaction. This does not represent full consumption of the cementitious material (see Figure 6.7, where unreacted particles clearly remain visible within the volume).

As infilling of the volume occurs it might be expected that the distribution of pores in the specimen might uniformly decrease toward a finer volume. However, this not entirely the case; a trend toward an increased volume of fine pores is shown here as larger pores become in-filled and and contribute to the volume at a finer diameter. As mix water becomes combined within the material the porosity shifts toward the more refined range and the volume within the fine pore diameter increases. Regions of a wider diameter exhibited a shift toward the finer sizes where the widest pores are located further toward the fine region as the sample ages. The decrease in porosity occurs as a result of both the loss of fine pores and the shift of coarse pores to a more refined diameter.

# Chapter 7

# Neutron Imaging

Having established the chemical characteristics (Chapter 4), morphological process (Chapter 5), and the development of the pore volume over a longer duration, the final part of this thesis aims to study how these characteristics may affect the durability of the binder via the water uptake process. As established in Chapter 2, imaging with neutrons is a technique which allows for the direct observation of this.

By directly imaging a specimen, no assumptions are made regarding the mass of the intruding front or the total saturated volume. The result is a highly accurate dataset from which the geometry of the intruding front, penetration depth, and the moisture content may be directly observed and quantified. Some caveats still result from sample preparation, which are discussed in Chapter 2. As partial (or complete) drying of the specimen is required to observe a moisture ingress front, this is carried out as a necessity.

Here, some restrictions also result from the spatial resolution of the instrument which limits somewhat confidence in the minimum observable pore size. Though the bulk porosity may be determined, the porosity found in the gel phase is not directly segmentable in a pore-size distribution due to this limitation.

## 7.1 Capillary Action

The penetration of moisture into the specimen results from the surface tension and adhesion of water to the surface in a capillary pore; a finer capillary will result in a greater influence of surface tension and a greater rise of water. Capillary action creates a pressure $P$ as described by Equation 7.1, where $r$ is the radius of the capillary (m), or pores in the case of this experiment, and $s$ is the surface tension of water in the capillary ($Nm^{-1}$).

$$P = \frac{2s}{r} \tag{7.1}$$

The pressure $P$ results from the balance of surface tension-driven upward motion, where $P = \rho g h$, Equation 7.2 may be written describing the displacement of water in a capillary $h$, where $\rho$ is the density of water and $g = 9.81$ Nkg$^{-1}$.

$$h = \frac{2s}{r\rho g} \tag{7.2}$$

The distance to which water may penetrate the specimen is limited by the interconnectivity of the structure; a longer distance length results in a higher penetration with lowered restriction. A calculation is given as an example by Claisse [110].

In this thesis, neutron imaging is used to observe water uptake in PC-BFS systems substituted with 75% and 90% BFS, at 28 and 90 days of hydration. Quantification is carried out based on known quantity step wedges. The greyscale intensity of known water content is directly attributed to moisture content in the specimen. The penetration depth of the front is determined from the mean greyscale profile of the specimen.

To begin with, the instrument and technique are described in Section 7.2, while the application of this to a cementitious sample is detailed in Section 7.3. Results and discussion are provided in Sections 7.5 and 7.4 for the two quantifications. Finally, conclusions are given in Section 7.6.

## 7.2 The Radiography Technique

Neutron radiography works on the principle of exploiting differences in the neutron cross sections of differing elements. The cross section is the likelihood of interaction of a neutron with the nucleus of any given atom, and may be thought of perhaps similarly to the attenuation of X-rays in materials of varying densities.

A neutron moderator is an isotope which has both a low mass and a large scatter cross section. The scattering cross section is the barn, which is an area equal to $10^{-28}$ m$^2$, or the cross sectional area of a uranium nucleus.

The likelihood of a scattering occurrence is higher for hydrogen than for calcium and silicon. It therefore follows that water, which has a high content of hydrogen, will cause a greater scattering of incident neutrons. The result is a high imaging contrast between hydrogen containing elements, such as liquid or gaseous water, and the sample itself. A straightforward segmentation is then possible.

### 7.2.1 The NEUTRA Instrument

The instrument used in this portion of the project was the NEUTRA "Neutronen Radiografie" facility at the Paul Scherrer Institute (PSI), Switzerland. The instrument sources neutrons from the Swiss Spallation Neutron Source (SINQ), described in Chapter 3. The NEUTRA instrument is described thoroughly in the literature [131]. A summary is provided here to supplement details of the SINQ facility previously provided (Chapter 3).

The beamline was one of the first to provide a state of the art facility with a large field of view (FoV) for radiographic imaging. The beamline is made up of several integral components and is shown diagrammatically in [131]. An inner collimator is placed within the shield surrounding the lead target system and $D_2O$ moderator tank. A shutter isolates the hutch. At the source end lies an outer collimator consisting of an aluminium tube which is held under vacuum. The acquisition end of the beamline contains the experimental station, which is accessed by a labyrinth and interlocked gate, connecting the control station to the instrument. At the very end of the beamline a three centimetre layer of boron carbide acts as a beam stop.

In the experimental hutch lies a sample positioning device placed close to the end of the guide tube. The positioning device allows the sample to move in the horizontal plane relative to the beam to assist with sample alignment without interference. The energy of neutrons provided to the instrument is determined by the moderator surrounding the SINQ target. The mean energy was measured in the literature at 25 MeV [131]. The outer collimator divides into three parts, with each part being used for a certain purpose based on the collimation, beam diameter, and flux available in that section of the tube. The outer position, used here, provides a beam diameter of 400 mm, and a neutron flux of $3 \times 10^6$ n $cm^{-2}s^{-1}$ [131].

### 7.2.2 Scintillation Reactions

Scintillation is the process of light emission when phosphor is struck by a photon or charged particle. A number of scintillation detectors are commonly used at the NEUTRA beamline. These consist in the most part of charged coupled device (CCD) or charged metal oxide semiconductor (CMOS) imaging sensors coupled to a thin lithium, boron, or gadolinium scintillator similarly to the configuration shown in Figure 7.1. The reactions of materials typically acting as scintillators are provided in Table 7.1. The scintillator interacts with an incident neutron and emits a charged particle, which then interacts with a phosphor screen, emitting visible light. As described in [246] the depth of scintillator relates directly to the spatial resolution of the instrument.

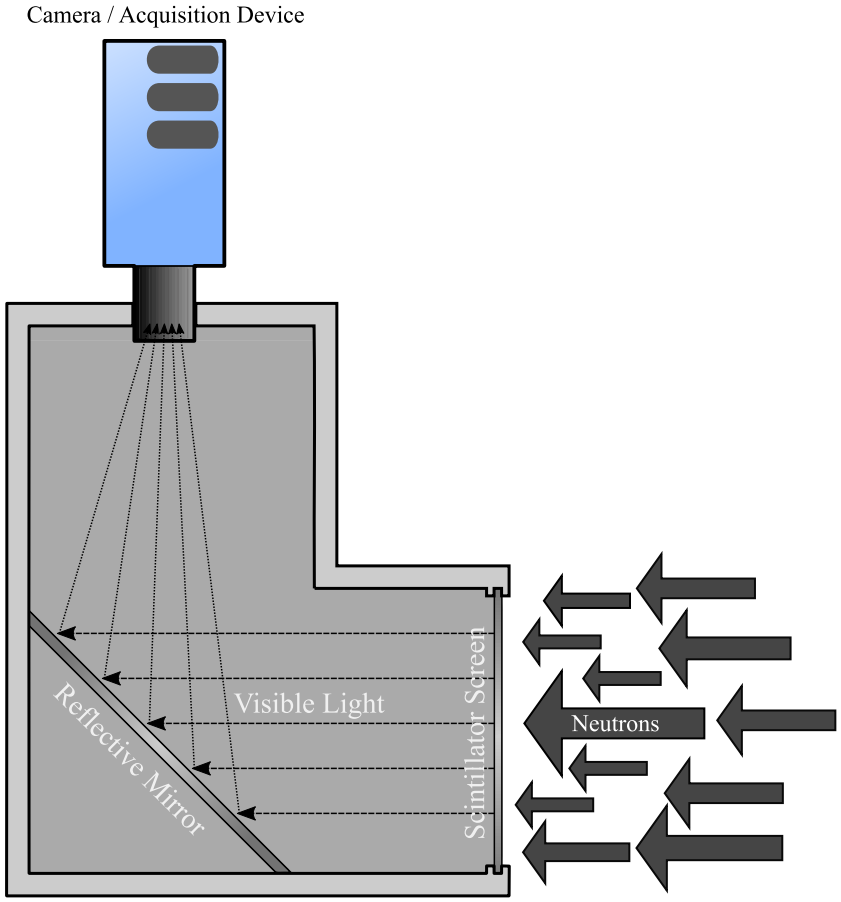


Figure 7.1: The scintillator, mirror, and capture device configuration in the mirror box placed to the rear of the experiment position. In the case of this experiment, a lithium scintillator is attached to a phosphor screen.

Table 7.1: Scintillation Reactions from [246]

| Material | Reaction | |
|---|---|---|
| Lithium | $^{1}n + {}^{6}Li \longrightarrow {}^{4}He + {}^{3}H$ | ( + 4.79 MeV) |
| Boron (1) | $^{1}n + {}^{10}B \longrightarrow {}^{7}Li + {}^{4}He$ | ( + 2.78 MeV) |
| Boron (2) | $^{1}n + {}^{10}B \longrightarrow {}^{7}Li + {}^{4}He + \gamma$ | ( + 0.48 MeV) |
| Gadolinium | $^{1}n + {}^{155}Gd \longrightarrow {}^{156}Gd + \gamma$ | ( + 7.9 MeV) |

### 7.2.3 Scintillator Degradation

Commonly referred to as scintillator "burn-in" is the degradation of the scintillator screen, which is tackled by flat field corrections described in Section 7.3.2. When exposed to the beam current for an extended period of time the scintillator degrades as a result of the reactions provided in Table 7.1. The result is a modification in the intensity of data across the screen which must be mathematically corrected. This correction is carried out in Section 7.3.2.

### 7.2.4 Quantification

It is also possible to make quantitative measurements using neutron radiography results due to the high dynamic range of available detectors. The QNI software package [247] may be used to correct for neutron scattering. Quantification is carried out in this thesis in hardened cementitious samples of selected blended systems by a step wedge calibration (Section 7.3.2) for both simplicity and demonstration of the method. A correction for scattering is made here by data derived from the placement of a borated polymer block in front of the experimental configuration, followed by subtraction of observed scattering artefacts.

## 7.3 Imaging a Cementitious Sample

Samples were first prepared as described in Chapter 3. In this chapter cements were cast to a block from which prismatic samples 40 mm $\times$ 40 mm $\times$ 100 mm were cut using a bandsaw. Samples were cast using two compositions, one of 75% BFS and one of 90% Samples were cured sealed from the environment for periods of 28 and 90 days before preconditioning. Non-bound water was removed from the specimen by oven drying at 105°C for 72 hours. Drying did not noticeably result in cracking of specimens. Once prepared the long edges of samples are sealed with aluminium tape to ensure uni-directional permeation was observed.

### 7.3.1 Configuring the Instrument

The configuration of the capillary suction experiment carried out here is provided in Figure 7.2. A gadolinium scintillator was placed approximately 25 mm to the rear of the sample which was connected via a mirror box to an Oxford Instruments Andor NEO sCMOS camera. The FoV was sufficient to comfortably hold four specimens in place while images are acquired. The instrument was configured with the samples held in the position three which

lies furthest from the guide tube to the rear of the hutch. This resulted in a larger beam diameter at the cost of a very slightly lower neutron flux. The result was a marginally higher exposure time, which here was of negligible importance. The FoV of the instrument is 306 $\times$ 306 mm in this position, which allowed four samples to be observed. The nominal pixel size is 0.1 mm which was easily sufficient for the aim of this thesis. The quoted value by the facility is 0.15 mm, though on measurement of the image this was found to lie closer to 0.1 mm, which was the value taken and used here.

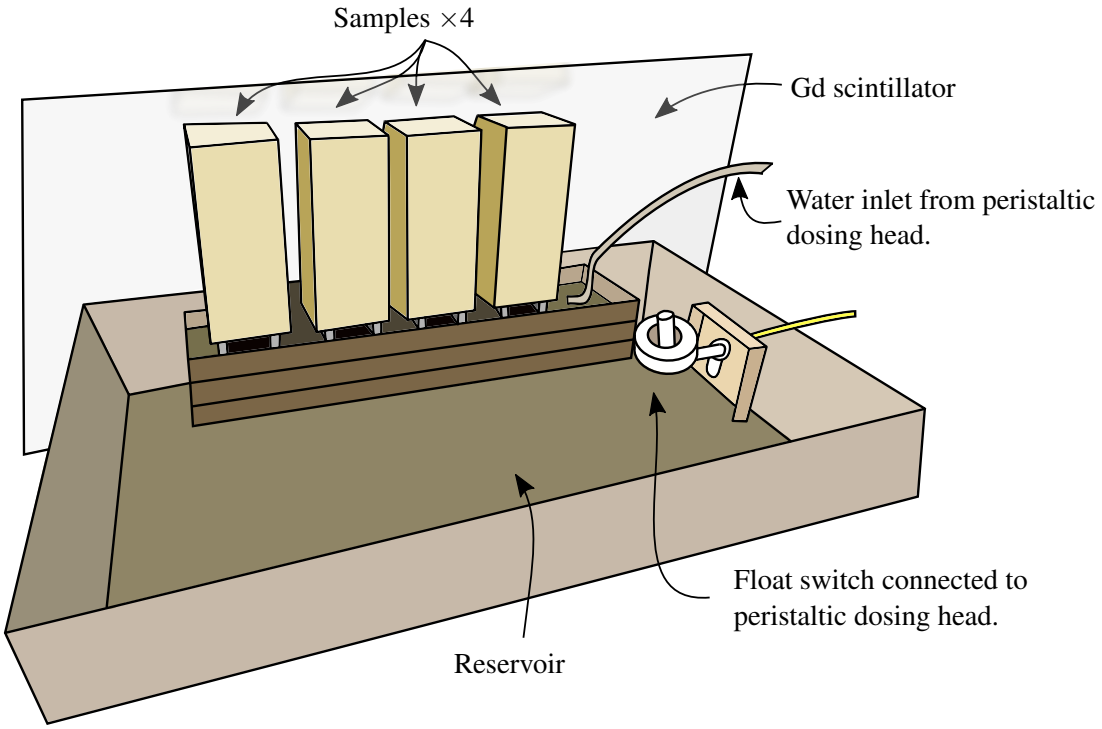


Figure 7.2: The configuration of the NEUTRA instrument.

Samples were placed on narrow aluminium supports attached to the bottom of a tray 60 mm in depth. The tray itself sits on a supporting stack held at the top of a large water container. The bottom of the sample sits approximately 2 mm below the waterline. This allows for uptake to take place with minimal disturbance from the configuration of the experiment, and was in close agreement with the method outlined in ASTM C1585 [8].

Water was supplied as required to the sample by means of a peristaltic dosing head and float switch attached to a small reservoir within the hutch. The dosing head was controlled by an Arduino Uno microcontroller programmed in C++ and a relay to provide isolation of electronics in contact with water from the higher-current supply. The dosing head was triggered when the water level had dropped to slightly above the base of the specimen, which

prevented the sample from running dry at any point during the experiment. A microcontroller was used as it was theoretically possible to monitor the dosing rate of the container during the experiment and measure the moisture uptake of the specimen through maintenance of the level, though it was decided not to carry this out here due to the difficulty in separating the contribution of each specimen in this signal.

Single samples of the compositions previously mentioned were tested due to time restrictions in beamline scheduling. Because of this, no repeat samples were tested. Initially, a dry specimen which had not yet been imaged was placed within the beam and five acquisitions of the sample taken, alongside ten open beam and dark current images. A borated polymer block was placed in front of the sample set and a series of images were taken which allowed for the correction of back-scatter from the mirror and experiment configuration.

Once the block was removed, water was poured into the tray to below the sample level such that moisture uptake does not begin. The hutch was sealed and the peristaltic dosing head activated remotely, allowing the remaining volume below the specimen to fill. An image of the sample was acquired every five minutes with an exposure time of 80 seconds for a total of 24 hours. Data were written to disk at every acquisition and periodically verified during the experiment to ensure correct acquisitions were being taken.

### 7.3.2 Data Processing

Data were processed using the Python code with a detailed description provided in Appendix F. This allows for complete "hands off" batch processing. Firstly all open beam images were corrected for the dark current signal which removes noise artefacts from the image by subtraction[1]. A mean dark current image was used for this, and this accounted for pixels which were repetitively observed as hot spots.

Disk read-write times were isolated from the header in each image. The human-readable timestamps were converted to a UNIX epoch value[2]. This is expressed as an integer for each sample in the experiment. The epoch timestamp for the first scan was then subtracted from the timestamp at each subsequent datum providing the time in seconds relative to the beginning of the experiment. The actual time between each datum was extracted as 5 minutes and 10 seconds. The additional 10 seconds accounts for the disk and camera i/o and was incorporated into the experiment times quoted.

A mean flat field image was calculated from data collected at the beginning and end of the experiment, the dark current having previously been subtracted. The system then iterates

[1]The camera was additionally vacuum cooled to -40°C to reduce heating effects.

[2]Date-time expressed in seconds since midnight on January 1st 1970.

through the stack. In each slice the dark current was subtracted and the image divided by the open beam. The result was then re-scaled by the mean intensity of the open beam data. The data were also corrected for the influence of the dry specimen in the same manner. This isolates the contribution of free water (intruding moisture) from any bound water (hydrates) and hydroxyl groups $(OH)^-$ present within the microstructure.

Each sample was then cropped from the resulting array to enable analysis of each specimen in isolation. For debugging purposes images may be written to disk at this point.

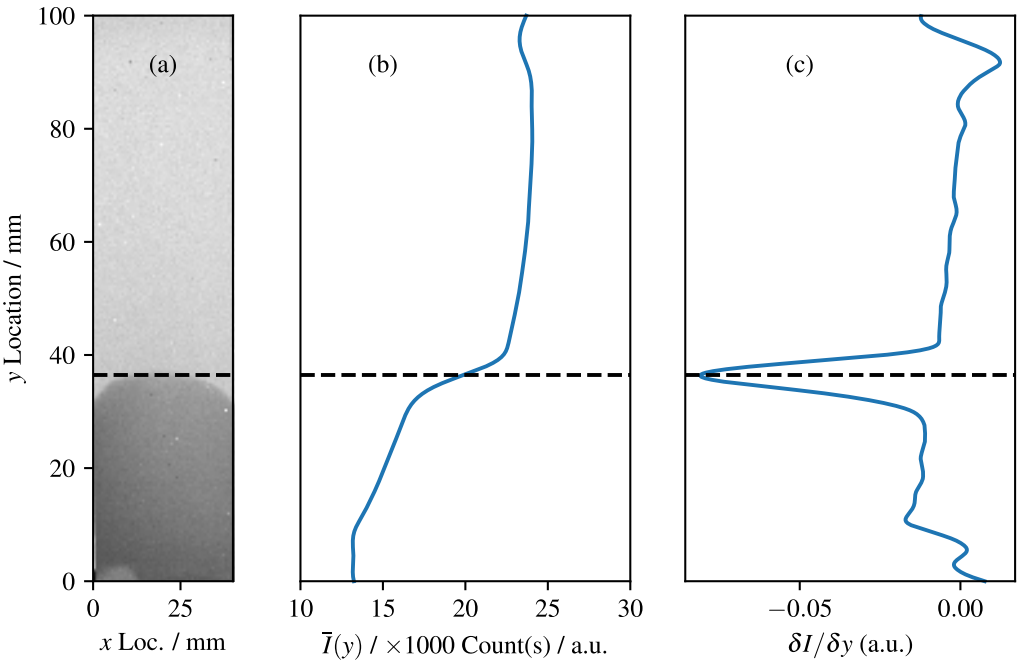


Figure 7.3: The radiograph (a) showing water uptake is integrated in the $x$ direction to give an intensity profile (b); the uptake front is located by identifying the inflection point (c).

### Extracting the Front Location

The intensity of each sample in the $y$ direction was integrated in $x$ to provide mean intensity as a function of $y$, as shown in Figure 7.3(b). The signal was somewhat noisy due to detector artefacts which remain impossible to entirely eliminate. So, the signal was smoothed by convolving a scaled Hann function window of equivalent length 0.5 mm on the data in the $y$ direction [248] (simplified, reproduced in Appendix F), and the resulting profile was re-binned. A first order derivative of the array was taken, which provides the rate of change of intensity with respect to the depth through the $y$ axis. The water ingress front was defined as the location of the maximum in the derivative, which was the point at which the mean

intensity changes from dark to light. Optical verification was carried out in isolated frames to ensure the depth was correctly resolved.

### 7.3.3 Quantifying the Moisture Content

Extraction of the moisture content was carried out by calibration to an image with a known content. A series of aluminium step wedges were placed in front of a specimen which had been prepared for testing in the manner shown in Figure 7.4. These contained a cross section of water with a known depth in a narrow step between 0.5 and 5.0 mm in 0.5 mm steps. Images were corrected for the dark current, open beam, the dry specimen, and scattering as discussed previously. The resulting image is shown in Figure 7.5. The mean grayscale intensity of each step was then calculated.

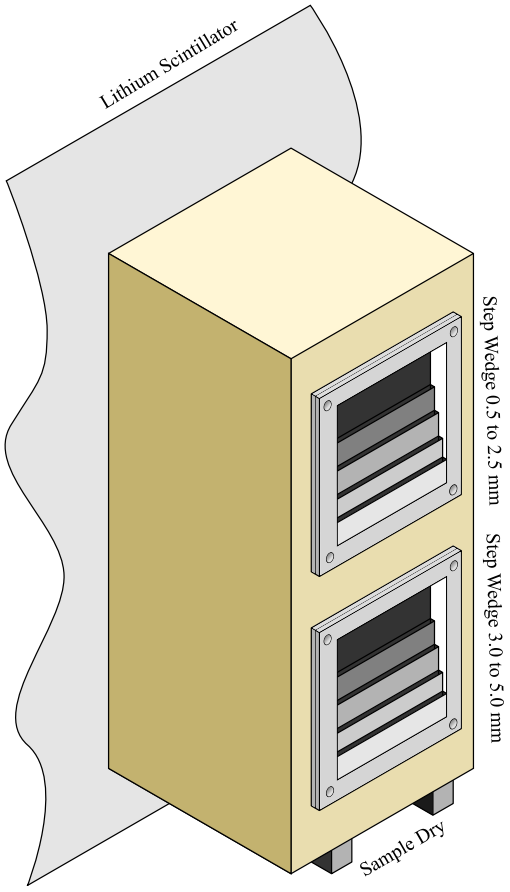


Figure 7.4: Step wedges placed in front of a cement specimen. Water was placed into each step of known depth and an acquisition taken, shown in Figure 7.5. The wedges are aluminium which has a low neutron cross section and were subtracted from the image.

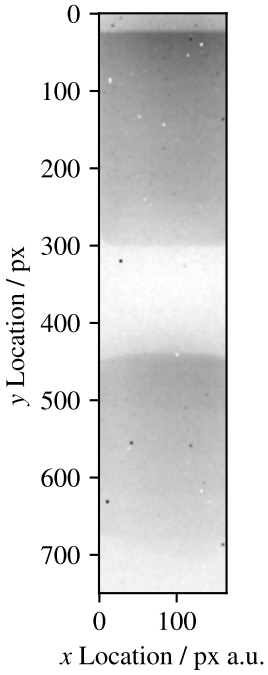


Figure 7.5: The corrected step wedge image. The greyscale intensity reduces where neutrons are scattered in the hydrogen-rich wedges (contrast adjusted for visualisation). The attenuation here is linear to the step thickness.

Figure 7.6 shows the relationship between greyscale intensity and moisture content. The moisture content was calculated by a simple division knowing the thickness of water in-front of the specimen and the thickness of the specimen itself. These results were fitted to a linear function by least squares fitting [249]. Knowing the equivalent pixel size and the specimen depth the moisture content may be directly calculated in each specimen in a single matrix operation.

### 7.3.4 Mercury Porosimetry

In order to provide validation of the quantified porosity by another technique, a 90% BFS material of 90 days age was tested using a mercury porosimeter to calculate the total pore volume of the specimen. The test was repeated twice and a mean volume calculated. It was possible to carry this out upon only a single set of samples due to breakage of the instrument.

For the verification two specimens of approximately 2.4 g were cut from the centre of a 15 ml centrifuge tube. Free water was removed by quenching the samples in isopropyl alcohol to constant mass before drying in a vacuum desiccator for 1 hour.

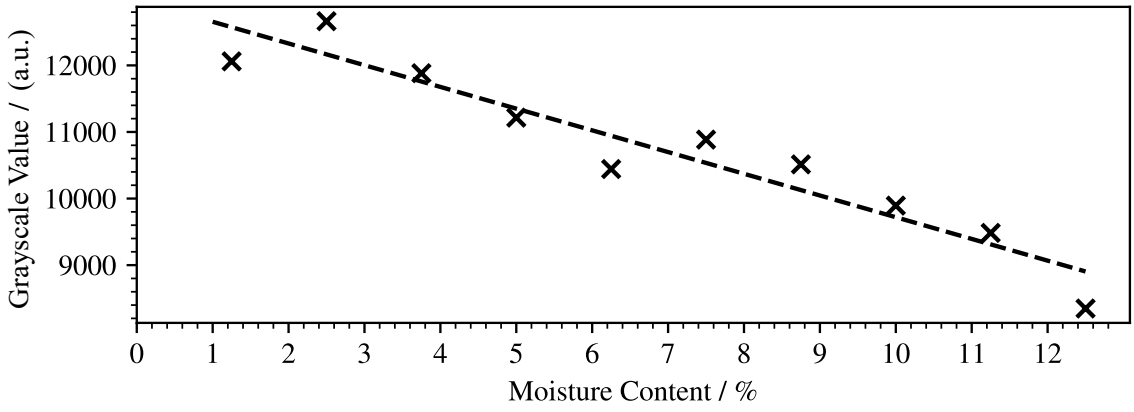


Figure 7.6: Relationship between greyscale intensity and moisture content. Data are taken from two specimens of 75% BFS hydrated for 28 and 90 days.

The mercury porosimeter used was a Micromeritics Poresizer 9320 with a 15 mL penetrometer. The density of mercury was taken as 13.5 $gcm^{-3}$. The sample was intruded to a maximum pressure of 206.4 MPa (absolute) which was sufficient to intrude a pore of 6 nm in diameter, as calculated by the Washburn equation [9] assuming a contact angle of 130° and a surface tension of 0.485 N $m^{-1}$ (see Table 2.2).

## 7.4 Quantification of the Absorbed Volume

Selected quantified data from the 75% BFS system across the entire observation time are shown in Figure 7.7 while the 90% BFS system is shown in Figure 7.8.

It is clear from the presented data that the front was non-horizontal. The assumption made in [8] is not entirely correct and provides only an approximation as to the actual response of the system. This was evidenced in all quantified figures where the absorption was shown. Across the first few hours of absorption the profile shown was far closer to the parabolic curve described in [110]. The shape of the front results from resistance to water uptake at the sealed boundary and the manner in which a three dimensional sample has been represented in a two-dimensional image. The absorption was most certainly one directional and so uni-axial flow was achieved through this configuration by sealing of the specimen walls.

A small region of lower moisture content was observed towards the bottom left hand side of the 75% BFS sample where moisture was first observed (see Figure 7.7). Water remaining on the stand from a previous test has not been fully removed and has the sample at this

point. This may be regarded as insignificant; the front location was unaffected and remains negligibly higher than zero in the first scan.

Some free water has remained present within one of the specimens, which develops only a significant artefact after 12 hours in the 90% system at 90 days hydration. This is shown by the dip in the data at the centre of the sample. The centre of the specimen was still slightly wet and this moisture has been subtracted during data correction. This was not correctable, though regardless of this the trend of water uptake shown in Figure 7.10 remains followed with no shoulder in the data which would be expected around the 10 mm location if the front movement were to slow significantly. This is where the front comes into contact with the remaining water and would be expected to slow. A similar artefact may also be observed in the data provided in [114] where a minor volume of water appears to remain within the centre of the sample which possibly forms an artefact when the authors have subtracted the dry sample.

The volume of each pixel is known from pixel dimensions and the depth of each specimen. The width and height were verified from direct measurement of the image. The moisture content through the depth of the sample for each pixel is also known, and so the volume of water within the depth represented by each pixel may be calculated.

By taking the total number of pixels with a non-zero content the bulk volume $V_B$ containing water was calculated. Additionally, the volume of the front was determined from the front intrusion and sample depth for verification of the calculation. A flat front geometry was assumed for this. These results show excellent agreement; the value determined from pixel quantity lies within $\pm 6\%$ of the front volume determined by direct measurement for every sample. The difference was accounted for as a result of making the assumption regarding the geometry of the front.

Mercury porosimetry of the isolated sample shows some agreement with the data calculated from the moisture content distribution with the caveat that it was only possible to collect data from a single specimen. This datum is shown in Table 7.2.

The final part of the quantification produces a histogram of moisture content in the sample. The distribution of moisture content in the final acquisition is shown in the data presented in Figure 7.9. Data were clipped such that regions containing a moisture content of zero were removed. These results cause compression in the visualisation of the remaining data and were neglected; for clarity only regions containing water were used to calculate the porosity. The origin represents the divide in the sample caused by the moving front.

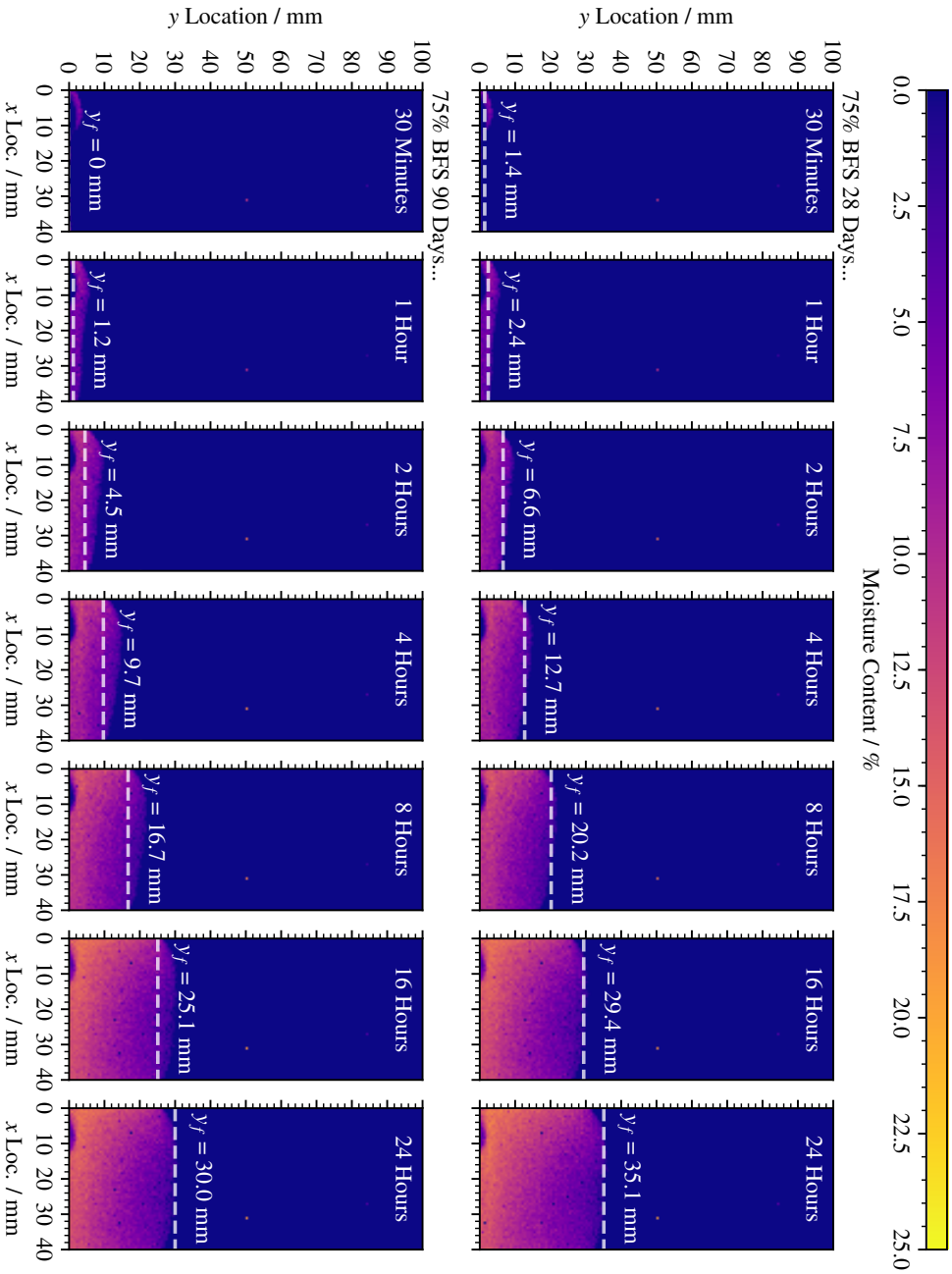


Figure 7.7: Spatially distributed moisture content of the 75% BFS system during a capillary absorption experiment at 28 (top) and 90 (bottom) days as a function of time.

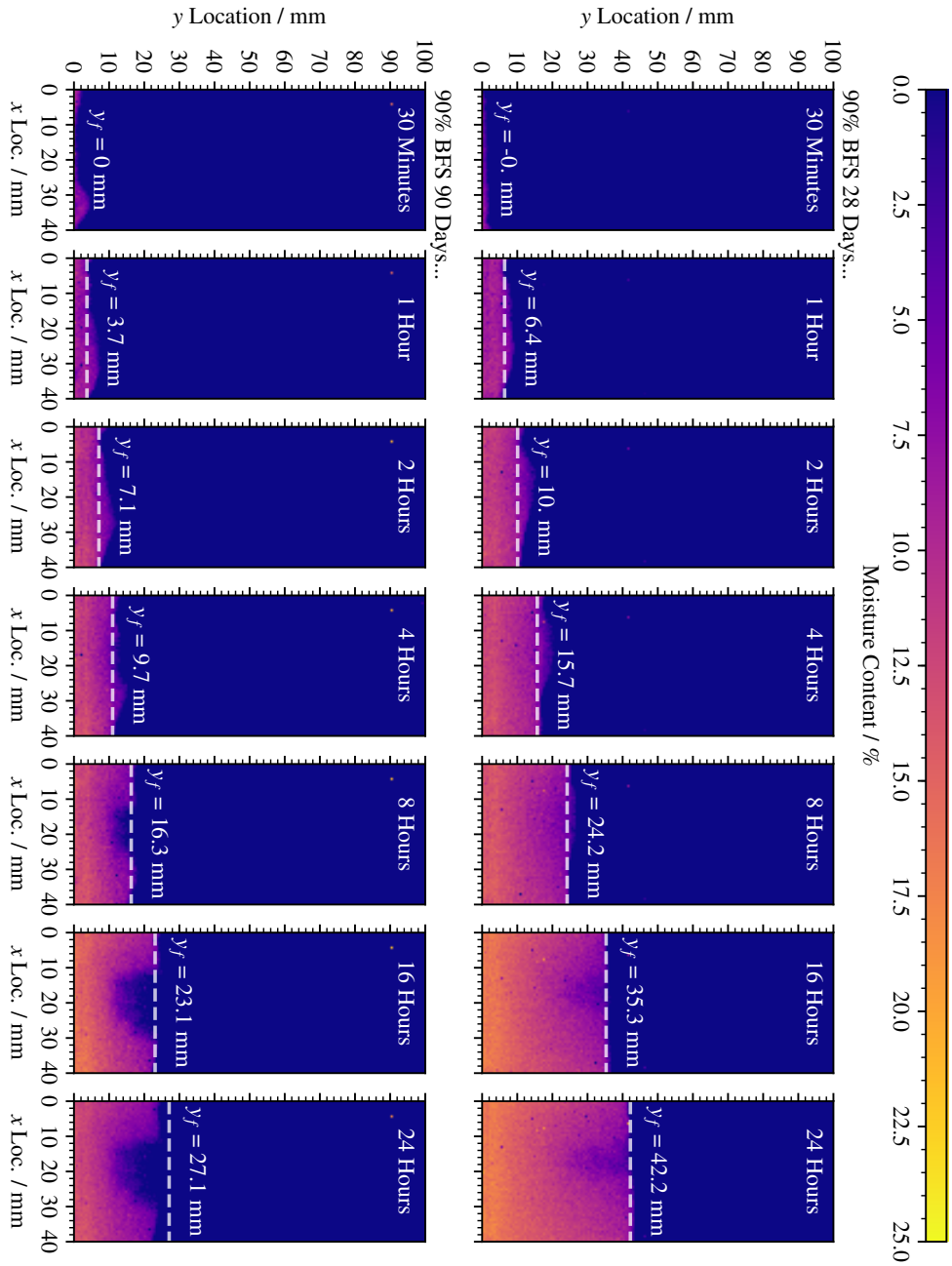


Figure 7.8: Spatially distributed moisture content of the 90% BFS system during a capillary absorption experiment at 28 (top) and 90 (bottom) days as a function of time.

Table 7.2: Wet bulk volume (WBV) and sample porosity determined by neutron radiography (NR), standard deviation(STDev), and porosity determined by mercury porosimetry (MIP).

| | | | Porosity | | |
|---|---|---|---|---|---|
| Sample | Age | WBV / $cm^3$ | NR / % | STDev | MIP / % |
| 75% BFS | 28 Days | 58.4 | 9.3 | 3.85 | - |
| | 90 Days | 50.7 | 7.2 | 3.13 | 8.4 |
| 90% BFS | 28 Days | 71.3 | 12.1 | 3.51 | - |
| | 90 Days | 43.7 | 10.1 | 4.63 | - |

### 7.4.1 Accessible Porous Volume

Acquired at the end of the experiment after 24 hours, the data show a clear difference in moisture content between samples. The two profiles shown in Figure 7.9 show a shift toward a lower moisture content as the sample age increases, which has occurred due to the refinement of the pore structure; large regions in the pore space have become more restricted as the degree of hydration has increased.

The data shown in Figure 7.9 are not a direct pore size distribution; the spatial resolution of the instrument does not allow for this and the depth of the sample will result in the merging of fine pores through the depth of the specimen, causing them to appear larger. To attempt such a quantification would possibly be misleading. However, the total pore volume may be determined and the reduction in pore volume is clear. Table 7.2 shows the pore volume as calculated by the quantification and mercury porosimetry on isolated samples. As samples have hydrated the pore volume has decreased, and done so significantly. The reaction of the pore structure to an increasing degree of hydration is well described in the literature [4, 250].

## 7.5 Absorption of Moisture in Hydrated Cement Paste

The time resolved front locations for all tested materials are shown in Figure 7.10. The uptake of these systems as a function of the square root of time is also shown. These data show a linear relationship as expected as by the example data provided in the ASTM C1585 standard [8].

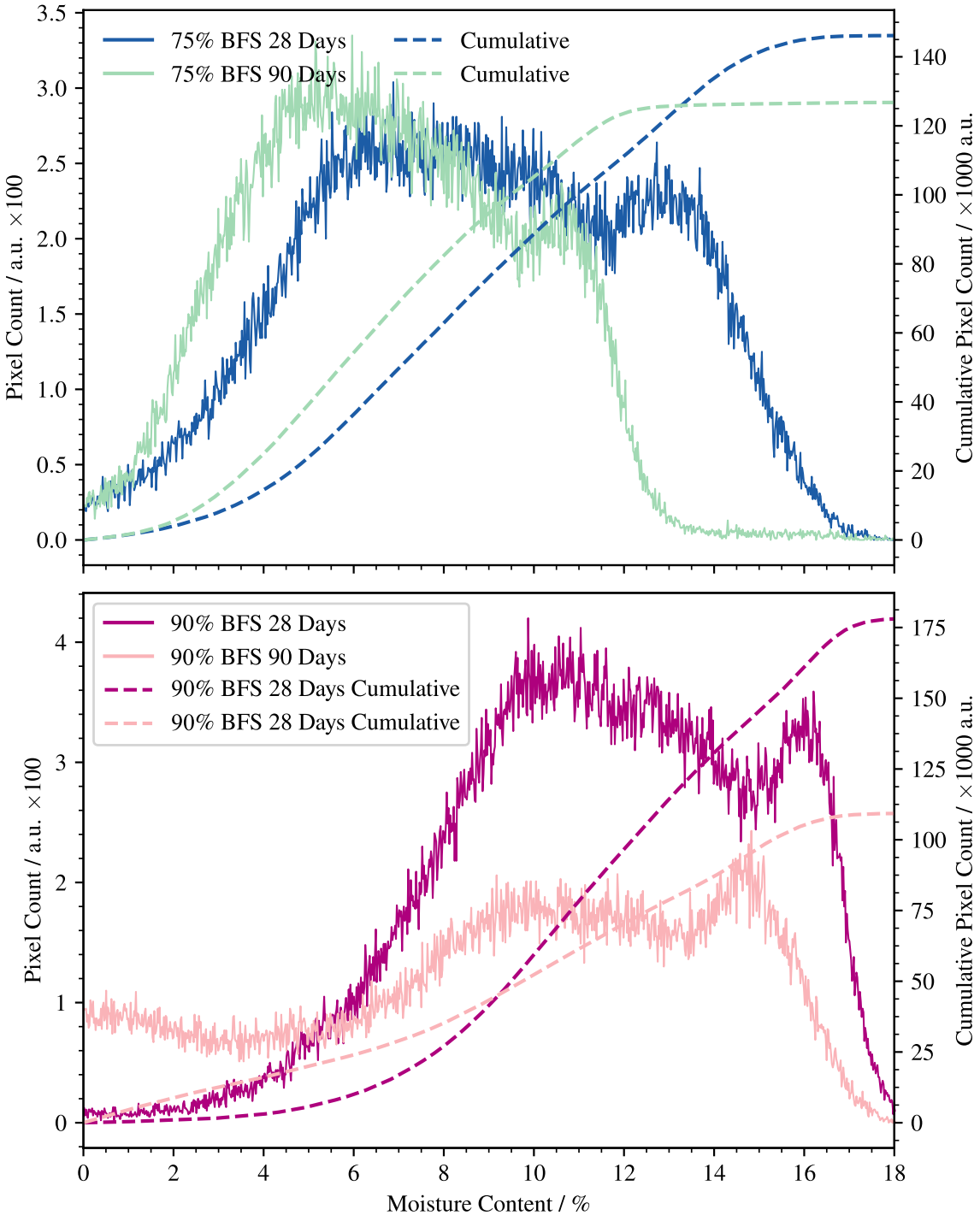


Figure 7.9: Moisture content distributions for the 75% (top) and 90% (bottom) systems cured for 28 and 90 days. Values of zero moisture content are neglected to prevent compression of the data.

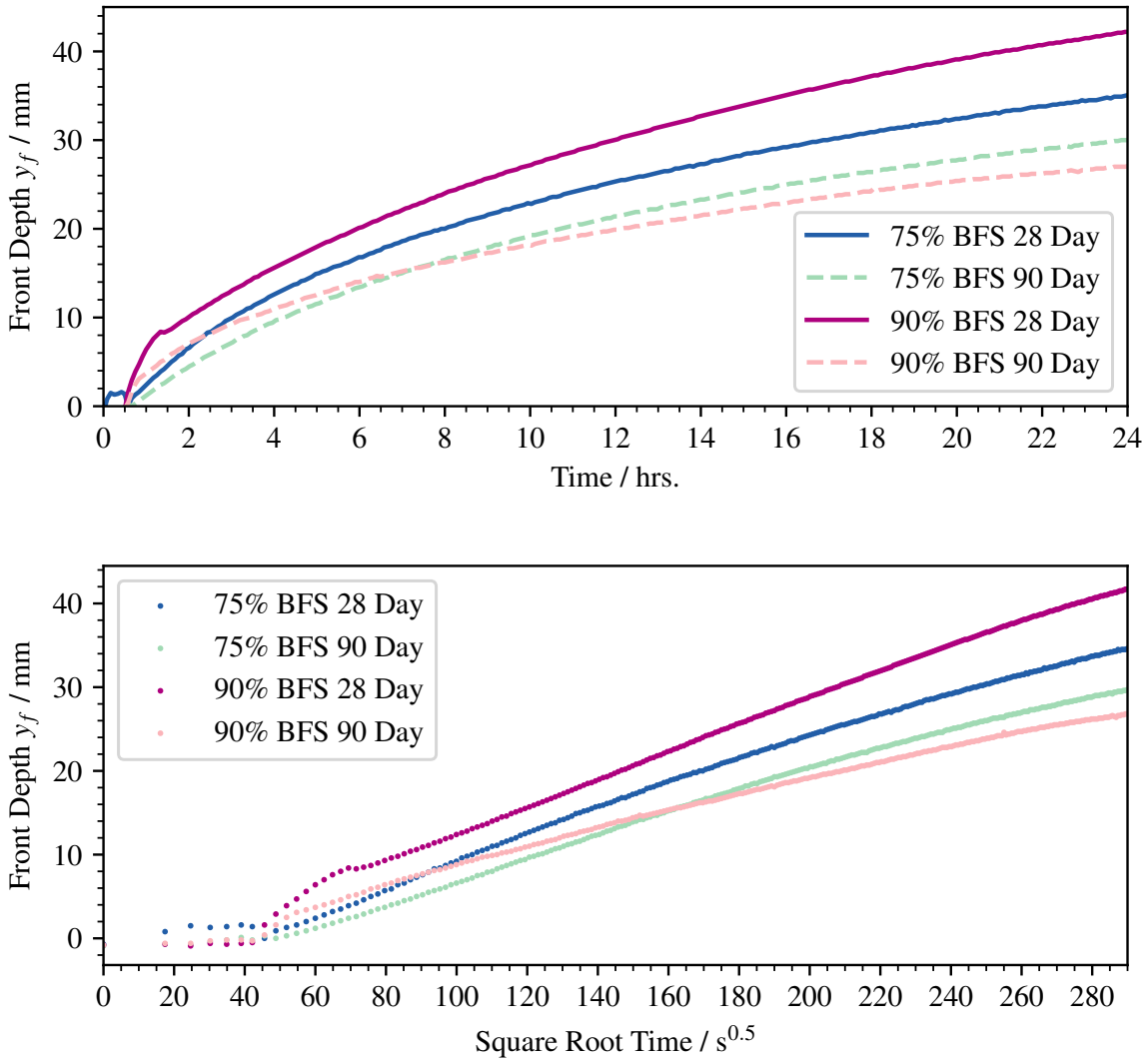


Figure 7.10: Moisture uptake of all cementitious systems evaluated across the first 24 hours (a) and (equivalently) the first 290 $s^{0.5}$ (b).

## The ASTM C1585 Test Method

For comparison to the neutron imaging data previously captured water uptake data were also acquired using the ASTM C1585-13 [8] standard. The C1585 standard was selected due to the simple nature of the application of this technique; there is no requirement for any particularly specialised equipment (see Chapter 2).

Here, the standard was modified by the use of prismatic specimens as opposed to cylindrical which are specified by the standard. The cross sectional area calculation was modified to account for this. Processed data for the 75% and 90% BFS materials are shown in Figures 7.11 and 7.12 respectively alongside the data captured by neutron imaging. The part of the figures marked (a) shows the processed data captured in the capillary suction test, with the range in raw data also highlighted. The portion of the figures marked (b) compares these data to the neutron imaging data across the first 24 hours of the test, while in the portion marked (c) data were projected from the neutron imaging experiments across the 7 day duration of the ASTM C1585 test, data from which are also shown. Projection was carried out by least squares regression fitting to a linear function with time expressed in $^{0.5}$.

### 7.5.1 Discrepancies

In the neutron imaging data a minor discrepancy from a smooth, monotonic curve was observed after approximately 1 hour in the 90% BFS system at 28 days hydration. This was not completely explicable, though may be attributed to a temporarily observed artefact in the acquisition, as it was not possible to isolate any kind of significant crack or defect in the sample into which water may rapidly absorb (see also page 150).

There was also an evident challenge with the data acquired by the ASTM C1585 test, where a set of tested samples (at 90 days hydration in Figure 7.12) has resulted in the reporting of an absorption which was significantly higher than one might expect. A possible explanation for this is that one or more samples have cracked, perhaps due to thermal expansion while drying or shrinkage of the specimen during the hydration reaction. This has caused the calculated data to yield a mean absorption that has a minimal difference between 28 and 90 days as a 28 day sample has failed.

### 7.5.2 A Data Discrepancy?

Ignoring the potentially defective sample(s) previously identified, the neutron imaging data and the data acquired by the capillary suction test show quite a large difference between the two methods (see portions of figures marked (b) and (c)). This ought not be an effect of the

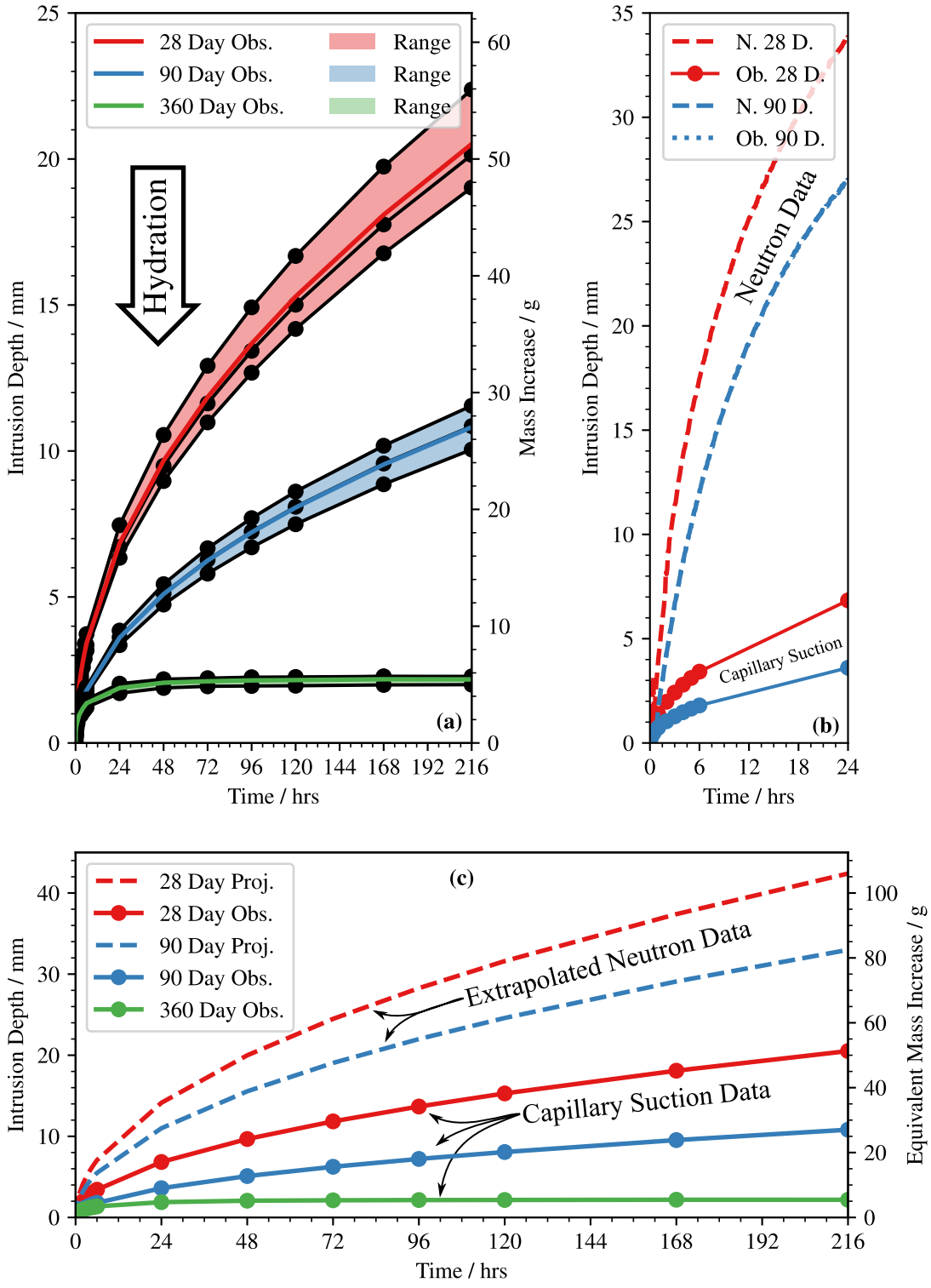


Figure 7.11: Capillary suction and neutron imaging calculation for the 75% BFS material at the indicated times. The material was tested in the laboratory as per the ASTM C1585 [8] standard. Ob(s). - observed by ASTM C1585, N. - observed by Neutron Imaging. In part (a) the coloured line is the mean value of all three specimens.

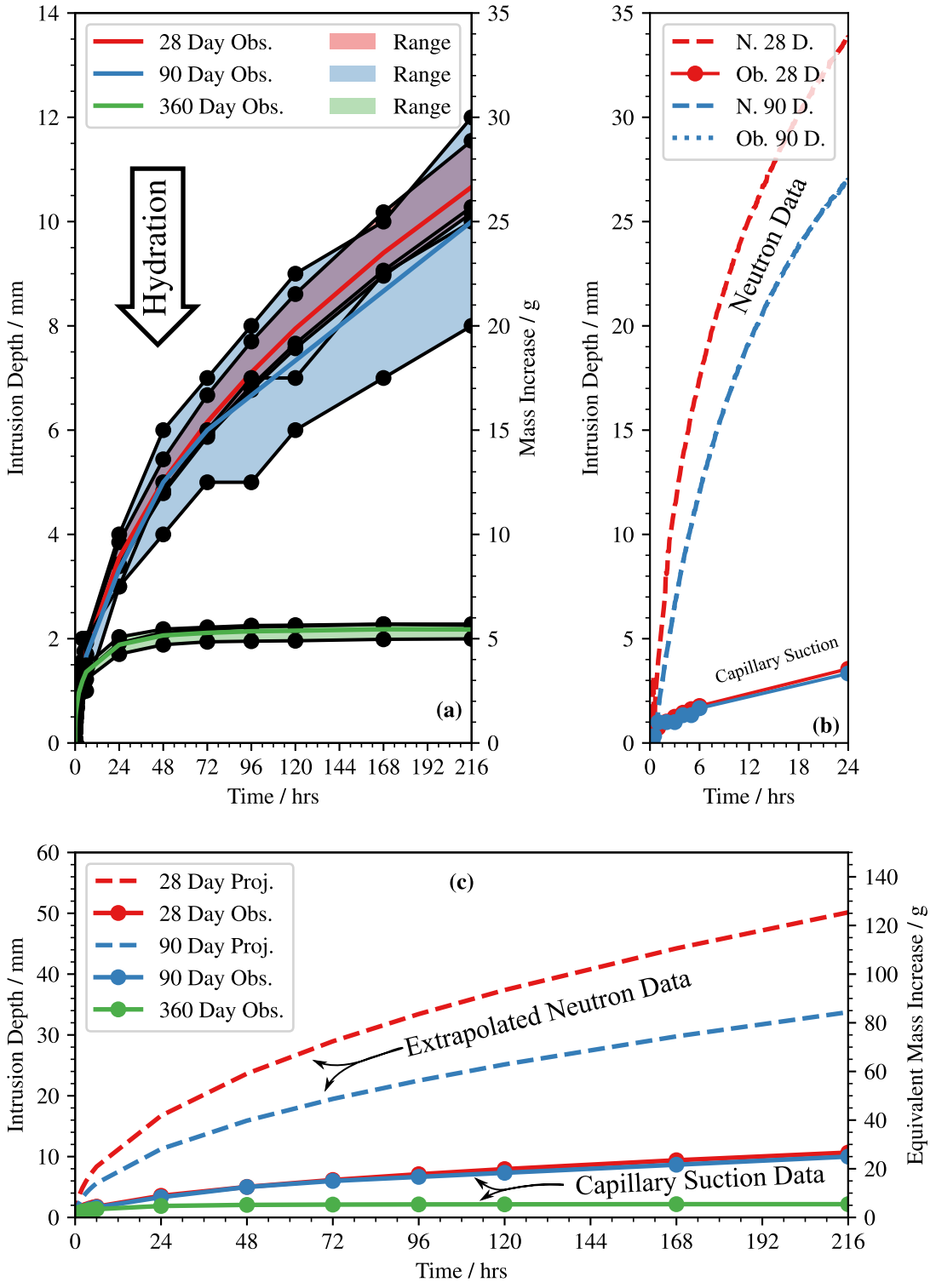


Figure 7.12: Capillary suction and neutron imaging calculation for the 90% BFS material at the indicated times. The material was tested in the laboratory as per the ASTM C1585 [8] standard. Ob(s). - observed by ASTM C1585, N. - observed by Neutron Imaging. In part (a) the coloured line is the mean value of all three specimens.

sample geometry. The first thing to note is that the neutron imaging data is extrapolated to 7 days given the trend observed over 24 hours. This may be part of the effect that is observed here; the extrapolation may very well push beyond the acceptable limit of what may be described as representative. Alternatively, this may have been caused by either interaction of neutrons with the specimen above the wetting front (which the ASTM test standard is insensitive to), or possibly be related to the assumptions being made by the calculations performed by the ASTM standard [8][3].

In this standard, it is assumed that the permeation of water into the specimen takes the form of a solid, monolithic volume, which was discussed in Chapter 2. This is possibly not an entirely representative assumption and may provide a value slightly different to that which was directly observed here by radiographic imaging Here, the water will permeate into pores which make up between 5% and 13% of the bulk and not a solid volume as assumed by the standard (see Page 166 of Chapter 8 for summary porosities.

### The Absolute Minimum Discrepancy

Before preconditioning of the sample in the oven, at a water-cement ratio of 0.35 the sample ought to be 25.9% water. Hence, to a unity mass of anhydrous cement 0.35 g of water per g of cement is added, and therefore water makes up $0.35/(0.35 + 1) = 0.259$, or 25.9% of the body by mass. A discrepancy of $1/0.259 = 3.86\times$ ought therefore to be observed. However, the actual discrepancy observed is *considerably* higher than this so dehydration of the specimen in the oven and the possibility of the decomposition of hydrates from the microstructure must also be accounted for.

### The Discrepancy: Accounting for Preconditioning

The sample selected for comparison here is the one which shows the lowest quantity of both limestone and carbonation. This is the green line showing the derivative and total mass loss with temperature of the 90% sample at 28 days hydration in Figure 7.13. Here, it is assumed that mass loss due to off-gassing of $CaCO_3$ is negligible; all of the lost mass is a result of stripping of $H_2O$ from thermal decomposition.

[3]Note also the difference in geometry between the samples tested in the neutron experiment and the by the ASTM standard. In future work the test should be repeated with the same prismatic sample geometry as the neutron experiment in order to eliminate the sample geometry variable in its entirety, even though this should not have a significant effect. These data could also be verified by periodically breaking a sample open to directly observe the wetting front.

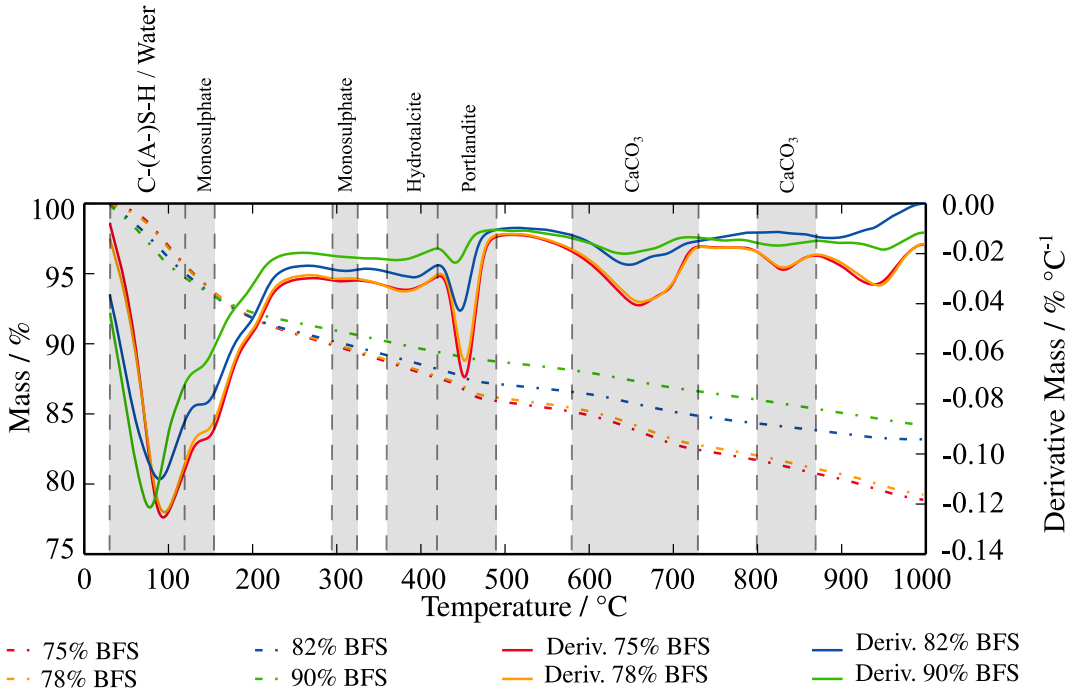


Figure 7.13: Thermogravimetry at 28 days for explanation of the discrepancy observed between the ASTM C1585 [8] and radiography-derived data. This figure is reproduced from Chapter 3 for the purpose this section.

For comparison here the successful experiment shown in Figure 7.12 will be used. Consider, for a moment, the thermogravimetry data acquired during the intial characterisation of the material in Figure 7.13. The interest here is in the data leading up to the oven temperature at which free water was removed from the sample, which was $105 \pm 5$°C (assume for the purposes of this calculation that the oven remained precisely at 105°C). Here, the cement was dried in isopropyl alcohol before testing.

Once all water, whether free or bound to hydrates, has been stripped from the specimen, what remains is a sample (of original mass of unity) having 0.86 g of solids remaining. Therefore it may be said that 100 g of cement dried with isopropyl alcohol has 14 g of water bound to hydrates and 86 g of solids. Originally, this 86 g of solids was blended with $86 \times 0.35 = 30.1$ g of water yielding a total mass of approximately 116.1 g. Before heating the specimen, pre-treatment by quenching in isopropyl alcohol has removed 16 g of a sample with 86 g of cementious product.

Heating between room temperature and 105°C has removed approximately a further 7 g of water from the sample. Therefore, by this calculation 86 g of cement blended with 30.1 g

of $H_2O$ loses $7 + 16 = 23$ g of water up to 105°C. $(23/30.1) \times 100 = 76.4\%$ of free water has therefore been lost from the specimen.

Knowing the original water content of 25.9% previously determined, and knowing that 76.4% of this 25.9% is lost on heating to 105°C, it may be said that the space available for water uptake, if this amount of free water is removed, is $0.76 \times 0.259 \times 100 = 19.7\%$. Calculating a factor accounting for this yields a discrepancy of $5.1\times$, which is close to that observed by the techniques. In this case the C1585 standard may not be making the optimum assumption about the intruding geometry in the case of these specimens. The calculation here does match the differences shown in Figure 7.12, though it is reiterated that this is simply based on an extrapolation, and so it is decided in this research that no firm conclusion as to the suitability of the standard can be drawn from these results.

## Degree of Hydration and Water Absorption

By neutron imaging, the results shown in Figure 7.10 quite clearly a significant difference in absorption between both systems after 28 days and 90 days of hydration. The 75% slag cement shows a decrease of approximately 10% in the front location at the end of the experimental duration while at 90% substitution a more significant decrease of approximately 40% occurs at the same point after 24 hours. The literature suggests that the reaction of blast furnace slag in the material results in a pore structure that is more tortuous and finer in nature [245, 251] compared to plain Portland cement based materials. In conclusion, the evidence suggests replacement of higher volumes of Portland cement with slag decreases the uptake of moisture into the specimen at the same age. As the slag has reacted, the system has become more resistant to permeating water. This has happened to the extent that the uptake after 90 days by the 90% system is lower than that of the 75% at this age. This occurs in spite of the fact that the rate of reaction of the slag is significantly lower than that of the Portland cement, as has been established in Chapter 4 and shown by Prentice et al. [175].

From these data it may be concluded that more highly substituted systems actually show a greater degree of resistance to water ingress, at least in the case of this experiment at 90 days but not at 28 days of curing. To make such a statement one must also consider the total porous volume and not simply the rate at which water is able to enter. Data are somewhat lacking from this technique and to make such a statement may require more samples, and a study of the uptake of the specimen at a greater degree of hydration. Due to instrument scheduling and the limited amount of instrument time available, it is very challenging to produce data regarding samples at a greater degree of hydration than this, at least in this instance. To produce a full empirical model regarding the uptake of these specimens the

degree of hydration of the system is also necessary and may be calculated by extending the method provided in Chapter 4 over samples hydrated for a number of years.

At 360 days of age the absorption of water into the specimen has further diminished. The interconnectivity of pores has reduced sufficiently to disconnect some regions from the surface. While the decrease in pore diameter may have increased the ability for water to move further up the sample by Equation 7.1, the constriction in pore size has entirely blocked off some pores.

## 7.6 Conclusions

Quantified neutron imaging has provided a useful method for the observation of the direct moisture uptake in cement specimens both from a qualitative and quantitative point of view. Using this method it was possible to semi- non-destructively observe the moisture penetration profile which would normally require some kind of post-mortem testing where the sample is fractured. The technique has allowed for spatially resolved quantification of the moisture content in the specimen and has provided the ability to directly resolve the front location. A number of observations have been made resulting from the presented work.

The reduction in uptake of water between 28 days was observed in most systems though far more apparent in the 90% BFS system, which shows a reduction of 35%. This was attributed to a greater reduction in porosity due to the reaction of the slag, which shows a clear difference at a significantly higher degree of substitution, especially across a longer duration (and, therefore, a higher degree of hydration). The reaction of the slag was clearly significantly slower, which was shown by comparing the data captured at 28 days between the materials substituted with 75% and 90% BFS, and then observing the difference at 90 days which inverts.

Some minor artefact within the quantified specimens was apparent. These are insignificant in a practical sense, and do not appear to affect the observed rate of movement of the front through the specimen, which was still readily quantified from these data.

The calculated porosity was inversely proportional to the degree of hydration though no relationship was drawn between these parameters in this thesis as some kind of quantification of the degree of hydration is required which has not yet been determined. This was fully expected due to the reaction of cement particles in-filling the volume of the pore structure, which was additionally shown in Chapter 6. It was also challenging to produce an accurate pore size distribution due to the spatial resolution of the instrument, though results do suggest

the distribution of pore sizes does shift towards a finer structure at a later age observed by this technique.

ASTM C1585 provides results which lie somewhat below the results observed directly by Neutron imaging and this standard, therefore, provides us with a result which is not particularly similar what was observed by direct imaging. This may be a result of several of the effects previously discussed. If such a discrepancy is forthcoming, it might be concluded that this test is acceptable for, for example, a simple comparative test, though this might not be the best option for use in a research-focussed context, in which a higher accuracy result may be a desired outcome.

In testing further samples it would be of interest to perhaps extend the data here to a wider range of compositions, including alkali activated geopolymer materials, and that the dataset here would likely benefit from a supplementary specimen of pure Portland cement. Finally, it might be interesting to carry out some kind of tomographic study in three-dimensions, for which a smaller sample is likely required to produce a shorter acquisition time and allow the uptake of water to be captured in-situ. The quantification of moisture content may, perhaps, prove challenging where a cylindrical specimen is characterised, though is likely not entirely impossible given the correct equipment. Neutron tomography would also be better suited to the production of a physical pore size distribution [114], though this will also depend on the spatial resolution capabilities of the instrument. In order to produce some kind of an understanding of how the sample degrades by the processes observed here, some kind of in-situ imaging of the microstructure while the degradation process is occurring may prove useful.

# Chapter 8

# Summary & Conclusions

This thesis quite clearly shows how complex the hydration of cement materials is. The substitution of Portland cement by supplementary cementitious material has a dramatic complexification of both the hydration reaction and the characterisation of this. In the cases shown in this thesis advanced characterisation techniques must be used to observe both dynamic processes occurring within the microstructure and the permeation of moisture into the specimen. In Chapter 2 a number of gaps in the literature were identified, many of which have now been filled in this thesis.

Chapter 3 introduces the materials used here and carried out an initial characterisation of both the geometric (physical) and chemical properties of the anhydrous precursors and materials hydrated to a relatively short period. The formation of hydrate phases was shown, including portlandite, and a modification of amorphous calcium silicate hydrate (C-S-H) identified as calcium aluminate silicate hydrate (C-(A)-S-H) due to the presence of slag, which results in the substitution of aluminium within this phase. Ettringite (AFt) and monosulfoaluminate (AFm) were identified, and these were resolved in data acquired both by X-ray diffraction and thermal analysis. The low resolution of the diffractometer and the peak divergence characteristics results in the merging of peaks of the AFm phases (monosulfoaluminate and hemicarboaluminate) together and these are not resolved in isolation.

## 8.1 Hydration Chemistry: Chapter 4

In Chapter 4 the first days of the hydration reaction were observed in-situ and the reaction of the slag by the partial or no known crystal structure (PONKCS) method [183] was assessed. This showed the reaction of the slag across the first hours, which reduced in fraction most dramatically in the material substituted to 75% slag due to the abundance of Portland cement and slightly reduced volume of slag from the most highly substituted material. The formation of C-(A)-S-H, ettringite, and portlandite was observed as the cement enters the acceleration period in the thermal output, and the depletion of sulphates within the clinker was also shown.

The resolution of the synchrotron instrument used was sufficiently high to resolve peaks that appeared to otherwise merge together on the laboratory diffractometer. The instrument produced sharp Bragg peaks. For example, the Portlandite reflection at 32° $2\theta$ ($\lambda = 1.5419$ Å) shown in, for example, Figure 3.4 partially merged with the $C_3S$ peak, but this did not occur at approximately 18.5° $2\theta$ ($\lambda = 0.82570(1)$ Å) in Figure 4.5 where these peaks were easily isolated from one another.

Ettringite forms immediately, most likely from the moment the anhydrous cement comes into contact with water. Across the first minutes of the reaction amorphous product forms (in spite of the fact the amorphous hydrate content is set to zero in the first scan). A narrow layer of hydrate was identified in Chapter 5, though it is unlikely that this volume makes up an observable fraction by Rietveld refinement. The volume observed in this chapter is the precipitation of disordered hydration products in the pore volume. Hydration products in the pore volume are also identified in Chapter 5 by computed tomography.

The deposition of C-S-H and C-(A)-S-H occurs in the acceleration stage of the hydration reaction on the clinker-solution interface. By this technique the formation of this marries well with the observed thermal output by isothermal conduction calorimetry (Chapter 3. Formation of this phase slows, though does not cease entirely, during deceleration of the hydration reaction after a number of hours.

## 8.2 The Morphology of Hydration: Chapter 5

When Portland cement reacts, a barrier forms within the microstructure that appears to thinly coat unreacted particles in the suspension. The small amount of hydrate shown does not grow through the dormant period of the reaction. No attempt is made to answer the question as to precisely why growth of hydrates begins, as processes occurring at the interface of the

anhydrous particle and the hydrate layer could not be observed as this lies below the spatial resolution achievable using this technique.

A narrow barrier is also formed upon slag cements at both degrees of substitution studied. This appears to be a leached layer forming upon the particle surface, and this layer is revealed only by the back-application of the threshold values which were determined in the final stack where all morphological phases were visible. It appears that the formation of this barrier was perhaps the mechanism which slows the hydration reaction; it forms early on and ceases in thickening when the material reaches the induction stage after a number of minutes. The morphology of the barrier is non-uniform, and appears to deposit more extensively upon the Portland cement though the segmentation of an isolated slag particle either computationally (see Section 8.5) or by eye is really required to verify this. This reinforces the hypothesis that the formation of this layer is a leaching process.

During the dormant period the formation of precipitates ceases, which is consistent with the hypothesis formed here that the formed barrier has restricted access of the mix water to the interface between the anhydrous particle and the narrow layer.

## 8.3 Filling of the Porous Volume: Chapter 6

In Table 8.1 the porosity of all materials tested by the various methods is summarised. Several gaps remain in the data presented here, the majority of which result from instrument failure during testing or limitations in beam-time scheduling which allows for only a limited number of specimens to be characterised. Computed tomography allows for rapid sample acquisition and data processing. Ideally repeat samples ought to have been imaged, though this is not possible due to these restrictions.

In analysing the pore volume as a whole, a strong trend was observed as the material hydrates; the porosity decreases as the in-filling of hydrates into the pore structure constricts the volume. This additionally increases the tortuosity of the pore structure though this was not determined using this technique (see Section 8.5). Differing values resulted from the different length-scales upon which properties of the material may be resolved. The volumes observed by computed tomography are generally lower than those observed by neutron radiography. As water has absorbed, the C-(A)-S-H gel has become saturated which has contributed to the attenuation of neutrons in the specimen. This is not the case for results from tomographic analysis in which the porous C-(A)-S-H volume merely appears as a monolithic solid phase with a pore volume which is not observable due to the length scale on which the instrument operates.

Table 8.1: The resolved porosity of specimens across the studied time-frame by the various techniques applied in this thesis.

| | | Porosity (vol. %) By | | |
|---|---|---|---|---|
| Material Composition | Sample Age | Mercury | Tomography | Radiography |
| 75% BFS | 1 Days | - | 12.7 | - |
| | 3 Days | - | 9.8 | - |
| | 5 Days | - | 9.4 | - |
| | 7 Days | - | 8.0 | - |
| | 28 Days | - | 7.3 | 9.3 |
| | 90 Days | - | - | 7.2 |
| | 360 Days | - | 7.1 | - |
| 78% BFS | 1 Days | - | 14.4 | - |
| | 5 Days | - | 13.7 | - |
| | 7 Days | - | 11.8 | - |
| | 14 Days | - | 5.9 | - |
| | 28 Days | - | 6.4 | - |
| | 360 Days | - | 7.3 | - |
| | 25 Year | - | 6.9 | - |
| 90% BFS | 1 Days | - | 18.7 | - |
| | 5 Days | - | 13.8 | - |
| | 7 Days | - | 10.3 | - |
| | 28 Days | - | 7.8 | 12.1 |
| | 90 Days | 8.4 | 7.3 | 10.1 |
| | 360 Days | - | 5.6 | - |

A refinement of the pore structure by both neutron radiography and computed tomography was shown. By radiography, the quantified moisture content of the specimen, which were equated directly to the porosity assuming full saturation below the wetting front, shifts toward a lower content which shows the refinement of the pore volume, though here only the number of pixels counted is considered, and not a quantitative volume. Here the two techniques provided a fundamentally different metric; pores were directly counted by one technique, and the moisture content of a series of pixels quantified by another, which itself does not reveal a size distribution and is merely indicative of the changes occurring within the sample. As the pore volume constricts, the mean moisture content through the depth of the specimen reduces and the tortuosity increases. This was revealed by a lower uptake of moisture into the specimen by both the neutron imaging and the ASTM test.

## 8.4 The Action of the Porous Volume: Chapter 7

The ASTM C1585 [8] test proved to be of intrerest and may to have under-reported the values of absorption, assuming that the extrapolation to 7 days worth of data carried out in Chapter 7 is valid, and that there is no interaction of neutrons above the permeating front. The ASTM C1585 standard has also assumed the sample absorbs moisture in a solid block, with a depth determined based on the cross sectional area of the specimen. This may be a limitation of the standard, where in reality, the uptake is higher as the mass of water spreads through the pore volume alone and does not take up the entire cross section of the sample. In spite of this it was concluded that such an analysis is still be suitable for judging the performance of samples prepared in the same manner with minor variations in, for example, composition, the degree of hydration, or the addition of supplementary cementitious materials. The results showed also a difference due to the sample geometry which enables a higher uptake across the first 24 hours in a taller specimen. This is an imperfect comparison and these ought to be repeated with similarly sized specimens for a firm conclusion to be formed here.

As the sample saturates, the moisture content at the base of the specimen reaches a value which was interpreted as full saturation (and therefore the porosity). The geometry of the wetting front is irregular, and this is also the case in three dimensions where restriction of water permeation on each edge resulted in the reduced moisture content in this location. In three dimensions restriction will occur and the shape of the front will form some sort of paraboloid which could not be observed in two dimensions. The assumption that the front location is linear was shown to be not entirely correct, though is certainly the best possible assumption by the standardised technique, and is, therefore, the method adopted in this thesis.

## 8.5 Prospects for the Future

There are several methodological holes which might be filled by both the further development of the techniques identified here and the application of data analysis methods which have not been entirely filled within this thesis.

### 8.5.1 Training a Computer to Identify a Slag Grain

Firstly, a method by which supplementary cementitious materials, most notably blast furnace slags, might be identified computationally would prove highly useful in the correct segmentation of these materials. Blast furnace slag particulate is fairly distinctive in that it has an angular geometry and entrapped air voids, which were identified in Chapter 6. If it might be possible to acquire tomographic images of unreacted slag particles and a negative image series of, say, a hydrated Portland cement it might subsequently be possible to effectively train a computer to segment the material [252] and rapidly identify slag particles. After regions are identified particles could then be located within the slice by Canny edge detection [253] in samples where overlapping grayscale intensities occur but the geometry remains distinctive. This could be applied to both blended cements and this could be verified by secondary techniques such as backscattered electron imaging with an energy-dispersive X-ray detector, the method identified by Kocaba et al. [254] as the most accurate.

### 8.5.2 An Extension to the Visible Cement Dataset?

As of writing, the visible cement dataset [84] is now 17 years old. As more cements are developed it might now be time to either update or extended this to provide an extensive sample set. This could be provided with the tools described in 8.5.1 to provide a full toolkit for researchers to rapidly identify these phases in microstructural images.

### 8.5.3 Analysing the Porous Volume

In addition to this, further analysis of the pore structure may be carried out using computational methods. Promentilla et al. [91] and Provis et al. [90] used a random walk algorithm to analyse the capillary pore volume in this manner, which has not been carried out here. The pore volume might be more readily identified by a method which marks the structure such as Wood's metal intrusion porosimetry [255] with the caveat that like mercury intrusion porosimetry this applied a high pressure to the sample, along with inevitable heating of the specimen to melt the Wood's metal.

### 8.5.4 Subatomic Particles

As higher and higher fluxes are achieved at neutron facilities it may become possible to perform fast neutron tomography on a sample. This will provide, in addition to already available techniques such as nuclear magnetic resonance (NMR), a method by which the ingress of water into the specimen will be able to be observed as a time-resolved process in-situ in three dimensions without transferring the specimen into and out of the beam during testing. Unlike the data acquired in Chapter 7 this will enable a pore size distribution to be directly segmented similarly, in a potentially similar manner to the method provided in Chapter 6.

## 8.6 Our Understanding of Cement

So, as this thesis is drawn to a close, it is now possible to sum up how the results presented here have provided a large improvement in the knowledge base surrounding highly substituted cementitious materials. This includes, of course, those used in the nuclear field, though it is still challenging to draw a firm conclusion as to the suitability of the use of cements in the nuclear field in general. While the materials presented in this thesis show a fairly low porosity which may suggest good durability properties, it is not necessarily possible to predict the performance of these materials over a lifespan of thousands of years and it must simply be concluded that we don't really know what could happen centuries down the line.

This thesis also presents the application of advanced characterisation techniques, which have in some cases found little use in the study of these materials. The manner in which some of the experiments may be executed from a practical sense has been shown, and by this the hydration reaction demonstrated both chemically and morphologically using cutting-edge synchrotron imaging and diffractometry. Using similarly advanced facilities, the moisture uptake has been observed within the porous body by quantified neutron radiography. These are specialist techniques, and it is not expected that these would come into everyday use in general research field, though this is still of interest and has provided a good pair of techniques to aim to characterise these.

Some further knowledge gaps and some areas for further research have been uncovered, and these offer some scope for future development of our understanding of how these perform and how we might be able to process data emanating from tests such as the ones carried out here. The future potentially holds bright new applications for these and similar materials, as cements with a lower environmental impact are sought after. As the population of the world expands and should our climate becomes more aggressive, more durable materials

will become necessary to ensure the security of our lifestyles, and concretes produced from these and similar cements may very well play a part in this.

Cements are so widely used that as a material these are inevitably going to continue to play an enormous role for centuries, though the form in which we find this will very likely change, perhaps beyond recognition.

# References


[1] J. H. Sharp, J. Hill, N. B. Milestone, and E. W. Miller. Cementitious systems for encapsualation of intermediate level waste. In *9th ASME International Conference on Radioactive Waste Management and Environmental Remediation: Volumes 1, 2, and 3*. ASME, 2003.

[2] NDA: Nuclear Decommissioning Authority. Radioactive Wastes in the UK: A Summary of the 2016 Inventory. Techreport, NDA: Nuclear Decommissioning Authority, 2016.

[3] R. G. W. Vasconcelos, N. Beaudoin, A. Hamilton, N. C. Hyatt, J. L. Provis, and C. L. Corkhill. Characterisation of a high pH cement backfill for the geological disposal of nuclear waste: The Nirex reference vault backfill. *Applied Geochemistry*, 89:180–189, 2018.

[4] J. W. Bullard, H. M. Jennings, R. A. Livingston, A. Nonat, G. W. Scherer, J. S. Schweitzer, K. L. Scrivener, and J. J. Thomas. Mechanisms of cement hydration. *Cement and Concrete Research*, 41(12):1208–1223, 2011.

[5] M. C. Schlegel, A. Sarfraz, U. Mueller, U. Panne, and F. Emmerling. First seconds in a building's life - in situ synchrotron X-ray diffraction study of cement hydration on the millisecond timescale. *Angewandte Chemie International Edition*, 51(20):4993–4996, 2012.

[6] K. L. Scrivener and A. Nonat. Hydration of cementitious materials, present and future. *Cement and Concrete Research*, 41(7):651–665, 2011.

[7] N. C. Collier, J. H. Sharp, N. B. Milestone, J. Hill, and I. H. Godfrey. The influence of water removal techniques on the composition and microstructure of hardened cement pastes. *Cement and Concrete Research*, 38(6):737–744, 2008.

[8] ASTM International. C1585: Standard Test Method for Measurement of Rate of Absorption of Water by Hydraulic-Cement Concretes, 2013.

[9] E. W. Washburn. The dynamics of capillary flow. *Physical Review*, 17(3):273, 1921.

[10] S. Diamond. Mercury porosimetry: An inappropriate method for the measurement of pore size distributions in cement-based materials. *Cement and Concrete Research*, 30 (10):1517–1525, 2000.

[11] BSI (British Standards Institution). BS EN 197-1, Cement-Part 1: Composition, specifications and conformity criteria for common cements, 2011.

[12] K. L. Scrivener, P. Juilland, and P. J. M. Monteiro. Advances in understanding hydration of portland cement. *Cement and Concrete Research*, 78:38–56, 2015.

[13] L. Nicoleau and A. Nonat. A new view on the kinetics of tricalcium silicate hydration. *Cement and Concrete Research*, 86:1–11, 2016.

[14] V. Kocaba. Development and evaluation of methods to follow microstructural development of cementitious systems including slags. *EPFL, Switzerland*, 2009.

[15] R. A. Sanderson, G. M. Cann, and J. L. Provis. Comparison of calorimetric methods for the assessment of slag cement hydration. *Advances in Applied Ceramics*, 116(4): 186–192, 2017.

[16] I. Pane and W. Hansen. Investigation of blended cement hydration by isothermal calorimetry and thermal analysis. *Cement and Concrete Research*, 35(6):1155–1164, 2005.

[17] C. Jolicoeur and M-A. Simard. Chemical admixture-cement interactions: Phenomenology and physico-chemical concepts. *Cement and Concrete Composites*, 20 (2-3):87–101, 1998.

[18] A. Moore and H. F. W. Taylor. Crystal structure of ettringite. *Nature*, 218(5146): 1048–1049, 1968.

[19] A. E. Moore and H. F. W. Taylor. Crystal structure of ettringite. *Acta Crystallographica Section B Structural Crystallography and Crystal Chemistry*, 26(4):386–393, 1970.

[20] P. K. Mehta. Mechanism of expansion associated with ettringite formation. *Cement and Concrete Research*, 3(1):1–6, 1973.

[21] H. Bouzabata, S. Multon, A. Sellier, and H. Houari. Swellings due to alkali-silica reaction and delayed ettringite formation: Characterisation of expansion isotropy and effect of moisture conditions. *Cement and Concrete Composites*, 34(3):349–356, 2012.

[22] Y. Thiebaut, S. Multon, A. Sellier, L. Lacarrière, L. Boutillon, D. Belili, L. Linger, F. Cussigh, and S. Hadji. Effects of stress on concrete expansion due to delayed ettringite formation. *Construction and Building Materials*, 183:626–641, 2018.

[23] P. W. Brown and P. LaCroix. The kinetics of ettringite formation. *Cement and Concrete Research*, 19(6):879–884, 1989.

[24] H. N. Stein and J. M. Stevels. Influence of silica on the hydration of $3\,CaO\,SiO_2$. *Journal of Applied Chemistry*, 14(8):338–346, 2007.

[25] L. Nicoleau, A. Nonat, and D. Perrey. The di- and tricalcium silicate dissolutions. *Cement and Concrete Research*, 47:14–30, 2013.

[26] H. M. Jennings and P. L. Pratt. An experimental argument for the existence of a protective membrane surrounding portland cement during the induction period. *Cement and Concrete Research*, 9(4):501–506, 1979.

[27] L. D. Mitchell, M. Prica, and J. D. Birchall. Aspects of Portland cement hydration studied using atomic force microscopy. *Journal of Materials Science*, 31(16):4207–4212, 1996.

[28] P. Juilland, E. Gallucci, R. Flatt, and K. L. Scrivener. Dissolution theory applied to the induction period in alite hydration. *Cement and Concrete Research*, 40(6):831–844, 2010.

[29] P. Barnes and J. Bensted. *Structure and Performance of Cements*. CRC Press, 2001.

[30] S. Garrault, E. Finot, E. Lesniewska, and A. Nonat. Study of C-S-H growth on $C_3S$ surface during its early hydration. *Materials and Structures*, 38(4):435–442, 2005.

[31] S. Joseph, S. Bishnoi, K. Van Balen, and O. Cizer. Effect of the densification of C-S-H on hydration kinetics of tricalcium silicate. *Journal of the American Ceramic Society*, 101(6):2438–2449, 2017.

[32] C. Naber, F. Bellmann, T. Sowoidnich, F. Goetz-Neunhoeffer, and J. Neubauer. Alite dissolution and C-S-H precipitation rates during hydration. *Cement and Concrete Research*, 115:283–293, 2019.

[33] S. T. Bergold, F. Goetz-Neunhoeffer, and J. Neubauer. Quantitative analysis of C-S-H in hydrating alite pastes by in-situ XRD. *Cement and Concrete Research*, 53:119–126, 2013.

[34] P. Juilland, A. Kumar, E. Gallucci, R. J. Flatt, and K. L. Scrivener. Effect of mixing on the early hydration of alite and OPC systems. *Cement and Concrete Research*, 42 (9):1175–1188, 2012.

[35] B. Lothenbach, K. L. Scrivener, and R.D. Hooton. Supplementary cementitious materials. *Cement and Concrete Research*, 41(12):1244–1256, 2011.

[36] E. Gruyaert, N. Robeyst, and N. De Belie. Study of the hydration of portland cement blended with blast-furnace slag by calorimetry and thermogravimetry. *Journal of Thermal Analysis and Calorimetry*, 102(3):941–951, 2010.

[37] G. De Schutter and L. Taerwe. General hydration model for portland cement and blast furnace slag cement. *Cement and Concrete Research*, 25(3):593–604, 1995.

[38] J.-I. Escalante-Garcia and J.H. Sharp. The chemical composition and microstructure of hydration products in blended cements. *Cement and Concrete Composites*, 26(8): 967–976, nov 2004.

[39] E. L'Hôpital, B. Lothenbach, D. A. Kulik, and K. L. Scrivener. Influence of calcium to silica ratio on aluminium uptake in calcium silicate hydrate. *Cement and Concrete Research*, 85:111–121, 2016.

[40] Shao-Dong Wang and Karen L. Scrivener. Hydration products of alkali activated slag cement. *Cement and Concrete Research*, 25(3):561–571, 1995.

[41] T. C. Powers, L. E. Copeland, J. C. Hayes, and H. M. Mann. Permeablity of portland cement paste. *Proceedings of the American Concrete Institute*, pages 285–298, 1954.

[42] S. Goto and D. M. Roy. The effect of w/c ratio and curing temperature on the permeability of hardened cement paste. *Cement and Concrete Research*, 11(4):575–579, 1981.

[43] M. A. Sanjuán and R. Muñoz-Martialay. Influence of the water/cement ratio on the air permeability of concrete. *Journal of Materials Science*, 31(11):2829–2832, 1996.

[44] Z. Lafhaj, M. Goueygou, A. Djerbi, and M. Kaczmarek. Correlation between porosity, permeability and ultrasonic parameters of mortar with variable water/cement ratio and water content. *Cement and Concrete Research*, 36(4):625–633, 2006.

[45] J. Castro, D. P. Bentz, and J. Weiss. Effect of sample conditioning on the water absorption of concrete. *Cement and Concrete Composites*, 33(8):805–813, 2011.

[46] BSI (British Standards Institution). BS 8500: Complementary British Standard to BS EN 206, 2015.

[47] O. M. Jensen and P. F. Hansen. Water-entrained cement-based materials. *Cement and Concrete Research*, 31(4):647–654, 2001.

[48] S. Kosmatka and W. C. Panarese. *Design and Control of Concrete Mixtures*. Portland Cement Assn, 1988.

[49] F. R. McMillan and I. Lyse. Some permeability studies of concrete. In *Proceedings of the American Concrete Institute (ACI)*, 1929.

[50] D. Whiting. Permeability of selected concretes. *ACI Special Publication 108*, pages 195–222, 1988.

[51] P. A. Claisse. *Civil Engineering Materials*. Elsevier Science & Technology, 2015.

[52] J. Bijen. Benefits of slag and fly ash. *Construction and Building Materials*, 10(5): 309–314, 1996.

[53] H. A. Brodersen. *Zur Abhängigkeit der Transportvorgänge verschiedener Ionen im Beton von Struktur und Zusammensetzung des Zementsteins*. PhD thesis, Rheinisch-Westfälische Technische Hochschule (RWTH) Aachen, 1982.

[54] A. Bouikni, R.N. Swamy, and A. Bali. Durability properties of concrete containing 50% and 65% slag. *Construction and Building Materials*, 23(8):2836–2845, 2009.

[55] ASTM International. C642: Standard Test Method for Density, Absorption, and Voids in Hardened Concrete, 2013.

[56] BSI (British Standards Institution). BS 1881-122: Testing concrete. Method for determination of water absorption., 1996.

[57] T. J. Mays. A new classification of pore sizes. In *Studies in Surface Science and Catalysis*, volume 160, pages 57–62. Elsevier, 2007. doi: 10.1016/s0167-2991(07)80009-7.

[58] ISO (International Organization for Standardization). ISO 15901-1:2016: Evaluation of pore size distribution and porosity of solid materials by mercury porosimetry and gas adsorption – Part 1: Mercury porosimetry, 2016.

[59] ASTM International. D4284: Standard Test Method for Determining Pore Volume Distribution of Catalysts and Catalyst Carriers by Mercury Intrusion Porosimetry, 2012.

[60] ASTM International. D4404: Standard Test Method for Determination of Pore Volume and Pore Volume Distribution of Soil and Rock by Mercury Intrusion Porosimetry, 2018.

[61] H. L. Ritter and L. C. Drake. Pressure porosimeter and determination of complete macropore-size distributions. *Industrial & Engineering Chemistry Analytical Edition*, 17(12):782–786, 1945.

[62] J. Van Brakel, S. Modrý, and M. Svatá. Mercury porosimetry: state of the art. *Powder Technology*, 29(1):1–12, 1981.

[63] H. Giesche. Mercury porosimetry: A general (practical) overview. *Particle & Particle Systems Characterization*, 23(1):9–19, 2006.

[64] J-P. Gorce and N. B. Milestone. Probing the microstructure and water phases in composite cement blends. *Cement and Concrete Research*, 37(3):310–318, 2007.

[65] R. A. Cook and K. C. Hover. Mercury porosimetry of hardened cement pastes. *Cement and Concrete Research*, 29(6):933–943, 1999.

[66] R. L. Day and B. K. Marsh. Measurement of porosity in blended cement pastes. *Cement and Concrete Research*, 18(1):63–73, 1988.

[67] B. J. Christensen, T. O. Mason, and H. M. Jennings. Comparison of measured and calculated permeabilities for hardened cement pastes. *Cement and Concrete Research*, 26(9):1325–1334, 1996.

[68] R. Kumar and B. Bhattacharjee. Porosity, pore size distribution and in situ strength of concrete. *Cement and Concrete Research*, 33(1):155–164, 2003.

[69] D. Shi and D. N. Winslow. Contact angle and damage during mercury intrusion into cement paste. *Cement and Concrete Research*, 15(4):645–654, 1985.

[70] R. A. Olson, C. M. Neubauer, and H. M. Jennings. Damage to the pore structure of hardened portland cement paste by mercury intrusion. *Journal of the American Ceramic Society*, 80(9):2454–2458, 2005.

[71] F. Moro and H. Boehni. Ink-bottle effect in mercury intrusion porosimetry of cement-based materials. *Journal of Colloid and Interface Science*, 246(1):135–149, 2002.

[72] D. Windslow and S. Diamond. A mercury porosimetry study of the evolution of porosity in portland cement. *Technical Publications of the Joint Highway Research project*, 1969.

[73] K. Tanaka and K. Kurumisawa. Development of technique for observing pores in hardened cement paste. *Cement and Concrete Research*, 32(9):1435–1441, 2002.

[74] T. Deboodt, D. Wildenschild, J. H. Ideker, and O. B. Isgor. Use of iodine for improving phase quantification using X-ray tomography. *Cement and Concrete Research*, 116: 102–112, 2019.

[75] A. C. Kak and M. Slaney. *Principles of Computerized Tomographic Imaging (Classics in Applied Mathematics)*. Society for Industrial and Applied Mathematics, 1987.

[76] B. A. Dowd, G. H. Campbell, R. B. Marr, V. V. Nagarkar, S. V. Tipnis, L. Axe, and D. P. Siddons. Developments in synchrotron X-ray computed microtomography at the National Synchrotron Light Source. In U. Bonse, editor, *Developments in X-Ray Tomography II*. SPIE, 1999.

[77] F. Fusseis, X. Xiao, C. Schrank, and F. De Carlo. A brief guide to synchrotron radiation-based microtomography in (structural) geology and rock mechanics. *Journal of Structural Geology*, 65:1–16, 2014.

[78] P. F. J. New, W. R. Scott, J. J. A. Schnur, K. R. Davis, and J. M. Taveras. Computerized axial tomography with the emi scanner. *Radiology*, 110(1):109–123, 1974.

[79] D. C. Hatcher. Operational principles for cone-beam computed tomography. *The Journal of the American Dental Association*, 141:3S–6S, 2010.

[80] I. L. Morgan, H. Ellinger, R. Klinksiek, and J. N. Thompson. Examination of steel and concrete by computerized tomography. *Metal Construction*, 2:115–123, 1979.

[81] J. C. Elliott and S. D. Dover. X-ray microtomography. *Journal of Microscopy*, 126(2): 211–213, 1982.

[82] D. P. Bentz, N. S. Martys, P. Stutzman, M. S. Levenson, E. J. Garboczi, J. Dunsmuir, and L. M. Schwartz. X-Ray microtomography of an ASTM C109 mortar exposed to sulfate attack. *MRS Proceedings*, 370:77, 1994.

[83] S. P. Shah and S. Choi. Nondestructive techniques for studying fracture processes in concrete. *International Journal of Fracture*, 98(3):351, 1999.

[84] D. P. Bentz, S. Mizell, S. Satterfield, J. Devaney, W. George, P. Ketcham, J. Graham, and J. Porterfield. The visible cement data set. *Journal of Research of the National Institute of Standards and Technology*, 107(2):137, 2002.

[85] E. J. Garboczi and J. W. Bullard. Shape analysis of a reference cement. *Cement and Concrete Research*, 34(10):1933–1937, 2004.

[86] J. W. Bullard and E. J. Garboczi. A model investigation of the influence of particle shape on portland cement hydration. *Cement and Concrete Research*, 36(6):1007–1015, 2006.

[87] M. Koster, J. Hannawald, and W. Brameshuber. Simulation of water permeability and water vapor diffusion through hardened cement paste. *Computational Mechanics*, 37 (2):163–172, 2006.

[88] T. J. Chotard, M. P. Boncoeur-Martel, A. Smith, J. P. Dupuy, and C. Gault. Application of X-ray computed tomography to characterise the early hydration of calcium aluminate cement. *Cement and Concrete Composites*, 25(1):145–152, 2003.

[89] N. Burlion, D. Bernard, and D. Chen. X-ray microtomography: Application to microstructure analysis of a cementitious material during leaching process. *Cement and Concrete Research*, 36(2):346–357, 2006.

[90] J. L. Provis, R. J. Myers, C. E. White, V. Rose, and J. S. J. Van Deventer. X-ray microtomography shows pore structure and tortuosity in alkali-activated binders. *Cement and Concrete Research*, 42(6):855–864, 2012.

[91] M. A. B. Promentilla, T. Sugiyama, T. Hitomi, and N. Takeda. Quantification of tortuosity in hardened cement pastes using synchrotron-based X-ray computed microtomography. *Cement and Concrete Research*, 39(6):548–557, 2009.

[92] E. Gallucci, K. L. Scrivener, A. Groso, M. Stampanoni, and G. Margaritondo. 3d experimental investigation of the microstructure of cement pastes using synchrotron X-ray microtomography. *Cement and Concrete Research*, 37(3):360–368, 2007.

[93] A. du Plessis and W. P. Boshoff. A review of X-ray computed tomography of concrete and asphalt construction materials. *Construction and Building Materials*, 199:637 – 651, 2019.

[94] X. Xiao, F. Fusseis, and F. De Carlo. X-ray fast tomography and its applications in dynamical phenomena studies in geosciences at the Advanced Photon Source. In S. R. Stock, editor, *Developments in X-Ray Tomography VIII*. SPIE, 2012.

[95] F. De Carlo and B. Tieman. High-throughput X-ray microtomography system at the Advanced Photon Source beamline 2-BM. In U. Bonse, editor, *Developments in X-ray Tomography IV*. SPIE, 2004.

[96] A. A. MacDowell, D. Y. Parkinson, A. Haboub, E. Schaible, J. R. Nasiatka, C. A. Yee, J. R. Jameson, J. B. Ajo-Franklin, C. R. Brodersen, and A. J. McElrone. X-ray microtomography at the Advanced Light Source. In S. R. Stock, editor, *Developments in X-ray Tomography VIII*. SPIE, 2012.

[97] T. Bultreys, W. De Boever, and V. Cnudde. Imaging and image-based fluid transport modeling at the pore scale in geological materials: A practical introduction to the current state-of-the-art. *Earth-Science Reviews*, 155:93–128, 2016.

[98] S. S. Singh, T. J. Stannard, X. Xiao, and N. Chawla. In situ X-ray microtomography of stress corrosion cracking and corrosion fatigue in aluminum alloys. *JOM: The Journal of The Minerals, Metals & Materials Society (TMS)*, 69(8):1404–1414, 2017.

[99] H. Su, T. Yoshimura, H. Toda, M. S. Bhuiyan, K. Uesugi, A. Takeuchi, N. Sakaguchi, and Y. Watanabe. Influences of hydrogen micropores and intermetallic particles on fracture behaviors of Al-Zn-Mg-Cu aluminum alloys. *Metallurgical and Materials Transactions A*, 47(12):6077–6089, 2016.

[100] D. P. Finegan, M. Scheel, J. B. Robinson, B. Tjaden, I. Hunt, T. J. Mason, J. Millichamp, M. Di Michiel, G. J. Offer, G. Hinds, D. J. L. Brett, and P. R. Shearing. In-operando high-speed tomography of lithium-ion batteries during thermal runaway. *Nature Communications*, 6(1), 2015.

[101] S. Faulwetter, A. Vasileiadou, M. Kouratoras, T. Dailianis, and C. Arvanitidis. Micro-computed tomography: Introducing new dimensions to taxonomy. *ZooKeys*, 263: 1–45, 2013.

[102] S. M. Walker, D. A. Schwyn, R. Mokso, M. Wicklein, T. Mueller, M. Doube, M. Stampanoni, H. G. Krapp, and G. K. Taylor. In vivo time-resolved microtomography reveals the mechanics of the blowfly flight motor. *PLoS Biology*, 12(3):e1001823, 2014.

[103] T. Lowe, R. J. Garwood, T. J. Simonsen, R. S. Bradley, and P. J. Withers. Metamorphosis revealed: Time-lapse three-dimensional imaging inside a living chrysalis. *Journal of The Royal Society Interface*, 10(84):20130304–20130304, 2013.

[104] D. A. Matthijs De Winter, C. T. W. M. Schneijdenberg, M. N. Lebbink, B. Lich, A. J. Verkleij, M. R. Drury, and B. M. Humbel. Tomography of insulating biological and geological materials using focused ion beam (FIB) sectioning and low-kV BSE imaging. *Journal of Microscopy*, 233(3):372–383, mar 2009. doi: 10.1111/j.1365-2818.2009.03139.x.

[105] C. Holzapfel, W. Schäf, M. Marx, H. Vehoff, and F. Mücklich. Interaction of cracks with precipitates and grain boundaries: Understanding crack growth mechanisms through focused ion beam tomography. *Scripta Materialia*, 56(8):697–700, apr 2007. doi: 10.1016/j.scriptamat.2006.12.025.

[106] Alexandra Velichko and Frank Mücklich. Quantitative 3d characterisation of graphite morphology in cast iron – correlation between processing, microstructure and properties. *International Journal of Materials Research*, 100(8):1031–1037, aug 2009. doi: 10.3139/146.110148.

[107] P. Trtik, B. Münch, P. Gasser, A. Leemann, R. Loser, R. Wepf, and P. Lura. Focussed ion beam nanotomography reveals the 3d morphology of different solid phases in hardened cement pastes. *Journal of Microscopy*, 241(3):234–242, sep 2010. doi: 10.1111/j.1365-2818.2010.03433.x.

[108] Lorenz Holzer, Beat Muench, Markus Wegmann, Philippe Gasser, and Robert J. Flatt. FIB-nanotomography of particulate systems—part i: Particle shape and topology of interfaces. *Journal of the American Ceramic Society*, 89(8):2577–2585, aug 2006. doi: 10.1111/j.1551-2916.2006.00974.x.

[109] P. Trtik, J. Dual, B. Münch, and L. Holzer. Limitation in obtainable surface roughness of hardened cement paste: 'virtual' topographic experiment based on focussed ion

beam nanotomography datasets. *Journal of Microscopy*, 232(2):200–206, oct 2008. doi: 10.1111/j.1365-2818.2008.02090.x.

[110] P. A. Claisse. *Transport Properties of Concrete*. Woodhead Publishing, 2014.

[111] C. Hall. Water sorptivity of mortars and concretes: a review. *Magazine of Concrete Research*, 41(147):51–61, 1989.

[112] BSI (British Standards Institution). BS 1881-208: Testing concrete. Recommendations for the determination of the initial surface absorption of concrete, 2011.

[113] M. Levitt. The ISAT–A non-destructive test for the durability of concrete. *British Journal of Non Destructive Testing*, 13.4, 1971.

[114] P. J. McGlinn, F C. de Beer, L P. Aldridge, M. J. Radebe, R. Nshimirimana, D. R. M. Brew, T. E. Payne, and K. P. Olufson. Appraisal of a cementitious material for waste disposal: Neutron imaging studies of pore structure and sorptivity. *Cement and Concrete Research*, 40(8):1320–1326, 2010.

[115] Patrick J Barrie. Characterization of porous media using NMR methods. In *Annual Reports on NMR Spectroscopy*, pages 265–316. Elsevier, 2000. doi: 10.1016/s0066-4103(00)41011-2.

[116] H. Justnes, I. Meland, J. O. Bjoergum, J. Krane, and T. Skjetne. Nuclear magnetic resonance (NMR) —a powerful tool in cement and concrete research. *Advances in Cement Research*, 3(11):105–110, jul 1990. doi: 10.1680/adcr.1990.3.11.105.

[117] P. J. McDonald, A. M. Gajewicz, and R. Morrell. The characterisation of cement based materials using $t_2$ $^1$H nuclear magnetic resonance relaxation analysis. 2016.

[118] P. F. Faure and S. Rodts. Proton NMR relaxation as a probe for setting cement pastes. *Magnetic Resonance Imaging*, 26(8):1183–1196, oct 2008. doi: 10.1016/j.mri.2008.01.026.

[119] P. J. McDonald, J.-P. Korb, J. Mitchell, and L. Monteilhet. Surface relaxation and chemical exchange in hydrating cement pastes: A two-dimensional NMR relaxation study. *Physical Review E*, 72(1), jul 2005. doi: 10.1103/physreve.72.011409.

[120] Karen Friedemann, Wiete Schönfelder, Frank Stallmach, and Jörg Kärger. NMR relaxometry during internal curing of portland cements by lightweight aggregates. *Materials and Structures*, 41(10):1647–1655, jan 2008. doi: 10.1617/s11527-008-9355-0.

[121] N. Nestle. NMR relaxometry study of cement hydration in the presence of different oxidic fine fraction materials. *Solid State Nuclear Magnetic Resonance*, 25(1-3):80–83, jan 2004. doi: 10.1016/j.ssnmr.2003.05.003.

[122] A. C. A. Muller, K. L. Scrivener, A. M. Gajewicz, and P. J. McDonald. Densification of c–s–h measured by $^{1}$H NMR relaxometry. *The Journal of Physical Chemistry C*, 117(1):403–412, dec 2012. doi: 10.1021/jp3102964.

[123] A. C. A. Muller, K. L. Scrivener, A. M. Gajewicz, and P. J. McDonald. Use of bench-top NMR to measure the density, composition and desorption isotherm of c–s–h in cement paste. *Microporous and Mesoporous Materials*, 178:99–103, sep 2013. doi: 10.1016/j.micromeso.2013.01.032.

[124] A.C.A. Muller and K.L. Scrivener. A reassessment of mercury intrusion porosimetry by comparison with 1 h NMR relaxometry. *Cement and Concrete Research*, 100: 350–360, oct 2017. doi: 10.1016/j.cemconres.2017.05.024.

[125] N. Fischer, R. Haerdtl, and P. J. McDonald. Observation of the redistribution of nanoscale water filled porosity in cement based materials during wetting. *Cement and Concrete Research*, 68:148–155, feb 2015. doi: 10.1016/j.cemconres.2014.10.013.

[126] E. H. Lehmann, H. Pleinert, and L. Wiezel. Design of a neutron radiography facility at the spallation source SINQ. *Nuclear Instruments and Methods in Physics Research Section A: Accelerators, Spectrometers, Detectors and Associated Equipment*, 377(1): 11–15, 1996.

[127] E. Calzada, B. Schillinger, and F. Gruenauer. Construction and assembly of the neutron radiography and tomography facility ANTARES at FRM II. *Nuclear Instruments and Methods in Physics Research Section A: Accelerators, Spectrometers, Detectors and Associated Equipment*, 542(1-3):38–44, 2005.

[128] J. Thewlis. Neutron radiography. *British Journal of Applied Physics*, 7(10):345–350, 1956.

[129] H. Kallmann. Neutron radiography. *Research; a journal of science and its applications*, pages 254–260, 1948.

[130] M. R. Hawkesworth and J. Walker. Review: Radiography with neutrons. *Journal of Materials Science*, 4(9):817–835, 1969.

[131] E. H. Lehmann, P. Vontobel, and L. Wiezel. Properties of the radiography facility NEUTRA at SINQ and its potential for use as European reference facility. *Nondestructive Testing and Evaluation*, 16(2-6):191–202, 2001.

[132] T. Minniti, W. Kockelmann, G. Burca, J. F. Kelleher, S. Kabra, S. Y. Zhang, D. E. Pooley, E. M. Schooneveld, Q. Mutamba, J. Sykora, N. J. Rhodes, F. M. Pouzols, J. B. Nightingale, F. Aliotta, L. M. Bonaccorsi, R. Ponterio, G. Salvato, S. Trusso, C. Vasi, A. S. Tremsin, and G. Gorini. Materials analysis opportunities on the new neutron imaging facility IMAT@ISIS. *Journal of Instrumentation*, 11(03):C03014, 2016.

[133] T. Minniti, K. Watanabe, G. Burca, D. E. Pooley, and W. Kockelmann. Characterization of the new neutron imaging and materials science facility IMAT. *Nuclear Instruments and Methods in Physics Research Section A: Accelerators, Spectrometers, Detectors and Associated Equipment*, 888:184–195, 2018.

[134] H. Justnes, K. Bryhn-Ingebrigtsen, and G. O. Rosvold. Neutron radiography: an excellent method of measuring water penetration and moisture distribution in cementitious materials. *Advances in Cement Research*, 6(22):67–72, 1994.

[135] F. C. De Beer, J. J. Le Roux, and E. P. Kearsley. Testing the durability of concrete with neutron radiography. *Nuclear Instruments and Methods in Physics Research Section A: Accelerators, Spectrometers, Detectors and Associated Equipment*, 542(1-3):226–231, 2005.

[136] K. Van Tittelboom, D. Snoeck, P. Vontobel, F. H. Wittmann, and N. De Belie. Use of neutron radiography and tomography to visualize the autonomous crack sealing efficiency in cementitious materials. *Materials and Structures*, 46(1-2):105–121, 2013.

[137] D. Snoeck, S. Steuperaert, K. Van Tittelboom, P. Dubruel, and N. De Belie. Visualization of water penetration in cementitious materials with superabsorbent polymers by means of neutron radiography. *Cement and Concrete Research*, 42(8):1113–1121, 2012.

[138] M. Kanematsu, I. Maruyama, T. Noguchi, H. Iikura, and N. Tsuchiya. Quantification of water penetration into concrete through cracks by neutron radiography. *Nuclear Instruments and Methods in Physics Research Section A: Accelerators, Spectrometers, Detectors and Associated Equipment*, 605(1-2):154–158, 2009.

[139] P. Zhang, F. H. Wittmann, T. Zhao, and E. H. Lehmann. Neutron imaging of water penetration into cracked steel reinforced concrete. *Physica B: Condensed Matter*, 405 (7):1866–1871, 2010.

[140] P. Trtik, B. Münch, W. J. Weiss, A. Kaestner, I. Jerjen, L. Josic, E. Lehmann, and P. Lura. Release of internal curing water from lightweight aggregates in cement paste investigated by neutron and X-ray tomography. *Nuclear Instruments and Methods in Physics Research Section A: Accelerators, Spectrometers, Detectors and Associated Equipment*, 651(1):244–249, 2011.

[141] P. A. Claisse, H. Elsayad, I. Hanaa, and I. G. Shaaban. Absorption and sorptivity of cover concrete. *Journal of Materials in Civil Engineering*, 9(3):105–110, 1997.

[142] Y. Zhao, S. Xue, S. Han, Z. Chen, S. Liu, D. Elsworth, L. He, J. Cai, Y. Liu, and D. Chen. Effects of microstructure on water imbibition in sandstones using X-ray computed tomography and neutron radiography. *Journal of Geophysical Research: Solid Earth*, 122(7):4963–4981, 2017.

[143] A. Dara, B. A. Moradi, P. Vontobel, and S. E. Oswald. Mapping compensating root water uptake in heterogeneous soil conditions via neutron radiography. *Plant and Soil*, 397(1-2):273–287, 2015.

[144] M. A. Ahmed, M. Zarebanadkouki, F. Meunier, M. Javaux, A. Kaestner, and A. Carminati. Root type matters: measurement of water uptake by seminal, crown, and lateral roots in maize. *Journal of Experimental Botany*, 69(5):1199–1206, 2018.

[145] A. Smith, H. Botha, F. C. de Beer, and E. Ferg. The examination, analysis and conservation of a bronze Egyptian Horus statuette. *Nuclear Instruments and Methods in Physics Research Section A: Accelerators, Spectrometers, Detectors and Associated Equipment*, 651(1):221–228, 2011.

[146] J. L. Kickhofel, R. Zboray, M. Damsohn, A. Kaestner, E. H. Lehmann, and H.-M. Prasser. Cold neutron tomography of annular coolant flow in a double subchannel model of a boiling water reactor. *Nuclear Instruments and Methods in Physics Research Section A: Accelerators, Spectrometers, Detectors and Associated Equipment*, 651(1):297–304, 2011.

[147] N. Takenaka, H. Asano, K. Sugimoto, H. Murakawa, N. Hashimoto, N. Shindo, K. Mochiki, and R. Yasuda. Visualization of dynamic 3-d water behavior in polymer electrolyte fuel cell by using neutron image intensifier. *Nuclear Instruments and*

*Methods in Physics Research Section A: Accelerators, Spectrometers, Detectors and Associated Equipment*, 651(1):277–281, 2011.

[148] C. Galle. Effect of drying on cement-based materials pore structure as identified by mercury intrusion porosimetry. *Cement and Concrete Research*, 31(10):1467–1477, 2001.

[149] ASTM International. C642: Standard Test Method for Density, Absorption, and Voids in Hardened Concrete, 1997.

[150] ASTM International. C642: Standard Test Method for Density, Absorption, and Voids in Hardened Concrete, 2006.

[151] ASTM International. C642: Standard Test Method for Density, Absorption, and Voids in Hardened Concrete, 2011.

[152] ASTM International. C1585: Standard Test Method for Measurement of Rate of Absorption of Water by Hydraulic-Cement Concretes, 2004.

[153] ASTM International. C1585: Standard Test Method for Measurement of Rate of Absorption of Water by Hydraulic-Cement Concretes, 2011.

[154] B. B. Sabir, S. Wild, and M. O'Farrell. A water sorptivity test for mortar and concrete. *Materials and Structures*, 31(8):568–574, 1998.

[155] W. Z. Zheng, X. M. Hou, D. S. Shi, and M. X. Xu. Experimental study on concrete spalling in prestressed slabs subjected to fire. *Fire Safety Journal*, 45(5):283–297, 2010.

[156] P. Kalifa, F-D. Menneteau, and D. Quenard. Spalling and pore pressure in HPC at high temperatures. *Cement and Concrete Research*, 30(12):1915–1927, 2000.

[157] J. Piasta, Z. Sawicz, and L. Rudzinski. Changes in the structure of hardened cement paste due to high temperature. *Matériaux et Constructions*, 17(4):291–296, 1984.

[158] H. S. Wong, M. Zobeland N. R. Buenfeld, and R. W. Zimmerman. Influence of the interfacial transition zone and microcracking on the diffusivity, permeability and sorptivity of cement-based materials after drying. *Magazine of Concrete Research*, 61(8): 571–589, 2009.

[159] F. S. Rostasy, R. Weiss, and G. Wiedemann. Changes of pore structure of cement mortars due to temperature. *Cement and Concrete Research*, 10(2):157–164, 1980.

[160] M. Saeidpour and L. Wadsö. Moisture equilibrium of cement based materials containing slag or silica fume and exposed to repeated sorption cycles. *Cement and Concrete Research*, 69:88–95, 2015.

[161] M. C. R. Farage, J. Sercombe, and C. Gallé. Rehydration and microstructure of cement paste after heating at temperatures up to 300°C. *Cement and Concrete Research*, 33 (7):1047–1056, 2003.

[162] M. Wu, B. Johannesson, and M. Geiker. A study of the water vapor sorption isotherms of hardened cement pastes: Possible pore structure changes at low relative humidity and the impact of temperature on isotherms. *Cement and Concrete Research*, 56: 97–105, 2014.

[163] E. J. Butcher and M. Hayes. Product longevity for ALFA: Characterisation of historic Magnox encapsulation plant cementation samples. Private Communication, 2010.

[164] S. Lowell, J. E. Shields, and M. Thommes. *Characterization of Porous Solids and Powders: Surface Area, Pore Size and Density*. Springer Netherlands, 2010.

[165] P. C. Hewlett and M. Liska (eds). *Lea's Chemistry of Cement and Concrete*. Elsevier, 2019.

[166] ASTM International. C150: Standard specification for Portland cement, 2018.

[167] J. F. Lamond and J. H. Pielert, editors. *Significance of Tests and Properties of Concrete and Concrete-Making Materials*. ASTM International, 2006.

[168] BSI (British Standards Institution). BS EN 196-6: Methods of testing cement. Determination of fineness, 2018.

[169] BSI (British Standards Institution). BS 12: Portland Cement, 1910.

[170] D. P. Bentz, E. J. Garboczi, C. J. Haecker, and O. M. Jensen. Effects of cement particle size distribution on performance properties of portland cement-based materials. *Cement and Concrete Research*, 29(10):1663–1671, 1999.

[171] M. Kerker. *The Scattering of Light and Other Electromagnetic Radiation*. Elsevier, 1969.

[172] I. B. Celik. The effects of particle size distribution and surface area upon cement strength development. *Powder Technology*, 188(3):272–276, 2009.

[173] Y. M. Zhang and T. J. Napier-Munn. Effects of particle size distribution, surface area and chemical composition on portland cement strength. *Powder Technology*, 83(3): 245–252, 1995.

[174] R. H. Bogue. Calculation of the compounds in portland cement. *Industrial & Engineering Chemistry Analytical Edition*, 1(4):192–197, 1929.

[175] D. P. Prentice, S. A. Bernal, M. Bankhead, M. Hayes, and J. L. Provis. Phase evolution of slag-rich cementitious grouts for immobilisation of nuclear wastes. *Advances in Cement Research*, 30(8):345–360, 2018.

[176] H. F. W. Taylor. Modification of the Bogue calculation. *Advances in Cement Research*, 2(6):73–77, 1989.

[177] V. S. Ramachandran, R. M. Paroli, J. J. Beaudoin, and A. H. Delgado. *Handbook of thermal analysis of construction materials*. Noyes Publications, 2002. ISBN 0-8155-1487-5.

[178] X. Wu, D. M. Roy, and C. A. Langton. Early stage hydration of slag-cement. *Cement and Concrete Research*, 13(2):277–286, 1983.

[179] R. Taylor, I. G. Richardson, and R. M. D. Brydson. Composition and microstructure of 20-year-old ordinary portland cement–ground granulated blast-furnace slag blends containing 0 to 100% slag. *Cement and Concrete Research*, 40(7):971–983, 2010.

[180] J. I. Escalante-Garcia and J. H Sharp. The microstructure and mechanical properties of blended cements hydrated at various temperatures. *Cement and Concrete Research*, 31(5):695–702, 2001.

[181] J. Bensted. Some applications of conduction calorimetry to cement hydration. *Advances in Cement Research*, 1(1):35–44, 1987.

[182] G. S. Pawley. Unit-cell refinement from powder diffraction scans. *Journal of Applied Crystallography*, 14(6):357–361, 1981.

[183] N. V. Y. Scarlett and I. C. Madsen. Quantification of phases with partial or no known crystal structures. *Powder Diffraction*, 21(4):278–284, 2006.

[184] H. M. Rietveld. A profile refinement method for nuclear and magnetic structures. *Journal of Applied Crystallography*, 2(2):65–71, 1969.

[185] R. Snellings, G. Mertens, Ö. Cizer, and J. Elsen. Early age hydration and pozzolanic reaction in natural zeolite blended cements: Reaction kinetics and products by in situ synchrotron X-ray powder diffraction. *Cement and Concrete Research*, 40(12):1704–1713, 2010.

[186] M. Merlini, M. Gemmi, G. Cruciani, and G. Artioli. High-temperature behaviour of melilite: in situ X-ray diffraction study of gehlenite–åkermanite–Na melilite solid solution. *Physics and Chemistry of Minerals*, 35(3):147–155, 2007.

[187] C. Hesse, F. Goetz-Neunhoeffer, J. Neubauer, M. Braeu, and P. Gaeberlein. Quantitative in situ X-ray diffraction analysis of early hydration of portland cement at defined temperatures. *Powder Diffraction*, 24(02):112–115, 2009.

[188] S. P. Thompson, J. E. Parker, J. Potter, T. P. Hill, A. Birt, T. M. Cobb, F. Yuan, and C. C. Tang. Beamline I11 at Diamond: A new instrument for high resolution powder diffraction. *Review of Scientific Instruments*, 80(7):075107, 2009.

[189] S. P. Thompson, J. E. Parker, J. Marchal, J. Potter, A. Birt, F. Yuan, R. D. Fearn, A. R. Lennie, S. R. Street, and C. C. Tang. Fast X-ray powder diffraction on I11 at Diamond. *Journal of Synchrotron Radiation*, 18(4):637–648, 2011.

[190] A. Coelho. TOPAS Academic Technical Reference. Technical report, Coelho Software, 2012.

[191] G. W. Brindley. XLV. the effect of grain or particle size on X-ray reflections from mixed powders and alloys, considered in relation to the quantitative determination of crystalline substances by X-ray methods. *The London, Edinburgh, and Dublin Philosophical Magazine and Journal of Science*, 36(256):347–369, 1945.

[192] D. Jansen, Ch. Stabler, F. Goetz-Neunhoeffer, S. Dittrich, and J. Neubauer. Does ordinary portland cement contain amorphous phase? a quantitative study using an external standard method. *Powder Diffraction*, 26(01):31–38, 2011.

[193] C. R. Hubbard and R. L. Snyder. RIR - measurement and use in quantitative XRD. *Powder Diffraction*, 3(02):74–77, 1988.

[194] A. Hajimohammadi, J. L. Provis, and J. S. J. van Deventer. Time-resolved and spatially-resolved infrared spectroscopic observation of seeded nucleation controlling geopolymer gel formation. *Journal of Colloid and Interface Science*, 357(2):384–392, 2011.

[195] B. Y. Lee and K. E. Kurtis. Influence of $TiO_2$ nanoparticles on early $C_3S$ hydration. *Journal of the American Ceramic Society*, 93(10):3399–3405, 2010.

[196] R. J. Hill and C. J. Howard. Quantitative phase analysis from neutron powder diffraction data using the Rietveld method. *Journal of Applied Crystallography*, 20(6):467–474, 1987.

[197] B. Lothenbach and F. Winnefeld. Thermodynamic modelling of the hydration of portland cement. *Cement and Concrete Research*, 36(2):209–226, 2006.

[198] A. Coelho. TOPAS and TOPAS-academic: an optimization program integrating computer algebra and crystallographic objects written in C++. *Journal of Applied Crystallography*, 51(1):210–218, 2018.

[199] A. G. De La Torre, S. Bruque, J. Campo, and M. A. G Aranda. The superstructure of $C_3S$ from synchrotron and neutron powder diffraction and its role in quantitative phase analyses. *Cement and Concrete Research*, 32(9):1347–1356, 2002.

[200] W. G. Mumme, R. J. Hill, G. Bushnell-Wye, and E. R. Segnit. Rietveld crystal structure refinements, crystal chemistry and calculated powder diffraction data for the polymorphs of dicalcium silicate and related phases. *Neues Jahrbuch fuer Mineralogie - Abhandlungen*, 169(1):35–68, 1995.

[201] P. Mondal and J. W. Jeffery. The crystal structure of tricalcium aluminate, $Ca_3Al_2O_6$. *Acta Crystallographica Section B Structural Crystallography and Crystal Chemistry*, 31(3):689–697, 1975.

[202] A. A. Colville and S. Geller. The crystal structure of brownmillerite, $Ca_2FeAlO_5$. *Acta Crystallographica Section B Structural Crystallography and Crystal Chemistry*, 27(12):2311–2315, 1971.

[203] A. G. De la Torre, M-G. López-Olmo, C. Álvarez-Rua, S. García-Granda, and M. A. G. Aranda. Structure and microstructure of gypsum and its relevance to rietveld quantitative phase analyses. *Powder Diffraction*, 19(03):240–246, 2004.

[204] A. Kirfel and G. Will. Charge density in anhydrite, $CaSO_4$, from X-ray and neutron diffraction measurements. *Acta Crystallographica Section B Structural Crystallography and Crystal Chemistry*, 36(12):2881–2890, 1980.

[205] E. N. Maslen, V. A. Streltsov, N. R. Streltsova, and N. Ishizawa. Electron density and optical anisotropy in rhombohedral carbonates. III. synchrotron X-ray studies of $CaCO_3$, $MgCO_3$ and $MnCO_3$. *Acta Crystallographica Section B Structural Science*, 51(6):929–939, 1995.

[206] F. Goetz-Neunhoeffer and J. Neubauer. Refined ettringite ($Ca_6Al_2(SO_4)_3(OH)_{12}\cdot 26H_2O$) structure for quantitative X-ray diffraction analysis. *Powder Diffraction*, 21(01):4–11, 2006.

[207] H. E. Petch. The hydrogen positions in portlandite, $Ca(OH)_2$ as indicated by the electron distribution. *Acta Crystallographica*, 14(9):950–957, 1961.

[208] T. Runčevski, R. E. Dinnebier, O. V. Magdysyuk, and H. Poellmann. Crystal structures of calcium hemicarboaluminate and carbonated calcium hemicarboaluminate from synchrotron powder diffraction data. *Acta Crystallographica Section B Structural Science*, 68(5):493–500, 2012.

[209] M. A. T. M. Broekmans and H. Poellmann, editors. *Applied Mineralogy of Cement & Concrete*. deGruyter Boston, 2018.

[210] M. Hellenbrandt. The inorganic crystal structure database (ICSD)—present and future. *Crystallography Reviews*, 10(1):17–22, 2004.

[211] P. Faucon, A. Delagrave, C. Richet, J. M. Marchand, and H. Zanni. Aluminum incorporation in calcium silicate hydrates (C-S-H) depending on their ca/si ratio. *The Journal of Physical Chemistry B*, 103(37):7796–7802, sep 1999.

[212] J. Y. Buffiere, E. Maire, J. Adrien, J. P. Masse, and E. Boller. In situ experiments with X-ray tomography: An attractive tool for experimental mechanics. *Experimental Mechanics*, 50(3):289–305, 2010.

[213] R. Snellings, G. Mertens, R. Adriaens, and J. Elsen. In situ synchrotron X-ray powder diffraction study of the early age hydration of cements blended with zeolitite and quartzite fines and water-reducing agent. *Applied Clay Science*, 72:124–131, 2013.

[214] M. A. G. Aranda. Recent studies of cements and concretes by synchrotron radiation crystallographic and cognate methods. *Crystallography Reviews*, 22(3):150–196, 2015.

[215] K. L. Scrivener. Backscattered electron imaging of cementitious microstructures: Understanding and quantification. *Cement and Concrete Composites*, 26(8):935–945, 2004.

[216] J. Stark. Recent advances in the field of cement hydration and microstructure analysis. *Cement and Concrete Research*, 41(7):666–678, 2011.

[217] S. Diamond. The microstructure of cement paste and concrete—a visual primer. *Cement and Concrete Composites*, 26(8):919–933, 2004.

[218] R. Ylmén, U. Jäglid, B. M. Steenari, and I. Panas. Early hydration and setting of portland cement monitored by IR, SEM and Vicat techniques. *Cement and Concrete Research*, 39(5):433–439, 2009.

[219] D. Gürsoy, F. De Carlo, X. Xiao, and C. Jacobsen. TomoPy: a framework for the analysis of synchrotron tomographic data. *Journal of Synchrotron Radiation*, 21(5): 1188–1193, 2014.

[220] D. M. Pelt, D. Gürsoy, D. Palenstijn, W. J. Sijbers, F. De Carlo, and K. J. Batenburg. Integration of TomoPy and the ASTRA toolbox for advanced processing and reconstruction of tomographic synchrotron data. *Journal of Synchrotron Radiation*, 23(3): 842–849, 2016.

[221] B. Münch, P. Trtik, F. Marone, and M. Stampanoni. Stripe and ring artifact removal with combined wavelet—fourier filtering. *Optics Express*, 17(10):8567, 2009.

[222] M. Vogelgesang, L. Rota, L. E. Ardila P., M. Caselle, S. Chilingaryan, and Kopmann. High-throughput data acquisition and processing for real-time X-ray imaging. In S. R. Stock, B. Müller, and G. Wang, editors, *Developments in X-Ray Tomography X*. SPIE, 2016.

[223] D. Paganin, S. C. Mayo, T. E. Gureyev, P. R. Miller, and S. W. Wilkins. Simultaneous phase and amplitude extraction from a single defocused image of a homogeneous object. *Journal of Microscopy*, 206(1):33–40, 2002.

[224] K. Pulli, A. Baksheev, K. Kornyako, and V. Eruhimov. Realtime computer vision with OpenCV. *Queue - Processors*, 10(4):40, 2012.

[225] The GTK Team. The GTK Project. Accessed July 2015. URL `https://www.gtk.org/`.

[226] S. van der Walt, J. L. Schoenberger, J. Nunez-Iglesias, F. Boulogne, J. D. Warner, N. Yager, E. Gouillart, and T. Yu. scikit-image: image processing in python. *PeerJ*, 2: e453, 2014.

[227] J. C. Yoo and T. H. Han. Fast normalized cross-correlation. *Circuits, Systems and Signal Processing*, 28(6):819–843, 2009.

[228] Z. Wang, A. C. Bovik, H. R. Sheikh, and E. P. Simoncelli. Image quality assessment: from error visibility to structural similarity. *IEEE Transactions on Image Processing*, 13(4):600–612, 2004.

[229] Z. Wang and A. C. Bovik. A universal image quality index. *IEEE Signal Processing Letters*, 9(3):81–84, 2002.

[230] J. Ahrens, B. Geveci, and C. Law. Paraview: An end-user tool for large data visualization. *The visualization handbook*, 717, 2005.

[231] A. O. de Carvalho Filho, W. Borges de Sampaio, A. C. Silva, A. Cardoso de Paiva, R. A. Nunes, and M. Gattass. Automatic detection of solitary lung nodules using quality threshold clustering, genetic algorithm and diversity index. *Artificial Intelligence in Medicine*, 60(3):165–177, 2014.

[232] M. A. B. Promentilla, T. Sugiyama, T. Hitomi, and N. Takeda. Characterizing the 3D pore structure of hardened cement paste with synchrotron microtomography. *Journal of Advanced Concrete Technology*, 6(2):273–286, 2008.

[233] E. Pustovgar, J. B. d'Espinose, M. Palacios, A. Andreev, R. Sangodkar, B. Chmelka, and R. J. Flatt. Revealing the steps of tricalcium silicate hydration. In *Proceedings 14th ICCC Beijing*, 2015.

[234] S. Bae, M. Kanematsu, D. Hernández-Cruz, J. Moon, D. Kilcoyne, and P. Monteiro. In situ soft X-ray spectromicroscopy of early tricalcium silicate hydration. *Materials*, 9(12):976, 2016.

[235] I. Odler and R. Wonnemann. Effect of alkalies on portland cement hydration II. alkalies present in form of sulphates. *Cement and Concrete Research*, 13(6):771–777, 1983.

[236] A. Bazzoni. *Study of early hydration mechanisms of cement by means of electron microscopy*. PhD thesis, EPFL, Switzerland, 2014.

[237] E. Gallucci, P. Mathur, and K. L. Scrivener. Microstructural development of early age hydration shells around cement grains. *Cement and Concrete Research*, 40(1):4–13, 2010.

[238] S. A. Bernal, J. L. Provis, A. Fernández-Jiménez, P. V. Krivenko, E. Kavalerova, M. Palacios, and C. Shi. *Binder Chemistry – High-Calcium Alkali-Activated Materials - State of the Art Report RILEM TC 224-AAM*. Springer Netherlands, 2014.

[239] D. A. Geddes, X. Ke, S. A. Bernal, M. Hayes, and J. L. Provis. Metakaolin-based geopolymers for nuclear waste encapsulation. In *RILEM Bookseries*, pages 183–188. Springer Netherlands, 2017.

[240] I. G. Richardson. The nature of C-S-H in hardened cements. *Cement and Concrete Research*, 29(8):1131–1147, 1999.

[241] J. Alkemper and P. W. Voorhees. Quantitative serial sectioning analysis. *Journal of Microscopy*, 201(3):388–394, 2001.

[242] P. A. Yushkevich, Y. Gao, and G. Gerig. Itk-snap: An interactive tool for semi-automatic segmentation of multi-modality biomedical images. In *2016 38th Annual International Conference of the IEEE Engineering in Medicine and Biology Society (EMBC)*, pages 3342–3345, 2016.

[243] F. De Carlo, X. Xiao, and B. Tieman. X-ray tomography system, automation, and remote access at beamline 2-BM of the Advanced Photon Source. In U. Bonse, editor, *Developments in X-Ray Tomography V*. SPIE, 2006.

[244] P. A. Wedding, D. Manmohan, and P. K. Mehta. Influence of pozzolanic, slag, and chemical admixtures on pore size distribution and permeability of hardened cement pastes. *Cement, Concrete and Aggregates*, 3(1):63–67, 1981.

[245] R. D. Hooton. Permeability and pore structure of cement pastes containing fly ash, slag, and silica fume. In *Blended cements*, pages 128–143. ASTM International, 1986.

[246] Paul Scherrer Institute (PSI). Neutron Imaging Detectors. Accessed December 2015, 2019 (updated since accessed). URL `https://www.psi.ch/en/niag/neutron-imaging-detectors`.

[247] R. K. Hassanein. *Correction methods for the quantitative evaluation of thermal neutron tomography*. PhD thesis, ETH Zurich, 2006.

[248] B. K. Jones D. Beazley. *Python Cookbook*. O'Reilly UK Ltd., 2013. ISBN 1449340377.

[249] E. Jones, T. Oliphant, and P. Peterson. SciPy: Open source scientific tools for Python. Accessed November 2015, 2001. URL `https://www.scipy.org/`.

[250] E. Berodier and K. L. Scrivener. Evolution of pore structure in blended systems. *Cement and Concrete Research*, 73:25–35, 2015.

[251] C. L. Page, N. R. Short, and A. El-Tarras. Diffusion of chloride ions in hardened cement pastes. *Cement and oncrete research*, 11(3):395–406, 1981.

[252] S. Guido. *Introduction to Machine Learning with Python*. O'Reilly UK Ltd., 2016. ISBN 1449369413.

[253] L. Ding and A. Goshtasby. On the canny edge detector. *Pattern Recognition*, 34(3): 721–725, 2001.

[254] V. Kocaba, E. Gallucci, and K. L. Scrivener. Methods for determination of degree of reaction of slag in blended cement pastes. *Cement and Concrete Research*, 42(3): 511–525, 2012.

[255] R. R. Lloyd, J. L. Provis, K. J. Smeaton, and J. S. J. van Deventer. Spatial distribution of pores in fly ash-based inorganic polymer gels visualised by wood's metal intrusion. *Microporous and Mesoporous Materials*, 126(1-2):32–39, 2009.

[256] Y. S. Chu, C. Liu, D. C. Mancini, F. De Carlo, A. T. Macrander, B. Lai, and D. Shu. Performance of a double-multilayer monochromator at beamline 2-BM at the Advanced Photon Source. *Review of Scientific Instruments*, 73(3):1485–1487, 2002.

[257] T. van der Vaeren. Designing a beam dump for a 600 MeV Myrrha linear proton accelerator. Master's thesis, Belgian Nuclear Research Centre, 2011.

# Appendix A

# Particle Accelerators

Here, the operation, design, and use of synchrotron and neutron facilities is provided here for conciseness in the body of the thesis and to avoid repetition. Section A.1 relates directly to the work completed in Chapters 4, 5, and 6. Chapter 7 is covered by the descriptions provided in Section A.4.

## A.1 Synchrotron Light

Due to an exceptionally high X-ray flux and therefore the ability to acquire data at a very high temporal resolution, a synchrotron particle accelerator makes a perfect source from which photons can be sourced to rapidly observe dynamic processes. The facilities used in this thesis are the Diamond Light Source (referred to as DLS) and the Advanced Photon Source (referred to as APS). Here a brief description of these sources is provided, which gives context to the chapters following.

The typical form of a synchrotron is shown in Figure A.1. This is a powerful source of radiation which is emitted when the direction of travel of a charged particle is changed by an electromagnetic force. This occurs in a storage ring which is held under vacuum. A high energy electron beam orbits the ring. From the sky the storage ring may appear to be perfectly circular, though this is not the case. The ring is made up of a series of straight joined segments which form a polygonal ring. The ring at the Diamond Light Source is made up from 24 straight segments which are closed forming a loop. The Advanced Photon Source has a storage ring consisting of 40 straight segments. The rings have a circumference of approximately 560 m and 1100 metres at these facilities respectively.

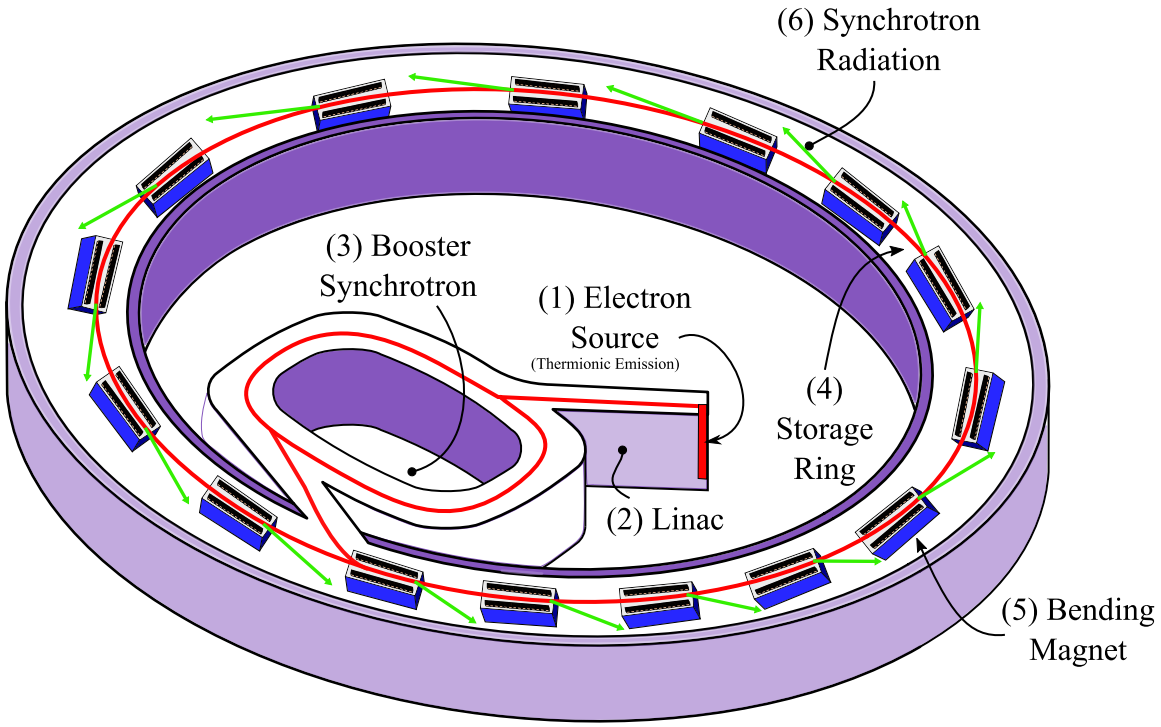


Figure A.1: The typical configuration of a synchrotron, simplified.

### A.1.1 Generating Electrons

The beam is initially generated by an electron gun. A cathode is heated in a vacuum, and electrons are emitted from the surface. These electrons accelerate toward a positively charged anode. The beam is accelerated to a far higher energy level (keV to MeV) in a linear accelerator (LINAC), which uses radio frequency cavities (RF cavities). These are small devices using a magnetic field oscillating at a radio frequency to boost the energy of the beam.

Electrons are injected to a booster synchrotron, which is a smaller ring contained within the central area of the storage ring (see Figure A.1). In the case of the Diamond Light Source this ring is made up of two straight segments with curves at either end. The beam is accelerated in the ring to extraction energy in the GeV range by additional RF cavities before injection into the storage ring. The accelerator facility is not used to produce synchrotron radiation, and only serves to provide a stream of electrons to the main ring.

### A.1.2 Filling the Beam

The beam depletes and energy is lost in transmission of electrons around the ring. Both the Diamond Light Source and Advanced Photon Source are able to run a continuous fill of the storage ring, known as “top-up” mode. In order to maintain the flux across the facility the

current in the storage ring is kept approximately constant by frequent injection. Alternatively the energy of the storage ring may be allowed to deplete and the ring is filled only when the energy of the beam drops below a certain threshold.

### A.1.3 Bending Magnets

As electrons orbit the facility, the beam must change trajectory at each vertex. This is induced by a dipole bending magnet which deflects the beam from one straight segment to another. The change in direction results in the emission of very bright synchrotron radiation of a high flux and high brilliance. The resulting radiation contains frequencies across the entire electromagnetic spectrum which are filtered using a monochromator where a specific energy is required. Otherwise the beam is left unfiltered which yields a higher flux.

### A.1.4 Insertion Devices

In addition to a bending magnet certain beamlines are provided with a brighter source by the addition of insertion devices which are placed either into or close to the storage ring. These are known as either undulators or wigglers depending on the manner in which the insertion device manipulates the electron beam.

## A.2 The I11 Instrument at the Diamond Light Source

Like many synchrotron based instruments I11 is well described in the literature [188]. As such the reader is further referred to the development papers when considering aspects of the instrument which may lie beyond the scope of this thesis. A brief description is provided here with the aim of providing a foundation upon which the method, analysis, and results may be understood.

I11 sources radiation from the storage ring of a synchrotron accelerator, further brightened by an insertion device, in this case a vacuum undulator. A collimator ensures a parallel beam is produced, followed by the selection of the desired wavelength, set by a double crystal monochromator and set of harmonic rejection mirrors [188].

Samples are first prepared in a laboratory accessible from the main ring of the facility and within close proximity to the end-station. It is possible to transfer samples from the laboratory to the experimental hutch within a number of minutes.

The primary end-station is photographed in Figure A.2. For dynamically changing materials samples are placed into a rotating store, which is accessed by a robotic arm. The

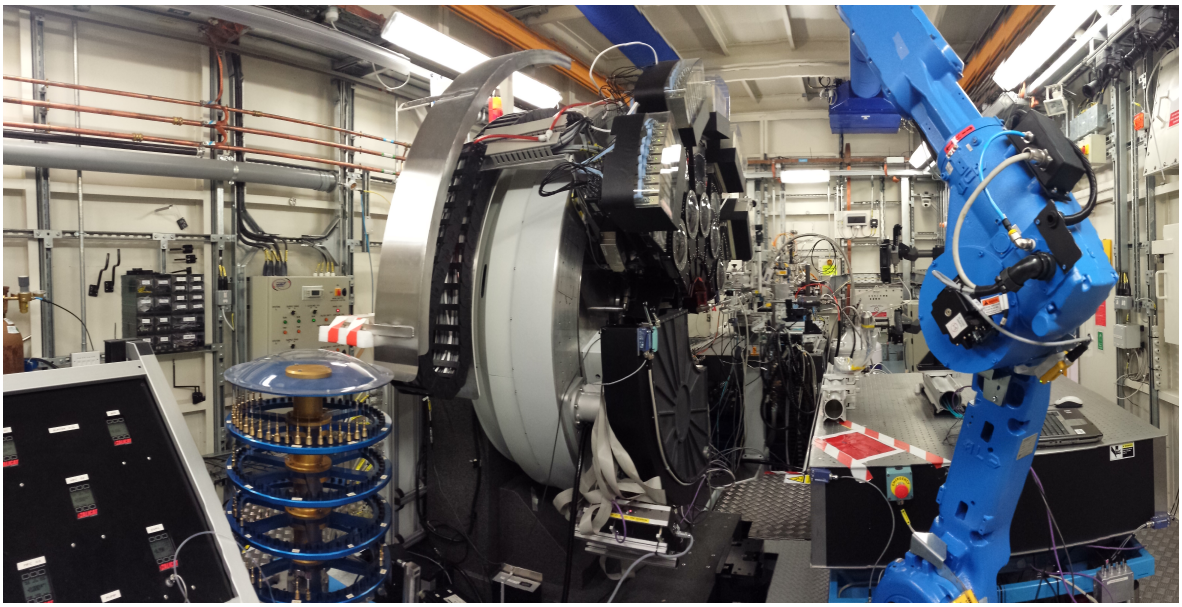

Figure A.2: The I11 instrument, showing the Mythen Position Sensitive Detector (PSD), bottom of the $\delta$ circle, the Multi-analyser Crystal (MAC), top of the $\delta$ circle, and sample cassette to the left.

controlling computer is programmed to automatically retrieve the sample at set intervals and place it into the beam for analysis. The facility is equipped with an array of multi-analyser crystals (MAC detector) for very high resolution scans for samples upon which a time resolved study is not so critical. This detector is capable of achieving a step resolution of $0.002°2\theta$. In the case of this thesis, these detectors are used where either the reaction has sufficiently slowed or anhydrous precursor materials are being characterised. The facility is further equipped with a Mythen Silicon Position Sensitive Detector (PSD which allows for very rapid acquisitions of high resolution [189], achieving a $2\theta$ step size of $0.004°$.

## A.3 The 2-BM Instrument at the Advanced Photon Source

The 2-BM instrument is a flexible microtomography beamline at the Advanced Photon Source synchrotron[1] (APS)[2]. The instrument is well described in the literature [95, 243]. A summary is provided here in order to supplement this.

The instrument sources photons from a dipole bending magnet and has an energy range of 11 to 35 keV filtered by a double-multilayer monochromator. The energy range may additionally be set to a "pink beam" spectrum to maintain a high flux while reducing beam hardening artefacts [256]. A beam diameter of 25 mm $\times$ 4 mm cross section allows for the observation of a fairly large specimen.

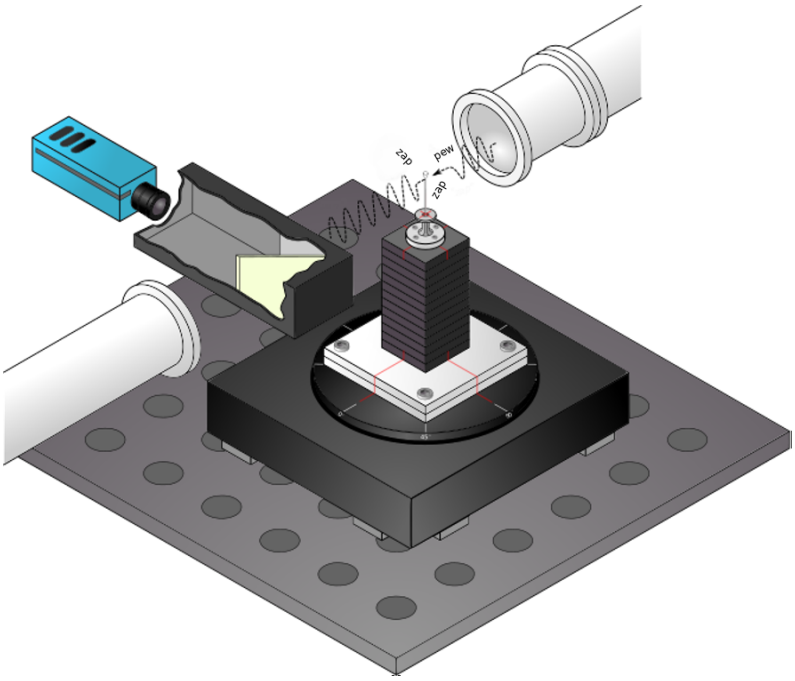


Figure A.3: Configuration of the 2-BM instrument endstation.

A self-levelling rotational stage is located below the centre of the beam, and contains a height-adjustable sample stack shown in Figure A.3. A silicon scintillator is located to the rear of the sample, which is connected to a mirror box and camera. Several cameras are available, including PCO.edge 30 fps high resolution and PCO.dimax 2000 fps high speed sCMOS devices.

The result of the high spatial resolution and high flux is the ability to carry out three dimensional fast tomography in-situ with a sub-second time resolution. Alternatively rapid

[1] See also Section A.1.
[2] Chicago, IL, USA.

high resolution tomography may be carried out on temporally static samples should the correct detector configuration be installed.

Fast tomography provides the ability to carry out tomography where very rapid processes such as chemical reactions are occurring. It becomes possible to effectively "freeze" the microstructure in three dimensions and resolve changes in the structure in-situ.

## A.4 The Neutron Spallation Reaction

In nuclear physics, spallation occurs when a target nucleus which is bombarded by subatomic particles breaks into several smaller parts. In a spallation neutron source, a proton beam is fired into a heavy metal target which typically consist of mercury, tantalum, or lead.

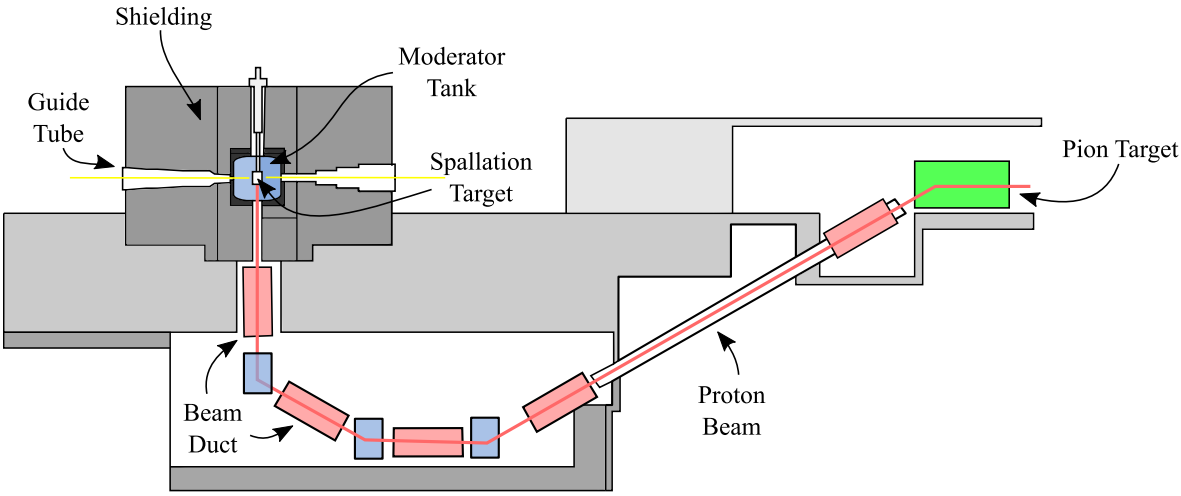


Figure A.4: The proton guide path to the spallation target (approximated) at the SINQ neutron source, adapted from van der Vaeren [257]. The spallation target is shown in Figure A.5.

At the Swiss spallation neutron source (SINQ), the beam is generated from a tank of hydrogen ions, which consists of a single proton and an orbiting electron. The electron is stripped and the proton accelerated to an energy of 0.87 MeV in a Cockroft Walton column. Protons are then accelerated to an energy of 72 MeV in an injector cyclotron and are then accelerated to 590 MeV in the main-ring cyclotron. The beam is then transported to the target through the floor of the hall after being decelerated slightly to 570 MeV (Figure A.4). After passing through the floor, the beam is transferred to the target hall.

Once within the target hall, the beam is guided to the target which is located within a shielded $D_2O$ moderator tank shown in Figure A.5. Neutrons spall from the bombarded target and decelerate in the heavy water moderator. This entire process is non-critical; no

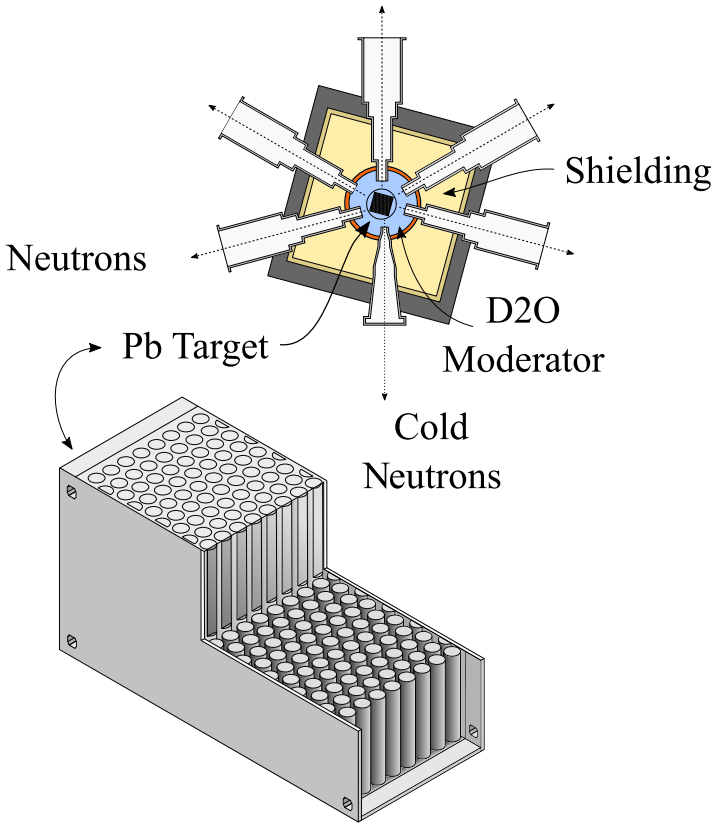


Figure A.5: The target at the SINQ source, located toward the centre-left of Figure A.4

chain reaction is involved. Cutting the proton beam immediately ceases spallation. The neutrons are then used for instruments in beamlines attached to the source.

# Appendix B

# 90% BFS Data

The data shown in Figure B.1 were removed from Figure 4.11 on page 82 for clarity in the plotted data.

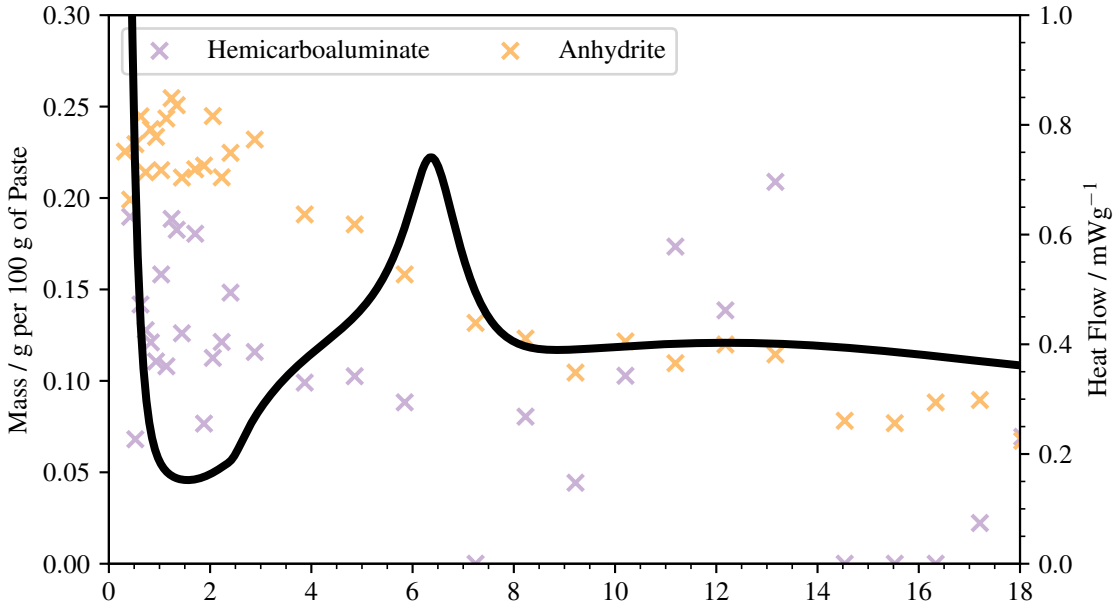


Figure B.1: The data removed from Figure 4.11.

# Appendix C

# Reconstructing Slices into a 3D Stack

This script runs an iterative reconstruction of an in-situ hdf file from the 2-BM instrument. Implementation here is designed for in-situ tests. The `tomopy` package provides us with base reconstruction methods. `tomocuda` allows for data correction on a graphics processing unit (GPU) which is theoretically capable of carrying out more floating point operations per second (FLOPS). `dxchange` provides i/o functions for tomopy. `datetime` gives us date and time output for logging.

```
import tomopy
import tomocuda
import os
import numpy as np
from tomopy.recon.rotation import write_center
from tomopy.recon.rotation import find_center_vo
from tomopy.recon.algorithm import recon
import dxchange as tir
import datetime
```

Set some directory information. We need the directory, the input file and the flat and open beam files. `offset` is the vertical portion of the stack from the end and beginning which is ignored. `margin_slices` removes artefacts from the beginning and end of each chunk. `chunk_size` is a memory restriction which limits the amount of data loaded in a single reconstruction iteration. If we have enough random access memory (RAM) we can do the entire stack in one hit.

```
offset            =  0 # See above.
total_num_slices  =  2000 # See above.
chunk_size        =  200 # See above.
if chunk_size > total_num_slices:
    chunk_size  =  total_num_slices

margin_slices  =  30 # See above.
num_chunk  =  np.int(total_num_slices/chunk_size) + 1
if total_num_slices == chunk_size:
    num_chunk  =  1

z    =  10
eng  =  27
pxl  =  0.875
zinger_level  =  200

data_dir   =  '' # String, input data directory.
file       =  '' # String, input data file.
file_flat  =  '' # String, open beam file.
file_dark  =  '' # String, Dark current file.
```

```
output_dir    =  data_dir
file_name     =  os.path.join(data_dir, file)
flat_name     =  os.path.join(data_dir, file_flat)
dark_name     =  os.path.join(data_dir, file_dark)
output_file   =  output_dir+'/recon_'+file.split(".")[-2]+'/recon_'+file.split(".")[-2]+'_'
```

Let's read some data from the filesystem and slice the data here, we will work with a smaller data volume to get the center of rotation of the specimen; this makes the operation faster as a reconstruction of the full stack is not required here. In the acquisitions from 2-BM these are stored in the `data_dark` volume in the hierarchical data format (HDF5). This is the raw data output format from the beamline.

```
data    =  tir.read_hdf5(file_name, '/exchange/data_dark',
                         slc = ((1801,2400), (700,720,1)))

white   =  tir.read_hdf5(flat_name, '/exchange/data_dark',
                         slc = ((1,9), (700,720,1)))

dark    =  tir.read_hdf5(dark_name, '/exchange/data_dark',
                         slc = ((1,9), (700,720,1)))

data_size  =  data.shape
theta  =  np.linspace(0,np.pi,num = data_size[0])
```

Take the data and open beam acquisitions, remove outliers from these. We do not remove outliers from the dark current results as these are inherently outliers. This is all done using the `tomocuda` toolkit which uses the NVIDIA CUDA interface.

```
data  =  tomocuda.remove_outlier_cuda(data,  zinger_level, size = 15)
white =  tomocuda.remove_outlier_cuda(white, zinger_level, size = 15)
```

We correct the data for open beam for scintillator artefacts and dark current for systematic noise. Data are normalized to scale values of air to 10 and everything else linearly inbetween. We remove the first slice as this becomes corrupt (reason unknown).

```
data  =  tomopy.prep.normalize.normalize(data,white,dark)
data  =  tomopy.prep.normalize.normalize_bg(data,air = 10)
data[0,:,:]  =  data[1,:,:]
```

Stripes are removed using the Fourier wavelet method. This is a quick operation so we carry this out using the CPU.

```
data  =  tomopy.prep.stripe.remove_stripe_fw(data, level = 6,
                                             wname = 'sym16',
                                             sigma = 2,
                                             pad = True)
```

Phase contrast is extracted and merged with the data using the normalisation parameter set by `rat`. We visually set this and leave it the same for all reconstructions.

```
rat   =  0.1e-02
data  =  tomopy.prep.phase.retrieve_phase(data,
```

```
data_size  =  data.shape
```

The center of rotation (axis of rotation) is estimated as the mid-point of the image and adjusted relative to this. An isolated slice is reconstructed with a varying center of rotation. The optimum center is then extracted by eye from the stack. This only needs to actually be run the first time around if the sample remains static, which it seems to.

```
start  =  1065 # Beginning of the center range.
end    =  1075 # End of the center range.
delta  =  0.1  # The iterative center adjustment.

# We write slices from 9 to 11 in the stack. Set dpath string to the output folder.
write_center(data[:,9:11,:],
     theta,
     dpath       =  '',
     cen_range   =  (start, end, delta))
```

The reconstruction is performed as a loop, so we define this as a function which takes the center of rotation and the time of the acquisition as arguments and writes the output back to disk.

```
def reconstruct(CR, time):
        re    =  CR
        out   =  output_file + str(time)
```

```
for ii in range(num_chunk):
    if ii == 0:
        SliceStart  =  offset + ii     * chunk_size
        SliceEnd    =  offset + (ii+1) * chunk_size
    else:
        SliceStart  =  offset + ii*(chunk_size-margin_slices)
        SliceEnd    =  offset + SliceStart + chunk_size
        if SliceEnd > (offset+total_num_slices):
    SliceEnd  =  offset+total_num_slices

 data   =  tir.read_hdf5(file_name,
                         '/exchange/data_dark',
                         slc = ((time - 599, time), (SliceStart, SliceEnd,1)))

 white  =  tir.read_hdf5(flat_name,
                         '/exchange/data_dark',
                         slc = ((1,9), (SliceStart, SliceEnd,1)))

 dark   =  tir.read_hdf5(dark_name,
                         '/exchange/data_dark',
                         slc = ((1,9), (SliceStart, SliceEnd, 1)))
 data_size  =  data.shape
 theta      =  np.linspace(0,np.pi,num = data_size[0])
```

```
# Replace damaged and corrupt images.
data[0,:,:]  =  data[1,:,:]

# remove zingers (pixels with abnormal counts)
data   =  tomocuda.remove_outlier_cuda( data,  zinger_level, size = 15)
white  =  tomocuda.remove_outlier_cuda( white, zinger_level, size = 15)

# Normalise the freshly loaded data.
data  =  tomopy.prep.normalize.normalize(data, white, dark)
data  =  tomopy.prep.normalize.normalize_bg(data, air = 10)

# Destriping...
data  =  tomopy.prep.stripe.remove_stripe_fw(data,
                                             level = 6,
                                             wname = 'sym16',
                                             sigma = 2,
                                             pad = True)

# Phase contrast operation...
data  =  tomopy.prep.phase.retrieve_phase(data,
                                          pixel_size = pxl,
                                          dist = z,
                                          energy = eng,
                                          alpha = rat,
                                          pad = True)
```

```
# Reconstruct the stack.
data_recon = recon(data,

# Write the reconstruction to disk.
tir.writer.write_tiff_stack(data_recon[np.int(margin_slices/2):
    (SliceEnd-SliceStart - np.int(margin_slices/2)),:,:],
                axis      = 0,
                fname     = out,
                start     = SliceStart+np.int(margin_slices/2),
                overwrite = True)
```

We call the previously defined function in an iterative for loop to reconstruct the stack. Centres of rotation are calculated and then verified by eye before we execute. Output is written to STDOUT for monitoring and debugging. Print some output for monitoring as well. This helps us keep track if it all goes wrong.

```
times  =  [] # Integer array of acquisition times.
ROT    =  [] # Floating point array of rotation centers.

print("Total Iterations: " + str(len(ROT)))
for ii in range(0, len(times)):
    print("Iteration " + str(ii + 1) + " Started... " + str(datetime.datetime.now()))
    reconstruct(ROT[ii], times[ii])
    print("Iteration " + str(ii + 1) + " Ended... "   + str(datetime.datetime.now()))

print("Ended... " + str(now))
```

# Appendix D

# Finding a Unique Volume

This script cross-correlates a subset in the $x$ and $y$ planes in each slice in the $z$ direction, finds the maximum regression coefficient, and then extracts everything and reports the result to the user. This is a remarkably simple process and requires only a few lines of code. For this procedure we need `numpy` for matrix operations, `skimage.io` (scikit-image i/o) for loading of image data, and `match_template` frok `skimage.feature` for the cross correlation function. `glob` is required for filesystem operations. We may add `matplotlib.pyplot` for debugging if required, but don't carry that out here.

```
import numpy as np
from skimage import io
from skimage.feature import match_template
import glob

# import matplotlib.pyplot as plt
# %matplotlib inline
```

This is all carried out on 8-bit lossy compressed (jpg in this case) images. The target subset is loaded from the jpg file `Subset.jpg` as provided in the following cell. We sort alphanumerically to get the stack in order.

```
curslice = '/home/james/Data/Subset.jpg'
files = sorted(glob.glob('/example/stack/*.jpg'))
```

Read the region of interest into the `ROI` matrix. Then iterate through the stack, sort it, and place each path into the `files` array.

```
ROI = io.imread(curslice)
results = np.zeros((len(files), 3))
```

Now we iterate through the stack, load the slice to memory, and cross correlate. The `print()` function is used for debugging and most of the time remains deactivated as shown. The result image is written to the `result` matrix. `np.unravel_index` allows us to address the flat array as a tuple of coordinate indices, and we can address this as, for example here, `result[y,x]`.

```
for ii in range(0, len(files)):
    #print("Image " + str(ii + 1) + ' of ' + str(len(files)))
    IMAGE = io.imread(files[ii])
    result = match_template(IMAGE, ROI)

    ij = np.unravel_index(np.argmax(result), result.shape)
    x,y = ij[::-1]
    R = result[y,x]

    results[ii][0] = R
    results[ii][1] = x
    results[ii][2] = y
```

We pull the z location as the maxima of the regression coefficient in the $z$ direction, and then extract the coordinate location of this position from the vector. Provide some output.

```
zloc = np.argmax(results[:,0])
        xloc = results[zloc,1]
        yloc = results[zloc,2]

        print("Success!")
        print("x Location: " + str(xloc))
        print("y Location: " + str(yloc))
        print("z Location: " + str(zloc))
```

# Appendix E

# Characterising the Pore Volume

This script allows for a pore size distribution to be generated as the result the calling of a function which returns the size distribution for further processing. Explanation is provided in commented lines. The following packages are required: `matplotlib.pyplot` for data visualisation. `glob` for filesystem parsing. `skimage` (scikit-image) for image processing. `scipy.stats` for statistics functions, in this case the standard error `sem` measurement.

```
import matplotlib.pyplot as plt
%matplotlib inline

import glob
import numpy as np
from skimage import data, io, filters, util,
from skimage import exposure, measure, morphology
from scipy.stats import sem

from matplotlib import rc
```

```
rc('font',**{'family':'serif','serif':['Times']})
rc('text', usetex=True)
from os.path import join

pagewidth = 6.12325
goldenrat = 1.61803398875
colors = ['#1b9e77',
          '#d95f02',
          '#7570b3',
          '#e7298a',
          '#66a61e',
          '#e6ab02']
```

Two assistance functions are first defined which calculate the diameter of a circle and volume of a cylinder from input.

```
def circ_area(diameter):
    return (np.pi * (diameter**2)) / 4

def cylinder_volume(diameter, depth):
    return ((np.pi * (diameter**2)) / 4) * depth
```

Define the function for stack processing. Calls to the function take the following arguments... `instack` The input stack directory - optional but required if `inbinfile` is undefined. `size` The size of the volume of interest - required. `startx` The starting $x$ location of the VOI - required. `starty` The starting $y$ location of the VOI - required. `nbins` The number of bins in the output histogram - required. `diamcutoff` The diameter cutoff of the output histogram - required. `inbinfile` An input binary file * optional. `outfile` An output binary file * optional.

```
def gen_distribution(instack, # The input stack.
                     size,              # The VOI Size
                     startx,            # The VOI x Location
                     starty,            # The VOI y Location
                     diamcutoff,        # The maximum allowed diameter.
                     inbinfile=None,    # An input binary file*.
                     outbinfile=None): # An output binary file*.
                                        # * = Optional

    # Load the directory from disk and sort alphanumerically.
    files = sorted(glob.glob(instack))

    # Record the depth of the stack
    # Calculate the area and volume of the VOI.
    depth = len(files)
    area   = size ** 2
    VOI_volume = area * depth
    print("Stack " + instack)
    print("Iterating through stack (depth " + \
    str(depth) + ") and loading to RAM...")


    # Read the first file from the stack and crop to the required dimensions.
    testdata = util.invert(io.imread(files[0]))[starty:starty + size, startx:startx + size]
    testdata = exposure.rescale_intensity(testdata,out_range=(0, 2**31 - 1))
```

```
# Show the image (debugging).
plt.imshow(testdata, cmap='gray')
plt.colorbar()
plt.show()

# If we've not got a binary input file continue.
# Otherwise load it from disk.
if (inbinfile == None):
    volume = np.zeros((depth, size, size), dtype=np.uint8)

markerpoints = np.arange(0, depth, 250)
for ii in range(0, depth):
    if (ii in markerpoints):
        print(r"Iteration " + str(ii))

# Load the slice from the disk and crop it.
this_slice   = util.invert(io.imread(files[ii]) \
                           [starty:starty+size, \
                           startx:startx+size])

# Produce a histogram (hist, bins).
hist, bins    = np.histogram(this_slice, bins='auto')
# Smooth the histogram down a bit.
smoothed_hist = hanning_smooth(hist, window_len = 26)
```

```
# Calculate the first order differential of the histogram.
diff_hist      = np.diff(smoothed_hist)
# Rebin the histogram after smoothing to resolve the correct location
bins           = np.linspace(bins[0], bins[-1], len(smoothed_hist))
# Perform the thresholding operation
cutoff         = bins[np.argmax(diff_hist)]

# Write the thresholded slice back to memory.
volume[ii]       = (this_slice < cutoff).astype(np.uint8) * 1
    print("Complete")
print("")
else: # Ignore everything if we've already got a binary stack.
    print("We already have a binary stack defined.")
    volume = np.load(inbinfile)


# If we've selected to write a binary file back to disk write it here.
if (outbinfile != None):
    print("inary stack output has been defined. Writing to disk.")
    np.save(outbinfile, volume)

# Now we label the thresholded stack in 3D.
# We could do this slice-wise, but this results in repeated labels.
print("")
print("Labelling thresholded stack.")
```

```
# Optional: Do a binary erosion to correct for any beam hardening.
# We do not carry this out here.
#volume  = (morphology.binary_erosion(volume, morphology.cube(3)))

# Label the volume as described above.
labels  = measure.label(volume)

# Determine the properties of each region.
regions = measure.regionprops(labels)

print("Calculating areas, diameters, and volumes.")
# Set some instrument constants...
ps = 0.875      # The pixel size is 0.875 um
pa = 0.875 ** 2 # The pixel area is 0.875 * 0.875 um^2
pv = 0.875 ** 3 # The pixel area is 0.875 * 0.875 * 0.875 um^3
# Allocate some vectors to store areas, diameters, and the volume.
areas   = np.zeros(len(regions))
diams   = np.zeros(len(regions))
pvolume = np.zeros(len(regions))

# Measure the diameter of each labelled region, calculate the volume.
for ii in range(0, len(regions)):
    diams[ii]   = regions[ii].equivalent_diameter * ps
    pvolume[ii] = regions[ii].area * pv
```

```
# Determine the porosity of each slice by nonzero elements.
slice_porosities = np.zeros(len(volume))
for ii in range(0, len(volume)):
    slice_porosities[ii] = \
    np.round((np.count_nonzero(volume[ii]) / area) * 100, 1)

# Round this for a result which might actually be something worth reporting
porosity = np.round(np.mean(slice_porosities), 1)

# Determine the standard error and standard deviations.
error = np.round(sem(slice_porosities), 2)
stdev = np.round(np.std(slice_porosities), 2)

# Determine the volume we have sampled
sampled_volume = (((size * 0.875) ** 2) * (depth * 0.875) * 10**-9)

# Density of the cement (ish), calculate the mass sampled.
bd = 0.001978 # grams per cubic mm
sampled_mass = np.round(sampled_volume * bd, 4)

# Print some output for the user.
print("VOI Size:   " + str(size))
print("VOI Depth: " + str(depth))
print("Calculated Porosity of Volume: " + str(porosity) + "%")
```

```
    print("Standard Error:      " + str(error) + "%")
    print("Standard Deviation: " + str(stdev) + "%")
    print("Sampled Volume: " + str(sampled_volume) + " mm3")
    print("Sampled Mass:   " + str(sampled_mass) + " g")

    nbins = 20
    hist, diams = np.histogram(diams[diams < diamcutoff], bins=nbins)
    volumes = cylinder_volume(diams[1:], ps) * hist
    print("")

    return (diams[2:],
            volumes[1:],
            porosity,
            stdev,
            error,
            sampled_volume,
            sampled_mass)
```

### Assistance Code for Visualisation

The execution of this is optional. This allows us to configure the script to the parameters we desire.

```
instack  = '/example/stack/*.tiff'
files = sorted(glob.glob(instack))
depth = len(files)
```

```
size = 700
depth = len(files)
startx = 300
starty = 1200
startz = 1
area   = size ** 2
VOI_volume = area * depth

testdata = util.invert(io.imread(files[1050])) \
[starty:starty + size, startx:startx + size]
        testdata = exposure.rescale_intensity(testdata,
                                              out_range=(0, 2**31 - 1))
plt.imshow(testdata, cmap='gray',  extent=(0, 700, 0, 700))

plt.xlabel('ROI $x$ Location / $\mu$m')
plt.ylabel('ROI $y$ Location / $\mu$m')
plt.savefig('90pctIsolatedSlice_HP.pdf', bbox_inches='tight')
```

# Appendix F

# Quantifying Neutron Data

This script takes images acquired at the NEUTRA facility and calculates the moisture absorption of the sample (front location) and calibrates the moisture content by the step wedge method described in Chapter 7.

We take the `time` module for time (epoch) calculations the data for which are pulled from the fits header. `scikit-image` is used for matrix (image) calculations. `scipy.optimize` provides the `curve_fit` and `leastsq` least squares regression fitting functions. `curve_fit` provides flexibility in the functions to which a fit may be performed (not limited to linear, even though this is used here). `astropy.io` provides functions for reading `fits` data from the filesystem. `numpy` provides extensive matrix operations. `glob` provides file system manipulation functions. The remaining modules and settings are used for production of graphics by this script and visualisation which is mainly neglected in this script and left to the user.

```
import time

from skimage import data, io, filters
from scipy.optimize import curve_fit
from scipy.optimize import leastsq
```

```
import astropy.io
from astropy.io import fits
import numpy as np
import glob

import matplotlib.pyplot as plt
from mpl_toolkits.axes_grid1 import make_axes_locatable
from matplotlib import rc
rc('font',**{'family':'serif','serif':['Times']})
rc('text', usetex = True)
%matplotlib inline

# Page width and height dimensions targeted at the thesis.
# Adjust as necessary, units inches.
pagewidth  =  6.12325
pageheight  =  8.82063
goldenrat  =  1.61803
colors  =  ['#1b9e77', '#d95f02', '#7570b3', '#e7298a']
```

**Notes:**

This script is designed to run on high RAM systems (> ~16 GB) where every image in raw format can be loaded to memory. In lower memory systems re-write the script to enable slice-wise processing of data (put the entirety of the script in a for loop or similar).

Visualisations are clipped to a maxima of 27500 for the purposes of data rendering with no rescaling (all values below 27500 remain correct; those above are clipped to white). This prevents hotspots in the image reducing the visual range of the produced figure. All calculations are carried out on the fully unmodified dataset.

Begin by defining some kind of a function for smoothing of data. Here we use a hanning window of defined length 50. This should be adjusted to provide the best result in the dataset being analysed.

```
def smooth(arr):
    cut_arr  =  np.r_[arr[length-1:0:-1], arr, arr[-2:-length-1:-1]]
    window   =  np.hanning(50)
    return np.convolve(w/w.sum(), cut_arr, mode = 'valid')
```

Pull data from the filesystem. File paths from all uptake, dark current, open beam, dry sample, black beam, wet and dry wedge images are defined from the filesystem and sorted alphanumerically. File paths conform to UNIX conventions.

```
files  =  sorted(glob.glob('WET/*.fits'))
dark   =  sorted(glob.glob('DARK/*.fits'))
openb  =  sorted(glob.glob('OB/*.fits'))
dry    =  sorted(glob.glob('DRY/*.fits'))
black  =  sorted(glob.glob('BB/*.fits'))
wedges_wet   =  sorted(glob.glob('Wedges/wedge_wet_sample_*.fits'))
wedges_dry   =  sorted(glob.glob('Wedges/wedge_dry_sample_*.fits'))
```

Load the first file and get width and height data from the header. We also take the total number of files here. Return some output to the user for debugging and good measure.

```
w  =  fits.open(files[0])[0].header['NAXIS2']
h  =  fits.open(files[0])[0].header['NAXIS1']
```

```
nfiles  =  len(files)
ndark   =  len(dark) - 1 # Final dark acquisition appears corrupt!
nopenb  =  len(openb)
ndry    =  len(dry)
nblack  =  len(black)
print('Width: ' + str(w) + ', ' + 'Height: ' + str(h))
print('Count: ' + str(nfiles))
print('Dark:  ' + str(ndark))
print('Open:  ' + str(nopenb))
print('Dry:   ' + str(ndry))
print('Black  ' + str(nblack))
```

Load Proton Doses from the ProtonDose.dat file. This is provided as output from the beamline. The grayscale intensity varies with the proton dose (low dose = low intensity). The mean proton dose is determined and a factor produced to normalise every image generated to the mean proton dose.

```
ProtonDoses  =  np.genfromtxt('ProtonDose.dat')
factors  =  np.empty(len(ProtonDoses))
meandose  =  np.mean(ProtonDoses)
for ii in range(0, len(factors)):
    factors[ii]  =  meandose / ProtonDoses[ii]
```

## Epoch Timestamp Calculation

Strip header data and calculate the timestamp of the epoch to each image i/o. It is assumed the i/o time is the same as the capture time. These data can also be used to verify the time-step of the instrument. Subtract time zero from each time stamp to give the acquisition time in seconds, taking zero as the first image.

```
times  =  np.zeros(len(files))
for ii in range(0, len(files)):
    hdul  =  fits.open(files[ii])
    date_time  =  hdul[0].header['DATE']
    pattern  =  '%Y-%m-%dT%H:%M:%S'
    times[ii]  =  int(time.mktime(time.strptime(date_time, pattern)))

zero  =  times[0]
for ii in range(0, len(times)):
    times[ii]  =  times[ii] - zero

delta  =  times[1] / 3600
```

## Dark Current and Open Beam Corrections

The dark current and open beam files are now loaded from the filesystem to three dimensional arrays. Corrections to dark current and open beam are carried out using these images which are acquired at the beamline during acquisition of the dataset. The dark current correction is a simple subtraction, while the open beam correction is a division-rescale operation.

### Dark Current (DC)

The dark current data accounts for systematic camera noise (noise which remains constant). Load dark current data and calculate the mean dark current value. This gives the noise which remains constant in every image. It is not possible to account for specular noise in acquisitions due to the variability in these data. The array is also flipped to place the sample region at the bottom of the image.

```
DC  =  np.empty((ndark, w, h))
for ii in range(0, len(DC)):
    DC[ii]  =  fits.getdata(dark[ii])[0]

DC_correction  =  np.flip(np.mean(DC, axis = 0), axis = 0)

fig  =  plt.figure(figsize = (pagewidth, pagewidth / goldenrat))
plt.imshow(DC_correction / 1000, cmap = 'gray')
plt.xlabel('x Location / px (a.u.)')
plt.ylabel('y Location / px (a.u.)')
plt.colorbar(label  =  r'Dark Current / $\times 1000$ Count(s) (a.u.)')

plt.savefig("Figures/DC.pdf", bbox_inches = 'tight')
```

### Open Beam (OB)

This is a similar operaton. The open beam data are loaded from the filesystem and the mean is once again taken for all open beam frames. The correction calculation requires a rescale factor (division-rescale operation).

```
OB  =  np.empty((nopenb, w, h))
for ii in range(0, len(OB)):
```

```
    OB[ii]  =  fits.getdata(openb[ii])[0]

OB_correction  =  (np.flip(np.max(OB, axis = 0), axis = 0) - DC_correction)
OB_correction  =  OB_correction.clip(min = 1)
OB_rescale_fac  =  np.mean(OB_correction)

fig  =  plt.figure(figsize = (pagewidth, pagewidth / goldenrat))
plt.imshow(OB_correction / 1000, cmap = 'gray')
plt.xlabel('x Location / px a.u.')
plt.ylabel('y Location / px a.u.')
plt.text(1250, 300, "Beam Shutter, Top", ha = 'center', color = '#ffffff')
plt.text(1250, 1750, "Scintillator", ha = 'center', color = '#000000')
plt.colorbar(label  =  r'Open Beam ($\times 1000$) Count(s) / a.u.')

plt.savefig("Figures/OB.pdf", bbox_inches = 'tight')
```

**Black Body (BB)**

Black body images account for scatter from the mirror. These are loaded in an identical manner to all other images and a mean is calculated which accounts for noisy regions in the data which are reproducable.

```
BB  =  np.empty((nblack, w, h))
for ii in range(0, len(black)):
    BB[ii]  =  np.flip(fits.getdata(black[ii]), axis = 1)

BB_correction  =  ((np.mean(BB, axis = 0)) - DC_correction).clip(min = 1)
```

```
plt.imshow(BB_correction.clip(max = 27500), cmap = 'gray')
plt.colorbar()
```

### Dry Sample (DRY)

The final corrections are now loaded from the filesystem. These account for the effect of the dry sample and any artefacting resulting from this. A rescale factor is also determined.

```
DRY  =  np.empty((ndry, w, h))
for ii in range(0, len(DRY)):
    DRY[ii]  =  fits.getdata(dry[ii])[0]

DRY_mean  =  np.flip(np.mean(DRY, axis = 0), axis = 0)
DRY_Correction  =  ((((DRY_mean / OB_correction) * OB_rescale_fac))
   - DC_correction).clip(min = 1)
DRY_Correction  =  (DRY_Correction - BB_correction).clip(min = 0)
DRY_rescale_fac  =  np.mean(DRY_Correction)

plt.imshow(DRY_Correction.clip(max = 27500), cmap = 'gray')
plt.colorbar()
```

## Raw Data (RAW)

Load the raw data from the filesystem into RAM, correct for the dry sample uptake as images are loaded during the loop. When correcting for dark current it must be ensured that no values appear where the matrix becomes negative because of specular noise. The corrected acquisition is clipped to a minima of 1.0. We need to also ensure we NEVER divide by a negative or zero value.

Clipping to zero results in infinity `inf` values in the result so these data are clipped to unity, as are corrections for dry samples and open beam data. Corrections are also carried out for the proton dose at this point.

```
RAW  =  np.empty((nfiles, w, h))
mdry  =  np.mean(DRY)

for ii in range(0, len(RAW)):
    # Pull the raw data from disk and correct for the proton dose.
    rawdata   =  fits.getdata(files[ii])[0] * factors[ii]
    # Flip the raw data array (origin to bottom left) to match the human view.
    rawdata  =  np.flip(rawdata, axis = 0)
    # Subtract the dark current and correct for the open beam and dry sample.
    RAW[ii]  =  (rawdata - DC_correction)
    RAW[ii]  =  (RAW[ii] / OB_correction)  * OB_rescale_fac
    RAW[ii]  =  ((RAW[ii] / DRY_Correction) * DRY_rescale_fac)
    RAW[ii]  =  (RAW[ii] - BB_correction)
    # Clip the raw data to a minima of unity.
    RAW[ii]  =  RAW[ii].clip(min  =  1)

# Show the raw data for debugging purposes (if wanted)
# plt.imshow(RAW[-1].clip(max=27500), cmap='gray')
# plt.colorbar()
```

The sample has been corrected for dark current, open beam, dry data artefacts, and back scattering. Now each sample is cropped directly from the corrected raw data. The crop dimensions may be adjusted here by changing the x and y values. Width and height ought to remain constant for the experiment.

```
width   =  400
height  =  1050

x  =  340
y  =  1000
Sample2  =  np.empty((nfiles, height, width))
for ii in range(0, len(RAW)):
    Sample2[ii]  =  RAW[ii][y:y+height, x:x+width]

x  =  900
y  =  1000
Sample4  =  np.empty((nfiles, height, width))
for ii in range(0, len(RAW)):
    Sample4[ii]  =  RAW[ii][y:y+height, x:x+width]

x  =  1490
y  =  1000
Sample14  =  np.empty((nfiles, height, width))
for ii in range(0, len(RAW)):
    Sample14[ii]  =  RAW[ii][y:y+height, x:x+width]

x  =  2030
y  =  1000
Sample16  =  np.empty((nfiles, height, width))
for ii in range(0, len(RAW)):
```

```
    Sample16[ii]  =  RAW[ii][y:y+height, x:x+width]

plt.imshow(Sample2[-1].clip(max = 27500), cmap = 'gray')
plt.colorbar()
```

Front locations are now calculated. The mean grayscale value across the $y$ direction is integrated in the $x$. This is smoothed using the convolution of a Hann window across the data as per the previously defined function.

```
s2_frontlocs   =  np.empty(len(files))
s4_frontlocs   =  np.empty(len(files))
s14_frontlocs  =  np.empty(len(files))
s16_frontlocs  =  np.empty(len(files))

for ii in range(0, len(files)):
    profile  =  smooth(np.mean(Sample2[ii].clip(max  =  18000))
    s2_frontlocs[ii]  =  height - np.argmin(np.diff(profile))

    profile  =  smooth(np.mean(Sample4[ii].clip(max  =  18000), axis = 1))
    s4_frontlocs[ii]  =  height - np.argmin(np.diff(profile))

    profile  =  smooth(np.mean(Sample14[ii].clip(max  =  18000), axis = 1))
    s14_frontlocs[ii]  =  height - np.argmin(np.diff(profile))

    profile  =  smooth(np.mean(Sample16[ii].clip(max  =  18000), axis = 1))
    s16_frontlocs[ii]  =  height - np.argmin(np.diff(profile))
```

## Quantification by Step Wedges

Quantification of the moisture content of the system is carried out by calibrating images to the grayscale value produced by known quantities of water placed in front of a sample. Load dry and wet wedges into memory. Correct for dark current, open beam, and dry samples. Rescale the corrected array and write to a text image which can be loaded to a third-party package to determine the grayscale intensity of each block.

```
dry_wedges  =  np.empty((len(wedges_dry), w, h))
wet_wedges  =  np.empty((len(wedges_wet), w, h))
corr_wedges  =  np.empty((len(wedges_dry), w, h))

for ii in range(0, len(wedges_dry)):
    rawdata  =  fits.getdata(wedges_dry[ii])[0]
    dry_wedges[ii]  =  (np.flip((rawdata)) - DC_correction).clip(min = 1)

    rawdata  =  fits.getdata(wedges_wet[ii])[0]
    wet_wedges[ii]  =  (np.flip((rawdata)) - DC_correction).clip(min = 1)

mean_dry  =  np.mean(dry_wedges, axis = 0) / OB_correction
mean_wet  =  np.mean(wet_wedges, axis = 0) / OB_correction
corr_dry_wedges  =  (mean_dry * OB_rescale_fac - BB_correction)
corr_wet_wedges  =  (mean_wet * OB_rescale_fac - BB_correction)

DRY_rescale_fac  =  np.mean(corr_dry_wedges)
DRY_Correction  =  (corr_wet_wedges / corr_dry_wedges) * DRY_rescale_fac
```

```
np.savetxt('/home/james/Data/wedges.txt',
   DRY_Correction.clip(max = 27500)[1000:1750,1385:1550])
```

Grayscale intensity values are held in the `GSV` array, with upper and lower bounds in `UB` and `LB` respectively. The pixel volume is known, and the percentage equivalent of each step thickness is calculated knowing the pixel geometry.

Two functions are defined. A linear $y = mx + c$ function and a function which returns $x$ as a function of $y$. Optimization is carried out using the `scipy.optimize` module and is applied to the mean, upper, and lower bounds of the data. There is also some visualisation in this code.

```
# Grayscale value of each step wedge externally reported.
GSV  =  [13270.980, 12284.201, 11733.692,
         10982.286, 10483.478, 10270.661,
         10334.157, 10368.810, 9716.7920,
         9117.4940]

# Lower bound of each step wedge externally reported.
LB   =  [12635.052, 11611.407, 10904.477,
         10253.253, 9177.3310, 8379.4360,
         10904.687, 9278.4990, 8478.0520,
         7471.5600]

# Upper bound of each step wedge externally reported.
UB   =  [13982.405, 13090.503, 12363.196,
         12548.141, 10938.053,
         11501.653, 12972.963, 11156.311,
         10998.677, 10035.324]
```

```
pixel_volume  =  0.1 * 0.1 * 40
contents      =  np.arange(0.5, 5.1, 0.5) / pixel_volume

def func(m, x, c):
    return m * x + c

def invfunc(m, y, c):
    return (y - c) / m

# Fit to the mean Grayscale Value
popt, pcov  =  curve_fit(func, contents, GSV)
GSV_mval    =  popt[0]
GSV_cval    =  popt[1]

# Fit to the Upper Bound
popt, pcov  =  curve_fit(func, contents, LB)
LB_mval     =  popt[0]
LB_cval     =  popt[1]

# Fit to the Lower Bound
popt, pcov  =  curve_fit(func, contents, UB)
UB_mval   =  popt[0]
UB_cval   =  popt[1]
```

```
# Quick visualisation for debugging.
fig  =  plt.figure(figsize = (pagewidth, 3))
plt.scatter(contents, np.divide(GSV,1000), marker = 'x', c = 'k')
xrange  =  np.arange(1, 12.5, 0.1)

yvals  =  func(GSV_mval, xrange, GSV_cval)
plt.plot(xrange, yvals / 1000, c = 'k', ls = '--', label = 'Linear Fit')

yvals  =  func(UB_mval, xrange, UB_cval)
plt.plot(xrange, yvals / 1000, c = 'k', ls = '--',
 alpha = 0.5, label = 'Min. / Max. Bounds')

yvals  =  func(LB_mval, xrange, LB_cval)
plt.plot(xrange, yvals / 1000, c = 'k', ls = '--', alpha = 0.5)

plt.legend()

plt.xlabel(r"Moisture Content / \%")
plt.ylabel(r"Mean Grayscale Intensity / $\times 1000$ a.u.")
plt.minorticks_on()
ticks  =  plt.xticks(np.arange(0, 13.1, 1))
plt.savefig("LSQFit.pdf", bbox_inches = 'tight')
```

### Final Calibration

The final calibration computes a new equivalent intensity where the intensity defined is the calibrated moisture content of the sample. This is done iteratively for the entire dataset.

```
for ii in range(0, len(Sample2)):
    Sample2[ii]   =  invfunc(GSV_mval, Sample2[ii],  GSV_cval).clip(min = 0)
    Sample4[ii]   =  invfunc(GSV_mval, Sample4[ii],  GSV_cval).clip(min = 0)
    Sample14[ii]  =  invfunc(GSV_mval, Sample14[ii], GSV_cval).clip(min = 0)
    Sample16[ii]  =  invfunc(GSV_mval, Sample16[ii], GSV_cval).clip(min = 0)
```

What is left is a series of three dimensional arrays which contain moisture content for each pixel in each acquisition. We also have a series of vectors containing the location of the front. These may then be used for visualisation (not shown here). The porosity may also be calculated from these data assuming full saturation of each pore (nonzero array elements).